Vietnam Ministry of Science and Technology

P-ISSN 2525-2461 • E-ISSN 2615-9937

Vietnam Journal of Science, Technology and Engineering

MARCH 2023 • VOLUME 65 NUMBER 1

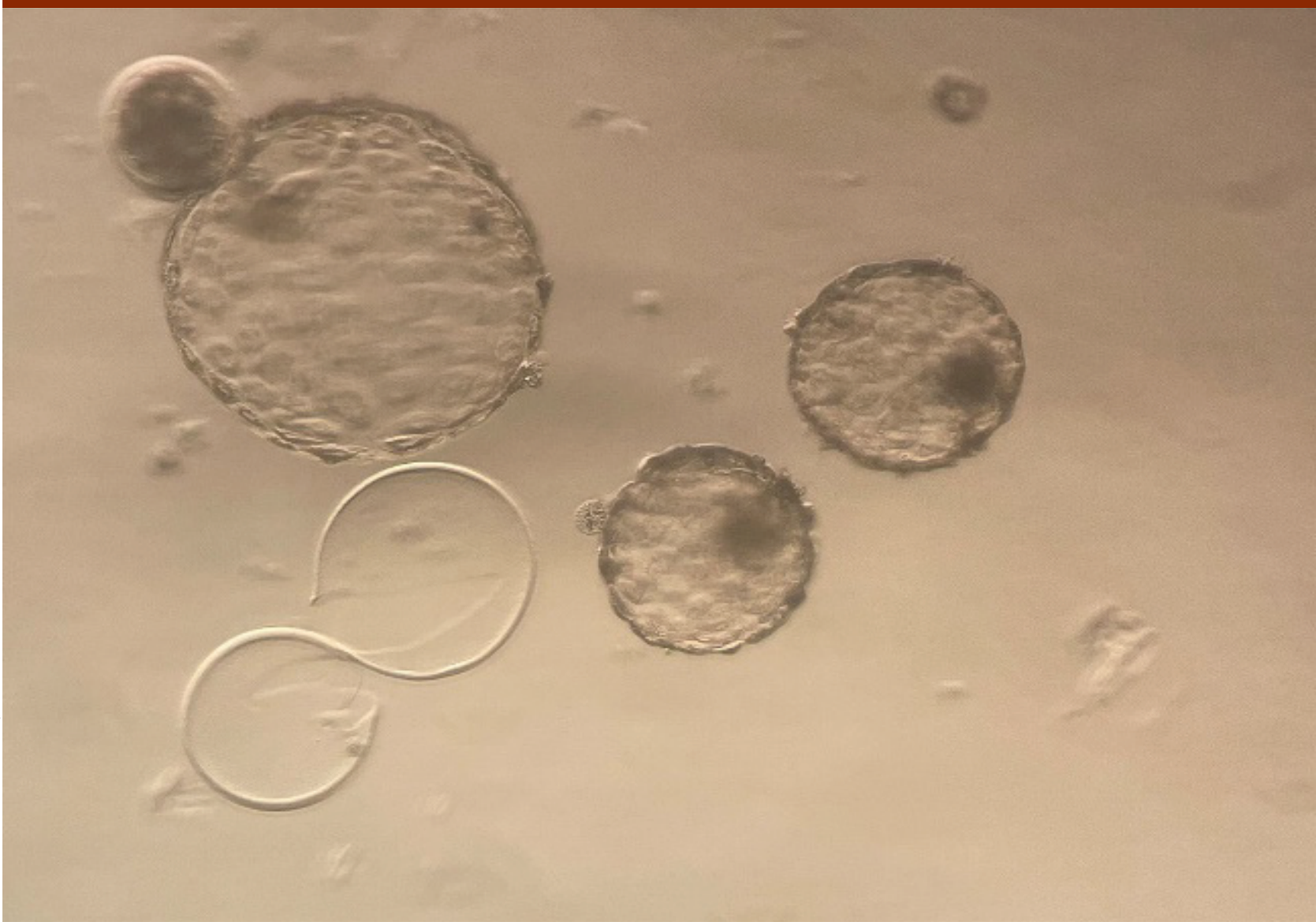

Influence of fetal calf serum on the production of bovine embryos *in vitro*

VIETNAM JOURNAL OF SCIENCE, TECHNOLOGY AND ENGINEERING * MARCH 2023 * VOLUME 65 NUMBER 1

vietnamscience.vn or vietnamscience.vjst.vn

Vietnam Journal of Science, Technology and Engineering (VJSTE) **is a quarterly double-blind peer-reviewed academic journal. VJSTE publishes research articles and review articles in all areas of science, technology and engineering with the focus on the physical sciences, life sciences and environmental sciences including the following topics:**

- **Physical Sciences**
- **Agriculture**
- **Medicine**
- **Pharmacology**
- **Biology**
- **Biotechnology**
- **Biomedical Applications**
- **Ecology**
- **Climatology**
- **Environmental Science.**

CLASSIFICATION SCHEME

1. **Mathematics and Computer Science**
   - **1.1. Mathematics**
   - **1.2. Computer Science**
   - **1.3. Computational Science**
2. **Physical Sciences**
   - **2.1. Physics**
   - **2.2. Chemistry**
   - **2.3. Engineering**
3. **Life Sciences**
   - **3.1. Agriculture**
   - **3.2. Medicine**
   - **3.3. Pharmacology**
   - **3.4. Biology**
   - **3.5. Biotechnology**
   - **3.6. Biomedical Applications**
4. **Earth Sciences**
   - **4.1. Geography**
   - **4.2. Geology**
   - **4.3. Geophysics**
   - **4.4. Oceanography**
5. **Environmental Sciences**
   - **5.1. Ecology**
   - **5.2. Climatology**
   - **5.3. Environmental Science**

CONTENTS

MARCH 2023 • VOLUME 65 NUMBER 1

CONTENTS

MARCH 2023 • VOLUME 65 NUMBER 1

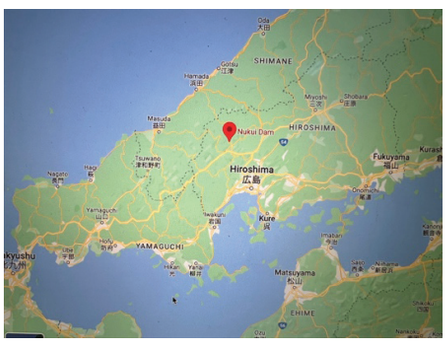

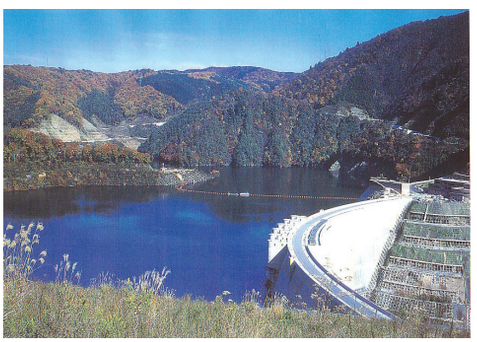

LIFE SCIENCES

ENVIRONMENTAL SCIENCES

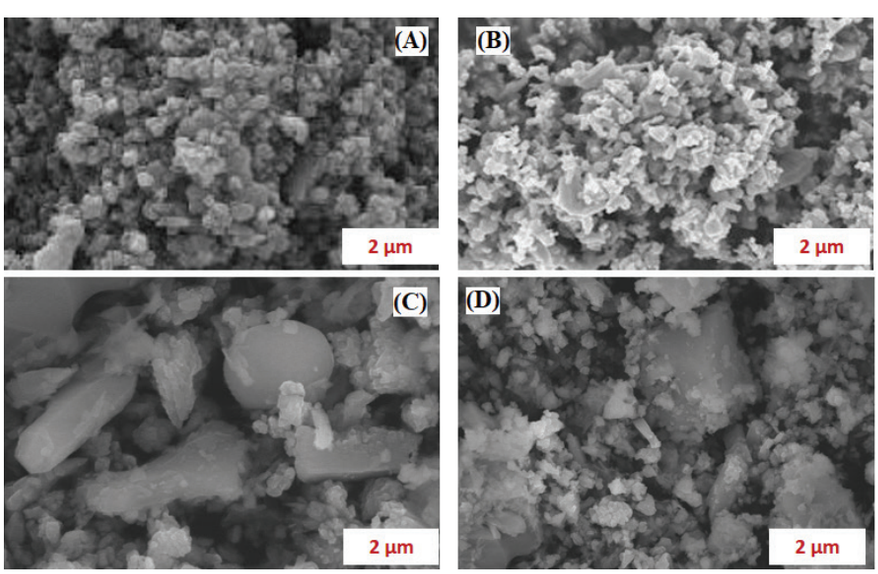

DOI: 10.31276/VJSTE.65(1).03-08

3D printable concrete: Mixture design and laboratory test methods

Thi Loan Pham[1, 2*], Xiao Jian Zhuang[1], Thi Hoai Thu Nguyen[2], Phan Anh Nguyen[2], Duy Thanh Trinh[2], Trong Quang Do[2]

[1]Department of Structural Engineering, Tongji University, 1239 Siping Road, Shanghai, PR China
[2]Department of Civil Engineering, Haiphong University, 171 Phan Dang Luu, Ngoc Son Ward, Kien An District, Hai Phong City, Vietnam

Received 8 December 2021; revised 22 February 2022; accepted 2 March 2022

Abstract:

Experimental results of the mix design and fresh properties of a proposed concrete for 3D printing are presented in this paper. Layer-by-layer sample components were built by the designed concrete and extruded through a nozzle. The two most critical rheological properties of the designed mix are extrudability and buildability as they are both highly influenced by mix proportion and the presence of superplasticizers. Therefore, this study focused on mix proportion design approaches and laboratory test methods, which generally allowed access to the fresh concrete's printable properties. Because they are efficient and convenient in construction, materials including cement, fly ash, natural sand, and superplasticizer were selected for mixing proportion analysis. Slump-flow tests, V-funnel tests, buildability tests, and extrudability tests were also employed to access the printability of the proposed mixture in this study. This first analysis on the mixture design approach and laboratory test methods to evaluate the printable properties of 3D-printable concrete can be considered a reference and orientation to further develop 3D printing technology in Vietnam.

Keywords: **buildability test, extrudability test, slump-flow test, V-funnel test, 3D concrete printing technology.**

Classification numbers: **2.1, 2.3**

1. Introduction

Researchers worldwide have been paying attention to 3D printing, also known as additive manufacturing, for a few decades. The idea of 3D printing has also attracted the attention of engineers, architects, and investors because of its capability to transform a drawing into an object. Since the construction industry has adopted this new technology, its usage needs to be extended beyond making quick prototypes to the final production of structures. Since 2014, many well-known buildings, bridges, and architectural icons have been constructed on-site by applying 3D printing technology [1-5]. These achievements offer insights into the full potential that 3D printing technology can bring to the construction industry. However, there are only a few published documents about material requirements for 3D printability despite its rapid growth. In a successful process extrusion, i.e., in order to be extruded through the nozzle, the material must be flowable enough. Nevertheless, when a layer is extruded, it must have sufficient shear strength to resist deformation due to its self-weight and the weight of the layers printed above it. From a rheological aspect, while inside the pump and nozzle, the material must be liquid-like with low viscosity, but once printed out, it must transition into solid-like behaviour with enough strength to prevent deformation.

Fortunately, contour crafting (CC) and binder jetting are successful printing methods for cement-based materials [6, 7]. Moreover, attempts to develop appropriate printing methods for cement-based materials have been investigated by many researchers as well [8-13]. In this study, the authors employed the results of J. Jo, et al. (2020) [14] and C. Zhang, et al. (2019) [15] as basic directions to design the mix proportion of the tested concrete. The main constituents of the mixtures mentioned here are cement, sand, and fly ash, which has been selected by other authors as well. Then, V-funnel tests, buildability tests, and extrudability tests were carried out to reveal the printability of the concrete. The V-funnel and buildability tests are simple and relatively

*Corresponding author: Email: loanpt297@gmail.com

reliable tests [16]. This first analysis on the mixture design approach and laboratory test methods to evaluate printable properties of 3D printing concrete can be considered a reference and orientation to develop 3D printing technology in Vietnam.

In summary, this study suggests a mix proportion design approach and laboratory tests that access printable properties of fresh concrete with convenient applications.

2. Materials and process for printability

The sources of the materials used in this work can be found in previous research by the authors [17]. For the reader's convenience, the contents are briefly re-introduced. Cement Portland by Chinfon (OPC) and Fly-ash (FA) by Hai Phong Thermal Power Plant were used to form the binder component. A commercially available manufactured sand with a nominal maximum aggregate size of 1.25 mm was used. Superplasticizer SikaPlast-398 (SP) was used to adjust the workability of the fresh concrete. The constitutions of the concrete are presented in Fig. 1.

(A) Cement (B) Fly ash (C) Sand (D) Superplasticiser

Fig. 1. Constitutions of the proposed concrete.

Fresh and hardened concrete mechanical properties of a mix design are required to meet the performance, as shown in Fig. 2.

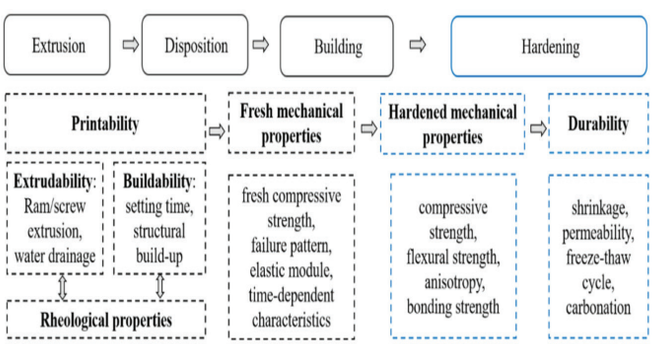

Fig. 2. The performance of 3D printing concrete during the printing and hardened processes [18].

Compared to traditional construction, fresh concrete properties play an essential role in concrete development. Therefore, the printability of the concrete is firstly investigated in the process of 3D printing technology. The ability of the material and nozzle combination to produce a well-controlled filament is related to printability [19]. In this research, the ability of fresh concrete to (1) be extruded continuously, without surface fracture; (2) not cause jamming or clogging of the nozzle; and (3) build up with acceptable deformation before setting are all considered printability characteristics, which has also been explained in other words by authors [19-22]. These characteristics can also be considered as extrudability and buildability.

3. Mixture proportion design

Investigations on the effect of material composition on the properties of 3D-printability have been carried out by many other authors [10, 11, 18, 20, 21, 23-25]. While there is still limited research on mixture design approaches, some highlighted results can be found in other research [9, 14, 15, 26]. Among these advances, the results of C. Zhang, et al. (2019) [15] and J. Jo, et al. (2020) [14] were referred to when proposing the mix proportions.

According to J. Jo, et al. (2020) [14], the amount of sand can be determined based on the equation below:

$$S=0.4B \quad (1)$$

where B is the binder (mm); S is the amount of sand with a diameter smaller than 0.7 mm.

Following the authors, they added a sand with 0.7 mm maximum size to avoid bleeding or clogging while printing to produce a suitable mortar mixture. According to C. Zhang, et al. (2019) [15], the amount of sand can be determined based on the equation below:

$$m_{1.18}=4.22F+351 \quad (2)$$

Note: From natural sand by sieve of 1.18 mm square hole is fine sand; F is the flowability of cement paste (mm); $m_{1.18}$ is the amount of sand (gram/litre).

The research results of Eq. (1) and Eq. (2) help to quantify the ratio of binder and fine aggregate (sand). However, other factors used in this study including fly ash, superplasticizer ratio, water ratio, and sand diameter are different from the studies of the two above authors. Therefore, concrete with the mixture proportions designed in this study should be further evaluated for printability by the test methods presented in this study.

To calculate the amount of sand, the flowability test of the binder needs to be done for different values of slump flow. The test procedure can be referred to in Ref. [27]. To replace the maximum amount of fly ash to cement, but also while minimizing the effects on the compressive strength of the concrete, the ratio between fly ash and cement was determined to be 4:6. The water to cement ratio was 0.3 because the workability of the concrete was adjusted with a superplasticizer. The fine sand used in this study is from natural sand filtered through a 1.25-mm square hole sieve, which is much larger than that of Junho and only a little larger than that of Zhang. The flow slump value was then measured as 240 mm, as shown in Fig. 3.

Fig. 3. Flow-slump of the tested binder.

According to the Eq. (1) and Eq. (2), the amount of sand was calculated. However, the ratio of sand to binder by Zhang and Junho has a large gap, so the authors propose a range from 0.4 to 2.4 with specific values. Then, five initial mixes with different proportions of sand/binder were designed, as shown in Table 1.

Table 1. Concrete mixture proportion.

Mix label	Fly ash to cement	Water to binder	Sand to binder	SP to binder (%)
Z_2.4	0.667	0.30	2.4	1.2
J_0.4	0.667	0.30	0.4	0.2
M1_1.1	0.667	0.30	1.1	0.6
M2_0.8	0.667	0.30	0.8	0.4
M3_0.5	0.667	0.30	0.5	0.2

Note: Ratio by weight and to the binder.

4. Laboratory test methods and results

4.1. V-funnel test

The viscosity and the deformability of fresh concrete can be evaluated with the V-funnel test. After filling the V-funnel with the prepared fresh concrete, it was lifted and the concrete was passed through the opening well with no segregation or jamming. According to previous research, this value of time, V_t, falls within the typical range of 9 to 25 s [16]. The time (Vt) to empty the concrete was listed in Table 2 with the range of 15 and 25 s corresponding to Z_2.4 and J_0.4, respectively. The test was carried out as shown in Fig. 4.

Table 2. The time (V_t) of the V-funnel tests.

Mix label	V_t (s)	Description
Z_2.4	9	Segregation/jamming
J_0.4	25	No segregation/no jamming
M1_1.1	11	Segregation but no jamming
M2_0.8	14	Segregation but no jamming
M3_0.5	24	No segregation/no jamming

(A) Z_2.4 **(B) J_0.4**

(C) M1_1.1 **(D) M2_0.8** **(E) M3_0.5**

Fig. 4. V-funnel tests.

According to Table 2, with V_t = 9, 11, and 14 s, the three mix labels Z_2.4, M1_1.1, and M2_0.8 had segregation. Meanwhile, segregation did not occur with the mix labels J_0.4 and M3_0.5. In the V-funnel tests, only mix label Z_2.4 caused jamming.

4.2. Buildability test

The slump height remains of the concrete cylinder under the force of gravity can be used to evaluate the yield stress and the buildability of the tested concrete. The height and diameter of the cylinder mould were chosen to be the same value of 80 mm due to the previous research done by the authors [15]. Therefore, the buildability is assessed by the shape and the remaining height of the cylinder sample. If significant deformation is not observed after lifting the mould away, it can be concluded that the concrete has appropriate buildability.

The slumps of the mixtures are shown in Table 3. The concrete cylinder slump remained in a range from 8 to 22 mm, and the specimen did not deform after lifting the mould away, as shown in Fig. 5. These values mean that the concrete has enough solid ability.

Table 3. The slump of the samples in the buildability test.

Mix label	S (mm)	Description
Z_2.4	8	No deformation/appropriate buildability
J_0.4	22	Significant deformation/inappropriate buildability
M1_1.1	11	Lightly deformation/appropriate buildability
M2_0.8	12	Somewhat deformation/appropriate buildability
M3_0.5	13	A little deformation/appropriate buildability

(A) Z_2.4 (B) J_0.4 (C) M1_1.1

(D) M2_0.8 (E) M3_0.5

Fig. 5. The slump of the sample in the buildability test.

The concrete cylinder with mix label J_0.4 indicated an incapacity for buildability with a slump of 22 mm and unacceptable deformation. The four other mix labels, on the other hand, proved to be appropriate for buildability. The mix label Z_2.4 had a slump of the concrete cylinder at 8 mm with almost no deformation. On the other hand, the three mix labels M1_1.1, M2_0.8, and M3_0.5 demonstrated a modest deformation phenomenon with slumps of 11, 12, and 13 mm, respectively.

4.3. Extrudability test

The print system used in this study was designed and created based on the screw principle as presented in Fig. 6. The ability to transport the fresh concrete through a hopper and screwing system into a nozzle where it produces a continuous filament is considered extrudability. In this research, the extrudability was tested with filaments of 25 mm wide (printed from a 25 mm nozzle). The filaments must be homogeneous and continuously extruded without blockage, cracking, or segregation throughout the extrusion process. A printed sample, furthermore, must be well-shaped to retain its formation.

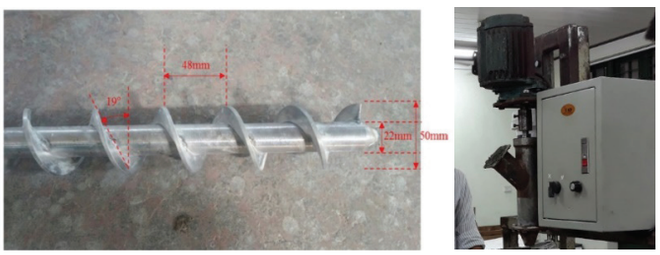

(A) Screw detail (used with permission from [14]) (B) Print-head system

Fig. 6. Screw and nozzle drive.

Table 4. Characteristics of printed mixtures.

Mix label	Extruded continuously	Blockage	Cracking/ segregation	Shape retention
Z_2.4	No	No	Seriously	Bad
J_0.4	Yes	No	No	Bad
M1_1.1	Yes	No	Yes	Acceptable
M2_0.8	Yes	No	Yes	Normal
M3_0.5	Yes	No	Yes	Good

In Table 4, the extrusion process was not continuous with only mix label Z 2.4, which had serous cracking and segregation without blocking resulting in poor form retention. Mix label J_0.4 failed to maintain good form despite a continuous extrusion demonstration that was free of blockage, breaking, or segregation. The three other mix labels M1_1.1, M2_0.8, and M3_0.5 were continuously extruded with satisfactory form retention and no blockage but did experience a breaking or segregation phenomenon as shown in Fig. 7.

(A) Z_2.4

(B) J_0.4

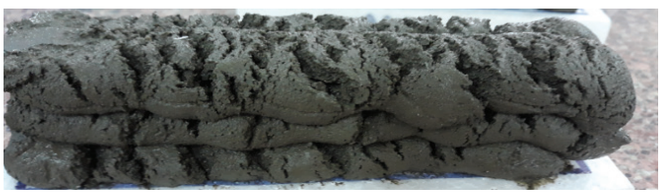

(C) M1_1.1

(D) M2_0.8

(E) M3_0.5

Fig. 7. Printed samples.

5. Results and discussion

Based on the investigation presented above, some highlighted discussions and suggestions can be given.

Firstly, a series of preliminary mixtures was tested to find out the maximum particle grading including sand, cement, and fly ash for extrudability. With the mechanics of the printing system as shown in Fig. 6, natural sand filtered through a 1.25-mm square hole sieve was available. Then, the mix of available particle combinations was experimented with the admixture dosages varied by 0.2-1.2% to approach the optimum flowability, buildability, and extrudability. Based on the present study, the authors developed a mix proportion design process as presented in Fig. 8.

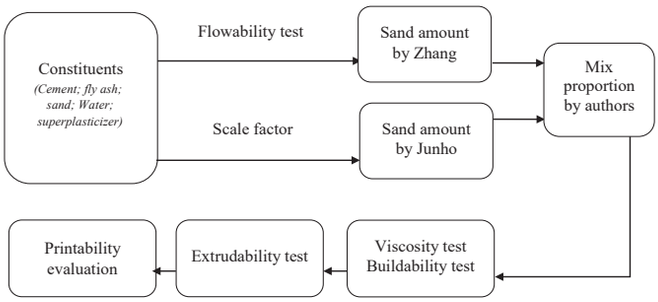

Fig. 8. Mix proportion design process proposed.

Secondly, the workability was significantly influenced by the dosage of the superplasticizer. In the series, increasing the superplasticizer dosage from 0.2 to 1.2% by weight of binder increased the workability, i.e., reduced V_t from 25 to 9 s (Table 2). The superplasticizer thus proved crucial for printing concrete to attain reasonable workability and high strength with a low water-binder ratio. However, ease of flow through the V-funnel does not equate to printability. In particular, the mix label Z_2.4 had a flow time of 9 s, but the printed concrete was too hard to guarantee the continuity of the printed filaments. The reason behind this is the amount of sand in this mixture was the largest.

Meanwhile, the printed pattern ensures continuity in the J_ model with a relatively long flow time of 22 s, but the printed filaments were seriously deformed. The reason is due to it having the least amount of sand and unreasonable additives. In the remaining samples, with a decrease in sand content and a corresponding decrease of superplasticizer, the flow time increased and the printability of the sample also gradually improved. This study found that assessing the workability of concrete through the V-funnel test is reasonable. However, the results of the flow time tests provide a relatively limited preliminary assessment of the printability of the concrete.

Thirdly, the qualitative relationship between buildability and extrudability is relatively straightforward. When the Z_2.4 mix produced a good result with an 8 mm slump, the extrudability test was a bit difficult to complete, and the printability test revealed that the sample did not satisfy the printable quality due to extensive cracking. Meanwhile, the extrudability test was easier to perform with the J_ 0.4 mix with a slump of 22 mm, but the result of the printability test showed that the sample did not meet the printable quality due to excessive deformation. The rest of the samples show an increasing slump, the extrusion test not difficult, and the print quality also improving. The mixtures M2_0.8 and M3_0.5 give the best print quality as captured in Figs. 7D, E.

Finally, owing to its great sensitivity to workability and extrudability, the ratio of sand to binder should not exceed 1.2, and the superplasticizer dosage should be tightly controlled.

6. Conclusions

Based on the test results of the first analysis on mixture proportion design approach, and the tests used to evaluate

rheological properties for the 3D printing concrete in Vietnam, some conclusions and suggestions are given:

(1) The mix proportion design process suggested in this study is reliable and feasible.

(2) The mixture proportion design approach presented herein is appropriate and reliable.

(3) The V-funnel test and buildability test employed in this study are efficient for designing and evaluating concrete before printing.

(4) The ratio between sand and binder should exceed 1.2, and the superplasticizer dosage needs to be tightly controlled.

(5) The assessment of printability through the extrudability test may be different when using different printing nozzles.

(6) Increasing the number of extrusion experiments is necessary for the recommendation of an optimal concrete mix for the screw printhead as performed in this study.

CRediT author statement

Thi Loan Pham: Conceptualization, Methodology, Data Analysis; Xiao Jian Zhuang: Supervision; Thi Hoai Thu Nguyen: Writing - Original draft preparation; Phan Anh Nguyen: Laboratory test; Duy Thanh Trinh: Laboratory test; Trong Quang Do: Reviewing and Editing.

ACKNOWLEDGEMENTS

The authors would like to acknowledge the financial support from the National Natural Science Foundation of China (51950410599), the material support from Thanh Hung Concrete Joint Venture Company, and the laboratory support at Haiphong University, Vietnam. The authors specially thank to Mr. Vu Hong Luan at VIDPOL Joint Stock Company for creating the experimental equipment.

COMPETING INTERESTS

The authors declare that there is no conflict of interest regarding the publication of this article.

REFERENCES

[1] L. Stinson (2019), "World's largest 3D-printed building completed in Dubai", *Curbed*, https://archive.curbed.com/2019/12/30/21035765/world-largest-3d-printed-building-dubai-apis-cor, accessed 18 August 2021.

[2] L. Alter (2018), "3D printed house displayed at Milan design week", *Treehugger*, https://www.treehugger.com/green-architecture/3d-printed-house-displayed-milan-design-week.html, accessed 18 August 2021.

[3] 3D Sourced (2021), "The 12 most exciting 3D printed house builds 2021", https://3dsourced.com/guides/3d-printed-house-2/#4_ICON, accessed 18 August 2021.

[4] S. Saunders (2018), "Robotic 3D printed YHNOVA house officially inaugurated, tenants to move in soon", *3D Print*, https://3dprint.com/207936/3d-printed-yhnova-house-done/, accessed 18 August 2021.

[5] A. Frearson (2014), "Chinese company 3D prints 10 buildings in a day usingconstruction waste", *Dezeen*, https://www.dezeen.com/2014/04/24/chinese-company-3d-prints-buildings-construction-waste/, accessed 18 August 2021.

[6] H. Lee, C.H.J. Lim, M.J. Low, et al. (2017), "Lasers in additive manufacturing: A review", *Int. J. Precis. Eng. Manuf. Technol.*, **4**, pp.307-322, DOI: 10.1007/s40684-017-0037-7.

[7] R. Dou, T. Wang, Y. Guo, et al. (2011), "Ink-jet printing of Zirconia: Coffee staining and line stability", *J. Am. Ceram. Soc.*, **94(11)**, pp.3787-3792, DOI: 10.1111/j.1551-2916.2011.04697.x.

[8] B. Zhu, J. Pan, Z. Zhou, et al. (2019), "Development of 3D printable engineered cementitious composites with ultra-high tensile ductility for digital construction", *Mater. Des.*, **181**, DOI: 10.1016/j.matdes.2019.108088.

[9] Y. Weng, M. Li, M.J. Tan, et al. (2018), "Design 3D printing cementitious materials via Fuller Thompson theory and Marson-Percy model", *Constr. Build. Mater.*, **163**, pp.600-610, DOI: 10.1016/j.conbuildmat.2017.12.112.

[10] K. Manikandan, K. Wi, X. Zhang, et al. (2020), "Characterizing cement mixtures for concrete 3D printing", *Manuf. Lett.*, **24**, pp.33-37, DOI: 10.1016/j.mfglet.2020.03.002.

[11] A. Kazemian, X. Yuan, E. Cochran, et al. (2017), "Cementitious materials for construction-scale 3D printing: Laboratory testing of fresh printing mixture", *Constr. Build. Mater.*, **145**, pp.639-647, DOI: 10.1016/j.conbuildmat.2017.04.015.

[12] F. Hamidi, F. Aslani (2019), "Additive manufacturing of cementitious composites: Materials, methods, potentials, and challenges", *Constr. Build. Mater.*, **218**, pp.582-609, DOI: 10.1016/j.conbuildmat.2019.05.140.

[13] B. Lu, Y. Weng, M. Li, et al. (2019), "A systematical review of 3D printable cementitious materials", *Constr. Build. Mater.*, **207**, pp.477-490, DOI: 10.1016/j.conbuildmat.2019.02.144.

[14] J. Jo, B.W. Jo, W. Cho, et al. (2020), "Development of a 3D printer for concrete structures: Laboratory testing of cementitious materials", *Int. J. Concr. Struct. Mater.*, **14(1),** DOI: 10.1186/s40069-019-0388-2.

[15] C. Zhang, Z. Hou, C. Chen, et al. (2019), "Design of 3D printable concrete based on the relationship between flowability of cement paste and optimum aggregate content", *Cem. Concr. Compos.*, **104**, DOI: 10.1016/j.cemconcomp.2019.103406.

[16] G. Ma, L. Wang (2018), "A critical review of preparation design and workability measurement of concrete material for largescale 3D printing", *Front. Struct. Civ. Eng.*, **12(6)**, pp.382-400, DOI: 10.1007/s11709-017-0430-x.

[17] P.T. Loan, X.J. Zhuang, T.H.T. Nguyen, et al. (2021), "Experimental investigations on the rheological properties of the proposed 3D printing mortar", *Vietnam Journal of Science, Technology and Engineering*, **64(2)**, pp.50-53, DOI:10.31276/VJSTE.64(2).50-53.

[18] S. Hou, Z. Duan, J. Xiao, et al. (2020), "A review of 3D printed concrete: Performance requirements, testing measurements and mix design", *Constr. Build. Mater.*, **273**, DOI: 10.1016/j.conbuildmat.2020.121745.

[19] T. Wangler, N. Roussel, F.P. Bos, et al. (2019), "Digital concrete: A review", *Cem. Concr. Res.*,**123**, DOI: 10.1016/j.cemconres.2019.105780.

[20] Y. Chen, S.C. Figueiredo, Ç. Yalçinkaya, et al. (2019), "The effect of viscosity-modifying admixture on the extrudability of limestone and calcined clay-based cementitious material for extrusion-based 3D concrete printing", *Materials (Basel)*, **12(9)**, DOI: 10.3390/ ma12091374.

[21] B. Panda, M.J. Tan (2018), "Experimental study on mix proportion and fresh properties of fly ash based geopolymer for 3D concrete printing", *Ceram. Int.*, **44(9)**, pp.10258-10265, DOI: 10.1016/j.ceramint.2018.03.031.

[22] R.A. Buswell, S.Z. Jones, J. Dirrenberger, et al. (2018), "3D printing using concrete extrusion: A roadmap for research", *Cem. Concr. Res.*, **112**, pp.37-49, DOI: 10.1016/j.cemconres.2018.05.006.

[23] Y.W.D. Tay, Y. Qian, M.J. Tan (2019), "Printability region for 3D concrete printing using slump and slump flow test", *Compos. Part B: Engineering*, **174**, DOI: 10.1016/j. compositesb.2019.106968.

[24] S.A.O. Nair, S. Panda, M. Santhanam, et al. (2020), "A critical examination of the influence of material characteristics and extruder geometry on 3D printing of cementitious binders", *Cem. Concr. Compos.*, **112**, DOI: 10.1016/j.cemconcomp.2020.103671.

[25] T.T. Le, S.A. Austin, S. Lim, et al. (2012), "Mix design and fresh properties for high-performance printing concrete", *Mater. Struct.*, **45(8)**, pp.1221-1232, DOI: 10.1617/s11527-012-9828-z.

[26] Z. Liu, M. Li, Y. Weng, et al. (2019), "Mixture design approach to optimize the rheological properties of the material used in 3D cementitious material printing", *Constr. Build. Mater.*, **198**, pp.245-255, DOI: 10.1016/j.conbuildmat.2018.11.252.

[27] *GB/T 8077-2012 Methods for Testing Uniformity of Concrete Admixture*, General Administration of Quality Supervision, Inspection and Quarantine of the People's Republic of China, Standardization Administration of the People's Republic of China, 2012.

DOI: 10.31276/VJSTE.65(1).09-13

Fabrication, structural characteristics, and influence of Bi^{3+} doping concentration on UV-vis spectra of Bi^{3+}:SnO_2 nanocomposite materials

Thi Thu Hien Le[1*], Van Tuan Chu[1], Van Tuan Pham[2]

[1]Hung Yen University of Technology and Education, Dan Tien Commune, Khoai Chau District, Hung Yen Province, Vietnam
[2]International Training Institute for Materials Science (ITIMS), Hanoi University of Science and Technology, 1 Dai Co Viet Street, Bach Khoa Ward, Hai Ba Trung District, Hanoi, Vietnam

Received 25 January 2022; revised 17 March 2022; accepted 5 April 2022

Abstract:

Industrialization and modernization have led to environmental crises and increasingly serious energy shortages. Environmental chemicals or persistent organic pollutants pose a danger to ecological balance and many human health problems.The authors report the characteristics and optical properties of Bi^{3+}-doped SnO_2 quantum dots prepared by sol-gel and hydrothermal methods. The structure and morphology of the materials as a function of doping concentration were studied and analysed by X-ray diffraction (XRD) and scanning electron microscope (SEM). The structure of the material was assigned to the tetragonal crystal structures of the SnO_2 rutile phase, reported in JCPDS Card No. 41-1445. With the increase of Bi^{3+} doping, the crystallinity of Bi-doped SnO_2 worsened. The average sizes of the SnO_2 nanocrystals were within 3-8 nm. The effect of Bi^{3+} ion concentration on the absorbance properties of the materials was investigated by UV-Vis absorption spectra. The absorbance decreased with increasing the concentration of Bi^{3+} dopant in the SnO_2 lattice. The bandgap width decreased with Bi^{3+} dopant concentration. All Bi^{3+}-doped SnO_2 samples presented an enlargement of the light absorption range due to a bandgap width decrease.

Keywords: **Bi^{3+} doped SnO_2, photocatalysis, SnO_2 nanoparticle.**

Classification numbers: **2.1, 2.3**

1. Introduction

The rapid expansion of industrialization and population worldwide has led to increasing environmental crises and energy shortages [1, 2]. Environmental chemicals or persistent organic pollutants, which are produced every day, are not only dangerous to ecological equilibrium but can also lead to various health issues affecting humans [3, 4]. Thus, removing pollutants from wastewater has attracted intense research worldwide [5]. There are various treatment methods that have been developed such as chemical oxidation, coagulation, filtration, precipitation, ion exchange, biosorption, adsorption, reverse osmosis, and photocatalytic decay...[6-13]. Photocatalysis is a notable method of removing pollutants from wastewater with its low cost, high efficiency, and environmentally friendly properties. Photocatalysis uses energy from light with the help of semiconductor photocatalysts to carry out redox reactions on its surface thereby speeding up the rate of chemical reactions. Under sunlight irradiation, electrons in semiconductors absorb photons, produce photo-electron pairs, and move to the surface of the semiconductor where redox reactions take place through which organic pollutants are accelerated to decay into carbon dioxide and water [13, 14]. However, to achieve high efficiency and energy savings, semiconductor photocatalysts need to be low cost, non-toxic, stable in water, and have a wide absorption band that includes the visible light region [15].

Tin oxide (SnO_2) is an n-type semiconductor with a wide bandgap of approximately 3.6 eV and a high exciton binding energy of approximately 130 meV [16]. With excellent electrical, optical, and chemical properties, tin oxide has been applied to solar cells [17], transparent electrodes [18], catalytic materials [19], and solid-state chemical sensors [20]. Notably, tin oxide has been used as a catalyst and support for the catalyst in several organic reactions from its high acidity [21-23]. However, due to its wide bandgap, the absorption band of SnO_2 is in the ultraviolet region. Besides, the high recombination rate for electron-hole pairs makes the photocatalytic performance of SnO_2 not as high as expected [13]. To solve this problem, one proposed solution is doping SnO_2 with metal cations to narrow the bandgap and widen the absorption band. Cation metals have a low valance that accepts electrons and not only do they resist the recombination of photo-electron pairs, but they also create oxygen vacancies in the host lattice [24]. Therefore, the photocatalytic performance of doped SnO_2 material could be improved.

[*]Corresponding author: Email: hienle585@gmail.com

According to prior research, many metals have already been used to dope SnO_2 such as Ce [6], Bi [25], Co [26], Ag [21, 27], Ni [28, 29], Cr [15], Zn [30], and Ti [5]. Among these, bismuth-based semiconductors have the potential to increase the mobility of photoelectron carriers and reduce the bandgap [31, 32]. Bismuth has electronic structures in the 6s valence band, which is well dispersed in Bi^{3+}-doped compounds and has the potential to increase the mobility of photoelectron carriers and reduce the bandgap enough to cause the absorption to extend to longer wavelengths [14, 33].

In this work, sol-gel and hydrothermal methods were utilised to fabricate Bi^{3+}-doped SnO_2 nanocomposite materials. The structural and morphological characteristics of the materials were investigated using XRD and SEM. The effects of Bi^{3+} ion concentration on optical absorption characteristics of samples were studied using ultraviolet-visible absorption spectroscopy (UV-Vis).

2. Experimental design

The Bi^{3+}:SnO_2 nanocomposite materials were prepared by sol-gel and hydrothermal methods, which are described in Fig. 1.

Fig. 1. Diagram of Bi^{3+}-doped SnO_2 nanocomposite synthesis.

Firstly, bismuth nitrate pentahydrate ($Bi(NO_3)_3.5H_2O$) was mixed with deionised water and stirred at room temperature for 10 min. Then, a sufficient amount of nitric acid HNO_3 was added to the mixture to form a transparent solution (sol A). Secondly, tin tetrachloride ($SnCl_4.5H_2O$, ≥98%) was mixed with deionised water and stirred at room temperature for 30 min to prepare sol B1. Sodium hydroxide (NaOH, ≥98%) was mixed with deionised water and stirred under the same condition as sol B1 for 30 min to prepare sol B2. Subsequently, the B1 and B2 sols were slowly mixed and stirred at room temperature for 1 h to prepare sol B. Thirdly, the A and B sols were slowly mixed and stirred for 2 h to form a homogeneous mixture. The last sol was infused into Teflon and the hydrothermal process began at 180°C for 24 h. After the hydrothermal process, the sample was cooled down to room temperature. The sample was then filtered and rinsed several times with deionised water and ethanol (C_2H_5OH) by centrifuge. Finally, the sample was dried and mashed to obtain Bi^{3+}:SnO_2 powder. The samples with different Bi mass ratios (4, 8 wt%) were synthesised and labelled as 4Bi-96SnO_2 and 8Bi-92SnO_2, respectively. A similar procedure was used to synthesise pure SnO_2 nanoparticles without the addition of $Bi(NO_3)_3$.5H2O, which was labelled 0Bi-100SnO_2.

All chemicals were purchased from Merck and Sigma Aldrich. XRD measurements were performed at room temperature with a Siemens D5000 (Germany) apparatus with CuK_α radiation of wavelength λ=0.154 nm. SEM images were acquired by employing an S4800-Hitachi (Japan) SEM. The absorption properties were studied using a V-650 UV-vis spectrophotometer (Jasco, USA).

3. Results and discussion

The crystalline structure and phase content of the 0, 4, and 8% Bi^{3+}:SnO_2 samples were analysed by XRD and are shown in Fig. 2. In the figure, it is seen that the crystallisation of the SnO_2 in the materials is good. Diffraction peaks were assigned to the tetragonal crystal structures of the SnO_2 rutile phase, which are in good agreement with JCPDS Card No. 41-1445, and can be observed in the XRD patterns of all the samples. Diffraction peaks at 2θ=26.392, 33.717, 37.856, 51.631, 65.904, and 78.376 correspond to (110), (101), (200), (211), (112), and (321) lattice planes, respectively. The positions of the peaks were unchanged at different Bi mass ratio samples. Peaks corresponding to Bi or Bi_2O_3 phase were not observable. This revealed that Bi^{3+} dopants could be distributed in the SnO_2 nanoparticles to form a Bi-Sn-O solid solution [6]. The crystallinity of the samples was affected by doping Bi into the SnO_2 host lattice. The intensities of diffraction peaks decreased with the increase of Bi doping amount, demonstrating that doping with Bi^{3+} form defects in the system that

prevent crystal growth [34]. The average crystal size of SnO_2 nanocrystals were estimated by using the Debye-Scherrer equation with a shape factor of 0.9 as shown in Table 1. The results showed that the average size of crystals was approximate 3-8 nm. Additionally, the half-peak maximum width tended to increase slightly. Therefore, the average crystallite size of the obtained samples decreased as the Bi^{3+} doping concentration increased. Due to their small size, the surface-to-volume ratio was increased and created more oxygen vacancies increasing the catalytic efficiency of the material [6, 27].

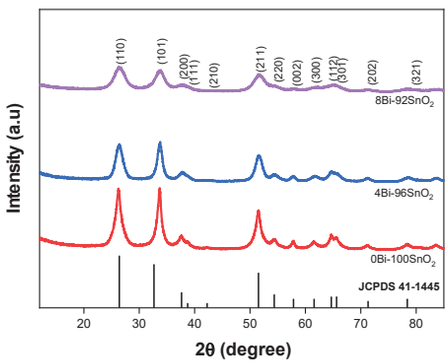

Fig. 2. XRD patterns of Bi^{3+}-doped SnO_2 nanocomposites with different Bi^{3+} mass ratios (0, 4, 8 wt%). Diffraction peak positions of SnO_2 are taken from JCPDS Card No.41-1445.

Table 1. XRD data and crystallite size of SnO_2 particles.

Bi^{3+} ratio (%W)	Peaks	2θ	FWHM	D (nm)
0	Peak 1(100)	26.243	1.599	5.33
	Peak 2 (101)	33.634	1.140	7.61
4	Peak 1(100)	26.392	1.629	5.23
	Peak 2 (101)	33.717	1.185	7.32
8	Peak 1(100)	26.457	2.51	3.40
	Peak 2 (101)	33.709	2.332	3.72

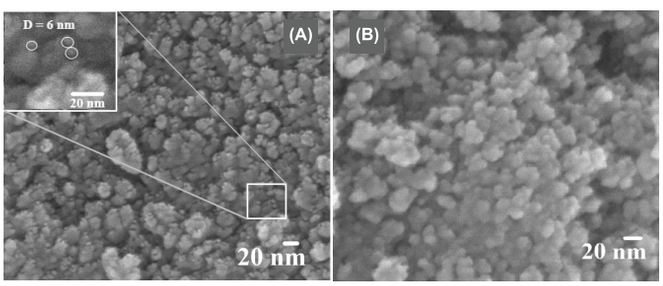

Fig. 3. SEM images of (A) pure SnO_2 and (B) 4Bi-96SnO_2. The inset shows a small area in the large-scale image.

Figure 3 presents the SEM images of pure SnO_2 and 4Bi-96SnO_2. Figs. 3A, 3B show the average size of pure SnO_2 and 4Bi-96SnO_2 is approximately 6 nm. These observations were consistent with the XRD results.

The optical absorption properties UV-Vis of the as-obtained 0, 4, and 8% Bi^{3+}-doped SnO_2 nanocomposites in the range from 200 nm to 800 nm are shown in Fig. 4. The UV-Vis spectrum showed that there was a strong absorption peak at 300 nm, which was the absorption peak of SnO_2. In addition, an absorption band between 280 and 350 nm that is characteristic of SnO_2-containing storage materials was also observed. The absorbance decreased with increasing the concentration of Bi^3dopant$^+$ in the SnO_2 lattice. This can be explained by the fact that light absorption of the Sn^{4+} ions was prevented by the Bi^{3+} impurity centres [13, 24]. The presence of Bi^{3+} created defects in the crystal lattice of the storage material thereby redistributing the atomic orbitals. There were a lot of free electrons, which appear with high mobility reducing the number of electrons at the ground level, therefore the absorbance of materials decreased. The bandgap energy (E_g) of the as-produced samples was estimated using Tauc's model:

$$(\alpha h\nu)^n = A(h\nu - Eg)$$

where α, hν, Eg, n, and A are the absorption coefficient, incident photon energy, energy gap, n (which depends on the nature of the energy transition, e,g., n=1/2 for the direct bandgap and n=2 for the indirect bandgap) and the proportionality constant, respectively [34, 35].

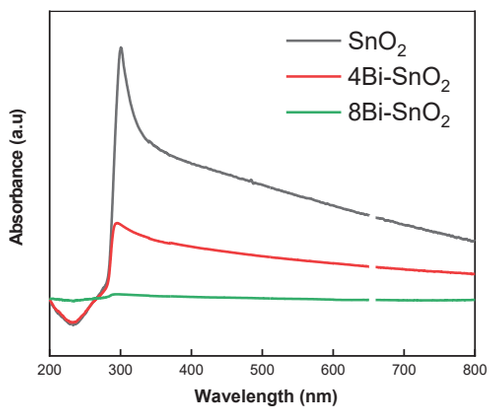

Fig. 4. UV-Vis spectra of Bi^{3+}-SnO_2 nanocomposite with Bi^{3+} mass ratios of 0% (grey), 4% (red), and 8% (green).

Figure 5 presents the variation of $(\alpha h\nu)^2$ with (hν) of all samples. The bandgap of the samples with Bi^{3+} concentrations of 0, 4, and 8% had values of 3.60, 3.16, and 2.55 eV, respectively. In the inset, the bandgap width is shown to decrease with Bi^{3+} dopant concentration. This is explained by the presence of the Bi dopant, which could result in the formation of more extrinsic defective energy levels in the bandgap of SnO_2, thus yielding new energy levels in the nanoparticles. Therefore, *sp-d*

exchange interactions between band electrons and localised *d* electrons of the Bi^{3+} ions with electronic states in the Sn^{4+} ions. The *s-d* exchange interaction lowers the conduction-band edge, but the virtual to *p-d* exchange interaction raises the valence-band edge, resulting in bandgap narrowing [6, 25]. The samples with 4 and 8% Bi^{3+} doping exhibited a red shift. This showed that the incorporation of Bi^{3+} dopant into the SnO_2 lattice made the absorption wavelength band of the material expand to the visible region.

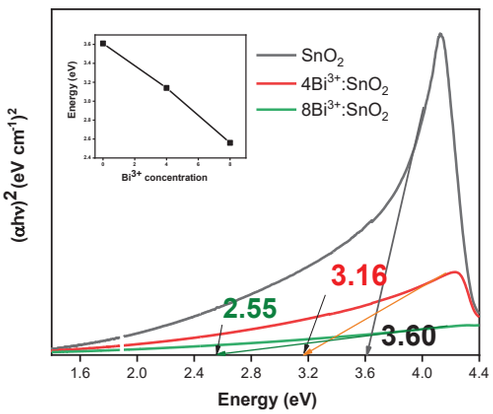

Fig. 5. Tauc's plots of pure SnO_2 and Bi^{3+}-doped SnO_2 with Bi^{3+} mass ratios of 0, 4, and 8%, respectively.

4. Conclusions

Bi^{3+}-doped SnO_2 nanocomposites with different Bi^{3+} concentrations were successfully synthesized by sol-gel and hydrothermal methods. Replacement of Sn^{4+} with Bi^{3+} in SnO_2 was confirmed by XRD, SEM, and UV-Vis diffuse reflectance spectroscopy. XRD analysis proved that all the samples were polycrystalline with diffraction lines assigned to the tetragonal rutile phases of SnO_2. The crystallinity of the samples decreased with the increase of Bi^{3+} dopant concentration. UV-vis spectra indicated that the bandgap of the materials decreased with increasing Bi^{3+} doping concentration thereby enlarging the light absorption range.

CRediT author statement

Thi Thu Hien Le: Data curation, Investigation, Conceptualization, Formal analysis, Writing- Reviewing and Editing; Van Tuan Chu: Conceptualization, Data curation; Van Tuan Pham: Supervision, Conceptualization, Formal analysis, Writing original draft.

COMPETING INTERESTS

The authors declare that there is no conflict of interest regarding the publication of this article.

REFERENCES

[1] Q. Schiermeier (2011), "Increased flood risk linked to global warming", *Nature*, **470**, DOI: 10.1038/470316a.

[2] S.N. Habisreutinger, P.L.S. Mende, J.K. Stolarczyk, et al. (2013), "Photocatalytic reduction of CO_2 on TiO_2 and other semiconductors", *Angew. Chem. Int. Ed.*, **52(29)**, pp.7372-7408, DOI: 10.1002/anie.201207199.

[3] N. Manjula, G. Selvan (2017), "Magnetic and antibacterial properties of Zr-doped SnO_2 nanopowders", *Journal of Materials Science: Materials in Electronics*, **28**, pp.15056-15064, DOI: 10.1007/s10854-017-7380-x.

[4] B. Wahlang (2018), "Exposure to persistent organic pollutants: Impact on women's health", *Rev. Environ. Health*, **33(4)**, pp.331-348, DOI: 10.1515/reveh-2018-0018.

[5] L. Ran, D. Zhao, X. Gao, et al. (2015), "Highly crystalline Ti-doped SnO_2 hollow structured photocatalyst with enhanced photocatalytic activity for degradation of organic dyes", *CrystEngComm*, **17(22)**, pp.4225-4237, DOI: 10.1039/C5CE00184F.

[6] A. Baig, V. Rathinam, J. Palaninathan, et al. (2020), "Facile synthesis of Ce-doped SnO_2 hollow structured photocatalyst with enhanced photocatalytic activity for degradation of organic dyes", *CrystEngComm*, **17(22)**, pp.4225-4237, DOI: 10.1007/s13738-020-02000-2.

[7] J. Wenk, M. Aeschbacher, E. Salhi, et al. (2013), "Chemical oxidation of dissolved organic matter by chlorine dioxide, chlorine, and ozone: Effects on its optical and antioxidant properties", *Environ. Sci. Technol.*, **47(19)**, pp.11147-11156, DOI: 10.1021/es402516b.

[8] L. Muruganandam, M. P. Kumar, A. Jen, et al. (2017), "Treatment of waste water by coagulation and flocculation using biomaterials", *IOP Conference Series: Materials Science and Engineering*, **263**, DOI: 10.1088/1757- 899X/263/3/032006.

[9] F. Liu, N.B. Nord, K. Bester, et al. (2020), "Microplastics removal from treated wastewater by a biofilter", *Water*, **12(4)**, DOI: 10.3390/w120.

[10] T.C. Jorgensen, L.R. Weatherley (2003), "Ammonia removal from wastewater by ion exchange in the presence of organic contaminants", *Water Research*, **37(8)**, pp.1723-1728, DOI: 10.1016/S0043-1354(02)00571-7.

[11]K. Singh, M.A. Renu (2017), "Heavy metal removal from wastewater using various adsorbents: A review", *Journal of Water Reuse and Desalination*, **7(4)**, pp.387-419, DOI: 10.2166/wrd.2016.104.

[12] K.T. Alexei Pervov, N. Makisha (2018), "Application of reverse osmosis techniques to treat and reuse biologically treated wastewater", *IOP Conf. Series: Materials Science and Engineering*, **365(6)**, DOI: 10.1088/1757-899X/365/6/062026.

[13] D. Toloman, A. Popa, M. Stefan, et al. (2020), "Enhanced photocatalytic activity of Co doped SnO_2 nanoparticles by controlling the oxygen vacancy states", *Optical Materials*, **110**, DOI: 10.1016/j.optmat.2020.110472.

[14] A. Alzamly, F. Hamed, T. Ramachandran, et al. (2019), "Tunable band gap of Bi^{3+}-doped anatase TiO_2 for enhanced photocatalytic removal of acetaminophen under UV-visible light irradiation", *Journal of Water Reuse and Desalination*, **9(1)**, pp.31-46, DOI: 10.2166/wrd.2018.021.

[15] T. Karimi, A. Haghighatzadeh (2019), "Enhanced photocatalytic activity of SnO_2 NPs by chromium (Cr) concentration", *Bulletin of Materials Science*, **42(158)**, DOI: 10.1007/s12034-019-1842-0.

[16] S.S. Pan, S.F. Yu, Y.X. Zhang, et al. (2013), "Crystallite size-modulated exciton emission in SnO_2 nanocrystalline films grown by sputtering", *Journal of Applied Physics*, **113(14)**, DOI: 10.1063/1.4800896.

[17] J.A. Smith, O.S. Game, J.E.Bishop, et al. (2020), "Rapid scalable processing of tin oxide transport layers for perovskite solar cells", *ACS Appl. Energy Mater.*, **3(6)**, pp.5552-5562, DOI: 10.1021/acsaem.0c00525.

[18] G. Lucarelli, M.B. Thomas (2019), "Development of highly bendable transparent window electrodes based on MoOx, SnO_2, and Au dielectric/metal/dielectric stacks: Application to indium tin oxide (ITO)-free perovskite solar cells", *Frontiers in Materials*, **6(310)**, DOI: 10.3389/fmats.2019.00310.

[19] T.A. Dontsova, A.S. Kutuzova, K.O. Bila, et al. (2020), "Enhanced photocatalytic activity of TiO_2/SnO_2 binary nanocomposites", *Journal of Nanomaterials*, **2020**, DOI: 10.1155/2020/8349480.

[20] I. Sayago, M. Aleixandre, J.P. Santos (2019), "Development of tin oxide-based nanosensors for electronic nose environmental applications", *Biosensors (Basel)*, **9(1)**, DOI: 10.3390/bios9010021.

[21] N.S. Kumar, M. Asif, T.R.K. Reddy, et al. (2019), "Silver quantum dot decorated 2D-SnO_2 nanoflakes for photocatalytic degradation of the water pollutant rhodamine B", *Nanomaterials (Basel)*, **9(11)**, DOI: 10.3390/nano9111536.

[22] L. Yang, J. Huang, L. Shi, et al. (2017), "Efficient hydrogen evolution over Sb doped SnO_2 photocatalyst sensitized by Eosin Y under visible light irradiation", *Nano Energy*, **36**, pp.331-340, DOI: 10.1016/j.nanoen.2017.04.039.

[23] P.S. Manjunathan, G.V. Shanbhag (2020), "Application of tin oxide-based materials in catalysis", *Tin Oxide Materials*, Elsevier, pp.519-553, DOI: 10.1016/B978-0-12-815924-8.00018-9.

[24] T. Entradas, J.F. Cabrita, S. Dalui, et al. (2014), "Synthesis of sub-5 nm Co-doped SnO_2 nanoparticles and their structural, microstructural, optical and photocatalytic properties", *Materials Chemistry and Physics*, **147**, pp.563-571, DOI: 10.1016/j.matchemphys.2014.05.032.

[25] L.P. Chikhale, J.Y. Patil, F.I. Shaikh, et al. (2014), "Effect of Bi doping on structural, morphological, optical and ethanol vapor response properties of SnO_2 nanoparticles", *Materials Science in Semiconductor Processing*, **27**, pp.121-129, DOI: 10.1016/j.mssp.2014.06.024.

[26] S. Asaithambi, P. Sakthivel, M. Karuppaiah, et al. (2019), "Preparation of SnO_2 nanoparticles with addition of Co ions for photocatalytic activity of brilliant green dye degradation", *Journal of Electronic Materials*, **48**, pp.2183-2194, DOI: 10.1007/s11664-019-07061-5.

[27] B. Babu, M. Cho, C. Byon, et al. (2018), "One pot synthesis of Ag-SnO_2 quantum dots for highly enhanced sunlight-driven photocatalytic activity", *Journal of Alloys and Compounds*, **731**, pp.162-171, DOI: 10.1016/j.jallcom.2017.10.011.

[28] H. Chen, L. Ding, W. Sen, et al. (2013), "Synthesis and characterization of Ni doped SnO_2 microspheres with enhanced visible-light photocatalytic activity", *The Royal Society of Chemistry*, **5(69)**, DOI: 10.1039/ C5RA10268E.

[29] M. Kandasamy, A. Seetharaman, D. Sivasubramanian, et al. (2018), "Ni-doped SnO_2 nanoparticles for sensing and photocatalysis", *ACS Applied Nano Materials*, **1(10)**, pp.5823-5836, DOI: 10.1021/acsanm.8b01473.

[30] C. Lu, J. Wang, F. Xu, et al. (2018), "Zn-doped SnO_2 hierarchical structures formed by a hydrothermal route with remarkably enhanced photocatalytic performance", *Ceramics International*, **44(13)**, pp.15145-15152, DOI: 10.1016/j.ceramint.2018.05.151.

[31] X. Meng, Z. Zhang (2015), "Facile synthesis of BiOBr/Bi WO heterojunction semiconductors with high visible-light-driven photocatalytic activity", *Journal of Photochemistry and Photobiology A: Chemistry*, **310**, pp.33-44, DOI: 10.1016/j.jphotochem.2015.04.024.

[32] X. Meng, Z. Zhang (2016), "Bismuth-based photocatalytic semiconductors: Introduction, challenges and possible approaches", *Journal of Molecular Catalysis A: Chemical*, **423**, pp.533-549, DOI: 10.1016/j.molcata.2016.07.030.

[33] Z.F. Huang, L. Pan, J.J. Zou, et al. (2014), "Nanostructured bismuth vanadate-based materials for solar-energy-driven water oxidation: A review on recent progress", *Nanoscale*, **6(23)**, pp.14044-14063, DOI: 10.1039/C4NR05245E.

[34] L. Chu, F. Duo, M. Zhang, et al. (2020), "Doping induced enhanced photocatalytic performance of SnO_2:Bi^{3+} quantum dots toward organic pollutants", *Colloids and Surfaces A: Physicochemical and Engineering Aspects*, **589**, DOI: 10.1016/j.colsurfa.2020.124416.

[35] A. Azam, S.S. Habib, N.A. Salah, et al. (2013), "Microwave-assisted synthesis of SnO_2 nanorods for oxygen gas sensing at room temperature", *Int. J. Nanomedicine*, **8**, pp.3875-3882, DOI: 10.2147/IJN.S51206.

DOI: 10.31276/VJSTE.65(1).14-18

Synthesis of a conjugated molecular triad based on 9,9-dioctyl-9H-fluorene for fluorescence sensing to determine mesotrione

Thao Phuong Le Nguyen[1], Thao Thanh Bui[1], Bao Kim Doan[1], Linh Phuong Bui[1], Tam Hoang Luu[2], Chau Duc Tran[2], Tung Viet Tuan Tran[1], Tsutomu Yokozawa[3], Ha Tran Nguyen[1, 2*]

[1]National Key Laboratory of Polymer and Composite Materials, Ho Chi Minh City University of Technology, Vietnam National University - Ho Chi Minh City, 1 Street 2, Linh Trung Ward, Thu Duc City, Ho Chi Minh City, Vietnam
[2]Faculty of Materials Technology, Ho Chi Minh City University of Technology, Vietnam National University - Ho Chi Minh City, 1 Street 2, Linh Trung Ward, Thu Duc City, Ho Chi Minh City, Vietnam
[3]Department of Materials and Life Chemistry, Kanagawa University, 27-1 Rokukakubashi, Yokohama, Japan

Received 11 November 2022; revised 10 December 2022; accepted 20 December 2022

Abstract:

A conjugated molecular triad based on pyrene and 9,9-dioctyl-9H-fluorene has been successfully synthesised via the Suzuki cross-coupling reaction with yield of 48%. In this polymerization, the $Pd(PPh_3)_4$ has been used as the catalytic in the presence of K_2CO_3 as base in a mixture of toluene/ethanol/H_2O at 80°C under N_2. The chemical structures of the conjugated molecules were determined via Fourier-transform infrared spectroscopy (FTIR) and nuclear magnetic resonance (^{1}H-NMR) that proved the chemical structure of 1,1'-(9,9-dioctyl-9H-fluorene-2,7-diyl)dipyrene. The optical properties of the molecules were investigated via UV-Vis in different concentration that exhibited the maximum absorption of 340 nm. The conjugated molecular triad also have been investigated by fluorescence spectroscopy that showed a mission peak at 475 nm under the excitation of 350 nm of wavelength. In addition, the 1,1'-(9,9-dioctyl-9H-fluorene-2,7-diyl)dipyrene exhibited a fluorescence quenching as a chemosensor in the presence of mesotrione, a nitroaromatic herbicide. This phenomenon proved the efficient energy and electron transfer from a photo-excited pyrene moiety to the ground state electron-deficient mesotrione as a result of Forster resonance energy transfer (FRET) mechanism..

Keywords: **chemosensor, conjugated molecular, mesotrione, nitroaromatic herbicide, pyrene.**

Classification numbers: **2.2, 2.3**

1. Introduction

Recently, nitroaromatic compounds (NACs) have been widely used in various industrial chemicals and pharmaceuticals such as in the synthesis of herbicides, dyes, explosives, and other intermediates [1-4]. NAC contamination in surface water, groundwater, and soil can cause serious health problems in living organisms [5-7]. Moreover, because NACs contain one or more electron-withdrawing nitro-groups, they slowly biodegrade in the environment [4, 5]. Most NACs are known as mutagenic and carcinogenic agents towards humans and cause the formation of methemoglobin upon acute exposure [5]. Therefore, tracing these compounds in the environment is of great importance.

Some advanced methods such as high-performance liquid chromatography (HPLC), gas chromatography coupled mass spectrometry (GC-MS), ion-mobility spectroscopy (IMS), and surface-enhanced Raman spectroscopy (SERS) have been used for the detection of NACs [8, 9]. Although most of these methods are capable of detecting low concentrations of NACs, they usually require complicated equipment and skilled operators, are time consuming, and lack portability. Recently, optical detection methods have emerged as a powerful alternative because of their low cost, high sensitivity and selectivity, and good portability [10]. Notably, fluorescent sensing has great promise for wide application due to its simplicity, ease of visualisation, and quick responses [11]. Thus, this method has become the focus of discussion in this research.

A wide range of fluorescent-based NAC sensors have been designed including organic dyes, conjugated polymers, quantum dots, metal-organic frameworks, and nanomaterials [12-26]. In the fluorescence method, the main interactions responsible for fluorescence quenching are photo-induced electron transfer and Forster resonance energy transfer [10]. L.L. Zhou, et al. (2016) [11] reported the synthesis of conjugated polymers based on benzo[5]helicene via the Sonogashira coupling, Suzuki coupling, and Yamamoto homocoupling reactions for the detection of NACs. A.S. Tanwar, et al. (2019) [24] reported the synthesis of 9.9-bis(6-bromohexyl)-2-phenyl-9H-fluorene and 9,9-bis (6-bromohexyl)-9H-fluorene via the Suzuki polymerization coupling reaction as a fluorescence sensor to detect picric acid. In addition, V. Saini, et al. (2020) [27] reported the synthesis of a compound based on benzimidazo-quinazolinone and pyridinium,

*Corresponding author: Email: nguyentranha@hcmut.edu.vn

named 1-(2-(6-oxobenzo [4,5]imidazo [1,2-*c*]quinazolin-5(6H)-yl)ethyl)pyridin-1-ium bromide (BZQZPy), for detection of 2,4,6-trinitrophenol (TNP) in aqueous media. The compound BZQZPy is highly sensitive and selective towards TNP with a high Stern-Volmer constant of $1.53x10^4$ M^{-1} and a low detection limit of 20 nM [28, 29].

During our research studies involving the synthesis of fluorescence sensors, we became interested in pyrene and its derivatives due to their good photophysical properties, structural characteristics, and high chemical stability. Pyrene has a large planar conjugated aromatic system, which allows for the formation of strong π-π interactions with NACs [10, 30-33]. Moreover, with its remarkable electron donor ability, pyrene can form a non-fluorescent charge transfer complex with electron-deficient molecules such as NACs [30]. In addition, fluorene is not only a strong electron donor moiety, but also exhibits a high fluorescent quantum yield due to the rigidity of the molecule's structure [34]. The alkyl group at the 9 position of fluorene could prevent self-quenching through π-π interaction and enhance the solubility of its derivatives in a common organic solvent [6, 35]. With the fascinating properties of pyrene and fluorene, we expect their incorporation to create a promising compound for fluorescence sensors in the detection of NACs.

In this paper, we report the synthesis of a conjugated oligomer based on pyrene and fluorene via the Suzuki coupling reaction. The structural characteristics of obtained oligomer are analysed via FTIR and ^{1}H-NMR spectroscopy. Then, its photophysical properties and fluorescence quenching response to NACs are investigated via UV-visible absorbance and photoluminescence (PL) spectroscopy for sensing applications.

2. Experimental design

2.1. Materials

N-bomosuccinimide (99%) and pyrene (98%) were purchased from Acros Organic. Mesotrione (98%), 2,2'-(9,9-dioctyl-9H-fluorene-2,7-dityl)bis(4,4,5,5-tetramethyl-1,3,2- dioxaborolane) (DFTD, 99%) and Tetrakis(triphenylphosphine)palladium(0) ($Pd(PPh_3)_4$, 99%) were purchased from Sigma-Aldrich (St. Louis, MO, USA). Potassium carbonate (K_2CO_3, 99%) was purchased from Acros and used as received. Chloroform ($CHCl_3$, 99.5%), dimethylfomamide (DMF, 99%) and toluene (99.5%) were purchased from Fisher/Acros and dried using molecular sieves under N_2. Dichloromethane (DCM, 99.8%), absolute ethanol (99%), and hexane (99%) were purchased from Fisher/Acros.

2.2. Characterisation

^{1}H-NMR spectroscopy was performed in deuterated chloroform ($CDCl_3$), with TMS as an internal reference, on a Bruker Avance 500 MHz. FTIR spectra were collected as the average of 64 scans with a resolution of 4 cm^{-1}, which were recorded from a KBr disk on an FTIR Bruker Tensor 27.

UV-visible absorption spectra of the compounds were recorded on an Agilent 8453 spectrometer over a wavelength range of 190-1100 nm. Fluorescence spectra of the compound in solution were measured on a Varian Cary Eclipse fluorescence spectrometer with slit widths of 5 nm.

2.3. Synthesis of 1-bromopyrene

Pyrene (1.00 g, 4.94 mmol) was added to 20 ml of anhydrous DMF that was charged in a 100-ml two-neck round-bottom flask. The mixture was cooled to 0ºC, followed by the slow addition of *N*-bromosuccinimide (NBS) (0.97 g, 5.43 mmol) to the reaction mixture. Then, the reaction mixture was stirred and warmed to room temperature overnight. To end the reaction, the reaction was quenched by the addition of ice water and extracted with chloroform (60 ml). The mixture was washed with brine (150 ml), dried over anhydrous K_2CO_3, and isolated by filtration. Then, the solvent was evaporated under vacuum pressure using a rotary evaporator. The obtained product was precipitated with cold hexane to obtain a pure white powder. Finally, the pure compound was dried under vacuum in an oven at 50ºC to obtain a white powder (yield=94%). ^{1}H-NMR (500 MHz, $CDCl_3$), δ (ppm): 8.45 (d, J=8.5 Hz, 1 H), 8.25-8.21 (m, 3 H), 8.19 (s, 1 H), 8.07-8.01 (m, 4 H).

2.4. Synthesis of 1,1'-(9,9-dioctyl-9H-fluorene-2,7-diyl) dipyrene (DFDP)

In a two-neck round-bottom flask, $Pd(PPh_3)_4$ (0.07 g, 0.06 mmol) and K_2CO_3 (138.2 mg, 3.16 mmol) were added into a mixture of toluene/ethanol/H_2O (10:2:1.5, v/v), then 1-bromopyrene (390.93 mg, 1.39 mmol) and DFTD (406.13 mg, 0.63 mmol) were added to the solution under nitrogen flux. The reaction mixture was degassed by three freeze-pump-thaw cycles to remove air and moisture in reaction. Then reaction was carried out at 80ºC under N_2 for 19 h. After the reaction mixture was cooled to room temperature, the mixture was extracted with chloroform three times (3×20 ml) and the combined organic layers were washed with 10% NaCl (150 ml), dried over K_2CO_3, and isolated by filtration. The solvent was rotary evaporated, and the products were purified by column chromatography on a silica gel column using a mixture of hexane and DCM (V/V = 5:1). Finally, the products were dried in a vacuum oven at 50ºC to obtain a light-yellow powder (DFDP, yield=48%).

^{1}H-NMR (500 MHz, $CDCl_3$), δ (ppm): 8.27 (m, 4H), 8.21 (d, J=7.6 Hz, 2H), 8.18 (d, J=7.5 Hz, 2H), 8.14-8.09 (m, 6H), 8.05-8.00 (m, 4H), 7.98 (d, J=8.0 Hz, 2H), 7.67 (m, 4H), 2.10 (t, 4H), 1.28-1.08 (m, 24H), 0.81 (t, 6H).

3. Results and discussion

3.1. Synthesis and oligomer structure

Pyrene and fluorene derivatives generally demonstrate promising optical properties as they both have an extensive π-system and high electron symmetry, which help improve fluorescence efficiency. Pyrene-fluorene hybrids are good potential materials for fluorescence chemosensor applications.

The synthetic route of DFDP is presented in Scheme 1. Here, 1-bromopyrene and DFDP were synthesized according

to the procedure reported in [36]. As shown in Scheme 1, the bromination reaction between pyrene and NBS at room temperature overnight afforded 1-bromopyrene with a yield of 94%. Then, the Suzuki reaction of 1-bromopyrene and DFTD was reacted using $Pd(PPh_3)_4$ as the catalyst in a mixture of toluene/ethanol/H_2O at 80°C under N_2 for 19 h, which was transformed into DFDP with a yield of 48%. After being purified by column chromatography, the compound DFDP was characterised by FTIR and ^{1}H-NMR spectrometry to confirm its chemical structure.

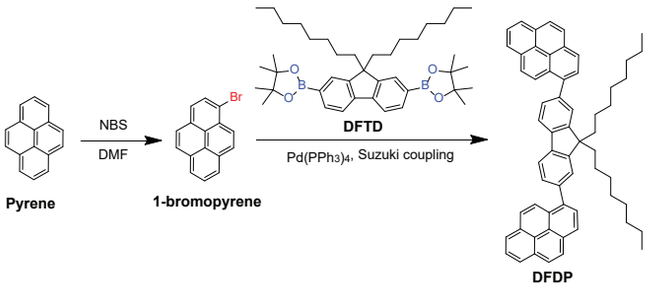

Scheme 1. Synthetic route for the conjugated oligomer DFDP.

DFDP was structurally elucidated by FT-IR analysis. The FT-IR spectrum of DFDP was scanned in the frequency region of 400-4000 cm^{-1} using an infrared spectrometer by employing the KBr pellet technique. In Fig. 1, the FTIR spectrum indicated bands in the range of 2840-2975 cm^{-1} related to -CH_2 and -CH_3 stretching, and the peak at 1461 cm^{-1} related to the -CH_3 bending of octyl brand chain. Meanwhile, the C=C stretching mode of the aromatic ring was present in the range 1620-1570 cm^{-1} and the band at 837 cm^{-1} was attributed to C-H bending. Thus, FT-IR spectroscopy was able to determine the chemical functional groups present within DFDP. To further investigate DFDP's chemical structure, ^{1}H-NMR spectroscopy was also used.

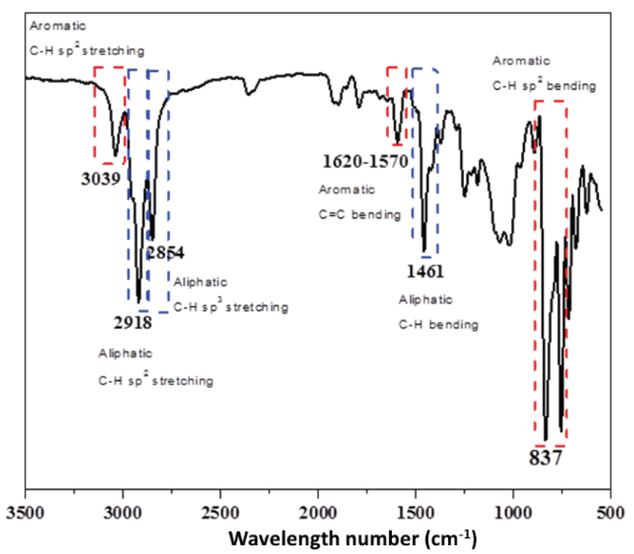

Fig. 1. FTIR spectrum of DFDP.

Figure 2 exhibits the ^{1}H-NMR spectrum of the obtained oligomer, which revealed characteristic peaks corresponding to the oligomer structure. In the ^{1}H-NMR spectrum of DFDP, signals observed from 0.8 to 2.1 ppm were assigned to the alkyl side chains. The peak at 7.67 ppm was attributed to the proton at position *x* in the fluorene unit and the proton at position *a* in the pyrene unit. However, the broad multiplets in the ranges 7.98 to 8.09 ppm and 8.18 to 8.3 ppm in the aromatic region corresponded to protons in the pyrene ring. In addition, the multiplets peak from 8.1 to 8.15 ppm were assigned to the protons of the pyrene unit at position *c* and to the fluorene unit at positions *y* and *j*. The results acquired from FT-IR and ^{1}H-NMR spectrometers were analysed for useful information about the structure and ultimately to confirm the successful synthesis of the conjugated oligomer DFDP.

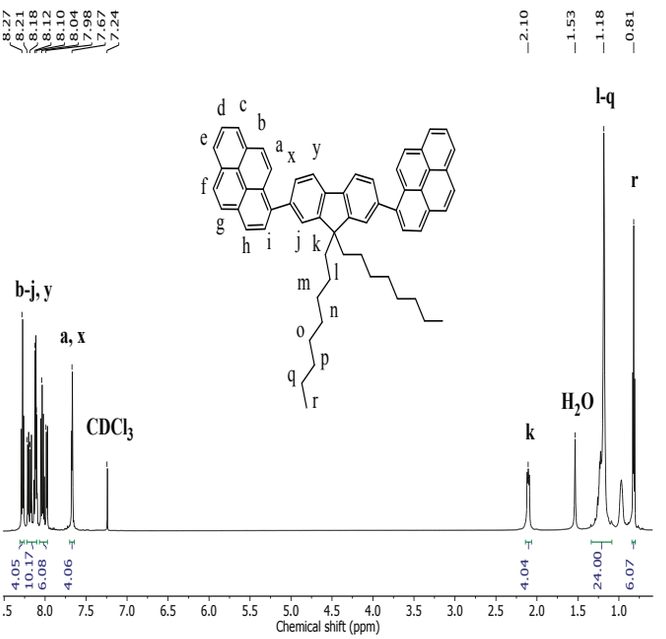

Fig. 2. ^{1}H-NMR spectrum of conjugated oligomer DFDP.

3.2. Optical properties

Figure 3A shows the UV-Vis absorption spectra of the oligomer DFDP in a dilute solution. The UV-Vis absorption of DFDP was investigated in $CHCl_3$ at different concentrations (5, 10, 20, and 30 µM). An absorption band emerged at 340 nm for the oligomer DFDP, while wavelengths from 400 nm onwards had no absorption. The absorption band at 340 nm was assigned to the electronic transition of fluorene and pyrene. Based on the Lambert-Beer law, the molar absorption coefficient ε of DFDP at a maximum wavelength of 340 nm is estimated to be 33525 $M^{-1}cm^{-1}$.

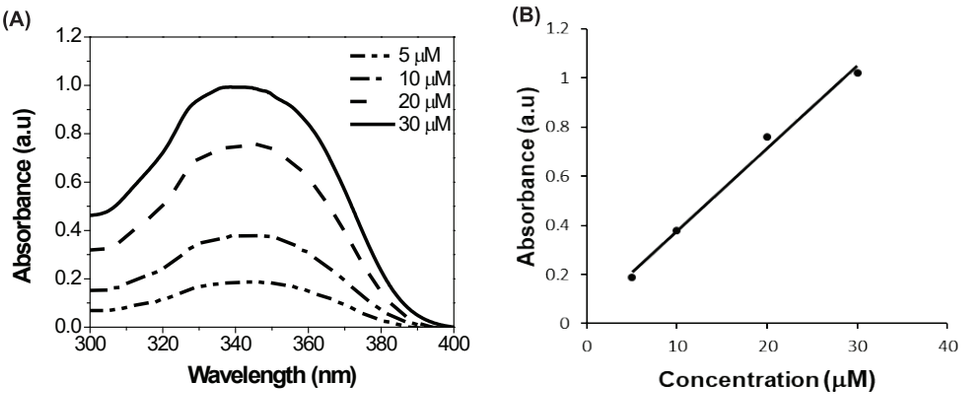

Fig. 3. (A) UV-vis absorption spectra of DFDP in different concentrations of $CHCl_3$ with a path length of 1 cm; (B) calibration curve of DFDP measured at λ_{max}.

3.3. Fluorescence quenching studies with mesotrione in solution

To obtain the quenching efficiencies of DFDP in the presence of a NAC, experiments using a microliter syringe were carried out in which the herbicide mesotrione was gradually added into oligomers dissolved in $CHCl_3$ (C_M=1.0 µl). From Fig. 4, the fluorescence intensities of the oligomer DFDP in solution gradually decreased with the increase of mesotrione concentration (0-7.5 mM), which can be clearly observed under the illumination of UV light by the naked eye. The fluorescence quenching can be explained by the structure of DFDP, which has a conjugated, electron-rich structure with significant electron-donating capabilities to NACs. The observed quenching process of DFDP was the result of the efficient energy and electron transfer from a photo-excited pyrene moiety to the ground state electron-deficient mesotrione.

Fig. 4. Fluorescence quenching of DFDP in $CHCl_3$ (1 µM) upon addition of mesotrione (0-7.5 mM).

To gain a complete understanding of the fluorescence quenching efficiency induced by mesotrione on DFDP, the fluorescence emission spectrums was evaluated using the Stern-Volmer equation:

$$\frac{I_0}{I} = 1 + K_{sv}C_A$$

where I_0 and I are noted as the fluorescence intensities in the absence and presence of the analyte (quencher, A), respectively; C_A denotes the molar concentration of the analyte, and K_{SV} denotes the Stern-Volmer quenching constant. Fig. 5B shows the linear responses of $[(I_0/I)-1]$ vs. the concentration of the nitroaromatic herbicide mesotrione with a correlation coefficient of 0.92, which determines the quenching efficiency of conjugated oligomer DFDP. The calculated Stern-Volmer constant (K_{SV}) of DFDP was 544 M^{-1} with the detection limit (DL) of mesotrione down to 0.2 mM based on the standard method reported.

4. Conclusions

In this research, a conjugated oligomer based on pyrene and fluorene, DFDP, was successfully synthesised at a 48% yield via the Suzuki cross-coupling reaction. The obtained oligomer DFDP was tested to trace the nitroaromatic herbicide mesotrione with a calculated Stern-Volmer constant K_{SV} of 544

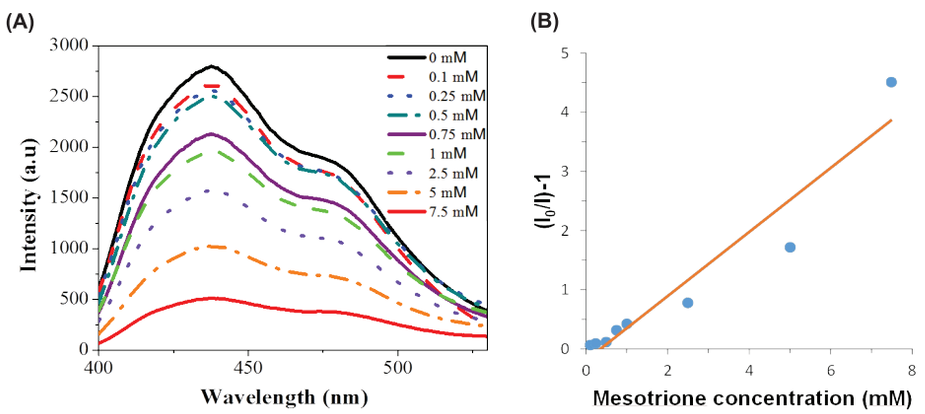

Fig. 5. (A) Fluorescence emission spectra of DFDP in $CHCl_3$ (1 µM) with increasing concentration of mesotrione and (B) the corresponding Stern-Volmer plot of DFDP.

M^{-1} and a detection limit of 0.2 mM. The results prove that the pyrene-based conjugated oligomer could be a promising candidate for real life applications like a fluorescence sensor of NACs.

CRediT author statement

Thao Phuong Le Nguyen: Conceptualization, Methodology, Formal analysis; Thao Thanh Bui: Conceptualization, Methodology, Formal analysis; Bao Kim Doan: Software, Data curation, Validation; Linh Phuong Bui: Software, Data curation, Validation; Tam Hoang Luu: Visualization, Investigation; Chau Duc Tran: Investigation; Tung Viet Tuan Tran: Software, Data curation, Validation; Tsutomu Yokozawa: Writing- Reviewing and Editing; Ha Tran Nguyen: Project administration.

ACKNOWLEDGEMENTS

This research is funded by Vietnam National University - Ho Chi Minh City under grant number 562-2022-20-02.

COMPETING INTERESTS

The authors declare that there is no conflict of interest regarding the publication of this article.

REFERENCES

[1] J.C. Spain (1995), *Biodegradation of Nitroaromatic Compounds*, Springer, 232pp, DOI: 10.1146/annurev.mi.49.100195.002515.

[2] Y. Mori, K. Kamata, N. Toda, et al. (2003), "Isolation of nitrophenols from diesel exhaust particles (DEP) as vasodilatation compounds", *Biol. Pharm. Bull.*, **26(3)**, pp.394-395, DOI: 10.1248/bpb.26.394.

[3] Y. Ohnishi, T. Kinouchi, Y. Manabe, et al. (1985), "Nitro compounds in environmental mixtures and foods", *Short-Term Bioassays in The Analysis of Complex Environmental Mixtures IV*, Springer, 10pp, DOI: 10.1007/978-1-4615-7849-9_16.

[4] X. Chen, X. Cheng, J.J. Gooding, et al. (2012), "Detection of trace nitroaromatic isomers using indium tin oxide electrodes modified using β-cyclodextrin and silver nanoparticles", *Anal. Chem.*, **84(20)**, pp.8557-8563, DOI: 10.1021/ac3014675.

[5] C.L. Zhang, Y.Y. Yu, Z. Fang, et al. (2018), "Recent advances in nitroaromatic pollutants bioreduction by electroactive bacteria", *Process Biochemistry*, **70**, pp.129-135, DOI: 10.1016/j.procbio.2018.04.019.

[6] P. Sam-ang, D. Raksasorn, M. Sukwattanasinitt, et al. (2014), "A nitroaromatic fluorescence sensor from a novel tripyrenyl truxene", *RSC Adv.*, **4(101)**, pp.58077-58082, DOI: 10.1039/C4RA11407H.

[7] F.A. Tafreshi, Z. Fatahi, S.F. Ghasemi, et al. (2020), "Ultrasensitive fluorescent detection of pesticides in real sample by using green carbon dots", *PLOS ONE*, **15(3)**, DOI: 10.1371/journal. pone.0230646.

[8] V. Gruznov, M.N. Baldin, B.G. Titov, et al. (2011), "Progress in methods for the identification of explosives in Russia", *Journal of Analytical Chemistry*, **66(11)**, DOI: 10.1134/S1061934811110074.

[9] K.E. Brown, M.T. Greenfield, S.D. McGrane, et al. (2016), "Advances in explosives analysis - Part I: Animal, chemical, ion, and mechanical methods", *Anal. Bioanal. Chem.*, **408(1)**, pp.35-47, DOI: 10.1007/s00216-015-9040-4.

[10] X. Sun, Y. Wang, Y. Lei, et al. (2015), "Fluorescence based explosive detection: From mechanisms to sensory materials", *Chem. Soc. Rev.*, **44(22)**, pp.8019-8061, DOI: 10.1039/C5CS00496A.

[11] L.L. Zhou, M. Li, H.Y. Lu, et al. (2016), "Benzo[5]helicene-based conjugated polymers: Synthesis, photophysical properties, and application for the detection of nitroaromatic explosives", *Polymer Chem.*, **7(2)**, pp.310-318, DOI: 10.1039/C5PY01794G.

[12] M. Chhatwal, R. Mittal, R.D. Gupta, et al. (2018), "Sensing ensembles for nitroaromatics", *J. Mater. Chem. C*, **6(45)**, pp.12142-12158, DOI: 10.1039/C8TC03929A.

[13] D.T. McQuade, A.E. Pullen, T.M. Swager, et al. (2000), "Conjugated polymer-based chemical sensors", *Chem. Rev.*, **100(7)**, pp.2537-2574, DOI: 10.1021/cr9801014.

[14] A. Rose, Z. Zhu, C.F. Madigan, et al. (2005), "Sensitivity gains in chemosensing by lasing action in organic polymers", *Nature*, **434(7035)**, pp.876-879, DOI: 10.1038/nature03438.

[15] V. Kumar, B. Maiti, M.K. Chini, et al. (2019), "Multimodal fluorescent polymer sensor for highly sensitive detection of nitroaromatics", *Scientific Reports*, **9(1)**, DOI: 10.1038/s41598- 019-43836-w.

[16] L.E. Kreno, K. Leong, O.K. Farha, et al. (2012), "Metal-organic framework materials as chemical sensors", *Chem. Rev.*, **112(2)**, pp.1105-1125, DOI: 10.1021/cr200324t.

[17] Z. Hu, B.J. Deibert, J. Li (2014), "Luminescent metal-organic frameworks for chemical sensing and explosive detection", *Chem. Soc. Rev.*, **43(16)**, pp.5815-5840, DOI: 10.1039/c4cs00010b.

[18] W.P. Lustig, S. Mukherjee, N.D. Rudd, et al. (2017), "Metal-organic frameworks: Functional luminescent and photonic materials for sensing applications", *Chem. Soc. Rev.*, **46(11)**, pp.3242-3285, DOI: 10.1039/c6cs00930a.

[19] C.J. Cumming, C. Aker, M. Fisher, et al. (2001), "Using novel fluorescent polymers as sensory materials for above-ground sensing of chemical signature compounds emanating from buried landmines", *IEEE Transactions on Geoscience and Remote Sensing*, **39(6)**, pp.1119-1128, DOI: 10.1109/36.927423.

[20] S.J. Toal, W.C. Trogler (2006), "Polymer sensors for nitroaromatic explosives detection", *J. Mater. Chem.*, **16(28)**, pp.2871-2883, DOI: 10.1039/B517953J.

[21] T.M. Swager (1998), "The molecular wire approach to sensory signal amplification", *Acc. Chem. Res.*, **31(5)**, pp.201-207, DOI: 10.1021/AR9600502.

[22] J.S. Yang, T.M. Swager (1998), "Porous shape persistent fluorescent polymer films: An approach to TNT, sensory materials", *J. Am. Chem. Soc.*, **120**, pp.5321-5322, DOI: 10.1021/ja9742996.

[23] D. Gao, Z. Wang, B. Liu, et al. (2008), "Resonance energy transfer-amplifying fluorescence quenching at the surface of silica nanoparticles toward ultrasensitive detection of TNT", *Anal. Chem.*, **80(22)**, pp.8545-8553, DOI: 10.1021/ac8014356.

[24] A.S. Tanwar, S. Patidar, S. Ahirwar, et al. (2019), "Receptor free" inner filter effect based universal sensors for nitroexplosive picric acid using two polyfluorene derivatives in the solution and solid states", *Analyst*, **144(2)**, pp.669-676, DOI: 10.1039/c8an01970c.

[25] A. Qin, L. Tang, J.W.Y. Lam, et al. (2009), "Metal-free click polymerization: Synthesis and photonic properties of poly(aroyltriazole)s", *Advanced Functional Materials*, **19(12)**, pp.1891-1900, DOI: 10.1002/adfm.200801933.

[26] Y. Liang (2019), "Core-modified of fluoranthene with "propeller" structure for highly sensitive detection of nitroaromatic compounds", *Spectrochimica Acta Part a Molecular and Biomolecular Spectroscopy*, **206**, pp.474-483, DOI: 10.1016/j.saa.2018.08.046.

[27] V. Saini, A. Gupta, K. Rangan, et al. (2020), "A selective turn-off fluorescence detection of nitroexplosive 2, 4, 6-trinitrophenol by pyridinium-based chemosensor in pure aqueous medium", *Dyes and Pigments*, **180**, DOI: 10.1016/j.dyepig.2020.108447.

[28] Y.H. Lee, H. Liu, J.Y.L. Prof, et al. (2010), "Dipyrenylcalix[4]arene-a fluorescence-based chemosensor for trinitroaromatic explosives", *Chemistry*, **16(20)**, pp.5895-5901, DOI: 10.1002/chem.200903439.

[29] N. Yan, J. Song, F. Wang, et al. (2019), "Pyrenoviologen-based fluorescent sensor for detection of picric acid in aqueous solution", *Chinese Chemical Letters*, **30(11)**, pp.1984-1988, DOI: 10.1016/j.cclet.2019.09.039.

[30] C. Wu, J.L. Zhao, X.K. Jiang, et al. (2016), "Click-modified hexahomotrioxacalix [3] arenes as fluorometric and colorimetric dual-modal chemosensors for 2, 4, 6-trinitrophenol", *Analytica Chimica Acta*, **936**, pp.216-221, DOI: 10.1016/j.aca.2016.06.045.

[31] S. Shanmugaraju, S. Joshi, P. Mukherjee, et al. (2011), "Fluorescence and visual sensing of nitroaromatic explosives using electron rich discrete fluorophores", *J. Mater. Chem.*, **21(25)**, pp.9130-9138, DOI: 10.1039/C1JM10406C.

[32] X. Feng, J.Y. Hu, C. Redshaw, et al. (2016), "Functionalization of pyrene to prepare luminescent materials-typical examples of synthetic methodology", *Chemistry*, **22(34)**, pp.11898-11916, DOI: 10.1002/chem.201600465.

[33] N. Venkatramaiah, A.D.G. Firmin, F. Paz, et al. (2014), "Fast detection of nitroaromatics using phosphonate pyrene motifs as dual chemosensors", *Chem. Commun.*, **50(68)**, pp.9683-9686, DOI: 10.1039/c4cc03980g.

[34] K.R.J. Thomas, A. Baheti (2013), "Fluorene based organic dyes for dye sensitised solar cells: Structure-property relationships", *Materials Technology*, **28(1-2)**, pp.71-87, DOI: 10.1179/1753555712Y.0000000036.

[35] S. Fratiloiu, S.M. Fonseca, F.C. Grozema, et al. (2007), "Opto-electronic properties of fluorene-based derivatives as precursors for light-emitting diodes", *J. Phys. Chem. C*, **111(15)**, pp.5812-5820, DOI: 10.1021/jp067923m.

[36] S. Matthias (2016), "Synthesis of 1-Bromopyrene and 1-Pyrenecarbaldehyde", *Organic Syntheses*, **93**, pp.100-114, DOI: 10.15227/orgsyn.093.0100.

DOI: 10.31276/VJSTE.65(1).19-24

Development of a miniaturised potentiostat for urea detection using the LMP91000

Chi Tran Nhu, Phu Nguyen Dang*, Tung Bui Thanh, Trinh Chu Duc

University of Engineering and Technology, Vietnam National University, Hanoi, 144 Xuan Thuy Street, Dich Vong Hau Ward, Cau Giay District, Hanoi, Vietnam

Received 5 September 2022; revised 15 November 2022; accepted 29 November 2022

Abstract:

In this report, we develop a low-cost cyclic voltammetry platform for electrochemical analyses based on the LMP91000 integrated circuit (IC). The proposed system can be suitable to detect chemicals of interest in food safety or biology. The system includes three main blocks: the electrodes, electrochemical measuring circuit, and data acquisition. An algorithm was also built to process and display the data on the screen. Experiments are carried out with a standard redox solution containing Fe(II)/Fe(III) 5 mM and KCl 0.1 mM to evaluate system performance and make comparisons to the commercial potentiostat. The results show that the obtained signals from the proposed system and the commercial potentiostat device are similar. With applications of the miniaturised potentiostat, a non-enzymatic electrochemical biosensor for urea detection was fabricated on cobalt sulphide materials (CoS) synthesized via a microwave assisted method. The sensing performance for urea was determined by changing the oxidation potential peak of 100 mV. The sensor had a linear range from 1-8 mM corresponding to the urea concentration in blood. The sensor sensitivity was comparable (7.5 $\mu AmM^{-1}cm^{-2}$) to some previous publications. With the achieved results, the proposed system demonstrates potential in urea detection and can be a prototype to develop a commercial device for point-of-care testing in the future.

Keywords: **electrochemical system, LMP91000, urea detection.**

Classification numbers: **2.2, 2.3**

1. Introduction

Electrochemical biosensors presently attract significant interest from research groups worldwide. Electrochemical biosensors are a subclass of biological sensors that includes biological sensing elements and electrochemical transducers [1]. These sensors show outstanding advantages in terms of sensitivity, low detection limits, and high specificity of biological recognition elements [2]. These recognition elements can be enzymes, antibodies, deoxyribonucleic acid or ribonucleic acid (DNA/RNA), tissues, or other biomolecules, which react selectively with the target analyte and subsequently provide an electrical signal proportional to the target analyte's concentration. The signal is converted and processed by the transducer and microcontrollers, respectively. Based on the nature of the biological sensing elements, there are two main types of electrochemical sensors: biocatalytic devices and affinity sensors [3]. While biocatalytic devices use enzymes to sense the target analyte, affinity sensors employ selective binding interactions between the analyte and a biological component. Electrochemical biosensors have been developed to detect a wide variety of analytes such as lactate [4, 5], sodium [6, 7], cocaine [8-10], alcohol [11, 12], and glucose [13, 14]. In addition, electrochemical biosensors have been used for the detection of some diseases in humans such as celiac disease [15], breast cancer [16, 17], prostate cancer [18], and the hepatitis B virus [19].

Potentiostats are a popular instrument designed to perform electrochemical measurements. They can control the working electrode's potential and have features for accurate measurements of the electrochemical cell [20]. Some commercial potentiostats used in laboratories include Sensit BT Model (PalmSens, The Netherlands), AutoLab (Metrohm, The Netherlands), and CS350 EIS Potentiostat/Galvanostat (Orrtestinstruments, China). However, these are expensive and sophisticated instruments that are difficult to apply to point-of-care applications. Presently, research groups around the world are focusing on the development of self-designed potentiostats to increase the affordability and accessibility of potentiostats as well as to miniaturize their electrochemistry hardware for at-home or portable diagnostic applications [21-24]. These potentiostats can be built from discrete electronic components or from an IC. One commonly used IC is the LMP91000 IC developed

*Corresponding author: Email: phund@vnu.edu.vn

by Texas Instruments, a programmable analogue front-end (AFE) for use in micro-power electrochemical sensing applications. The LMP91000 contains the core features of a benchtop potentiostat and is packed with a size of 4 mm × 4 mm [25]. The LMP91000 can perform some basic electrochemical techniques such as cyclic voltammetry (CV), chronoamperometry (CA), square wave voltammetry (SWV), and normal pulsed voltammetry (NPV) and has so far demonstrated its potential in some biomedical applications [25].

Urea is a waste product of living creatures and the major organic component of human urine. It is the final product of a chain of reactions that break down amino acids making up proteins. These amino acids are converted into ammonia, CO_2, water, and energy. However, ammonia is a substance that is harmful to the body, so must be eliminated. In the human body, the liver converts ammonia to urea, a non-toxic compound, which can then be safely transported in the blood to the kidneys, where it is eliminated in urine. Thus, urea is an important parameter for testing kidney and liver function. Urine and blood serum have normal urea concentrations in the range of 2.7 to 7.5 mM [26]. High concentrations of urea in body fluid can cause diseases such as kidney failure, urinary tract obstruction, or gastrointestinal blood loss while lower concentrations can lead to hepatic malfunction, cachexia, or nephritic disorder [27]. Therefore, it is important to precisely measure urea concentration in body fluid to monitor health. In this study, we propose an electrochemical system to detect urea using the LMP91000 IC with a Co-based metal catalyst. The system can read data from functionalized electrodes through its measuring circuit before being transferred to a PC for processing and analysis. An algorithm is built to process the obtained signal and compare it to the results from a commercial device to evaluate the algorithm's performance. The system is not only capable of detecting urea but can also be customized to detect other chemicals.

2. System design and experimental setup

2.1. Materials and components

An LMP91000EVN sensor was utilized as a miniaturised electrochemical measuring system and was purchased from Texas Instruments (USA). An Arduino UNO R3 KIT (Arduino.cc) was used as the micro-controller for the system to communicate with the measuring circuit and PC. Commercial electrodes were purchased from Biodevice Technology, Ltd. (Japan) for system evaluation. All chemicals were purchased from Sigma Aldrich, namely, polyvinyl pyrroidone K30, thioacetamide, cobalt (II) acetate, Nafion, potassium hydroxide (KOH), urea, and potassium chloride (KCl). A compact potentiostat, namely, the BDTminiSTAT100 from Biodevice Technology, Ltd. (Japan), was used to compare the performance of the system.

2.2. System design

The system includes three main blocks: the electrodes, electrochemical measuring circuit, and data acquisition. There are three electrodes used for performing electrochemical measurements i.e., the working, counter, reference electrodes. The working electrode was made of copper and fabricated by circuit board printing. After fabrication, this electrode was processed so that chemicals could be attached to it for urea detection. The counter electrode was made of platinum to ensure that its surface was not affected by the chemical reactions in the experiments. The final electrode is the reference electrode, which was a type of standard reference electrode with a stable and well-known electrode potential.

In this report, cyclic voltammetry measurements with a three-electrode system were used as the standard method for urea detection. An output voltage was generated by the LMP91000 proportional to the current flowing through the working electrode. The trans-impedance amplifier (TIA) provided the output voltage at the output stage. It converts the current flowing from the working electrode to the counter electrode into a voltage at a directly proportional rate as shown in the schematic diagram of the LMP91000 in Fig. 1A. To perform the desired measurements, some hardware configurations were performed manually (Fig. 1B) including the J_MENB jumper configured to enable manual operation mode. In manual mode, the Enable Module of the LMP91000 was tied to GND, which allows users to set function parameters such as TIA Control and RLOAD. While TIA Control changes the gain of trans-impedance amplifier, RLOAD is used to adjust the value of the current drawn from the sensor to the TIA during measurements. In our system, the TIA Control and the RLOAD were set with values of 3.5 kΩ and 10 Ω, respectively. Additionally, the R6 resistor was removed to connect an external reference voltage of 3.3 V between the VREF and GND test points instead of the default internal reference voltage of 2.5 V. This helps the output voltage of the board to reach 2.2 V if the internal zero parameter is assigned to be 67% of the reference voltage. In addition, the two-wire jumper was removed to activate three-electrode (working, counter, and reference) CV measurements for a portable potentiostat system.

To configure other parameters and receive data from the electrodes, an Arduino UNO R3 KIT was used as the central processing unit (CPU) of the system. The Arduino powers and communicates to the LMP91000 through I2C standard communication. The Arduino KIT and LMP91000 module were stacked to minimize the size of the device, as shown in Fig. 1B. The Arduino KIT was placed at the bottom of the stack and connected to the LMP91000 module. In addition

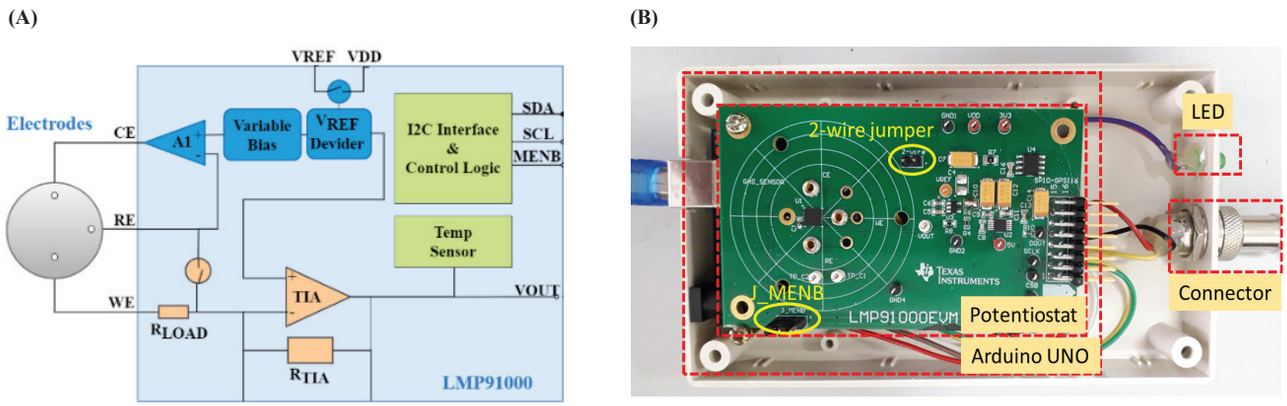

Fig. 1. (A) Block diagram of LMP91000 IC; (B) Image of the proposed system after assembly.

to the I2C connection, the output voltage of the LMP91000 (VOUT) was wired to the analogue input of the Arduino module (A0). A graphical user interface on the computer was developed using MATLAB software to receive and display the obtained data through a communication port (COM). The software plots the data on a graph with different colours for each scan making it is easy for users to observe and evaluate results. The LMP91000 module and Arduino UNO are the two main components of the proposed system. They were purchased from authorized retailers for $131.67 and $27.60, respectively. The cost of the other components was about $15. So, the total cost of the system is estimated to be about $174.27. This number is small compared to the ~$10,000 price tag of commercial device such as the Autolab Potentiostat or BDTminiSTAT100.

2.3. Experimental setup

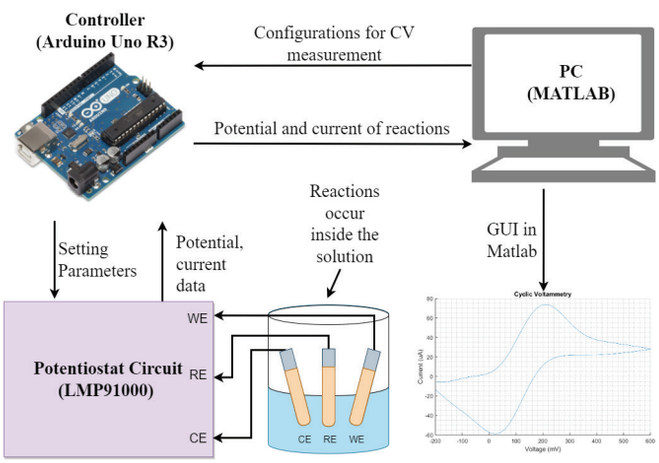

Fig. 2. Experimental setup diagram for urea detection.

The working electrode with a diameter of 10 mm was self-designed as a pad using Altium Designer software and fabricated by printed circuit board technology (PCB). The working electrode surface was then cleaned and functionalized by CoS materials according to a standard process (Fig. 2). Firstly, the copper electrode was cleaned by isopropyl alcohol (IPA) in an ultrasonic vibration tank about 10 minutes before being dried by pure nitrogen gas. Secondly, the CoS solution was made by adding 3 mg CoS into a solution including 1.6 ml distilled water, 0.4 ml ethanol, and 20 µl Nafion. Then, this mixture was placed in an ultrasonic vibration tank for 10 min to achieve a homogeneous solution. Finally, the CoS solution was dropped onto the copper electrode surface and dried under room temperature conditions. Following this, the three-electrode system was immersed in a solution with different urea concentrations. CV electrochemical measurements were made to investigate the change of the urea through an electrical signal. Some parameters were configured on software, including the potential range from -0.2 to 0.6 V, scan rate at 20 mV/s, and sample rate at 50 Hz.

3. Results and discussion

3.1. Signal processing algorithm

After assembly, the proposed system was tested with a standard redox solution containing Fe(II)/Fe(III) 5 mM and KCl 0.1 mM to evaluate system performance and make comparisons to the commercial potentiostat BDTminiSTAT100 (Biodevice Technology, Japan). Three electrodes were immersed in the redox solution and the measurement parameters were configured on the software with potential range from -0.2 to 0.6 V, scan rate at 10 mV/s, and sample rate at 50 Hz. The results show that the obtained signal had a standard duck-shaped CV plot as shown in Fig. 3A. However, the signal had some high frequency noise because it was raw data without any processing. Because the results will not be reliable with noisy data, a signal processing algorithm was developed as shown in Algorithm 1. Firstly, the software is connected to the Arduino KIT through COM port at the baud rate of 9600 bps and some function parameters were set to configure the system for CV measurements. After

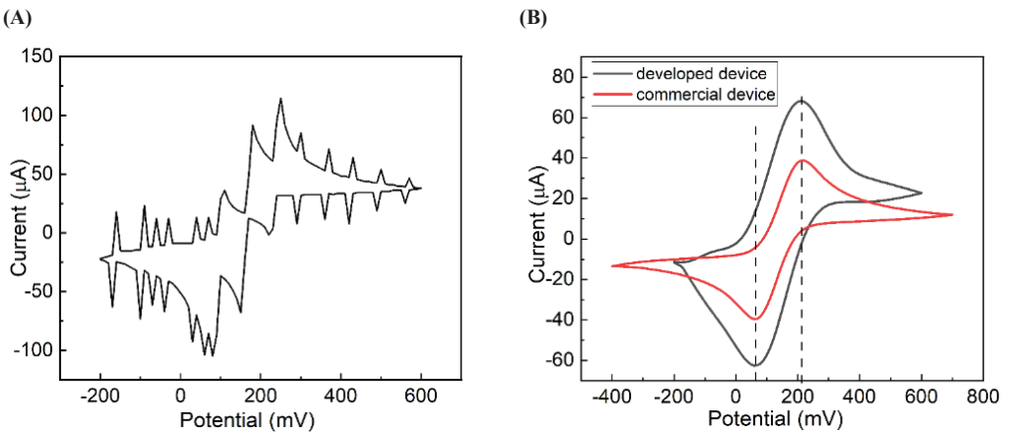

Fig. 3. Signal processing. (A) The initial signal from the proposed system with noise. **(B)** The signal after being processed compared to the signal from a commercial device.

Algorithm 1. Firmware for data acquisition.	
1	Begin serial communication at 9600 bps
2	Set function parameters: starting and ending voltages, step and cycle
3	Initialize the data array
4	While (i < ((ending voltage – starting voltage)/step +1)*cycle*2)
5	Take samples with ADC available on Arduino KIT
6	Convert and save samples into the data array
7	End While
8	Convert the data to the frequency domain using FFT
9	Apply low-pass filter with a cut-off frequency of 2 Hz
10	Convert the data back to the time domain using inverse fast fourier transform
11	Display the signal

configuration, the system carried out sampling through an analogue-to-digital converter (ADC) available on the Arduino KIT and transferred the data to PC. The obtained voltage data were converted into current and saved into a data array, which was initialized until the array contained a number of elements equal to ((ending voltage - starting voltage)/step +1)*cycle*2. Following this, the data was passed through a low-pass filter with a cut-off frequency of 2 Hz. This cut-off frequency was determined based on the conversion of the signal into the frequency domain using a fast fourier transform (FFT). Finally, the processed signal was displayed on a graph, e.g., the black line in Fig. 3B.

The results show the high-frequency noise was removed from the signal and thus significantly smoothed. The obtained signal had the standard duck shape, a characteristic of CV measurements with a redox solution. The same experiment was also performed with a commercial potentiostat from Bio Device Tech. The settings (scan rate, sample rate) were kept the same for both devices. The current signal from the device is displayed as the red line in Fig. 3B. It is clear that both data are similar in shape and have similar positions of oxidation and reduction peaks. The oxidation peaks appear at 200 mV, while the reduction peaks appear at 80 mV. There is a difference in current amplitude between the two signals because of the circuit resistor. The results show that the proposed algorithm helped the system operate like a commercial potentiostats and the obtained signal clearly exhibited the redox process of the solution. Besides, there are many advantages of the obtained signal from the proposed system compared to similar systems developed by other research groups [23-25] in terms of the shape of the signal and accuracy.

3.2. Electrochemical detection of urea

The three-electrode system was immersed in solutions with different urea concentrations. CV measurements were taken during each experiment to monitor the change of the current as it flowed through the liquid sample as the voltage value shifted. The results show that a signal peak began to appear when urea was in the sample and the value of the current peak increased considerably with increasing urea concentration as shown in Fig. 4A. This can be explained that urea was oxidized by KOH on the electrode surface of the CoS catalyst following a direct oxidation mechanism as shown in Eqs. (1)-(3) [28]:

At the anode:

$$CoS+OH^- \rightarrow CoSOH+ e^- \quad (1)$$

$$CO(NH_2)_2+6OH^- \rightarrow N_2+5H_2O+ CO_2+6e^- \quad (2)$$

At the cathode:

$$6H_2O+6e^- \rightarrow 3H_2+6OH^- \quad (3)$$

In Eq. (1), CoS was electrochemically oxidized to CoSOH, which participated in the urea oxidation reaction as a catalyst. Then, urea was oxidized by KOH

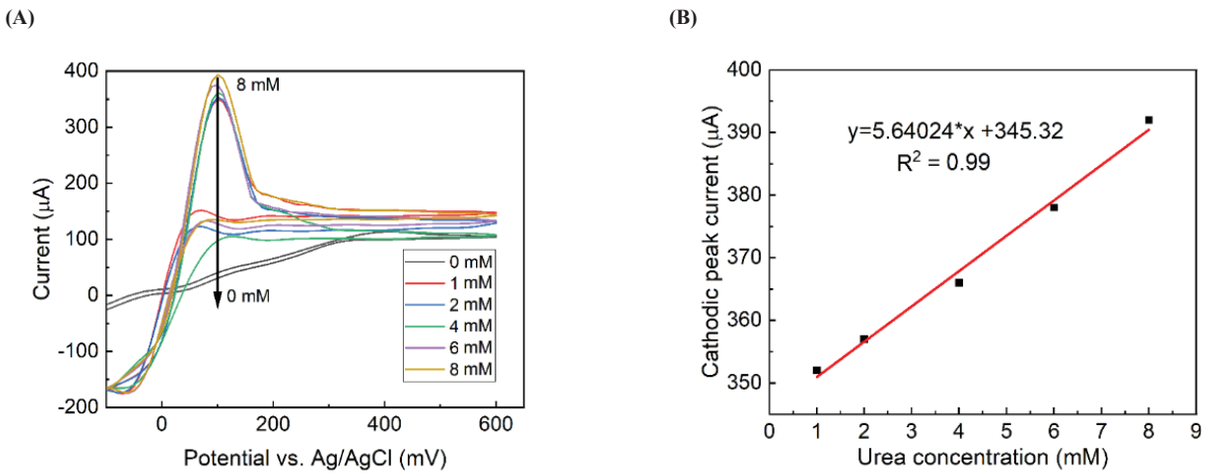

Fig. 4. (A) The electrochemical signal obtained from the proposed system with different urea concentrations; (B) Linear calibration line plotted between the magnitude of response current and urea concentration using the proposed system.

to release electrons, N_2, and CO_2 as shown in Eq. (2). So, more electrons were generated or the current response increased when the urea concentration changed from 1 mM to 8 mM. A linear trendline was fit to the relationship between the magnitude of the current response and urea concentration. The equation of best fit was $I_{response\ current}$ (μA) = 5.64024*urea concentration (mM) + 345.32, as shown Fig. 4B. From this linear relation, it is easy to determine the urea concentration through the current response.

A comparison between these results and results from other urea detection publications using non-enzymatic methods was performed as shown in Table 1. As can be seen, the CoS-based electrodes were more sensitive than Co-MOF. Notably, the working potential in this study was the lowest.

Table 1. Comparative data for electrochemical urea detection.

Electrodes	Electrolyte	Potential (V)	Sensitivity (μAmM^{-1})	Ref.
$NiCo_2O_4$	0.1 M NaOH	0.5	8.2	[29]
Co-MOF	0.1 M KOH	0.45	5	[30]
HEA: Graphene composite	1 M KOH	0.3	37.4	[31]
SnO_2	1 M KOH	0.65	18	[32]
CoS	0.1 M KOH	0.1	7.13	This work

4. Conclusions

In this work, a miniaturised potentiostat system using an LMP91000 analogue front-end was developed to detect urea concentration in solution. The system included three main blocks: the electrodes, the electrochemical measuring circuit, and data acquisition. The data was read from three-electrode system and transferred to PC through a COM port. An algorithm was developed to process the signal before display on the graphic user interface. The system was then tested with a standard redox solution and compared to a commercial potentiostat to evaluate the performance of the signal processing algorithm and the system in general. The results show that the obtained signals from the proposed system and the commercial potentiostat device are similar. The data clearly exhibit the redox process of the solution with oxidation and reduction peaks. Additionally, the system was used to detect urea in the solution. The working electrode surface was functionalized to attach CoS particles to it. The efficiency of the surface functionality process was confirmed by optical measurements. The results show that the system could detect and quantify urea concentration by CV measurements. Urea concentration was found to be proportional to the oxidation current peak by a first order function. Besides, the effect of scan rate on the signal and the selectivity of the proposed system were also investigated. The results show that the oxidation peak current increased linearly with the increase of the scan rate and that the electrodes have high selectivity with urea. With these achieved results, the proposed system not only demonstrated its potential in urea detection but also showed the ability to detect some other toxic substances such as nitrate or pesticides.

CRediT author statement

Chi Tran Nhu: Experiment, Writing, Review; Phu Nguyen Dang: Conceptualization, Measurement, Data analyst, Editing; Tung Bui Thanh: Writing, Editing, Data analyst; Trinh Chu Duc: Review, Data analyst, Editing.

ACKNOWLEDGEMENTS

This work has been supported by VNU University of Engineering and Technology under project number CN21.17.

COMPETING INTERESTS

The authors declare that there is no conflict of interest regarding the publication of this article.

REFERENCES

[1] Y. Huang, J. Xu, J. Liu, et al. (2017), "Disease-related detection with electrochemical biosensors: A review", *Sensors (Switzerland)*, **17(10)**, DOI: 10.3390/s17102375.

[2] N.J. Ronkainen, H.B. Halsall, W.R. Heineman, et al. (2010), "Electrochemical biosensors", *Chem. Soc. Rev.*, **39(5)**, pp.1747-1763, DOI: 10.1039/b714449k.

[3] C. Roychoudhuri (2008), *Fundamentals of Photonics*, SPIE, 418pp, http://spie.org/Publications/Book/784938, accessed 20 July 2022.

[4] W. Jia, A.J. Bandodkar, J.R. Windmiller, et al. (2013), "Electrochemical tattoo biosensors for real-time noninvasive lactate monitoring in human perspiration", *Analytical Chemistry*, **85(14)**, pp.6553-6560, DOI: 10.1021/ac401573r.

[5] W. Gao, S. Challa, K. Chen, et al. (2016), "Fully integrated wearable sensor arrays for multiplexed in situ perspiration analysis", *Nature*, **529**, pp.509-514, DOI: 10.1038/nature16521.

[6] A.J. Bandodkar, D. Molinnus, O. Mirza, et al. (2014), "Epidermal tattoo potentiometric sodium sensors with wireless signal transduction for continuous non-invasive sweat monitoring", *Biosens. Bioelectron.*, **54**, pp.603-609, DOI: 10.1016/j.bios.2013.11.039.

[7] B. Schazmann, D. Morris, C. Slater, et al. (2010), "A wearable electrochemical sensor for the real-time measurement of sweat sodium concentration", *Analytical Methods*, **2(4)**, pp.342-348, DOI: 10.1039/B9AY00184K.

[8] B.R. Baker, R.Y. Lai, M.S. Wood, et al. (2006), "An electronic, aptamer-based small-molecule sensor for the rapid, label-free detection of cocaine in adulterated samples and biological fluids", *J. Am. Chem. Soc.*, **128(10)**, pp.3138-3139, DOI: 10.1021/ja056957p.

[9] J.L. He, Y.F. Yang, G.L. Shen, et al. (2011), "Electrochemical aptameric sensor based on the Klenow fragment polymerase reaction for cocaine detection", *Biosens. Bioelectron.*, **26(10)**, pp.4222-4226, DOI: 10.1016/j.bios.2011.03.032.

[10] S. Rauf, L. Zang, A. Ali, et al. (2017), "Label-free nanopore biosensor for rapid and highly sensitive cocaine detection in complex biological fluids", *ACS Sensors*, **2(2)**, pp.227-234, DOI: 10.1021/acssensors.6b00627.

[11] J. Kim, I. Jeerapan, S. Imani, et al. (2016), "Noninvasive alcohol monitoring using a wearable tattoo-based iontophoretic-biosensing system", *ACS Sensors*, **1(8)**, pp.1011-1019, DOI:10.1021/acssensors.6b00356.

[12] A.S. Campbell, J. Kim, J. Wang (2018), "Wearable electrochemical alcohol biosensors", *Curr. Opin. Electrochem.*, **10**, pp.126-135, DOI: 10.1016/j.coelec.2018.05.014.

[13] C. Chen, Q. Xie, D. Yang, et al. (2013), "Recent advances in electrochemical glucose biosensors: A review", *RSC Adv.*, **3(14)**, pp.4473-4491, DOI: 10.1039/C2RA22351A.

[14] J. Wang (2008), "Electrochemical glucose biosensors", *Chem. Rev.*, **108(2)**, pp.814-825, DOI: 10.1021/cr068123a.

[15] N.J. Ronkainen, H.B. Halsall, W.R. Heineman, et al. (2010), "Electrochemical biosensors", *Chem. Soc. Rev.*, **39(5)**, pp.1747-1763, DOI: 10.1039/B714449K.

[16] A. Benvidi, A.D. Firouzabadi, M.D. Tezerjani, et al. (2015), "A highly sensitive and selective electrochemical DNA biosensor to diagnose breast cancer", *J. Electroanal. Chem.*, **750**, pp.57-64, DOI: 10.1016/j.jelechem.2015.05.002.

[17] H.A. Rafiee-Pour, M. Behpour , M. Keshavarz, et al. (2016), "A novel label-free electrochemical miRNA biosensor using methylene blue as redox indicator: Application to breast cancer biomarker miRNA-21", *Biosens. Bioelectron.*, **77**, pp.202-207, DOI: 10.1016/j.bios.2015.09.025.

[18] P.Y. Lin, K.L. Cheng, S. Gupta, et al. (2012), "Detection of alpha-methylacyl-CoA racemase (AMACR), a biomarker of prostate cancer, in patient blood samples using a nanoparticle electrochemical biosensor", *Biosensors*, **2(4)**, pp.377-387, DOI: 10.3390/bios2040377.

[19] A.D.L.E. Muniz, M.M. Costa, C.S. Espinel, et al. (2010), "Gold nanoparticle-based electrochemical magnetoimmunosensor for rapid detection of anti-hepatitis B virus antibodies in human serum", *Biosens. Bioelectron.*, **26(4)**, pp.1710-1714, DOI: 10.1016/j.bios.2010.07.069.

[20] M.D.M. Dryden, A.R. Wheeler (2015), "DStat: A versatile, open-source potentiostat for electroanalysis and integration", *PLOS ONE*, **10(10)**, DOI: 10.1371/JOURNAL.PONE.0140349.

[21] V. Bianchi, A. Boni, S. Fortunati, et al. (2020), "A wi-fi cloud-based portable potentiostat for electrochemical biosensors", *IEEE Trans. Instrum. Meas.*, **69(6)**, pp.3232-3240, DOI: 10.1109/TIM.2019.2928533.

[22] S.V. Raj, J. Stanley, T.G. SatheeshBabu (2018), "Fabrication of a configurable multi-potentiostat for LOC applications", *Mater. Today Proc.*, **5(8)**, pp.16732-16739, DOI: 10.1016/j.matpr.2018.06.038.

[23] A.R. Baranwal, S. Dudala, P. Rewatkar, et al. (2021), "Development of completely automated poly potential portable potentiostat", *ECS J. Solid State Sci. Technol.*, **10(2)**, DOI: 10.1149/2162-8777/abdc15.

[24] O.S. Hoilett, J.F. Walker, B.M. Balash, et al. (2020), "Kickstat: A coin-sized potentiostat for high-resolution electrochemical analysis", *Sensors (Switzerland)*, **20(8)**, pp.1-12, DOI: 10.3390/s20082407.

[25] A.F.D. Cruz, N. Norena, A. Kaushik, et al. (2014), "A low-cost miniaturised potentiostat for point-of-care diagnosis", *Biosens. Bioelectron.*, **62**, pp.249-254, DOI: 10.1016/j.bios.2014.06.053.

[26] D. Dutta, S. Chanda, A.K. Swain, et al. (2014), "SnO_2 quantum dots-reduced graphene oxide composite for enzyme-free ultrasensitive electrochemical detection of urea", *Analytical Chemistry,* **86(12)**, pp.5914-5921, DOI: 10.1021/ac5007365.

[27] A. Sharma, K. Rawat, H.B. Bohidar, et al. (2017), "Studies on clay-gelatin nanocomposite as urea sensor", *Appl. Clay Sci.*, **146**, pp.297-305, DOI: 10.1016/j.clay.2017.06.012.

[28] J. Jiang, Y. Sun, Y. Chen, et al. (2019), "One-step synthesis of nickel cobalt sulfide nanostructure for high-performance supercapacitor", *J. Mater. Sci.*, **54(18)**, pp.11936-11950, DOI: 10.1007/s10853-019-03746-8.

[29] C. Bao, Q. Niu, Z.A. Chen, et al. (2019), "Ultrathin nickel-metal-organic framework nanobelt based electrochemical sensor for the determination of urea in human body fluids", *RSC Adv.*, **9(50)**, pp.29474-29481, DOI: 10.1039/c9ra05716a.

[30] X. Wang, B. Liu, J. Li, et al. (2021), "Conductive 2D metal-organic framework (Co, NiCo, Ni) nanosheets for enhanced non-enzymatic detection of urea", *Electroanalysis*, **33(6)**, pp.1484-1490, DOI: 10.1002/elan.202060586.

[31] R. Ashwini, M.K.P. Kumar, M.Y. Rekha, et al. (2022), "Optimization of NiFeCrCoCu high entropy alloy nanoparticle - graphene (HEA-G) composite for the enhanced electrochemical sensitivity towards urea oxidation", *J. Alloys Compd.*, **903**, DOI: 10.1016/J.JALLCOM.2022.163846.

[32] S.G. Ansari, H. Fouad, H.S. Shi, et al. (2015), "Electrochemical enzyme-less urea sensor based on nano-tin oxide synthesized by hydrothermal technique", *Chem. Biol. Interact.*, **242**, pp.45-49, DOI: 10.1016/j.cbi.2015.09.014.

Polyamidoamine dendrite-tailored mesoporous nanosilica surfaces for high drug loading and controlled release

Hung-Cuong Luu[1, 2], Cuong Quoc Ngo[1, 2], Ngoc Hoi Nguyen[1, 3, 4], Dieu Linh Tran[1, 4], Dai Hai Nguyen[1, 3, 4], Cuu Khoa Nguyen[1*]

[1]Institute of Applied Materials Science, Vietnam Academy of Science and Technology, 1B TL29 Street, Thanh Loc Ward, District 12, Ho Chi Minh City, Vietnam
[2]Biomaterials and Nanotechnology Research Group, Faculty of Applied Sciences, Ton Duc Thang University, 19 Nguyen Huu Tho Street, Tan Phong Ward, District 7, Ho Chi Minh City, Vietnam
[3]Graduate University of Science and Technology, Vietnam Academy of Science and Technology, 18 Hoang Quoc Viet Street, Nghia Do Ward, Cau Giay District, Hanoi, Vietnam
[4]Institute of Chemical Technology, Vietnam Academy of Science and Technology, Thach Loc Ward, 1A TL29 District 12, Ho Chi Minh City, Vietnam

Received 20 June 2022; revised 6 September 2022; accepted 16 September 2022

Abstract:

Mesoporous silica nanoparticles (MSNs) have been demonstrated as a promising candidate in drug delivery applications. With the ambition of enhancing their drug loading capacity and controlled release, in this innovative study, MSNs were tailored with polyamidoamine (PAMAM) dendrimers thereby exerting advantageous properties onto the surface of the nanoplatforms. MSNs were prepared by Stöber's method, sequentially functionalised by amine groups, and respectively grafted with PAMAMs layer-by-layer. A correlation between zeta potential and logarithmic molar density of the amino groups was found, which uncovered a straightforward approach to quickly quantify the fabrication of amine-functionalised nanoparticles. Morphology and characterisation of the nanoparticles were carried out through transmission electron microscopy, dynamic light scattering, thermogravimetric analysis, and Fourier-transform infrared spectroscopy. Ninhydrin assay and zeta potential analysis were further employed to investigate the amine-modified nanomaterials. The drug loading and release profiles of particles were also studied. As a result, PAMAM-grafted MSNs, with the highest hydrodynamic size of 185.3 nm, exhibited high encapsulation efficiency (85.8%) and controlled release ability compared to conventional MSNs, suggesting that PAMAM-grafted MSNs would be a promising drug delivery system.

Keywords: **controlled release, drug delivery, mesoporous nanosilica, nanotechnology, polyamidoamine.**

Classification numbers: **2.2, 2.3, 3.6**

1. Introduction

Chemotherapy has become one of the most widely used therapeutics abundantly applied in clinics. However, the treatment of chemotherapy usually requires an excess of chemotherapeutic agents, which inevitably trigger damage to normal tissues [1, 2]. Fortunately, a nanotechnology-mediated approach to chemotherapy has exhibited great potential in enhancing effectiveness by alleviating side effects to healthy tissues and overcoming the drawbacks in the specificity of conventional medicine [3, 4]. With the development of technology, nanomaterials have been well-constructed and designed to improve their pharmacokinetic profile and treatment efficiencies [5]. Besides, with recent insight into the major underlying mechanism--the Enhanced Permeability and Retention (EPR) effect--the "golden age" of nanomedicine was officially born in which a myriad of nanomaterial platforms are being employed for research [6, 7].

Silica-based materials have sparked wide interest with their favourable properties such as chemical and thermal endurance, cytocompatibility, large surface area, and preparedness for surface functionalization [8, 9]. After the invention of Stöber's method based on the sol-gel principle, silica nanoparticles have gained increasing attention [10]. In biomedical applications, nanosilicas are able to be modified in a variety of pathways to become a promising vector for delivering genes [11], antigens [12], proteins [13], and drugs [14, 15], etc. Here, MSNs have emerged at the forefront of silica-based nanomaterials owing to their simple synthesis procedure and architectural control. However, MSNs have several shortcomings that can be enumerated such as the possibility of burst release depending on the interaction between the loaded substances and silica platform and difficulty crossing the epithelial barriers, which could reduce the impact of drugs against disease sites [16, 17]. Nevertheless, these weaknesses could be surmounted by engineered surface modification of MSNs [18, 19].

According to numerous exceptional features, PAMAM dendrimers have emerged as a compatible candidate to overcome the deficiencies of MSNs. PAMAM dendrimers are well-known for their applications in the biomedical field, especially their use in drug delivery [20, 21]. Besides their monodispersity and high aqueous solubility, the polyvalent surface and dendritic architecture, which are similar to biological systems, could augment penetration and functional performance [22, 23]. In addition, the unique hyperbranched structure of PAMAM dendrites generates an interior free-void volume and an exterior of highly dense layers of branches, which could enlarge the loading capacity and

*Corresponding author: Email: nckhoavnn@yahoo.com

decelerate the release rate of drugs. Overall, the combination of PAMAM dendrimers and MSNs could become a novel approach for nanomedicine technology.

In this study, we aimed to engineer conventional MSNs by tailoring PAMAM dendrites on MSN surfaces. The MSNs were synthesised via Stöber's method with nominal modification suggested by our group. The as-synthesised MSNs were further functionalised by amine groups before attaching the PAMAM dendrites. PAMAM grafting was carried out using the Michael reaction and amination reaction, respectively, to attain a third generation of PAMAM dendrimer. To demonstrate its successful preparation, we characterised the morphological and chemical properties of conventional MSNs and a series of PAMAM-modified MSNs by modern methods. The quantification of surface amine groups confirmed the accuracy of synthesis. Finally, with quercetin used as the model drug, the drug loading capacity and release profiles were investigated to validate the enhancement of PAMAM tailoring in comparison with the conventional MSNs in drug delivery ability.

2. Materials and methods

2.1. Materials

Tetraethyl orthosilicate (TEOS, 98%), cetrimonium bromide (CTAB, 98%), (3-aminopropyl)triethoxysilane (APTES, 99%), methyl acrylate (MA, 99%), ethylenediamine (EDA, 99%), ninhydrin (99%), polysorbate 80 (TWEEN 80, 99%), quercetin (QU) (95%), and other reagents were obtained from Merck (Germany). Acid acetic (99.7%) and ammonia (25-28%) were purchased from Xilong (China) Dialysis membrane tubing 12-16 kDa MWCO were purchased from Spectrum™ Labs Spectra/Por™ (USA).

2.2. Methods

The morphology of the particles was observed by scanning electron microscope (SEM, JSM-IT100, Japan) and transmission electron microscope (TEM, JEM-2100, Japan). The obtained SEM image was used to evaluate the mean size of nanoparticles in which ImageJ and Origin software were utilised to perform a size distribution plot. The hydrodynamic size was measured by dynamic light scattering (DLS, SZ-100, Japan), which was also used to determine the zeta potential of nanoparticles. Inherent chemical bonds were detected by Fourier transform-infrared spectrophotometer (FTIR, PerkinElmer, USA) using a KBr pellet. The absorbance measurements of the ninhydrin colorimetric assay were conducted by UV/visible scanning spectrophotometer (UV-Vis, Shimadzu UV-1800, Japan). Thermogravimetric analysis (TGA, Mettler Toledo TGA/DSC 3+, Sweden) was carried out to investigate the thermal stability of particles. The TG plot was recorded from 30 to 800ºC at a ramping rate of 10ºC.min^{-1} under the continuous flow of N_2 gas. X-ray powder diffraction (XRD) patterns were obtained by a diffractometer (Bruker D8 Advance, Germany).

2.3. Synthesis of amine-functionalised MSNs

The fabrication of the MSNs in this research was attempted via the Stöber method with minimal modification as mentioned in a previous publication [24]. The template of this approach was based on the sol-gel process in which TEOS was utilized as the silica precursor, ammonia as the catalyst for hydrolysis and condensation processes, and CTAB as the structure-forming agent. In brief, 2.6 g of CTAB (7.1 mmol) was dissolved in 64 ml of direct ink writing (DIW) and stirred for 30 min to create a homogeneous mixture. The mixture was heated up to 60ºC and the temperature was maintained for 30 min. During this process, the cationic surfactant molecules begin to aggregate to establish spherical micelles. Subsequently, 11.25 ml of EtOH and 550 µl of NH_3 2.8% were added to the above solution and stirred for 5 min at 300 rpm. In this experiment, we used EtOH as the solvent and DIW played a vital role as the reactant in the hydrolysis reaction. Separately, 8 ml of TEOS was transferred to a syringe dispenser and gradually dropped into the resulting solution. The reaction was carried out under vigorous stirring for 2 h at 60ºC. Then, the suspension was quickly cooled down to ambient temperature to terminate the reaction, then sonicated for 30 min. To purify the nanoparticles, the dispersion was dialysed against DIW for 3 h (MWCO 12-14 kDa) and against a mixture of ethanol/ammonia solution (1:1, v/v) for the next 2 d, and finally immersed in DIW for 1 d. After the dialysis process, the MSN-dispersed solution was freeze-dried for further functionalisation.

To chemically activate the surface of the nanoparticles, the inert hydroxyl groups on the spherical surfaces were tailored by amine groups [25]. We utilised the reaction with APTES for the amination of MSNs. Briefly, a suspension of lyophilised MSNs (1 g) in EtOH (20 ml) was gradually introduced into a mixture of APTES and EtOH (1:4, v/v). The reaction was stirred and kept stable at room temperature for 24 h. Ultimately, centrifugation and lyophilization were carried out to collect the amine-functionalised MSNs, which are so-called MSNs-G0.

2.4. Quantitative estimation of amine functional groups

The syntheses of PAMAM dendrites on the silica platforms require high accuracy of the number of moles of reactants; thus, the quantification of the surface concentration of amine is essential for later experiments [26]. We used the ninhydrin test, which is a colorimetric assay based on the reaction of ninhydrin with primary amines to generate a deep purple or blue colour known as Ruhemann's purple. Here, the calibration plot was constructed by preparing a set of highly pristine APTES solutions. The concentration range of the standard substance varied from 50 to 1000 ppm in absolute ethanol solvent. A solution of 0.35% ninhydrin in absolute ethanol (w/v) was carefully prepared and used as an indicator for all quantification assays. Then, 200 mg of functionalised nanoparticles were redispersed in absolute ethanol in a capped vial. Afterwards, the suspensions were placed in a bath sonicator for 30 min; in some cases, the redispersed samples were measured by DLS in order to determine that no aggregation or agglomeration had formed during the purification procedure. Subsequently, 1 ml of the ninhydrin solution was added to the sample-containing vials and placed in a bath sonicator for 10 min,

then transferred to a water bath that was previously set up at 65ºC for 30 min. The resulting dispersions were allowed to cool down to room temperature before undergoing centrifugation to remove the nanoparticles. The supernatant of each sample was pumped out and the absorbance was measured at a wavelength of 588 nm by a Shimadzu UV-1800 UV/visible scanning spectrophotometer. Measurements were conducted three times.

2.5. Synthesis of MSNs-G3

From the nanosilica platform, we developed PAMAM dendrites according to the convergent pathway reported with our nominally adjusted procedure [27, 28]. Briefly, a solution of MA dissolved in methanol was freshly prepared and stirred under nitrogen at 5ºC for 5 min. MSNs-G0 was suspended in a methanol solution and sonicated to be well dispersed. The suspension was added dropwise to the MA solution. After that, the mixture was allowed to react under vigorous stirring and a sealed system at ambient temperature for 4 d. Evaporation and dialysis against methanol were accomplished to eliminate excessive MA and obtain half-generation PAMAM nanoparticles which were denoted by MSNs-G0.5. Sequentially, full-generation PAMAMs were achieved with Michael's reaction. Similarly, a solution of EDA in methanol was also prepared with a blown nitrogen atmosphere at 5ºC for 5 min. A suspension of MSNs-G0.5 in methanol was moderately dropped into the EDA solution. Then, the reaction was carried out under the same conditions with half-generation PAMAM synthesis. Afterwards, unreacted EDA was initially removed *in vacuo* and dialysis against a mixture of toluene/methanol (9:1, v/v) to yield MSNs-G1. The product continually underwent similar routes to attain higher generation PAMAMs, finally stopping at MSNs-G3.

2.6. Loading and release of quercetin

To determine the enhancement in drug loading, an encapsulation of nanomaterials was conducted on the MSNs and MSNs-G3. QU was employed as a typical anticancer compound to evaluate the possibility of these nanosystems in drug delivery. The carriers (10 mg) were dispersed in 9 ml of methanol and ultrasonication was also carried out for 30 min. 1 mg of QU was dissolved in 1 ml of methanol and the solution was then added to the nanomaterial suspensions. The mixtures were allowed to stir overnight in the dark. Subsequently, excessive QU was expelled by the dialysis membrane before lyophilization to yield the drug-encapsulated nanoparticles. These QU-encapsulated were named QU@MSNs and QU@MSNs-G3, respectively. The supernatant containing the excess QU was collected to quantitatively calculate the encapsulation efficiency (%EE) and drug loading capacity (%LC) of the nanomaterials using the following equations:

$$\%EE = \frac{\text{weight of QU in nanoparticles}}{\text{initial weight of QU added}} \times 100\% \quad (1)$$

$$\%LC = \frac{\text{weight of QU in nanoparticles}}{\text{total weight of QU-loaded nanoparticles}} \quad (2)$$

The drug release profile was performed in phosphate buffered saline (PBS) buffer (pH 7.4) including TWEEN 80 (0.5%) at 37ºC using the dialysis method. Then, 2 mg of QU-loaded nanoparticles was dispersed in 2 ml of PBS buffer solution. The suspensions were transferred to dialysis bags (MWCO 12-14 kDa) and sequentially immersed into 18 ml of release medium. The release containers were placed in the dark and maintained at 37ºC until the experiments were completed. At specific intervals, 2 ml of release solution was pipetted out and stored in designated Eppendorf tubes. An equivalent volume of dialysate was refilled. Eventually, the collected samples were measured by UV-Vis spectroscopy at the wavelength of 372 nm to determine the amount of drug released.

2.7. Statistical analysis

All resultant data were illustrated as mean ± standard errors. Statistical evaluation of data was performed by using Student's t-test. A *p*-value smaller than 0.05 was considered statistically significant.

3. Results and discussion

3.1. Morphology and characterisation of MSNs

MSNs were synthesised by Stöber's method using a silicon resource from TEOS and CTAB as a structural platform for the silicon to condense onto. After that, the obtained MSNs were utilised as the starting material for surface modifications.

To determine the particle size and morphology of the silica nanoparticles, SEM and TEM were used (Figs. 1A, B). Basically, both SEM and TEM images showed that the nanosilica particles had a relatively spherical shape with uniform size and no observation of agglomeration or aggregation. By using ImageJ software with the SEM image, the mean size of nanomaterials was calculated as 68.04±5.91 nm (Fig. 1C). This figure could be considered higher than that of previous publications due to our modification in the synthesis route [18]. For the TEM result, the bolder-coloured interior of nanosilica particles was assigned to the silicon-enriched core, which took place during the initial condensation. The outer layer expressed a low density of materials, which consolidated the mesoporous construction of the nanoparticles.

The hydrodynamic diameter of the MSNs was investigated by DLS (Fig. 1D). We utilised a lyophilised nanosilica sample then redispersed it into DIW. The aqueous solution of MSNs was sonicated before the diameters of the particles were measured by scattering light. The DLS measurements were conducted three times with one-minute intervals, which showed that the average size of the nanoparticles in water medium was 135.5±4.5 nm. The resulting data revealed monodispersion in size distribution and colloidal stability of the materials (PDI 0.044) after undertaking dehydration and preservation in advance.

The chemical nature of nanosilica was affirmed by FTIR (Fig. 1D). The typical pattern of silica materials was revealed in the

fingerprint region, in which there was a strong absorbance of the Si-O-Si stretch around the wavelength of 1100 cm^{-1}. For the unmodified MSNs, the FTIR spectrum also showed a broad peak at a little over 3200 cm^{-1}, which was assigned to the hydroxyl groups overexpressed on particles' surfaces. Thus, the FTIR spectrum of MSNs basically confirms the successful synthesis of the nanosilica materials without by-products, excessive reagents, or contaminants. The hydroxyl-overexpressed surface of the MSNs was consolidated by zeta potential measurements as well. The negative isoelectric point was recorded at about -29.9 mV indicating the exposition of acidic -OH groups.

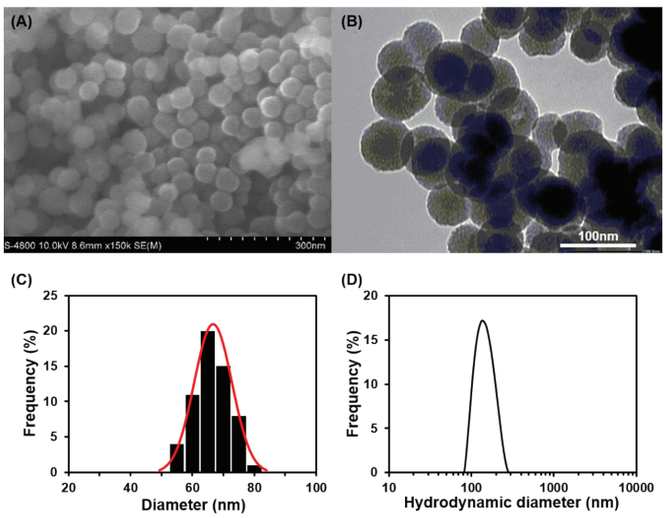

Fig. 1. (A) SEM image and (B) TEM image of MSNs, (C) size distribution computed by ImageJ software, and (D) hydrodynamic size distribution of MSNs.

3.2. Characterisation of MSNs-PAMAM

The series of PAMAM-grafted MSNs were fabricated via step-by-step synthesis routes in which zero-to-three generation PAMAM dendrimers were tailored onto the surface of MSNs (Scheme 1). Firstly, amine groups contained in APTES molecules are decorated on the surface of MSNs in lieu of hydroxyl groups. The amine-functionalised MSNs were employed as reacting cores and denoted by MSNs-G0. MSNs-G0 were reacted with MA via alkylation to obtain MSNs-G0.5, then reacted with EDA via amination to obtain MSNs-G1. The fabrication was respectively carried out with MA and EDA to finally achieve MSNs-G3.

First, DLS was utilised to assess the hydrodynamic sizes and colloidal stability of PAMAM-grafted MSNs (Fig. 2A). The DLS results of the mean hydrodynamic sizes of MSNs-G0, MSNs-G1, MSNs-G2, and MSNs-G3 in DIW were 137.5±4.5 nm, 142.7±4.0 nm, 167.4±4.5 nm, and 185.9±2.5 nm, respectively. In general, the particle sizes significantly increased over a generation, which is consistent with the layer-by-layer structure of PAMAM dendrites. In detail, the size increase between MSNs-G2 and MSNs-G1 showed the highest value at 17.3%, while that between

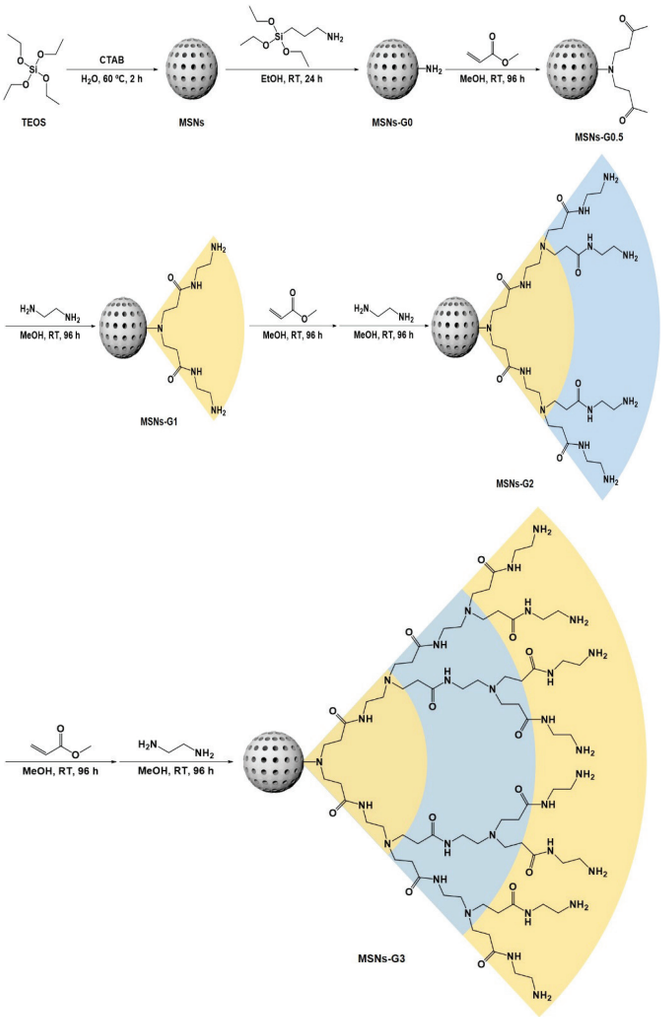

Scheme 1. Synthetic routes of MSNs and PAMAM dendrites-tailored MSNs.

MSNs-G3 and MSNs-G2 was 10.7%. These results demonstrate the shrinkage of the PAMAM structure commencing at the third generation due to the formation of back-folding, which is specifically attributed to the ionization of amide bonds generating an attractive effect between branches [29].

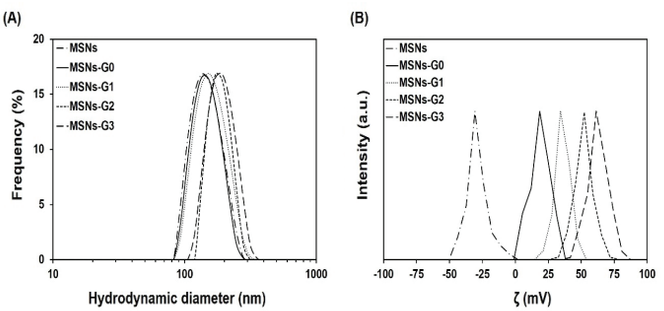

Fig. 2. (A) Hydrodynamic size distributions and (B) zeta potentials of MSNs in comparison with MSNs-PAMAM.

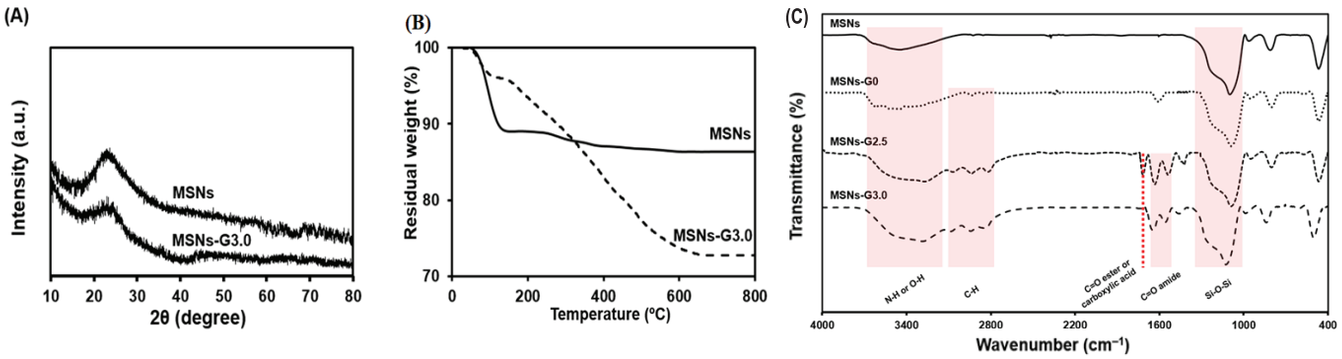

Fig. 3. (A) XRD patterns of MSNs and MSNs-G3.0, (B) thermal decomposition curves of MSNs and MSNs-G3.0, and (C) FTIR spectra of MSNs, MSNs-G0, MSNs-G2.5, and MSNs-G3.0.

In addition, the zeta potentials of nanoparticles were measured under the same conditions including dispersing medium, neutral pH, and particle concentration (Fig. 2B). The graph reveals that the electrokinetic potentials remarkably grew over the increase of PAMAM generations after each synthesis loop, which was attributed to the exponential rise in the number of amine groups attached to the ex-layer.

The thermal decomposition curve was further recorded to prove the successful modification of PAMAM onto the MSN surface (Fig. 3A). We show a comparison of thermograms of MSNs and MSNs-G3 to display the thermal nature of the modified and unmodified materials. For the MSNs plot, there was no evidence of significant degradation in the silica structure up to 800ºC, which confirms the thermal endurance of the silica cores. Notably, MSNs were demonstrated as an efficient adsorbent, which was confirmed by the weight loss of 11.0 wt% of water from 80 to just over 100ºC. Meanwhile, the residual weight of MSNs-G3 was 72.8 wt%, which is comparable to a previous publication [18]. Thus, the greater weight loss of nanomaterial was assigned to organic functionalities of PAMAM, which are easily decompose under high temperatures. Moreover, XRD patterns (Fig. 3B) reveal that MSNs-G3 still behave like an amorphous solid with a unique signal at 22º. Hence, this indicated that there was no change in the non-crystalline structure of MSNs after PAMAM waws modified onto their surface, which also indirectly confirmed that the weight loss occurring in the MSNs-G3 thermogram was only dependent on the attached PAMAM dendrites.

The development of PAMAM dendrites onto the surface of the MSNs was initially validated by FTIR (Fig. 3C). For MSNs-G0, the FTIR spectrum maintained the pattern of silica materials with strong absorption at approximately 1100 cm^{-1}. A broad double trough at the region from 3700 to 3300 cm^{-1} corresponded to adsorption caused by the N-H stretching motion of primary amines. The bending vibration of N-H linkage was also recorded at 1650 cm^{-1} [30]. In addition, the introduction of APTES molecules generated C-H bond stretching signals above 2800 cm^{-1}, which certify the successful functionalisation of the MSNs [31]. From a theoretical viewpoint, the group of half-generation PAMAMs including MSNs-G0.5, MSNs-G1.5, and MSNs-G2.5 or the group of full-generation PAMAMs including MSNs-G1, MSNs-G2, and MSNs-G3 exhibit an analogous pattern due to similarities in terms of chemical structure. Here, the representative spectra of MSNs-G2.5 and MSNs-G3 are presented. According to the Michael reaction with MA, the exposure of ester or carboxylic acid carbonyls was recognised in the band at 1715 cm^{-1} occurring in the spectrum of the half-generation dendrimer. For the full-generation dendrimer, the attachment of EDA eliminated ester carbonyls to form amide carbonyls, which led to the appearance of the specific double band from 1650 to 1550 cm^{-1}. In both half- and full-generation PAMAM dendrimers, the broad trough above 3300 cm^{-1} and amide carbonyl signal remained, which contributed to N-H and C=O stretching within the amide bonds [32]. For the entire synthesis process, silica patterns were observed in all spectra indicating that the silica cores were maintained. Hence, the FTIR spectra demonstrates the consistent grafting of PAMAM onto the surfaces of MSNs.

3.3. Quantification of amine groups of MSNs-PAMAM

The synthesis experiments of PAMAM generally require an excess of reagents to regulate the efficiency of reactions. So, the estimation of amine groups per weight is essential to avoid chemical overconsumption and is a useful tool to gauge reaction efficiency. Ninhydrin analysis was conducted by using a UV-vis spectrometer. Subsequently, the amine concentrations of MSNs-PAMAM were calculated from the intensity of reacted ninhydrin. Assuming there was one -NH_2 group in the MSNs-G0 sample, the molar density of amine groups from ninhydrin analysis was performed in comparison with the theoretical development of PAMAMs over a generation as follows (Table 1).

Table 1. Molar density of amines computed from ninhydrin analysis and zeta potential of nanoparticles.

Specimen	Assumed number of amine groups (*N*, group)	Molar density of amine groups (σ, mmol·g^{-1})	Zeta potential (ζ, mV)
MSNs	0	–	-29.9
MSNs-G0	1	0.617	20.1
MSNs-G1	2	1.351	36.0
MSNs-G2	4	2.649	51.8
MSNs-G3	8	5.207	62.7

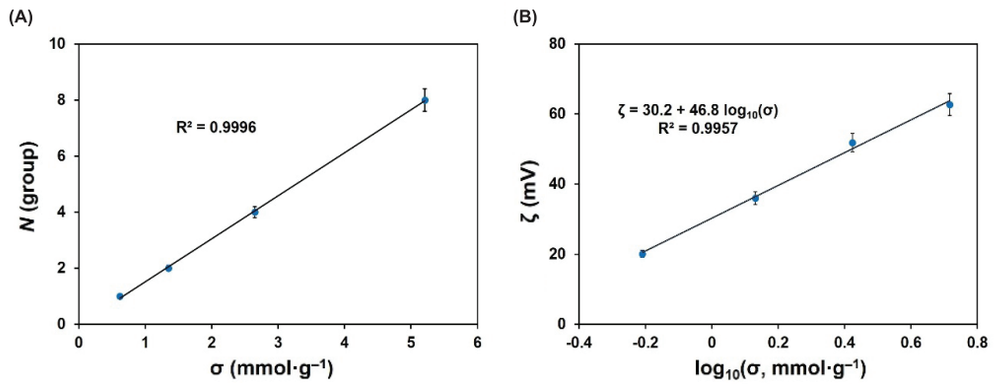

Fig. 4. Linear correlation of (A) molar density versus in the amine number of PAMAM-functionalised MSNs and (B) zeta potential of MSNs-PAMAM versus logarithmic molar density of amine groups.

As can be seen from Table 1, the increase in molar density of -NH_2 groups primarily reveals an exponential growth of PAMAM functionalities by generation. To determine the reaction efficiency, we plotted the molar density of amine groups (σ) as a function of the assumed number of those (Fig. 4A) and assessed the success of synthesis by the linearity of the trend line. Since the correlation coefficient R^2 was 0.9996, the fabrication of MSNs-PAMAM could be recognised as successful with high precision.

We further exploited the positive surface charge of PAMAM dendrites to anticipate the accuracy of modification via the correlation between the zeta potentials (ζ) of colloidal particles and the logarithm of the molar density (σ) (Fig. 4B) [33]. The resultant graph was described by the equation: $\zeta = 30.2+46.8 \log_{10}(\sigma)$ (R^2=0.9957), which demonstrated that the attachments of PAMAM were precise as well.

3.4. Drug loading and release studies

To determine the potential for high drug loading and controlled drug release, we carried out the encapsulation of QU into the PAMAM-grafted MSNs (MSNs-G1 to MSNs-G3) in comparison with conventional MSNs. The encapsulation efficiency (%EE), loading capacity (%LC), and cumulative release amount of QU were calculated following Equations (1) and (2) and are consequently summarized in Table 2. As a general rule, %EE and %LC increased with the generation of PAMAMs implying that the decoration of PAMAM dendrites made an impact on the loading capacity compared to the unmodified MSNs due to empty voids existing in the PAMAM structure.

Table 2. QU loading and cumulative release of QU-encapsulated nanoparticles.

Specimen	%EE	%LC	Cumulative release of QU (%)
QU@MSNs	51.7±0.210	4.7±0.019	85.4±4.4
QU@MSNs-G1	58.4±0.206	5.3±0.019	–
QU@MSNs-G2	76.6±0.109	7.0±0.010	–
QU@MSNs-G3	85.8±0.046	7.8±0.004	70.9±3.9

The drug release profiles were constructed with free drug, QU@MSNs, and QU@MSNs-G3 as a representative for PAMAM-modified MSNs (Fig. 5). For the free drug release profile, QU was rapidly released within 9 hours. By contrast, both MSNs and MSNs-G3 revealed promising potential in controlled release in which QU@MSNs only released 85.4±4.4% within 72 hours and were likely to continue. Meanwhile, the cumulative QU release of QU@MSNs-G3 reached a moderate percentage of 70.9±3.9% and had a saturation tendency, which is attributed to the hyperbranched construction of PAMAM dendrites becoming unintentional drug-capped barriers. However, these results still indicate that higher generation PAMAM remarkably slowed down drug release rate, which could be exploited in drug delivery systems to alleviate side effects that chemotherapeutics trigger.

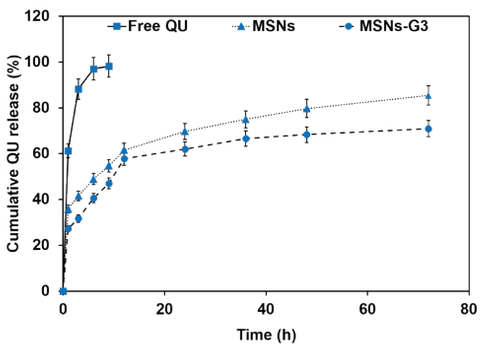

Fig. 5. Drug release profiles of QU@MSNs and QU@MSNs-G3 as compared to free QU in DIW.

4. Conclusions

To conclude, our group successfully synthesised highly monodispersed and spherical MSNs. The modification of PAMAM dendrites onto the surface of silica nanoparticles had outstanding results in which attached PAMAM residues possessed the consistency in chemical structure and appropriate particle sizes for employ as a drug delivery system. Besides, the syntheses of PAMAM-tailored MSNs were obtained with high accuracy and reaction efficiency, which was demonstrated by ninhydrin analysis. A correlation between zeta potential and logarithmic molar density of the amino groups was found, which uncovered a straightforward approach to quickly quantify the fabrication of amine-functionalised nanoparticles. This study initially affirms our viewpoint about the high drug loading capacity and controlled release capability of PAMAM-tailored MSNs to lay the groundwork for further research.

CRediT author statement

Hung-Cuong Luu: Methodology, Software, Conceiving and designing the analysis, Writing- Original draft preparation;

Cuong Quoc Ngo: Data curation, Software; Ngoc Hoi Nguyen: Visualization, Performing the analysis; Dieu Linh Tran: Conceiving and designing the analysis; Dai Hai Nguyen: Validation, Collecting the data, Contributing data or analysis tools; Cuu Khoa Nguyen: Investigation, Conceptualization, Supervision, Writing-Reviewing and Editing.

ACKNOWLEDGEMENTS

This research was funded by the Vietnam National Foundation for Science and Technology (NAFOSTED) under grant no. 104.02-2019.38.

COMPETING INTERESTS

The authors declare that there is no conflict of interest regarding the publication of this article.

REFERENCES

[1] R. Oun, Y.E. Moussa, N.J. Wheate (2018), "The side effects of platinum-based chemotherapy drugs: A review for chemists", *Dalton Trans.*, **47(19)**, pp.6645-6653, DOI: 10.1039/c8dt00838h.

[2] K. Krukiewicz, J.K. Zak (2016), "Biomaterial-based regional chemotherapy: Local anticancer drug delivery to enhance chemotherapy and minimize its side-effects", *Mater. Sci. Eng. C*, **62**, pp.927-942, DOI: 10.1016/j.msec.2016.01.063.

[3] C.Y. Zhao, R. Cheng, Z. Yang, et al. (2018), "Nanotechnology for cancer therapy based on chemotherapy", *Molecules*, **23(4)**, DOI: 10.3390/molecules23040826.

[4] M.W. Tibbitt, J.E. Dahlman, R. Langer (2016), "Emerging frontiers in drug delivery", *J. Am. Chem. Soc.*, **138(3)**, pp.704-717, DOI: 10.1021/jacs.5b09974.

[5] F.D. Cojocaru, D. Botezat, I. Gardikiotis, et al. (2020), "Nanomaterials designed for antiviral drug delivery transport across biological barriers", *Pharmaceutics*, **12(2)**, DOI: 10.3390/pharmaceutics12020171.

[6] F. Danhier (2016), "To exploit the tumor microenvironment: Since the EPR effect fails in the clinic, what is the future of nanomedicine?", *J. Controlled Release*, **244**, pp.108-121, DOI: 10.1016/j.jconrel.2016.11.015.

[7] D. Kalyane, N. Raval, R. Maheshwari, et al. (2019), "Employment of enhanced permeability and retention effect (EPR): Nanoparticle-based precision tools for targeting of therapeutic and diagnostic agent in cancer", *Mater. Sci. Eng. C*, **98(314)**, pp.1252-1276, DOI: 10.1016/j.msec.2019.01.066.

[8] N.T.N. Tram, L.P.P. Tran, N.T.T. Le, et al. (2019), "The engineering of porous silica and hollow silica nanoparticles to enhance drug-loading capacity," *Processes*, **7(11)**, DOI: 10.3390/pr7110805.

[9] F. Farjadian, A. Roointan, S.M. Samani, et al. (2019), "Mesoporous silica nanoparticles: Synthesis, pharmaceutical applications, biodistribution, and biosafety assessment", *Chem. Eng. J.*, **359**, pp.684-705, DOI: 10.1016/j.cej.2018.11.156.

[10] C. Despas, A. Walcarius, J. Bessiere (1999), "Influence of the base size and strength on the acidic properties of silica gel and monodispersed silica beads: Interest of impedance measurements for the in situ monitoring of the ionization process", *Langmuir*, **15(9)**, pp.3186-3196, DOI: 10.1021/la981217y.

[11] M. Babaei, H. Eshghi, K. Abnous, et al. (2017), "Promising gene delivery system based on polyethylenimine-modified silica nanoparticles", *Cancer Gene Ther.*, **24(4)**, pp.156-164, DOI: 10.1038/cgt.2016.73.

[12] T.L. Nguyen, B.G. Cha, Y. Choi, et al. (2020), "Injectable dual-scale mesoporous silica cancer vaccine enabling efficient delivery of antigen/adjuvant-loaded nanoparticles to dendritic cells recruited in local macroporous scaffold", *Biomaterials*, **239**, DOI: 10.1016/j.biomaterials.2020.119859.

[13] G.V. Deodhar, M.L. Adams, B.G. Trewyn (2017), "Controlled release and intracellular protein delivery from mesoporous silica nanoparticles", *Biotechnol. J.*, **12(1)**, DOI: 10.1002/biot.201600408.

[14] M. Manzano, M. Vallet-Regí (2020), "Mesoporous silica nanoparticles for drug delivery", *Adv. Funct. Mater.*, **30(2)**, DOI: 10.1002/adfm.201902634.

[15] M.C.R. Canas, L.M. Corredor, H.I. Quintero, et al. (2020), "Morphological and structural properties of amino-functionalized fumed nanosilica and its comparison with nanoparticles obtained by modified stöber method", *Molecules*, **25(12)**, DOI: 10.3390/molecules25122868.

[16] I.I. Slowing, J.L.V. Escoto, C.W. Wu, et al. (2008), "Mesoporous silica nanoparticles as controlled release drug delivery and gene transfection carriers", *Adv. Drug Delivery Rev.*, **60(11)**, pp.1278-1288, DOI: 10.1016/j.addr.2008.03.012.

[17] L.M. Kaminskas, B.J. Boyd, C.J.H. Porter, et al. (2011), "Dendrimer pharmacokinetics: The effect of size, structure and surface characteristics on ADME properties", *Nanomedicine*, **6(6)**, pp.1063-1084, DOI: 10.2217/nnm.11.67.

[18] B. Wang, K. Zhang, J. Wang, et al. (2020), "Poly(amidoamine)-modified mesoporous silica nanoparticles as a mucoadhesive drug delivery system for potential bladder cancer therapy", *Colloids Surf. B*, **189**, DOI: 10.1016/j.colsurfb.2020.110832.

[19] Y. Zhou, G. Quan, Q. Wu, et al. (2018), "Mesoporous silica nanoparticles for drug and gene delivery", *Acta Pharm. Sin. B*, **8(2)**, pp.165-177, DOI: 10.1016/j.apsb.2018.01.007.

[20] M.A. Mintzer, M.W. Grinstaff (2011), "Biomedical applications of dendrimers: A tutorial", *Chem. Soc. Rev.*, **40(1)**, pp.173-190, DOI: 10.1039/b901839p.

[21] I. Grabchev, D. Staneva, E.V. Tonkova, et al. (2017), "Antimicrobial and anticancer activity of new poly (propyleneamine) metallodendrimers", *J. Polym. Res.*, **24(11)**, pp.1-11, DOI: 10.1007/s10965-017-1387-0.

[22] S. Svenson, D.A. Tomalia (2012), "Dendrimers in biomedical applications-reflections on the field", *Adv. Drug Delivery Rev.*, **64**, pp.102-115, DOI: 10.1016/j.addr.2005.09.018.

[23] B. González, M. Colilla, J. Díez, et al. (2018), "Mesoporous silica nanoparticles decorated with polycationic dendrimers for infection treatment", *Acta Biomater.*, **68**, pp.261-271, DOI: 10.1016/j.actbio.2017.12.041.

[24] T.T.N. Thi, T.V. Tran, N.Q. Tran, et al. (2017), "Hierarchical self-assembly of heparin- PEG end-capped porous silica as a redox sensitive nanocarrier for doxorubicin delivery", *Mater. Sci. Eng. C*, **70(2)**, pp.947-954, DOI: 10.1016/j.msec.2016.04.085.

[25] T.N.T. Nguyen, D.H.N. Tran, L.G. Bach, et al. (2019), "Surface PEGylation of hollow mesoporous silica nanoparticles via aminated intermediate", *Prog. Nat. Sci. Mater. Int.*, **29(6)**, pp.612-616, DOI: 10.1016/j.pnsc.2019.10.002.

[26] Y. Sun, F. Kunc, V. Balhara, et al. (2019), "Quantification of amine functional groups on silica nanoparticles: A multi-method approach", *Nanoscale Adv.*, **1(4)**, pp.1598-1607, DOI: 10.1039/c9na00016j.

[27] D.T.D. Nguyen, L.G. Bach, T.H. Nguyen, et al. (2019), "Preparation and characterization of oxaliplatin drug delivery vehicle based on PEGylated half-generation PAMAM dendrimer", *J. Polym. Res.*, **26(5)**, pp.1-14, DOI: 10.1007/s10965-019-1779-4.

[28] M.N. Ho, L.G. Bach, D.H. Nguyen, et al. (2019), "PEGylated PAMAM dendrimers loading oxaliplatin with prolonged release and high payload without burst effect", *Biopolymers*, **110(7)**, DOI: 10.1002/bip.23272.

[29] P.K. Maiti, T. Cagin, S.T. Lin, et al. (2005), "Effect of solvent and pH on the structure of PAMAM dendrimers", *Macromolecules*, **38(3)**, pp.979-991, DOI: 10.1021/ma049168l.

[30] M. Khoeini, A. Najafi, H. Rastegar, et al. (2019), "Improvement of hollow mesoporous silica nanoparticles synthesis by hard-templating method via CTAB surfactant", *Ceramics International*, **45(10)**, pp.12700-12707, DOI: 10.1016/j.ceramint.2019.03.125.

[31] P. Larkin (2017), *Infrared and Raman Spectroscopy: Principles and Spectral Interpretation*, Elsevier, 286pp.

[32] M.T. Vu, L.G. Bach, D.C. Nguyen, et al. (2016), "Modified carboxyl-terminated PAMAM dendrimers as great cytocompatible nano-based drug delivery system", *International Journal of Molecular Sciences*, **20(8)**, DOI: 10.3390/ijms20082016.

[33] E. Soto-Cantu, R. Cueto, J. Koch, et al. (2012), "Synthesis and rapid characterization of amine-functionalized silica", *Langmuir*, **28(13)**, pp.5562-5569, DOI: 10.1021/la204981b.

DOI: 10.31276/VJSTE.65(1).32-37

Effect of thermal treatments (roasting, microwaving, steaming) on anti-nutritional factors and physical and antioxidant properties of black gram (*Vigna cylindrica* L. Skeels)

Ngoc Lieu Le[1, 2*], My Thi Huyen Le[1, 2], Nguyen Hoang Khoa Nguyen[1, 2], Linh Tran Khanh Vu[3]

[1]*International University, Vietnam National University - Ho Chi Minh City, Quarter 6, Linh Trung Ward, Thu Duc City, Ho Chi Minh City, Vietnam*

[2]*Vietnam National University - Ho Chi Minh City, Linh Trung Ward, Thu Duc City, Ho Chi Minh City, Vietnam*

[3]*Ho Chi Minh City University of Technology and Education, 1 Vo Van Ngan Street, Linh Chieu Ward, Thu Duc City, Ho Chi Minh City, Vietnam*

Received 17 June 2021; revised 7 July 2021; accepted 14 July 2021

Abstract:

The aim of this research was to investigate the effect of thermal treatments, including roasting, microwaving, and steaming, on anti-nutritional factors and physical and antioxidant properties of black gram (*Vigna cylindrica* L. Skeels). Regarding its physical properties, thermal treatment increased the water-holding capacity (WHC) and decreased the oil-holding capacity (OHC) of the black gram samples. No significant difference was observed between the roasted sample and the control. Regarding the chemical properties, anthocyanins accounted for the vast majority of total phenolic content (TPC). The steamed sample had the lowest TPC and anthocyanin values, which were 272.46 mg/100 g dry basis and 121.20 mg/100 g dry basis, respectively. Among the three types of thermal treatments, roasting resulted in the highest TPC content, which was 424.35 mg/100 g dry basis. Particularly, the steaming treatment led to the lowest anthocyanin content and antioxidant capacity (AC) in the flour sample; furthermore, there were no significant differences in the TPC and AC values between the microwaved and roasted samples. The phytate content was significantly reduced in all heat-treated samples and there were no significant differences among these cooked samples. The tannin content of the steamed sample was recorded to be the lowest, which was 164.19 mg/100 g dry basis. In summary, roasting, microwaving, and steaming significantly influenced the nutritive values of black gram (*Vigna cylindrica* L. Skeels).

Keywords: **anthocyanin, black gram, heat treatments, physical properties, phytate, tannin.**

Classification numbers: **2.2, 3.1**

1. Introduction

Black gram is widely cultivated in many areas with tropical climates like India, Asia, and Africa. Specifically, *Vigna cylindrica* is a breed of black gram that is broadly cultivated in Vietnam. Black gram is rich in protein and contains several components with desirable proportions including a low sodium content, high potassium content, complex carbohydrates, high fibre content, and a high content of essential, polyunsaturated fatty acids such as linoleic and linolenic acids with the ability to lower serum cholesterol in humans [1].

Despite having high nutritional values, the in-use proportion of nutrients in black gram is restrained by the presence of several anti-nutritional factors. According to H. Umaru, et al. (2007) [2], anti-nutritional factors (ANFs) can impair the function of the gastrointestinal tract, thereby interfering with the metabolic process. There are two types of ANFs that are the focus of this research: tannins and phytates. Tannins have been reported to block digestive enzymes and hence decrease the digestibility of most nutrients, particularly carbohydrates and proteins [3]. Meanwhile, phytates have been reported to bind with proteins and starch as well as crucial dietary minerals, thus lowering the bioavailability of these nutritional components in humans [4].

It is widely accepted that significant AC of food is related to high TPC [5]. Black gram has a rich content of antioxidants in its seed coat and contains high amounts of phenolic compounds that are believed to play an important role in promoting a healthy human diet [6]. This is especially true for anthocyanins, which are one

*Corresponding author: Email: lnlieu@hcnvn.edu.vn

subclass of phenolic compounds. These water-soluble pigments are also present in seed coat of black gram. The health-related functions of antioxidants are diverse. T.M. Djordjevic, et al. (2011) [7] demonstrated that antioxidants have the ability to reduce the occurrence of aging-related chronic diseases including heart disease and some types of cancer.

Black gram must experience an appropriate heat treatment before being consumed. Thus, this processing step results in changes to black gram's nutritional attributes, particularly, anti-nutritional factors and antioxidant properties. Therefore, this study was designed to compare the influences of different heat treatments on anti-nutritional factors like tannin and phytate contents, physical properties like oil and water holding capacities, and antioxidant properties of black gram. Comparisons among the three heat treatments could indicate which heat-applied treatment provides the most desirable results. Thus, this work can be used for further industrial scale and for potential health-concerned products on the Vietnam market.

2. Materials and methods

2.1. Materials and chemicals

Black gram (*Vigna cylindrica* (L.) Skeels) was purchased from the Big C Vietnam Supermarket in Ho Chi Minh city. All chemicals used for the project were supplied by several local distributors. For example, polyvinyl-polypirrolidone, sodium sulfate, hydrogen chloride, ferric chloride, sulphosalicylic acid, glycine, ethylenediamine tetraacetic acid, methanol, Folin-Ciocalteu reagent, sodium bicarbonate, gallic acid, potassium chloride, sodium acetate, 1,1-diphenyl-2-picrylhydrazyl (DPPH), and Trolox were purchased from local chemical distributors.

2.2. Sample preparation

Unqualified beans were hand-removed, which included broken beans, damaged beans, and small wrinkled beans. Selected beans then were washed by tap water to completely remove foreign materials such as sand, dust, and soil.

2.3. Thermal treatment methods

Roasting: A coffee bean roaster model CBR-101 with a maximum chamber capacity of 0.6 lb/250 g was used. Selected beans were roasted for 10 min at 160^{o}C and then were ground into flour [8]. This treatment was conducted with three replications. The final moisture content of the roasted beans was approximately 7%.

Microwave: Selected beans were soaked in tap water at room temperature for 18 h in a ratio of 1:5 (w/v) to reduce cooking time [8, 9]. They were then washed twice with tap water and left to drain in air. A microwave (Sharp R-209VN, China) was preheated to achieve standard uniform temperature by heating a porcelain bowl containing 300 ml of water for 30 s. The soaked beans were cooked at a power of 640 W for 5 min and then allowed to rest for 1 min in the microwave. The cooked gram was dried in the oven at 50^{o}C for 24 h to reach a moisture content of approximately 9.5% before it was finally ground into flour. This treatment was also conducted with three replications.

Steaming: Black gram was soaked for 18 h and steamed at 100^{o}C for 30 min [8]. The following steps, including draining, drying, cooling, and grinding, were carried out similarly to the microwave preparation. The moisture content of the dried samples was approximately 7-8%. The treatment was conducted with three replications.

Control sample: The washed bean was dried at 50^{o}C for 1 h and ground into flour. The moisture content of the control sample was approximately 14%.

2.4. Analytical methods

The WHC and OHC of the black gram flour were both determined by the method of C. Chau, et al. (1998) [10]. The TPC was evaluated using a Folin-Ciocalteu reagent by the method of V.L. Singleton, et al. (1965) [11]. A spectrophotometric pH differential method was used to analyse the monomeric anthocyanin content of the black gram flour extract [12]. The AC was evaluated through DPPH radical scavenging capacity according to W.B. Williams, et al. (1995) [13]. Phytic acid content was determined by the colorimetric method according to R.G. Villanova, et al. (1982) [14]. Analysis of tannin content was carried out using insoluble polyvinyl-polypirrolidone (PVPP), which binds tannins [15].

2.5. Data analysis

Collected data was subjected to analysis of variation (ANOVA) using the SPSS software version 22.0. Tukey's test was used for multiple comparisons. Differences were deemed significant at the $p<0.05$ level.

3. Results and discussion

3.1. Phytate content and tannin content

At a first glance, the thermal treatments did not significantly affect the phytate content of the samples (Fig. 1). It is clearly observed that there were no significant differences in phytate content among the steaming, microwaving, and roasting treatments. Phytate content

of the control sample was 15.31 mg/100 g dry solid and those of the heat-treated samples were 13.84 mg/100 g dry solid, 14.19 mg/100 g dry solid, and 13.91 mg/100 g dry solid for steaming, microwaving, and roasting, respectively. The observed reduction in phytate content of black gram during different heat treatments might be partly due to the heat-labile nature of phytate as well as the formation of insoluble complexes between phytate and other components [16]. For boiling and microwave, the loss of phytate content was also affected by the soaking period as phytate ions leach into the soaking water as a result of the concentration gradient.

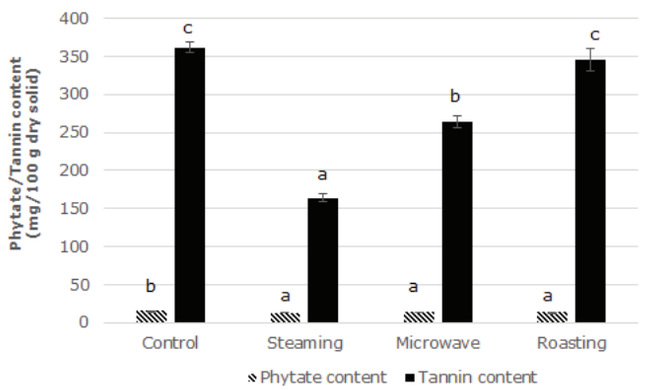

Fig. 1. Phytate content and tannin content of black gram flour after different heat treatments.

As for the values of tannin content, the steamed and microwaved sample experienced significant ($p<0.05$) reductions. However, there were no significant differences between the values of the raw and roasted ones. Particularly, the tannin contents of the control, roasted, steamed, and microwaved samples were 361.55 mg/100 g dry solid, 346.21 mg/100 g dry solid, 164.19 mg/100 g dry solid, and 264.68 mg/100 g dry solid, respectively. Thus, steaming caused the lowest value of tannin content, followed by microwave and roasting. The significant ($p<0.05$) reductions by steaming and microwaving could be explained by the nature of tannins. Tannins are mostly located at the seed coat [17] and are known to be polyphenols; moreover, all polyphenolic compounds are water-soluble [16]. Therefore, tannin losses may be caused by the leaching of tannins into soaking water under the influence of the concentration gradient [18].

The loss of tannin content was more obvious when black gram was cooked in a condition requiring a high amount of water like steaming. The explanation for this observation is clearly mentioned in a study by A.C. Laurena, et al. (1987) [19], which stated that the mechanism of polyphenol removal by steaming was similar to that by soaking in water, i.e., leaching. Furthermore, steaming provides a condition with a higher temperature, which aids the leaching process of polyphenolic compounds and causes it to occur at a faster rate. The steaming process also resulted in easier access to a protein and polyphenol interaction that promotes the inactivation of the latter due to the rapid disruption of cellular compartments. In this study, the total loss of tannin content in the steamed sample was 54.59%. Meanwhile, dry heat carried out by microwaving obtained a tannin loss of 26.79%. Roasting, however, only caused a 4.24% loss of tannin content. The reduction in tannin content of the microwaved and roasted samples agreed with earlier investigations of microwaved and roasted plant foodstuffs [20, 21]. Tannin losses during dry heat treatments might be due to the loss of compounds while treating at a high temperature. Furthermore, the loss of tannins may be due to a degradation or interaction with other components of the seeds, such as proteins, to form insoluble complexes [22].

3.2. WHC and OHC

Figure 2 indicates the effect of different heat treatments on the physical properties of black gram flour. As can be seen from the chart, the highest WHC was found for the steamed sample (2.36 g water/g flour) and the lowest WHC was found for the roasted sample (1.77 g water/g flour). There was no significant difference between the WHC values of the steamed sample and microwaved sample and these values were higher than that of the control sample. In previous studies, B.A. Acevedo, et al. (2017) [23] observed the same results on Dolichos bean and jack bean flours treated by steaming and microwaving. In general, these results are also supported by U. Singh (1988) [17], who demonstrated that during cooking and dehydration, protein denaturation and unfolding lead to the exposure of previously hidden peptide bonds and polar side chains, which can hold more water molecules. Meanwhile, the WHC of the roasted flour (1.77 g water/g flour) did not differ much from the control flour (1.61 g water/g flour). This result was explained by S. Ekanayake, et al. (2006) [24] as the degree of gelatinization (DG) of the roasted flour being lower than that of the wet-processed flours (soaked and cooked). Under low moisture content and high temperature, gelatinization of the roasted sample was considered more as a melting of crystallites. In other words, melting corresponds to the disappearance of native starch crystallinity at low hydration without a prior disappearance of granular shape.

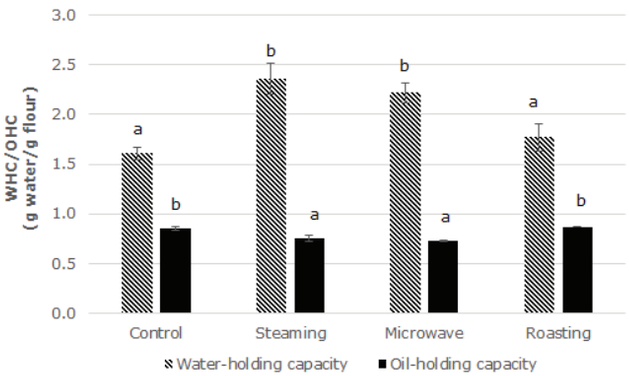

Fig. 2. WHC and OHC of black gram flour with different heat treatments.

Meanwhile, it was clear from the results that the OHCs of the steamed (0.76 g oil/g flour) and microwaved (0.73 g oil/g flour) samples were both lower than that of the control sample (0.85 g oil/g flour). Y. Aguilera, et al. (2009) [25] and K. Adebowale, et al. (2004) [26] demonstrated that the factor affecting OHC values of samples was the presence of the protein's non-polar side chains that bind with the hydrocarbon side chain of oil. When the protein was denatured by heat treatments, its secondary structure was lost, as well as the binding oil activity [27]. The results observed from this study were similar to the results of C.W. Hutton, et al. (1981) [28] which indicated that the OHC of soya protein decreased after heat treatments were applied.

3.3. TPC and anthocyanin content

Compared to the control samples, all heat-treated samples had significant ($p<0.05$) decreases in TPC index (Fig. 3). It is explicitly observed that steaming caused the greatest TPC loss in the black gram samples. Particularly, the TPC of the control sample showed a value of 488.68 mg/100 g dry basis while 272.46 mg/100 g dry basis was obtained for the steamed one. This significant loss could be explained by B. Xu, et al. (2008) [29], who demonstrated that thermal processing caused water-soluble phenolics to leach out and some phenolic compounds to be broken down. In addition, during soaking, some polyphenols in the seed coat were hydrolysed and diffused into the soaking water, which reduced the TPC of the sample. As compared to microwave cooking and roasting, steaming required the longest time for black gram to be cooked well; moreover, a large amount of water was needed to perform the treatment successfully. The observed reduction in TPC could be mainly due to leaching of these compounds from the seed coat into the soaking or steaming water. Therefore, the boiling method was believed to be the most favourable condition for the reduction of TPC among the applied heat treatments. In the present study, it was found that about 44.25% of phenolics leached into the soaking and cooking water. Similar to the trend of steaming, microwave cooking was observed to cause a TPC reduction to 379.92 mg/100 g dry basis while roasting reduced the TPC value to 424.35 mg/100 g dry basis. Particularly, microwave cooking lost about 22.26% of TPC and roasting lost about 13.16% of TPC. The significant reduction in TPC level could be attributed to an increase in the release of phytochemicals from the cell matrix as phenolic acids. In other words, cell membranes and cell walls were disrupted during thermal processing, which caused a release of soluble phenolic components from insoluble ester bonds.

Similar to the trend of TPC shown in Fig. 3, the anthocyanin content of all the heat-treated samples were significantly reduced ($p<0.05$). The steaming treatment caused the highest total anthocyanin loss in black gram flour, followed by the two remaining thermal treatments. Particularly, the loss of anthocyanin content in the steamed sample was 64.53%, while the loss in the microwaved and roasted sample were 32.92 and 32.15%, respectively. The anthocyanin content for the steamed, microwaved, and roasted samples were 220.47 mg/100 g dry basis, 112.48 mg/100 g dry basis, and 109.85 mg/100 g dry basis, respectively. Similar results were found from yellow soybeans treated with steaming [29], roasting, and microwaving [30]. For the steamed sample, a high content of anthocyanin was lost as it diffused into the cooking water. Moreover, the treatment method required a water condition for black gram to be cooked, which made anthocyanin leach out during the process. These reasons could explain the lowest value of anthocyanin content reported in the steamed sample.

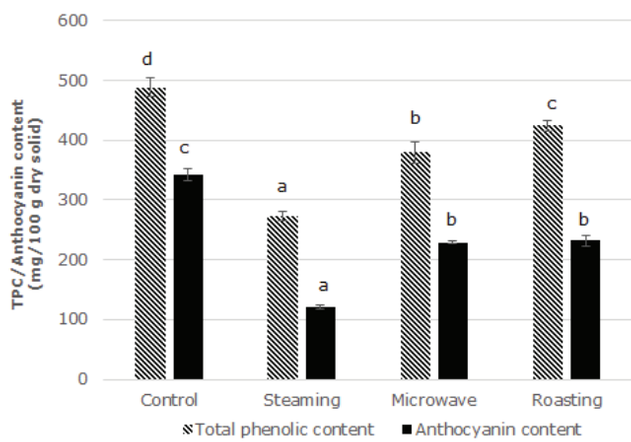

Fig. 3. TPC and anthocyanin content of black gram flour with different heat treatments.

3.4. AC

Under thermal processing conditions, the AC value of the control sample was significantly reduced ($p<0.05$) (Fig. 4). Previous studies reported similar results on roasted eclipse black beans (*Phaseolus vulgaris* L.) [29], roasted pinto and black beans (*Phaseolus vulgaris L.*) [31], and microwaved or roasted yellow soybeans (*Glycine max* L.) [30]. Particularly, steaming led to the lowest AC value in the flour sample with 157.30 mg/100 g dry solid, followed by microwaving with 281.33 mg/100 g dry solid, and roasting with 265.13 mg/100 g dry solid. Furthermore, there was no significant difference in AC between the microwaved sample and roasted sample. These results had a similar trend as the anthocyanin content shown in Fig. 3.

Moreover, as previously discussed about Fig. 3, anthocyanins accounted for the majority of the TPC in the black gram sample. Thus, the reduction in anthocyanin content after applying different heat treatments corresponded with the decrease of AC in the sample. In other words, cyaniding-3-glucoside was broken down via all three different cooking methods, which led to the reduction in the content of total phenolic acids as well as anthocyanins and, hence, the overall AC of cooked black gram samples decreased.

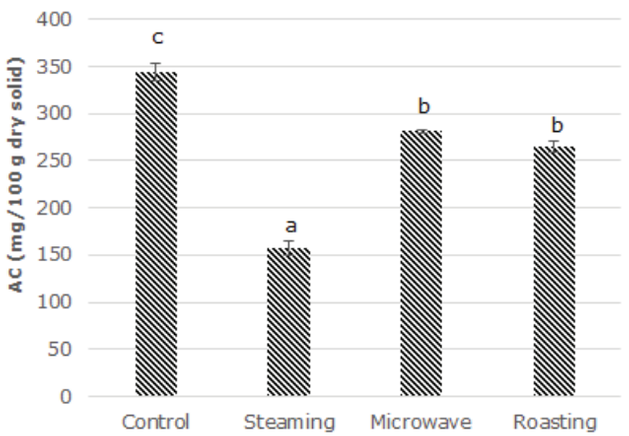

Fig. 4. AC of black gram flour with different heat treatments.

4. Conclusions

This study showed that roasting, microwaving, and steaming significantly affected anti-nutritional factors, as well as the physical and antioxidant properties, of black gram (*Vigna cylindrica* (L.) Skeels). For the most part, steaming reduced the anti-nutritional factors and antioxidant properties to the lowest levels while roasting caused the least decrease to these values. Therefore, the results from the three different heat treatments can be applied for further industrial scale and used for potential health-concerned products on the Vietnam market.

CRediT author statement

Ngoc Lieu Le: Conceptualization, Methodology, Supervision, Reviewing and Editing; My Thi Huyen Le: Experiment, Writing-Original draft preparation; Nguyen Hoang Khoa Nguyen: Data curation, Validation; Linh Tran Khanh Vu: Conceptualization, Writing- Reviewing and Editing.

ACKNOWLEDGEMENTS

This research is funded by Vietnam National University - Ho Chi Minh City under grant number C2019-28-08.

COMPETING INTERESTS

The authors declare that there is no conflict of interest regarding the publication of this article.

REFERENCES

[1] S.K. Sathe (1996), "The nutritional value of selected Asiatic pulses: Chickpea, black gram, mung bean and pigeon pea", *Food and Feed from Legumes and Oilseeds*, Springer, DOI: 10.1007/978-1-4613-0433-3_2.

[2] H. Umaru, R. Adamu, D. Dahiru, et al. (2007), "Levels of antinutritional factors in some wild edible fruits of Northern Nigeria", *Afr. J. Biotechnol.*, **6(16)**, pp.1935-1938, DOI: 10.5897/AJB2007.000-2294.

[3] N. Reddy, M. Pierson, S. Sathe, et al. (1985), "Dry bean tannins: A review of nutritional implications", *J. Am. Oil Chem. Soc.*, **62**, pp.541-549, DOI: 10.1007/BF02542329.

[4] B.Q. Phillippy (2003), "Inositol phosphates in foods", *Advances in Food and Nutrition Research*, **45**, pp.1-60, DOI: 10.1016/s1043-4526(03)45002-x.

[5] B. Xu, S.K. Chang (2008), "Total phenolics, phenolic acids, isoflavones, and anthocyanins and antioxidant properties of yellow and black soybeans as affected by thermal processing", *J. Agric. Food Chem.*, **56(16)**, pp.7165-7175, DOI: 10.1021/jf8012234 .

[6] A. Moure, J.M. Cruz, D. Franco, et al. (2001), "Natural antioxidants from residual sources", *Food Chem.*, **72(2)**, pp.145-171, DOI: 10.1016/S0308-8146(00)00223-5.

[7] T.M. Djordjevic, S.S.S. Marinkovic, S.I. Brankovic (2011), "Antioxidant activity and total phenolic content in some cereals and legumes", *Int. J. Food Prop.*, **14(1)**, pp.175-184, DOI: 10.1080/10942910903160364.

[8] A. Kataria, B. Chauhan, S. Gandhi (1988), "Effect of domestic processing and cooking on the antinutrients of black gram", *Food Chem.*, **30(2)**, pp.149-156, DOI: 10.1016/0308-8146(88)90152-5.

[9] D.M. Njoroge, P.K. Kinyanjui, C.M. Chigwedere, et al. (2016), "Mechanistic insight into common bean pectic polysaccharide changes during storage, soaking and thermal treatment in relation to the hard-to-cook defect", *Food Res. Int.*, **81**, pp.39-49, DOI: 10.1016/j.foodres.2015.12.024.

[10] C. Chau, P. Cheung (1998), "Functional properties of flours prepared from three Chinese indigenous legume seeds", *Food Chem.*, **61(4)**, pp.429-433, DOI: 10.1016/S0308-8146(97)00091-5.

[11] V.L. Singleton, J.A. Rossi (1965), "Colorimetry of total phenolics with phosphomolybdic-phosphotungstic acid reagents", *Am. J. Enol. Vitic.*, **16**, pp.144-158, DOI: 10.5344/ajev.1965.16.3.144.

[12] K. Wolfe, X. Wu, R.H. Liu (2003), "Antioxidant activity of apple peels", *J. Agric. Food Chem.*, **51(3)**, pp.609-614, DOI: 10.1021/jf020782a.

[13] W.B. Williams, M.E. Cuvelier, C. Berset (1995), "Use of a free radical method to evaluate antioxidant activity", *LWT-Food Sci. Technol.*, **28(1)**, pp.25-30, DOI: 10.1016/S0023-6438(95)80008-5.

[14] R.G. Villanova, R.J.G. Villanova, C.R.D. Lope (1982), "Determination of phytic acid by complexometric titration of excess of iron (III)", *Analyst*, **107(1281)**, pp.1503-1506, DOI: 10.1039/AN9820701503.

[15] S. Rakic, S. Petrovic, J. Kukic, et al. (2007), "Influence of thermal treatment on phenolic compounds and antioxidant properties of oak acorns from Serbia", *Food Chem.*, **104**, pp.830-834, DOI: 10.1016/j.foodchem.2007.01.025.

[16] E. Udensi, F. Ekwu, J. Isinguzo (2007), "Antinutrient factors of vegetable cowpea (*Sesquipedalis*) seeds during thermal processing", *Pak. J. Nutr.*, **6(2)**, pp.194-197, DOI: 10.3923/pjn.2007.194.197.

[17] U. Singh (1988), "Antinutritional factors of chickpea and pigeonpea and their removal by processing", *Plant Foods Hum. Nutr.*, **38(3)**, pp.251-261, DOI: 10.1007/BF01092864.

[18] K. Vijayakumari, P. Siddhuraju, K. Janardhanan (1997), "Effect of domestic processing on the levels of certain antinutrients in *Prosopis chilensis* (Molina) Stunz. Seeds", *Food Chem.*, **59(3)**, pp.367-371, DOI: 10.1016/S0308-8146(96)00249-X.

[19] A.C. Laurena, V.V. Garcia, E. Mae, et al. (1987), "Effects of heat on the removal of polyphenols and in vitro protein digestibility of cowpea (*Vigna unguiculata* (L.) Walp.)", *Plant Foods Hum. Nutr.*, **37(2)**, pp.183-192, DOI: 10.1007/BF01092054.

[20] R. Habiba (2002), "Changes in anti-nutrients, protein solubility, digestibility, and HCl-extractability of ash and phosphorus in vegetable peas as affected by cooking methods", *Food Chem.*, **77(2)**, pp.187-192, DOI: 10.1016/S0308-8146(01)00335-1.

[21] K. Nithya, B. Ramachandramurty, V. Krishnamoorthy (2007), "Effect of processing methods on nutritional and anti-nutritional qualities of hybrid (COHCU-8) and traditional (CO_7) pearl millet varieties of India", *J. Biol. Sci.*, **7(4)**, pp.643-647, DOI: 10.3923/jbs.2007.643.647.

[22] H.E.S. Embaby (2010), "Effect of soaking, dehulling, and cooking methods on certain antinutrients and in vitro protein digestibility of bitter and sweet lupin seeds", *Food Sci. Biotechnol.*, **19**, pp.1055-1062, DOI: 10.1007/s10068-010-0148-1.

[23] B.A. Acevedo, C.M. Thompson, N.S.G. Foutel, et al. (2017), "Effect of different treatments on the microstructure and functional and pasting properties of pigeon pea (*Cajanus cajan* L.), dolichos bean (*Dolichos lablab* L.) and jack bean (*Canavalia ensiformis*) flours from the north-east Argentina", *Int. J. Food Sci. Technol.*, **52(1)**, pp.222-230, DOI: 10.1111/ijfs.13271.

[24] S. Ekanayake, B.M. Nair, N.G. Asp, et al. (2006), "Effect of processing of sword beans (*Canavalia gladiata*) on physicochemical properties of starch", *Starch-Stärke*, **58(5)**, pp.215-222, DOI: 10.1002/star.200500449.

[25] Y. Aguilera, R.M. Esteban, V. Benitez, et al. (2009), "Starch, functional properties, and microstructural characteristics in chickpea and lentil as affected by thermal processing", *J. Agric. Food Chem.*, **57(22)**, pp.10682-10688, DOI: 10.1021/jf902042r.

[26] K. Adebowale, O. Lawal (2004), "Comparative study of the functional properties of bambarra groundnut (*Voandzeia subterranean*), jack bean (*Canavalia ensiformis*) and mucuna bean (*Mucuna pruriens*) flours", *Food Res. Int.*, **37(4)**, pp.355-365, DOI: 10.1016/j.foodres.2004.01.009.

[27] N. R.Guzman, J.G. Infante, R.G. Laredo, et al. (2008), "Physical properties of extruded products from three Mexican common beans (*Phaseolus vulgaris* L.) cultivars", *Plant Foods Hum. Nutr.*, **63**, pp.99-104, DOI: 10.1007/s11130-008-0076-x.

[28] C.W. Hutton, A.M. Campbell (1981), "Water and fat absorption", *Protein Functionality in Foods*, American Chemical Society, pp.177-200, DOI: 10.1021/bk-1981-0147.pr001.

[29] B. Xu, S.K. Chang (2008), "Effect of soaking, boiling, and steaming on total phenolic content and antioxidant activities of cool season food legumes", *Food Chem.*, **110(1)**, pp.1-13, DOI: 10.1016/j.foodchem.2008.01.045.

[30] H.W. Yang, C.K. Hsu, Y.F. Yang (2014), "Effect of thermal treatments on anti-nutritional factors and antioxidant capabilities in yellow soybeans and green-cotyledon small black soybeans", *J. Sci. Food Agric.*, **94(9)**, pp.1794-1801, DOI: 10.1002/jsfa.6494.

[31] B. Xu, S.K. Chang (2009), "Total phenolic, phenolic acid, anthocyanin, flavan-3-ol, and flavonol profiles and antioxidant properties of pinto and black beans (*Phaseolus vulgaris* L.) as affected by thermal processing", *J. Agric. Food Chem.*, **57(11)**, pp.4754-4764, DOI: 10.1021/jf900695s.

 DOI: 10.31276/VJSTE.65(1).38-42

Anionic competition on arsenate removal by modified granular ferric hydroxide adsorbent

Hoang Giang Pham[1], Tran Thanh Son Nguyen[1], Thi Thuy Pham[1*], Manh Khai Nguyen[1], Bart Vander Bruggen[2], Thi Thanh Mai Nguyen[3]

[1]*Faculty of Environmental Sciences, University of Science, Vietnam National University - Hanoi, 334 Nguyen Trai Street, Thanh Xuan Trung Ward, Thanh Xuan District, Hanoi, Vietnam*

[2]*Department of Chemical Engineering, Katholieke University of Leuven, Celestijnenlaan 200F, box 2424, B-3001 Heverlee (Leuven), Belgium*

[3]*Long Bien Secondary School, 16/163/3 Tu Dinh Street, Long Bien Ward, Long Bien District, Hanoi, Vietnam*

Received 27 April 2022; revised 24 June 2022; accepted 1 July 2022

Abstract:

The presence of inorganic forms of arsenic in water causing a serious threat to human health. Exposure of arsenic can cause serious diseases such as skin discoloration, cancer of skin, kidney and lung, blood vessel diseases, high blood pressure, and reproductive disorders. Removal of arsenic to provide safe drinking water was conducted to investigate the effects of individual and combined anions (sulphate, nitrate, phosphate, and chloride ions) on the arsenate adsorption capacity of modified granular ferric hydroxide adsorbent in batch experiments. The observed adsorption data fit the Langmuir model well. The presence of sulphate (400 mg/l), nitrate (15 mg/l), and chloride (250 mg/l) ions did not significantly affect the arsenate adsorption and the maximum adsorption capacity of arsenic was reduced by less than 5%. In contrary, phosphate ions showed strong competition for the adsorption process as the maximum adsorption capacity of the material was reduced by 59.8 and 73% at concentrations of 0.2 and 0.5 mg/l, respectively. The results also showed that phosphate anions were slightly preferable than arsenate in their competitive adsorption by the adsorbent.

Keywords: **arsenate, competing anions, iron hydroxide-based adsorbent.**

Classification numbers: **2.2, 5.3**

1. Introduction

Nowadays, there has been much research focused on inexpensive adsorbent materials to remove arsenic in water because of the serious effects arsenic has on human health. Among adsorbents, iron-based materials are the most studied because of their low cost, abundance, as well as their arsenic removal efficiency. Iron compounds including FeOOH, Fe_2O_3, $Fe(OH)_3$ [1-3]... or synthetic materials with the main component of iron such as laterite, hematite, nano-adsorbent particles [4-6]… have been studied with high arsenic treatment efficiency, low cost, and relatively easy operating conditions [2, 5, 6].

Among iron compounds, modified granular ferric hydroxide adsorbents are an iron-rich material combined with low cost and locally-sourced minerals such as bentonite, kaolinite, iron hydroxide or aluminium hydroxide, which are stable in a typical Vietnamese environment [3]. This study evaluated the arsenate removal efficiency of modified granular ferric hydroxide adsorbents under various parameters affecting the adsorption process such as pH, temperature, and time. In addition, this adsorbent was used in a pilot scale treatment system to demonstrate toxicant removal ability and economic efficiency.

However, the chemical composition of water such as phosphate or nitrate concentrations can significantly affect the removal of arsenic by an iron-based material through mechanisms similar to arsenate adsorption such as anions exchange because phosphate and arsenate can bond to amorphous, crystalline, or coprecipitated forms of iron or iron oxide [7, 8].

Batch studies were carried out using simulated groundwater to assess the effects of phosphate, nitrate, sulphate, and chloride on the removal of arsenic by a modified granular ferric hydroxide adsorbent. The findings presented in this paper will aid in the development of more effective arsenic treatment processes.

[*]*Corresponding author: Email: phamthithuy@hus.edu.vn*

2. Materials and methods

2.1. Materials

Adsorbent materials used in this study were developed by P.T. Thuy, et al (2020) consisted of 58.5 percent of iron hydroxide, 10 percent of aluminium hydroxide, 7.5 percent of bentonite, and 24 percent of kaolinite and was formed into tiny balls with practical sizes ranging from 5 to 10 mm [3].

Chemicals including NaCl, $NaNO_3$, Na_2SO_4, Na_2HPO_4, and $Na_2HAsO_4.7H_2O$ were pure reagent grade materials. Stock solutions of arsenate, chloride, sulphate, nitrate, and phosphate were prepared by dissolving the respective chemicals in deionized water. All these solutions were further diluted to suitable concentrations on the day of use.

2.2. Methods

The experiments were studied at room temperature. First, 50 ml of solution was prepared and placed into 100 ml flasks, then 0.1 g of adsorbent was added.

The initial concentrations of arsenic were 100; 200; 500; 1000 mg/l (in the form of arsenate). To study the effect of anions, the experiments were conducted with solutions that only contain arsenate or contain arsenate and one of the competing anions.

The purpose of this experiment is to evaluate the influence of anions in the real environment, thus, the concentrations of anions were selected based on QCVN 09-2015/BTNMT Vietnamese technical regulation on ground water quality (in the case of phosphate, it is based on QCVN 08-2015/BTNMT Vietnamese technical regulation on surface water quality). Concentrations of competing anions were sulphate (400 mg/l), chloride (250 mg/l), nitrate (15 mg/l), and phosphate (0.2 mg/l and 0.5 mg/l).

The pH was adjusted to 7 by HCl 0.1 M or NaOH 0.1 M. The mixture was shaken at 150 rpm for 120 min at room temperature (25°C). The effluent was filtered through a 0.45 µm filter paper, and concentrations of As (V) were analysed using (AAS) Shimadzu AA6800, concentrations of other anions were analysed by UV-VIS method.

2.3. Adsorption isotherm models

Adsorption isotherm models have been used to describe the interaction between arsenic in solution and the adsorbents. In addition, isotherm models can be used to explain the distribution of metal ions between the liquid and solid phase when equilibrium is reached. In this work, adsorption isotherm models were generated based on Freundlich and Langmuir models to evaluate the adsorption capacity of the material.

The Langmuir equation is given by:

$$q_e = q_m k_a C_e/(1+k_a C_e)$$

The linear form is:

$$C_e/q_e = (1/q_m)C_e + 1/(k_a q_m)$$

where q_e is the amount of ion adsorbed (mg/g); C_e is the equilibrium concentration (mg/l); q_m is the max adsorption capacity (mg/g); and k_a is the adsorption equilibrium constant.

The Freundlich equation is given by:

$$q_e = K_f C_e 1/n$$

The linear form is:

$$\ln q_e = \ln K_f + (1/n)\ln C_e$$

where the constant K_f is related to the adsorption capacity of materials and 1/n is related to the surface heterogeneity.

3. Results and discussion

3.1. The adsorption of arsenate onto modified granular ferric adsorbent

Figure 1A shows that the adsorption of arsenate (without competing anions) onto the adsorbent. Fig. 1B is the linear data fit to the Langmuir isotherm model and

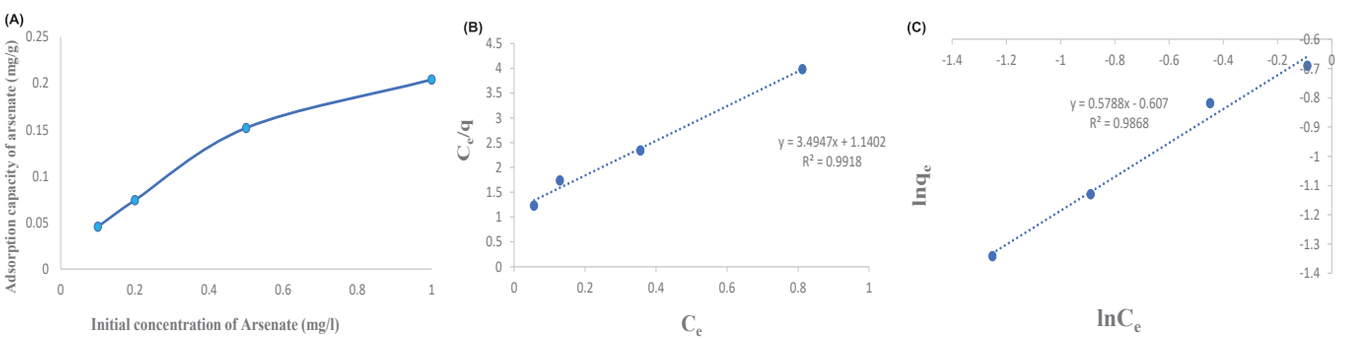

Fig 1. (A) Adsorption capacity of arsenate onto adsorbent; (B) Langmuir isotherm model fit and (C) Freundlich isotherm model.

Fig. 1C to the Freundlich isotherm model. The correlation coefficient of the Langmuir isotherm model is 0.99 and the Freundlich is 0.98, which also indicates that arsenate adsorption characteristics on the material was monolayer adsorption and energetically equivalent, that is, the energy of adsorption is equal to the surface.

Maximum adsorption capacity of adsorbent (q_m) following the Langmuir model is 0.286 mg/g and adsorption equilibrium constant is 3.07. This maximum adsorption capacity is higher than the result of P.T. Thuy, et al. (2020) [3] due to the difference in the particle sizes, for example, in this study it was 5-10 mm compared to about 20 mm in the previous. In case of the Freundlich model, the Freundlich constant (K_f) is 0.247.

3.2. The adsorption of arsenate onto modified granular ferric adsorbent in the presence of competing anions

Figure 2 shows a change in the arsenate adsorption process onto material in the presence of competing anions in solution. Samples containing monovalent anions (chloride and nitrate) showed differences in results ranging from 0 to 3%, which is almost no difference from samples containing arsenate only. In the case of the divalent anion sample (sulphate), arsenate adsorption capacity tends to decrease slightly in the range of 3-5%. The anions having almost no effect on the efficiency of the arsenate adsorption process indicates that the anion exchange mechanism has less contribution in the arsenate adsorption process of this material.

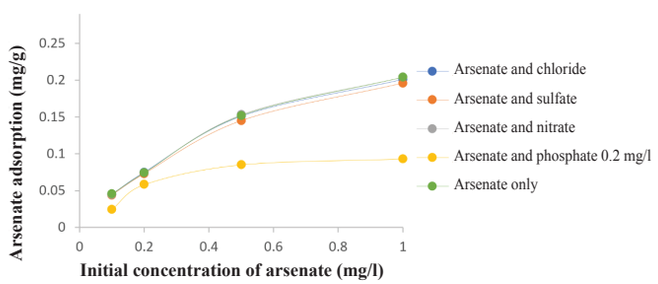

Fig. 2. Adsorption capacity of arsenate onto adsorbent under the influence of competing anions.

On the other hand, phosphate significantly reduced the adsorption capacity of arsenate. These decreases were from 0.456 to 0.246 mg/l (46% decrease) at an initial concentration arsenate = 0.1 and 2.04 to 0.62 mg/l (69.6% decrease) at initial arsenate concentration = 1 mg/l.

There are two main mechanisms for the interaction of anions on the surface of iron hydroxide.

First, the surface of the material is ionized by protons and anions, which will interact with the surface through the affinity adsorption mechanism [8, 9]:

$$SOH + H^+ \leftrightarrow SOH_2^+$$

$$SOH_2^+ + A^- \leftrightarrow SOH_2A.$$

Anions such as phosphate or arsenate form complexes with the surface of the material [10]:

$$FeOOH + 3H_2AsO_4^- + 3H^+ \rightarrow Fe(H_2AsO_4)_3 + 2H_2O$$

$$FeOOH + 3H_2PO_4^- + 3H^+ \rightarrow Fe(H_2PO_4)_3 + 2H_2O$$

It can be seen that the effect of affinity adsorption mechanism did not play big role. This is explained by the fact that this process depends on the protonation of the surface of the material. At the pH of the reaction (pH=7), the concentration of H^+ ions in the solution is not large enough for the protonation process.

On the other hand, the main mechanism for this competition is the similarity in the chemical properties of phosphate and arsenate (phosphorus and arsenic are both in the group VA). Predictably, phosphates have a complex on the iron surface thereby reducing the potential for iron-arsenate interactions like, for example, the following reaction:

$$Fe(H_2PO_4)_3 + H_2AsO_4^- \leftrightarrow Fe(H_2AsO_4)_3 + H_2PO_4^-.$$

3.3. Effect of phosphate concentration on arsenate adsorption capacity

Figure 3 shows that arsenate adsorption capacity decreased in the range of 22-55% at an initial phosphate concentration of 0.2 mg/l, and 60-70% with an initial phosphate concentration of 0.5 mg/l. It can also be seen that the adsorption capacity of arsenate remains constant when the initial arsenate concentration reaches 0.5 mg/l in solutions with phosphate anions, while this capacity continues to increase in samples without competing anions.

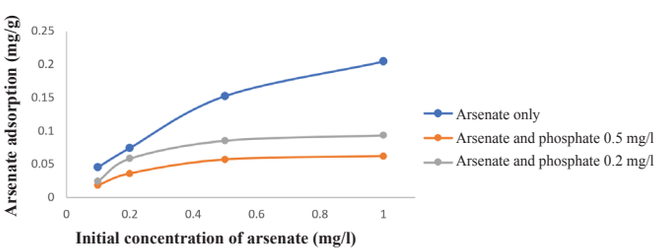

Fig. 3. Adsorption capacity of arsenate onto adsorbent under different concentrations of phosphate.

The Langmuir and Freundlich adsorption isotherm models of arsenate adsorption in the presence of phosphate are shown in Fig. 4. Similar to the case without competing anions, the adsorption processes were fitted to the Langmuir and Freundlich isotherm models with correlation coefficient of 0.97-0.98 and 0.82-0.89, respectively.

The Langmuir isotherm models show that the maximum adsorption capacity of arsenate decreased from 2.86 to 0.115 mg/g at a concentration of phosphate of 0.2 mg/l (59.8%) and from 2.86 to 0.077 mg/g at 0.5 mg/l (73% reduction).

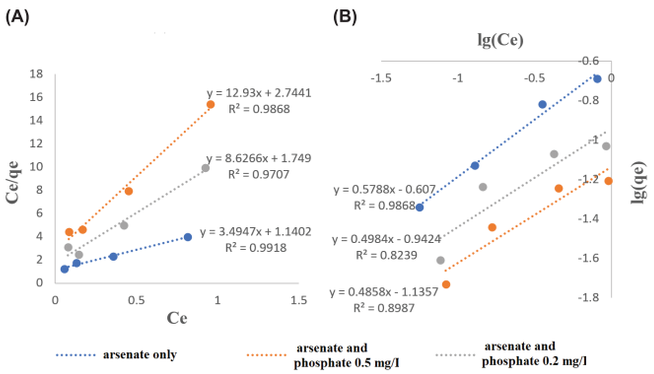

Fig. 4. (A) Langmuir isotherm model and (B) Freundlich isotherm model of arsenate adsorption under different concentrations of phosphate.

3.4. Concentration of competing anions after the adsorption process

The concentration of monovalent and divalent anions after the adsorption process showed no change. This confirms the prediction made in section 3.2 is correct, that is, these anions have absolutely no interaction with the surface of the material.

In the case of phosphate at low concentration (0.2 mg/l), almost all phosphate was adsorbed into the material. When the concentration of phosphate was 0.5 mg/l, 80-98% phosphorus was removed from the solution after the reaction ended (Fig. 5). It is also easy to see the adsorption competition between arsenate and phosphate as the higher the initial arsenate concentration, the lower the phosphate removal efficiency. This proves the above assumptions in section 3.1 about the similarity in chemical properties of these two compounds leading to a competitive reaction on the surface of the iron-rich material. The results also show phosphate anions were slightly preferable than arsenate in their competitive adsorption by the adsorbent.

The general equation describing the reaction between phosphate, arsenate, and the surface of the material can be expressed as follows:

$$S\text{-}PO_{4(s)} + H_3AsO_{4(eq)} \leftrightarrow S\text{-}AsO_{4(s)} + H_3PO_{4(eq)}$$

where $S\text{-}PO_{4(s)}$ and $S\text{-}PO_{4(s)}$ are complexes of arsenate and phosphate with the surface of the material.

The equilibrium constant of the reaction (K_c) will be:

$$K_c = [H_3PO_4]/[H_3AsO_4]$$

From the calculated data, it is shown that the equilibrium constant for the reaction (K_c) is 5.65±0.33.

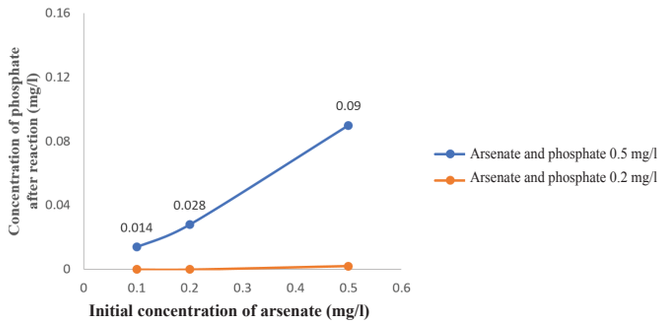

Fig. 5. Concentration of phosphate after the adsorption process.

In comparison to previous studies [8, 11, 12], both monovalent and divalent anions showed significant competition for arsenate adsorption on the material's surface. However, this study's adsorbent indicates that the impacts of these anions are very small, and that any anion competition in the environment is primarily due to phosphates.

4. Conclusions

The presence of sulphate (400 mg/l), nitrate (15 mg/l), and chloride (250 mg/l) ions did not significantly affect the arsenate adsorption, which indicated that the anion exchange mechanism has less contribution in the arsenate adsorption process of an iron-rich adsorbent. In contrary, phosphate ions showed strong competition for the adsorption process with arsenate. The maximum adsorption capacity of the Langmuir isotherm was reduced by 59.8 and 73% at phosphate concentrations of 0.2 and 0.5 mg/l, respectively, due to the similarity in chemical properties of phosphate and arsenate. Therefore, phosphate should be considered in the actual arsenate treatment, and arsenate removal procedures should be calculated based on the actual adsorption capacity in the presence of competing phosphates or phosphate removal prior to passing through arsenate removal materials.

CRediT author statement

Hoang Giang Pham: Conceptualization, Methodology, Formal analysis, Writing, Editing; Tran Thanh Son Nguyen: Data analyst; Thi Thuy Pham: Conceptualization, Methodology, Formal analysis, Writing, Review, Editing; Manh Khai Nguyen: Review, Data analyst; Bart Vander Bruggen: Review, Editing; Thi Thanh Mai Nguyen: Data analyst.

ACKNOWLEDGEMENTS

The research is funded by the Vietnam Ministry of Science and Technology under Independent project DTDL.CN-50/18.

COMPETING INTERESTS

The authors declare that there is no conflict of interest regarding the publication of this article.

REFERENCES

[1] R. Ozola, A. Krauklis, M. Leitietis, et al. (2019), "FeOOH-modified clay sorbents for arsenic removal from aqueous solutions", *Environmental Technology & Innovation*, **13**, pp.364-372, DOI: 10.1016/j.eti.2016.06.003.

[2] X. Yu, Y. Wei, C. Liu, et al. (2019), "Ultrafast and deep removal of arsenic in high-concentration wastewater: A superior bulk adsorbent of porous Fe_2O_3 nanocubes-impregnated graphene aerogel", *Chemosphere*, **222**, pp.258-266, DOI: 10.1016/j.chemosphere.2019.01.130.

[3] P.T. Thuy, H.H. Ngo, V.S. Tran, et al. (2020), "Removal of As (V) from the aqueous solution by a modified granular ferric hydroxide adsorbent", *Science of The Total Environment*, **706**, DOI: 10.1016/j.scitotenv.2019.135947.

[4] N.T. Hai, H.N. Tran, H.A. Vu, et al. (2020), "Laterite as a low-cost adsorbent in a sustainable decentralized filtration system to remove arsenic from groundwater in Vietnam", *Science of The Total Environment*, **699**, DOI: 10.1016/j.scitotenv.2019.134267.

[5] W. Shengsen, B. Gao, Y. Li, et al. (2015), "Removal of arsenic by magnetic biochar prepared from pinewood and natural hematite", *Bioresource Technology*, **175**, pp.391-395, DOI: 10.1016/j.biortech.2014.10.104.

[6] L. Adlnasab, N. Shekari, A. Maghsodi (2019), "Optimization of arsenic removal with Fe_3O_4@Al_2O_3@Zn-Fe LDH as a new magnetic nano adsorbent using Box-Behnken design", *Journal of Environmental Chemical Engineering*, **7(2)**, DOI:10.1016/j.jece.2019.102974.

[7] K.H. Goh, T.T. Lim (2005), "Arsenic fractionation in a fine soil fraction and influence of various anions on its mobility in the subsurface environment", *Applied Geochemistry*, **20(2)**, pp.229-239, DOI: 10.1016/j.apgeochem.2004.08.004.

[8] X. Meng, S. Bang, G.P. Korfiatis (2000), "Effects of silicate, sulfate, and carbonate on arsenic removal by ferric chloride", *Water Research*, **34(4)**, pp.1255-1261, DOI: 10.1016/S0043-1354(99)00272-9.

[9] Y.M. Pajany, C. Hurel, N. Marmier, et al. (2011), "Arsenic (V) adsorption from aqueous solution onto goethite, hematite, magnetite and zero-valent iron: Effects of pH, concentration and reversibility", *Desalination*, **281**, pp.93-99, DOI: 10.1016/j.desal.2011.07.046.

[10] F. Zhang, H. Itoh (2005), "Iron oxide-loaded slag for arsenic removal from aqueous system", *Chemosphere*, **60(3)**, pp.319-325, DOI: 1016/j.chemosphere.2004.12.019.

[11] X. Meng, G.P. Korfiatis, S. Bang, et al. (2002), "Combined effects of anions on arsenic removal by iron hydroxides", *Toxicology Letters*, **133(1)**, pp.103-111, DOI: 10.1016/S0378-4274(02)00080-2.

[12] M. Chen, K.S. Peltier, S.J. Randtke, et al. (2018), "Modeling arsenic (V) removal from water by micellar enhanced ultrafiltration in the presence of competing anions", *Chemosphere*, **213**, pp.285-294, DOI: 10.1016/j.chemosphere.2018.09.046.

Investigation of activated carbon derived from rice straw biomass for removal of phenol from aqueous solution

Thi Thu Hoai Pham*

Faculty of Food Technology, University of Economics - Technology for Industries, 456 Minh Khai Street, Vinh Tuy Ward, Hai Ba Trung District, Hanoi, Vietnam

Received 27 November 2022; revised 20 December 2022; accepted 5 January 2023

Abstract:

The rapidly developing of industry and population leads to various problems, such as an increase in the energy used and discharging of pollutants into the environment. Water pollution is a big issue in Vietnam as well as in the world. Therefore, finding the method for the treatment of water is urgent.This work investigated activated carbon derived from rice straw biomass (ACRS) for the adsorption of phenol. The surface morphology, surface functional group, and surface area of the ACRS were determined by scanning electron microscopy (SEM), Fourier transform infrared (FTIR) spectroscopy, and Brunauer-Emmett-Teller (BET) analysis, respectively. ACRS had a porous structure along with a larger surface area of 216.3 m^2/g, which effectively enhanced the adsorption performance of phenol. The removal performance of phenol increased with increasing the contact time (10-60 min), then reached equilibrium at 90 min. The maximum adsorption capacity of phenol using ACRS was 128.4 mg/g and the adsorption behaviour of the pollutant fit well to the Langmuir and Freundlich isotherms. Experimental results revealed that adsorption by surface area, activated sites, pores, and complexation between functional groups of the adsorbent and phenol were major mechanisms.

Keywords: **activated carbon, adsorbent, biomass, phenol, rice straw.**

Classification numbers: **2.2, 5.3**

1. Introduction

A high level of water pollution worsens the already troubling environmental situation by contaminating drinking water as untreated wastewater flows into surface water bodies at alarming rates. According to the United Nations economic and social commission for Asia and the Pacific 2022, 1.9 billion people throughout the region still lack access to safely managed drinking water and sanitation services. This potentially hazardous wastewater not only affects human health, but other inhabitants as well [1-3]. Phenol is commonly dumped from industrial effluents of various chemical manufacturing plants, for example, plastic, paper bleaching facilities, paint, pharmaceuticals, pesticides, petrochemicals, paint manufacturers. Humans suffer skin, eye, and mucous membrane irritation by phenol exposure. The United States Environmental Protection Agency (EPA) has placed a water purity requirement of less than 1.0 ppb of phenol in surface water [2-6]. Adsorption processes by carbon-based materials have been attractive to researchers for effective removal of organic compounds from water systems [7, 8]. Currently, biochar derived from waste materials are widely applied for the adsorption of organic pollutants like phenol. Indeed, Yusuff and co-workers used eucalyptus bark biochar to remove toxic heavy metal (Cr^{6+}) [9]. V.T. Quyen, et al. (2021) [10] and co-workers prepared biochar from coffee husks and applied it to remove heavy metals including Pb (II) and Cd (II) from wastewater. T. Wu, et al (2022) [11] also tried to remove methylene blue by using porous biochar derived from eggshells. In another example, G. Wang, et al. (2022) [12] and co-workers utilized porous biochar for chloramphenicol removal.

Biochar has various advantages such as low-cost, non-toxicity, and high adsorption performance for many kinds of pollutants. Many studies have investigated the use of biochar produced from agricultural waste materials to remove organic pollutants. As an agricultural country, Vietnam produces huge amounts of rice, over 44 M tons in 2020. Due to the high amount of rice production, a larger rice straw biomass was produced. Therefore, utilizing rice straw waste as a base material to make adsorbent is potentially ideal. Doing so will help decrease waste from agricultural activities as well as bring added value to solve water pollution. Therefore, the present study determines the potential of activated carbon derived from rice straw biomass for the adsorption of phenol. The adsorption behaviours at the solid-liquid interface were investigated by adsorption isotherms and the study of other factors like reaction times, adsorbent dose, and initial concentration of phenol.

*Email: ptthoai@uneti.edu.vn

2. Materials and methods

2.1. Prepare adsorbent

The rice straw waste used in this work was collected from a local corn farm (Nam Dinh city, Vietnam). Rice straw biomass was cut into small pieces, washed with DI water, dried at 80°C for 12 h, then pyrolyzed at a temperature of 450°C for 3 h using a furnace under N_2 gas. After cooling, the product after the pyrolyzed process (ACRS) was taken out and kept for further experiments.

2.2. Characterization of ACRS adsorbent

The specific surface area was determined using the Brunauer-Emmett-Teller (BET) method (Surface area analyser, JW-BK112, China). Scanning electron microscopy (SEM) images (SU-850, Hitachi, Japan) were recorded to investigate the morphology of the ACRS. The functional groups of adsorbents were identified by FTIR spectroscopy (Nicolet, 12- FTIR spectrometer, US).

2.3. Phenol removal

The bath adsorption experiment was performed by adding 0.5 g of adsorbent in a glass vial containing phenol solution (V=100 ml; C=10 mg/l; pH=6.0). The mixture was stirred at 200 rpm by magnetic stirrer at for different times. The sample was taken out, filtered by a 0.22-µm membrane, and analysed by high-performance liquid chromatography (HPLC) to determine the phenol concentration in the sample.

The adsorption capacities and the removal performance of phenol were calculated based on Eqs. (1) and (2):

$$q_e = \frac{(C_o - C_e)V}{m} \quad (1)$$

$$\text{Removal}(\%) = \frac{C_0 - C_t}{C_0} \times 100 \quad (2)$$

where q_e is the quantity of adsorbed phenol by 1 g ACRS (mg/g), C_o is the initial phenol concentration (mg/l), C_e is phenol concentration at equilibrium (mg/l), C_t is phenol concentration at time t (mg/l), V is the volume of phenol solution (ml), and m is the amount of dry ACRS (mg).

3. Results and discussion

3.1. Surface morphology of ACRS

Figure 1A shows an image and Fig. 1B displays the surface morphology of the ACRS adsorbent. It can be seen that the ACRS was black in colour like biochar and the surface morphology was jagged and broken with a porous structure. In general, the porous structure provides many active sites and pores to adsorb the pollutant in the solution [12-16].

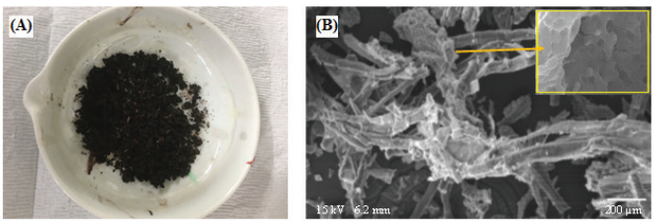

Fig. 1. (A) Image and (B) surface morphology of ACRS.

3.2. The surface area of ACRS

Figure 2 shows the gas adsorption-desorption isotherm on the surface of ACRS, which is classified as type IV along with the micro- and mesoporous structure of the adsorbent. The ACRS had a high surface area of 216.3 m^2/g and total pore volume of 0.382 cm^3/g. Table 1 compares the physical properties of ACRS and other adsorbents. The surface area and pore volume of the ACRS were higher than other materials, confirming the potential of ACRS for the adsorption of phenol [16-19].

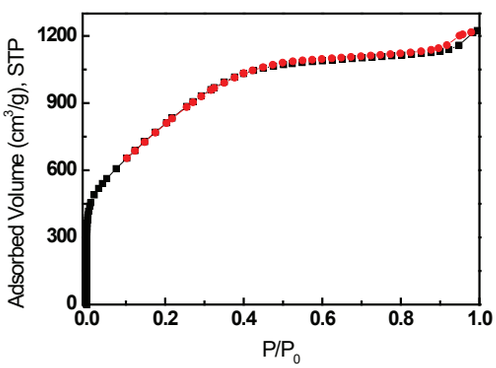

Fig. 2. N_2 adsorption-desorption isotherm analysis of ACRS.

Table 1. Surface area and pore volume of adsorbents.

Materials	S_{BET} (m^2/g)	V pores (cm^3/g)	References
ACRS	216.3	0.038	This study
Zeolite	24	0.011	[13]
Biochar	17.07	0.035	[14]
Pistachio shells biochar (300°C)	15.12	0.002	[15]
Pistachio shells biochar (600°C)	34.16	0.008	[15]

3.3. Surface functional groups of ACRS

Figure 3 shows the FTIR spectra of the adsorbent in the range of 400 to 4000 cm^{-1}. The peak around ~3620 cm^{-1} is associated with the bands of the O-H group in aromatic and aliphatic structures [10-12].

The peak appearing at 3300 cm^{-1} illustrates the N-H stretch in the amine group. The peak at ~2836 cm^{-1} is attributed to the presence of the aliphatic C-H stretch of CH, CH_2, and CH_3 groups. The O=C=C stretch is observed by a

noticeable peak at 2360 cm^{-1}. The peak at ~1665 cm^{-1} could be assigned to C=O bonds. The peak found below ~910 cm^{-1} is related to the out-of-plane stretching of C-H. These results suggest that ACRS contained various functional groups responsible for adsorbing phenol from solution [19-22].

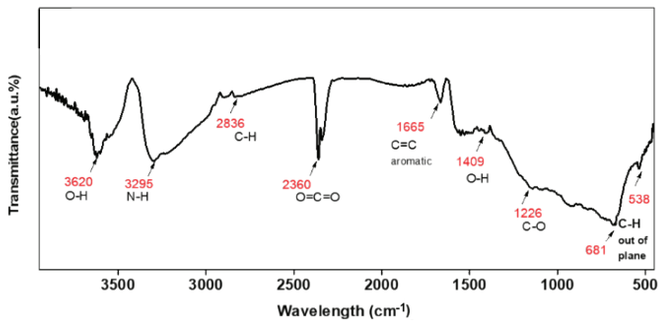

Fig. 3. Surface functional groups of ACRS.

3.4. Effect of contact time on the removal of phenol

Figure 4 displays the effect of time on the adsorption of phenol by ACRS. The removal performance of phenol increased with time, the efficiency was 12.3% at 10 min and it increased up to 93.5% after 90 min. After 90 min of reaction time, the adsorption of phenol by ACRS was negligible due to unavailable active sites, surface area, and pores to adsorb phenol pollutants [18-23]. As shown in Fig. 4, higher initial phenol concentration (50 mg/l) displayed a smaller removal efficiency (83.4%) compared low-level concentration (Co=10 mg/l and R=93.8%). At a low concentration of phenol, the adsorption nearly completed in 90 min, while with a high concentration of the pollutant, the adsorption equilibrium was found at 150 min.

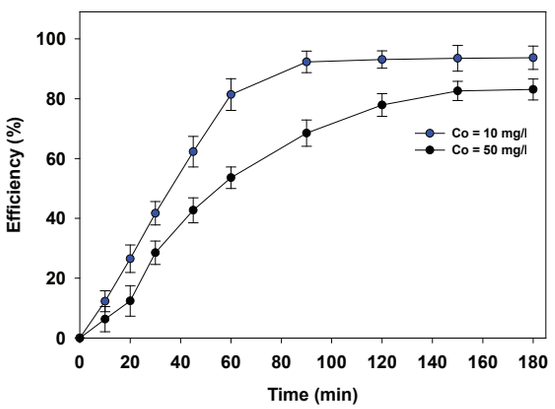

Fig. 4. Effect of reaction time on phenol adsorption by ACRS.

3.5. Effect of ACRS dose on the removal of phenol

The removal performance of phenol rapidly improved from 10.3 to 93.5% as the ACRS amount increased from 0.01 to 0.5 g, respectively (Fig. 5). This was due to the high surface area and active sites available at higher dosages [20-24]. Further increase in adsorbent dosage over 0.5 g did not contribute to any improvement in the removal performance of phenol.

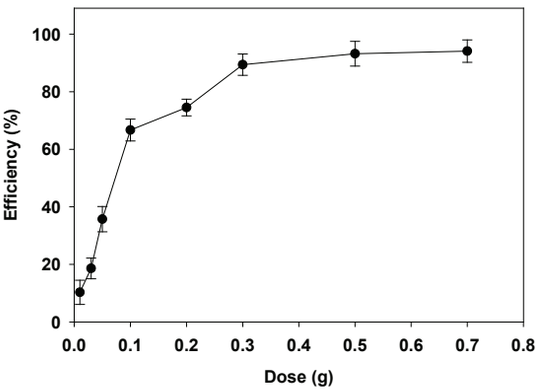

Fig. 5. Effect of ACRS dose on the removal of phenol.

3.6. Adsorption isotherms

Figure 6 displays a linear fit of the Langmuir and Freundlich models and the corresponding adsorption isotherms parameters are listed in Table 2.

The adsorption of phenol was fit to the Langmuir model (R^2=0.98) and Freundlich model (R^2=0.91). The maximum absorption capacity of phenol by ACRS obtained via the Langmuir isotherm was 128.4 mg/g. For the Freundlich model, the value of n is higher than 1.0, which indicates favourable adsorption of phenol onto ACRS [21-23].

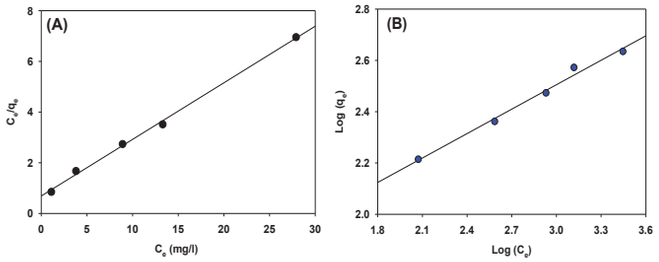

Fig. 6. Adsorption isotherms: (A) Langmuir model and (B) Freundlich model.

Table 2. Adsorption parameters of phenol provided by Langmuir and Freundlich isotherms.

Adsorbent	Langmuir model			Freundlich model		
	q_{max} (mg/g)	b (l/g)	R^2	n	K_F (mg/g)	R^2
ACRS	128.4	0.02	0.98	3.2	42.1	0.91

3.7. Adsorption mechanism

The adsorption mechanisms of phenol by using ACRS could include physisorption and chemisorption as listed in Fig. 7 [9-12]. The main physical adsorption mechanism was controlled by Van der Waals forces and electrical attraction. ACRS is an effective physical adsorbent for phenol removal because of its high surface area, many pores, and active adsorption sites [9, 10, 21-24].

In general, chemisorption occurs by the sharing of electrons between phenol and the surface of the adsorbent, then chemical bonds form between functional groups of phenol and the

adsorbent ACRS. Functional groups like C=O, N-H, and O-H of ACRS could interact with phenol through complexation, resulting in removed phenol from the solution [22-24].

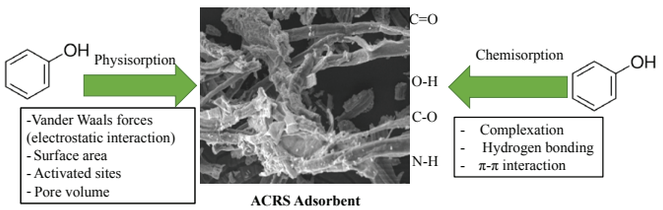

Fig. 7. Adsorption mechanisms of phenol by using ACRS adsorbent.

4. Conclusions

This work identified the potential of ACRS for adsorption of phenol in solution. The removal performance of phenol was over 93% within 90 min of contact time and 0.5 g ACRS. The adsorption data indicated that the adsorption of phenol was well fit by Freundlich and Langmuir isotherms and the maximum adsorption capacity of phenol was 128.4 mg/g. ACRS had a high adsorption performance of phenol due to its high surface area, porous structure, and its various functional groups like C=O, O-H, N-H, and O=C=C. This work provides a method to produce adsorbents from waste material that can be utilized for the removal of organic pollutants like phenol.

COMPETING INTERESTS

The author declares that there is no conflict of interest regarding the publication of this article.

REFERENCES

[1] X. Sun, C. Wang, Y. Li, et al. (2015), "Treatment of phenolic wastewater by combined UF and NF/RO processes", *Desalination*, **355**, pp.68-74, DOI: 10.1016/j.desal.2014.10.018.

[2] P. Kazemi, M. Peydayesh, A. Bandegi, et al. (2014), "Stability and extraction study of phenolic wastewater treatment by supported liquid membrane using tributyl phosphate and sesame oil as liquid membrane", *Chem. Eng. Res. Des.*, **92(2)**, pp.375-383, DOI: 10.1016/j.cherd.2013.07.023.

[3] S. Mohammadi, A. Kargari, H. Sanaeepur, et al. (2015), "Phenol removal from industrial wastewaters: A short review", *Desalination and Water Treatment*, **53(8)**, pp.2215-2234, DOI: 10.1080/19443994.2014.883327.

[4] G. Veeresh, P. Kumar, I. Mehrotra (2005), "Treatment of phenol and cresols in upflow anaerobic sludge blanket (UASB) process: A review", *Water Research*, **39(1)**, pp.154-170, DOI: 10.1016/j.watres.2004.07.028.

[5] G. Calleja, J. Serna, J. Rodríguez (1993), "Kinetics of adsorption of phenolic compounds from wastewater onto activated carbon", *Carbon*, **31(5)**, pp.691-697, DOI: 10.1016/0008-6223(93)90005-U.

[6] F. Orshansky, N. Narkis (1997), "Characteristics of organics removal by PACT simultaneous adsorption and biodegradation", *Water. Res.*, **31**, pp.391-398, DOI: 10.1016/S0043-1354(96)00227-8.

[7] I. Ali, V.K. Gupta (2006), "Advances in water treatment by adsorption technology", *Nature Protocols*, **1**, pp.2661-2667, DOI: 10.1038/nprot.2006.370.

[8] B.C. Pan, W. Du, W. Zhang, et al. (2007), "Improved adsorption of 4-phenol onto a novel hyper-cross-linked polymer", *Environ. Sci. Technol.*, **41**, pp.5057-5062, DOI: 10.1021/es070134d.

[9] A.S. Yusuff, M.A. Lala, E.O. Babatunde, et al. (2022), "$ZnCl_2$-modified eucalyptus bark biochar as adsorbent: Preparation, characterization and its application in adsorption of Cr(VI) from aqueous solutions", *South. African J. Chem. Eng.*, **42**, pp.138-145, DOI: 10.1016/j.sajce.2022.08.002.

[10] V.T. Quyen, T.H. Pham, J. Kim, et al. (2021), "Biosorbent derived from coffee husk for efficient removal of toxic heavy metals from wastewater", *Chemosphere*, **284**, DOI: 10.1016/j.chemosphere.2021.131312.

[11] T. Wu, G. Yang, J. Cao, et al. (2022), "Activation and adsorption mechanisms of methylene blue removal by porous biochar adsorbent derived from eggshell embrance", *Chemical Eng. Research and Design*, **188**, pp.330-341, DOI: 10.1016/j.cherd.2022.08.042.

[12] G. Wang, X. Yong, L. Luo, et al. (2022), "Structure-performance correlation of high surface area and hierarchical porous biochars as chloramphenicol adsorbents", *Separation and Purification Technology*, **296**, DOI: 10.1016/j.seppur.2022.121374.

[13] L. Tortet, E. Ligner, W. Blanluet, et al. (2017), "Adsorptive elimination of paracetamol from physiological solutions: Interaction with MFI-type zeolite", *Microporous and Mesoporous Mater.*, **252**, pp.188-196, DOI: 10.1016/j.micromeso.2017.06.027.

[14] Z. Zhang, G. Huang, P. Zhang, et al. (2023), "Development of iron-based biochar for enhancing nitrate adsorption: Effects of specific surface area, electrostatic force, and functional groups", *Science of the Total Environment*, **856**, DOI: 10.1016/j.scitotenv.2022.159037.

[15] S. Saghir, C. Pu, E. Fu, et al. (2022), "Synthesis of high surface area porous biochar obtained from pistachio shells for the efficient adsorption of organic dyes from polluted water", *Surfaces and Interfaces*, **34**, DOI: 10.1016/j.surfin.2022.102357.

[16] R.M. Zavod, J.J. Knittel (2013), "Drug design and relationship of functional groups to pharmologic activity", *Foye's Principles of Medicinal Chemistry*, **6**, pp.29-60.

[17] M.M. Harussani, S.M. Sapuan (2022), "Development of kenaf biochar in engineering and agricultural applications", *Chemistry Africa*, **5**, pp.1-17, DOI: 10.1007/s42250-021-00293-1.

[18] S.W. Rita, C.C. Hsu, T.J. Chang, et al. (2013), "A preliminary investigation of wastewater treatment efficiency and economic cost of subsurface flow oyster-shell-bedded constructed wetland systems", *Water*, **5(3)**, pp.893-916, DOI: 10.3390/w5030893.

[19] I. Mitra, N. Bar, S. Das, et al. (2019), "Rice husk: Green adsorbent for Pb(II) and Cr(VI) removal from aqueous solution-column study and GA-NN modeling", *SN Applied Science*, **1**, DOI: 10.1007/s42452-019-0513-5.

[20] C. Russo, M. Pawlyta, A.E. Tomiczek, et al. (2021), "On the application of electron energy-loss spectroscopy for investigating nanostructure of soot from different fuels", *Fuels*, **2(3)**, pp.367-375, DOI: 10.3390/fuels2030021.

[21] S. Yu, X. Wang, Y. Ai, et al. (2016), "Experimental and theoretical studies on competitive adsorption of aromatic compounds on reduced graphene oxides, *J. Mater. Chem.*, **4(15)**, pp.5654-5662, DOI: 10.1039/C6TA00890A.

[22] A. Singh, D.B. Pal, J.M. Jha, et al. (2021), "Low-cost biochar adsorbents prepared from date and delonix regia seeds for heavy metal sorption", *Bioresource Technology*, **339**, DOI: 10.1016/j.biortech.2021.125606.

[23] A. Imran, M. Asim, T.A. Khan (2012), "Low-cost adsorbents for the removal of organic pollutants from wastewater review", *Environmental Management*, **113**, pp.170-183, DOI: 10.1016/j.jenvman.2012.08.028.

[24] S.F. Lütkeet, A.V. Igansi, L. Pegoraro, et al. (2019), "Preparation of activated carbon from black wattle bark waste and its application for phenol adsorption", *J. Environ. Chem. Eng.*, **7(5)**, DOI: 10.1016/j.jece.2019.103396.

DOI: 10.31276/VJSTE.65(1).47-53

Effect of arbuscular mycorrhizal fungi inoculation on revegetation at Nukui Dam site, Japan

Minh Thi Nguyen[1*], Kazuhira Yokoyama[2], Takuya Marumoto[3]

[1]Faculty of Environment, Vietnam National University of Agriculture, Trau Quy Town, Gia Lam District, Hanoi, Vietnam
[2]Faculty of Agriculture, Yamaguchi University, 1677-1 Yoshida, Yamaguchi, Japan
[3]Takino filter Inc., 2-904-16 Hayama, Kudamatsu, Yamaguchi, Japan

Received 3 December 2021; revised 22 February 2022; accepted 1 March 2022

Abstract:

The establishment of the surviving arbuscular mycorrhizal (AM) fungi, *Gigaspora margarita* Becker & Hall, inoculated in revegetation at the Nukui Dam was studied. The population of AM fungi and AM colonization of three plant species Japanese hill cherry (*Prunus jamasakura* Sieb. ex Koidz, yamazakura-inoculated plant), eulalia (*Miscanthus sinensis* Anderss, susuki), and mugwort (*Artemisia vulgaris* Pampan, yomogi) were investigated to compare inoculated and non-inoculated treatments. The AM colonisation was enhanced in inoculated plots although natural or accidental AM fungi were involved in non-inoculated plots and successfully colonised. Coverage of soil surface was more than 80% and even reached nearly 100% in summer regardless of the soil amendment type. The number of spores and the percentage of colonisation of investigated plant roots, as well as the density of typical AM structures such as arbuscules, auxiliary cells, vesicles, and coiling hyphae by AM fungi in inoculated plots were higher than those in non-inoculated ones. Some spores were *Gigaspora* and *Glomus*-inoculated species and were relatively rich in inoculated plots of Yamazakura. There was a significant increase in the number of AM spores in inoculated treatments at a 5% confidence level (ANOVA, $p<0.05$) in Susuki and Yamazakura. Much more spores of *Gigaspora* sp. occurred in the rhizosphere soil of Yamazakura and Susuki plants in inoculated plots than in non-inoculated plots (2.33 and 3.73 times, respectively). The colonisation intensity and spore number in the rhizosphere were positively correlated. Therefore, inoculation at an early establishment should be important for the successive development of AM-plant symbiosis formation.

Keywords: **arbuscular mycorrhizal (AM) fungi, revegetation, soil amendment.**

Classification numbers: **3.1, 3.4**

1. Introduction

AM, the most widespread symbioses on Earth [1], is receiving attention because of the increasing range of their application in diverse, practical fields such as sustainable agriculture, reforestation programs, and ecosystem management [2].

Some plant species almost completely depend on mycorrhizal association for nutrient uptake [3]. Improved growth and survival of such species will help plants to establish themselves in a diverse ecosystem, an important criterion for revegetation success. Plants that are normally mycorrhizal will be at a competitive disadvantage in revegetation if phosphorus is limited and if few effective mycorrhizal fungi exist in the soil. Therefore, the presence of effective mycorrhizal fungi will likely need to be re-established in such cases. In general, plants from mature ecosystems require the presence of mycorrhizae for their development [4].

It is well known that AM fungi species of the genus *Gigaspora* appear to favour fluxes of carbon compounds from plant to soil biota ultimately resulting in enhanced soil aggregation, while *Glomus spp.* tend to favour root colonization, plant growth and productivity through improved mineral nutrition [5]. The management of AM during revegetation and reforestation is well documented [6, 7]. However, little is still known about the establishment and effect of the long-term survival of

*Corresponding author: Email: nguyenminhvn@hotmail.com

AM after revegetation. Indeed, to the best of the authors' knowledge, there is no report on relationships among AMs, soil amendments, and soil properties. The overall objective of the work presented in this paper is closely linked to the project "Utilization and management of symbiosis associations - Mycorrhiza (AM and Ectomycorrhizae (EM) in revegetation program at Nukui Dam".

In the experiment layout, there were different plots receiving different kinds of soil amendments. In this study, therefore, we summarized annual reports of that project and the evaluation after revegetation, especially through the viewpoint of the changes in soil properties. Additionally, we analysed the effect of AM fungi inoculation as a surplus on the various effects of the soil amendments after revegetation at Nukui Dam in order to clarify the relationship between AM establishment and soil properties with different soil amendments at Nukui Dam.

2. Materials and methods

2.1. Description of the study site

The Nukui Dam is the second highest arch dam in Japan. It is located across a narrow section of the Takiyama river in the Hiroshima Prefecture and has hillside slopes and banks ranging from 45 to 60° with a riverbed width ranging from approximately 40 to 60 m.

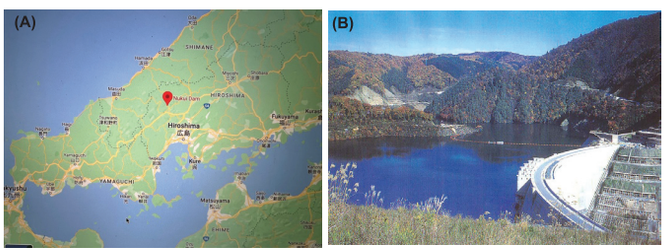

Fig. 1. (A) Location of Nukui Dam site on the map; (B) View of Nukui Dam. Red arrow indicates the study site on berm N°10.

The region extends from 34°36.6'' N latitude to 132°19.2'' E and from 270 to 386 m altitude with a catchment area of 1,700 km^2. The annual precipitation is approximately 2000 mm and the average annual temperature is roughly 13°C (cited from "Current activities on Dams in Japan, Japan commission on large dams, 2003").

The study site was berm N°10 - a part of the planting area at Nukui Dam, which was executed for a revegetation process in May 1998 (Fig. 1). The total area of this berm was 40.5 m^2 and was divided into 8 plots, each with an area of 3.0x1.5 m. Each plot was divided by plywood with a thickness of 2 cm.

The field sampling was carried out in September because the AM fungi spore populations are, in general, the greatest in the autumn in areas where there are marked warm/cold seasons [8, 9].

2.2. Revegetation program

Construction of the Nukui Dam began in July 1992. The dam's concrete placing commenced in May 1994, and the work was completed in December 1998. Regarding the preservation of the natural environment around the dam site, the research project of revegetation at Nukui Dam was done via cooperation between the dam construction office and Yamaguchi and Hiroshima Universities, Japan. The study on the N°10 berm started in 1998. Each plot (3x1.5 m) was filled with Masa soil (granite) with amendments shown in Table 1. Five seedlings of three tree species: Yamazakura (*P. jamasakura* Sieb. ex Koidz), Arakahi (*Quercus glauca* Thunb.), and Konara (*Quercus serrata* Thunb. Ex Muuray) were transplanted to every plot.

Table 1. Soil amendment in experimental plots in the N°10 berm at Nukui Dam site.

	Treatment							
	10-1	*10-2*	*10-3*	*10-4*	*10-5*	*10-6*	*10-7*	*10-8*
Masa soil (%)	60	54	60	54	59	35	60	54
Crushed sand (%)	24	23	24	23	20	20	24	23
Bark compost (%)	11		11		11		11	
Wheat straw compost (%)	5	10	5	10	10	15	5	10
Vermiculite (%)		5		5		15		5
Zeolite (%)		6		6		10		6
Bamboo charcoal (%)		2		2		5		2
Mycorrhizae fungi	+	+			+	+		
Fertilizer* (g.m^{-2})		90		90		90		90
Bonding agent (kg.m^{-3})								1.5

Fertilizer*: Green Map II (Sun Green Co. Ltd., Japan), N:P:K:Mg = 6:38:6:18.

Inoculation of AM fungi was carried out by mixing 15 g of an AM fungi spore-containing material, a Cerakinkong product (a commercial inoculum, Central Glass Co. Ltd, Tokyo) with soil around Yamazakura roots at transplanting in order to promote early rooting and initial growth of planted vegetation. The material contains at least spores of *Gigaspora margarita* Becker and Hall and *Glomus* sp. (ca. 2000 spores 100g^{-1}).

2.3. Soil and plant sampling

Soil was sampled along 8 plots of the N°10 berm, each with 5 cores (5x5x10 cm, each about 250 g in fresh weight) and composite giving pooled topsoil samples per plot. The soil samples were passed through a 2-mm sieve and then cautiously mixed before sub-sampling ca. 500 g of soil in every plot for physical, chemical, and biological analyses. A 100-g sub-sample of each plot was stored at 4°C for microflora analysis.

Additionally, randomly selected plants (containing rhizosphere and root zone soil) were gathered from 3 cores of each plot (3 plants/plot, separate for each plant) in order to estimate AM association and detect the survival of AM inoculated to the host plants with 3 replications. Three host plants were chosen for sampling: Japanese hill cherry (*P. jamasakura* Sieb. ex Koidz, Yamazakura-inoculated plant), Eulalia (*M. sinensis* Ander, Susuki), and Mugwort (*A. princes* Pampan, Yomogi). Susuki and Yomogi are popular herbaceous plants in Japan and were sampled to check the net amount of arbuscular mycorrhizae established from the inoculated plant. The hair roots were taken for Yamazakura because it is wood plant. After obtaining the root zone soil, the roots were washed gently under tap water to remove the adhering rhizosphere soil.

2.4. Quantification of the spore and AM colonization

The entire amount of rhizosphere and root zone soil from 3 plants of each species was processed to extract the spores, i.e., extramatricular chlamydospores, using the modified method of wet-sieving and decanting [10]. The rhizosphere soil amounted to about 500 g/plant.

Spores were counted under a dissecting microscope (Nikon) and collected individually using a pipette with a finely extruded tip and fine forceps and separated into different groups based on their morphology, colour, and type of hyphal attachment. After collecting, spores were sterilised by 2% Chloramine-T with 1200 mg/l streptomycin and stored at 4°C for further study.

The roots were cleared and stained by the modified method of P.P. Kormanik, et al. (1982) [11]. The stained roots were estimated by a magnified intersection method [12], where roots are observed at 200x magnification. Each type of arbuscules, vesicles, or hyphae were quantified separately. For quantification and observation of AM structures inside the root, the glass slide method was used and root samples were mounted in lacto-glycerol solution on microscope slides. They were then observed under a compound microscope (Nikon) at 100-400x magnifications. After measuring the root length, 100 random root segments per sample were observed. To obtain an estimate of intensity, a morphometric technique [13] could be used where a grid of dots was placed over an image of squashed roots and colonized cortical cells were counted.

After examining roots for the presence or absence of AM mycorrhizal structures, the number of root segments colonised was counted and expressed as a percentage of total root segments in the sample. The frequency of arbuscules, vesicles, spores, auxiliary cells, and external and internal hyphae connected to arbuscules at each observed cross section was estimated. The AM infection was calculated as follows:

$$\text{Percentage of AM colonization } (\%) = \frac{\text{AM root length}}{\text{root length total}} x\ 100$$

$$\text{AM structure } (\%) = \frac{\text{AM structure}}{\text{AM root length}} x\ 100$$

2.5. Soil analysis

The soil's chemical, physical, and microbiological properties were determined according to general methods [14].

2.6. Statistical analyses

Results were tested with STATISTICA (1998) by the analysis of variance (Microsoft Office 98). Means and standard deviations (StDev) were produced in Microsoft Excel (Windows 97). Correlation within and between the soil parameters and the AM fungi data were initially determined by performing linear regressions in Microsoft Excel (Windows 97). A single ANOVA analysis was simultaneously carried out to prove the validity of the regression [15]. In one indicated case, the least significant difference (LSD) test was applied to reveal tendencies.

3. Results

3.1. Soil properties and microflora

At the beginning of the experiment, the soil amendments to every plot in berm 10 were recorded and are provided in Table 1. Soil amendments were different at every plot to test the different raw materials in Japan and their effect in Arbuscular mycorrhizae symbiosis.

According to the annual reports of the project, the changes in soil properties, growth of the seedlings, and invasion of naturally occurring plants from 1998 and in this study were summarized and are provided in Table 2.

Table 2. The soil properties at start of revegetation execution.

Parameter	Inoculated treatment (1,2,5,6 treatments)	Non-inoculated treatment (3,4,7,8 treatments)
Total carbon (%)	0.70-0.98	0.66-0.88
Total nitrogen (%)	0.034-0.043	0.028-0.042
Available P (µg P.g^{-1})	2.2-15.2	0.1-1.8
CEC (mol.kg^{-1})	5.1-10.1	4.2-11.6
Exchange Mg (cmol.kg^{-1})	0.7-0.83	0.59-0.88
Exchange K (cmol.kg^{-1})	0.06-0.82	0.01-0.80
Exchange Ca (cmol.kg^{-1})	2.77-3.98	2.37-4.40
Exchange (cmol.kg^{-1})	0.07-0.10	0.06-0.11
pH_{H_2O}	6.81-7.53	7.05-7.83
pH_{KCl}	5.93-6.00	5.93-6.14
Biomass C (µg C.g^{-1})	29.5-81.0	22.7-86.8
Biomass N (µg N.g^{-1})	5.6-14.4	4.6-18.7

Ranges of the soil's chemical properties at the start of the experiment are shown in Table 2 in combination with those determined in the present study. These were strongly affected by the composition of soil amendments and fluctuated annually. We were unable to find any evidence that AM inoculation affected soil properties and their fluctuation.

There was slightly increasing carbon content and microflora in every plot compared with the preliminary data from the team at Hiroshima University during the first revegetation project at Nukui Dam (data not shown). The fact that the total nitrogen was currently highest compared to the preliminary data and that the phosphate and exchangeable cations improved with time confirmed the increasing nutrient content after carrying out revegetation at Nukui. In both undisturbed and cultivable systems, potential productivity is directly related to soil organic matter concentration and turnover [16].

In general, mycorrhizal associations can also enhance N grain in ecosystems by increasing N-fixing associations [2, 17-19]. The overview of these changes suggests that soil properties in the experiment have improved over time and with vegetation development. Although we could not find a statistical difference in soil properties because of the remaining effect of soil amendments at start, a tendency for nutrient enrichment was slightly promoted in the inoculated plots.

Among the three wood species, Yamazakura markedly survived and grew such that the GoH value (an index of wood biomass, where Go and H mean a diameter at a soil surface or height in cm, respectively) of Yamazakura reached more than 70 to 90% of the total GoH of three species (data not shown). There was a large difference in the total GoH value among AM-inoculated plots (for example, 8.76 for the 10-1 treatment and 1.89 for 10-5 treatment), which suggests that AM-inoculation would positively affect the survival of Yamazakura but would be inefficient for their growth.

The number of plant species that invaded naturally and became established in the experimental plots was 33. The susuki (*M. sinensis* Ander.) and mugwort (*A. princes* Pampan.), popular Japanese weeds, were predominated in field.

Coverage of the soil surface was more than 80% and sometimes reached nearly 100% in summer regardless of the soil amendment type.

The soil properties of each plot at sampling were according to inoculation and non-inoculation treatment. The values of pH_{H2O}, maximum water holding capacity, and bulk density were similar in both inoculated and non-inoculated treatments. However, two plots gave an EC value significantly higher than other, namely, the 10-3 and 10-7 plots (Table 3), and those plots had the same soil components (Table 1). The total carbon and nitrogen content and exchange cations in inoculated plots were slightly higher than those in non-inoculated plots, but the differences were insignificant statistically.

Table 3. The physical and chemical properties and microflora of soil at the Nukui Dam.

Parameter	pH		EC	MWHC	Bulk density		Total C
	H_2O	KCl	(µS.cm^{-1})	(g.100g^{-1})	(g.100g^{-1})	(g.100ml^{-1})	%
Treatment					*Crude*	*Fine*	
Non-inoculation	5.53±0.38	4.31±0.28	108.95±53.16	33.47±3.85	102.63±3.02	159.81±3.09	1.03±0.32
Inoculation	6.03±0.59	4.73±0.16	72.25±8.13	35.12±1.84	95.83±11.25	153.48±9.31	1.16±0.29

Parameter	Total N (%)	Available P	Ca	K	Mg	Na	Fungi	Bacteria
		(cmol.kg^{-1})					($x10^6$)	($x10^6$)
Treatment							CFU.g^{-1}	
Non-inoculation	0.06±0.029	0.35±0.09	4.33±0.38	0.68±0.25	0.91±1.12	0.74±0.69	4.31±2.67	5.61±4.03
Inoculation	0.08±0.022	0.36±0.13	4.52±1.29	0.85±0.23	1.61±1.57	0.55±0.38	5.06±2.56	6.35±5.11

There was a slightly higher number of fungi and bacteria in the inoculated than in the non-inoculated treatments (Table 3), but not a significant difference in the experimental treatments (StDev, ANOVA). The

fungi quantity ranged from 4.31±2.67 to 5.06±2.56x10^4 CFU.g-^{1} in dry soil. The highest bacteria number was obtained at the 10-1 plot-inoculated treatment and the lowest in the non-inoculated treatment.

3.2. Spore number in rhizosphere soil of plant roots

Spores picked up from the Yamazakura and Susuki rhizosphere soil (250 cm^3) in the inoculated plots were mainly obtained from the sieved size range of 106-210 µm or 210-500 µm. There was a significant increase in the number of spores in inoculated treatments at 5% confidence level (ANOVA, $p<0.05$) in Susuki and Yamazakura (Fig. 2A).

Inoculation of AM fungi promoted the occurrence of spores and colonization to plant roots. The obtained results showed that the AM colonization rate in inoculated plots was higher than in non-inoculated plots. In addition, the density of typical structures (arbuscule, vesicle, coil hyphae, auxiliary cell) of AM was also much larger in inoculated treatments compared with non-inoculated treatments. This is a well-known response that has been widely reported in the literature [20].

Apart from AM efficiency on vegetation development, the rate of inoculated AM fungi at start should be discussed. There were some spores of *Gigaspora* sp. Many more

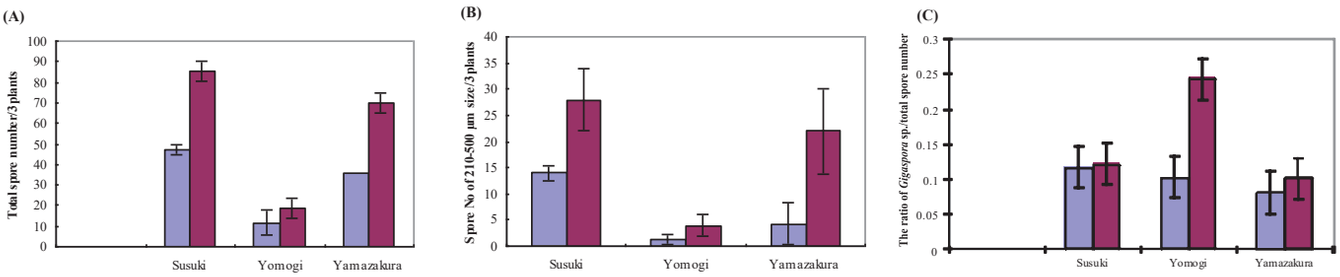

Fig. 2. (A) The total spore number in Rhizosphere soil; (B) Spore number in 210-500 µm sieved Rhizosphere soil; (C) The ratio of *Gigaspora* sp. to the total spore number. Legend: non-inoculated AM (■) and inoculated AM (■).

There was a 5.2 times difference in the number of spores of large size (>210 µm) between inoculated and non-inoculated treatments in Yamazakura. Clearly, plant hosts vary markedly in their ability to affect spore production by *Gigaspora* and *Glomus*. By observation of morphology and size of spores, the spores of *Gigaspora* sp. in inoculated plots were greater in number than in non-inoculated ones among all investigated plants (Fig. 2C).

In investigated plants, Yamazakura would receive the strongest benefits for their initial growth just after transplanting among three species. The primary effect of AM inoculation might be to hold AM-propagule levels higher in comparison to non-inoculated plots. This might help the establishment of invading weeds such as Susuki and Yomogi rather than Konera and Arakashi seedlings. The higher propagule level might support AM formation with Susuki (Fig. 2A) and Susuki could make abundant AM propagules in the next generation. This could result in AM activity in inoculated plots for long periods. The above advantages, however, do not show statistical differences among plant flora and biomass because the effect of soil amendment remains active.

Gigaspora sp. spores occurred in rhizosphere soil of Yamazakura and Susuki plant in inoculated plots than in non-inoculated plots (2.33 and 3.73 times, respectively). Further study is necessary to detect the inoculated strain, *Gigaspora margarita,* after revegetation process.

Although Yamazakura was an inoculated plant, the AM colonization was highest in Susuki. The reason might be that *Gigaspora* sp. had a greater effect on Susuki than other host plants, confirming the results of other workers in our laboratory.

3.3. The AM colonization in plant roots

In Yamazakura, high potential plots that showed a very high percentage of root infection were inoculated with treatments when ranges of infection were in the range of 72.16-84.0%. The minimum infection was found in non-inoculated treatment to be 38.33%. Moreover, the coiling hyphae of infection roots increased notably in inoculated treatments, twice higher compared to in non-inoculated ones. At the same time, there was a significant increase of arbuscules as well as vesicles and auxiliary cells in inoculated plots (Figs. 3A-E).

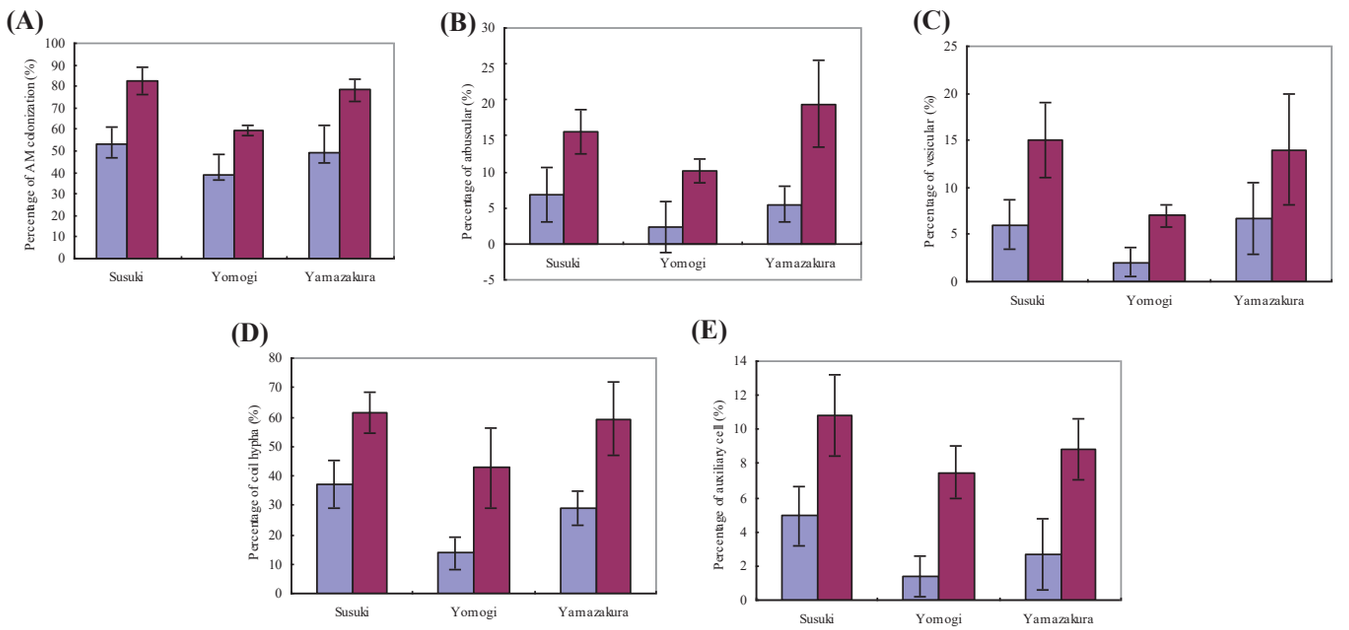

Fig. 3. AM colonization and structure in plant root. (A) Percentage of AM colonization (%); (B) Percentage of arbuscular; (C) Percentage of vesiclar; (D) Percentage of coil hypha; and (E) Percentage of auxiliary cells. Legend: Non-inoculated AM (■) and inoculated AM (■).

Similar results were obtained from Susuki roots on AM colonization. The AM colonization was high in both inoculated and non-inoculated treatments ranging from 47.06 to 88.18%. In inoculated plots, coil hyphae formed the main components of the AM colonisation. In non-inoculated treatments, a smaller proportion of infected root length (<10%) contained arbuscules, auxiliary cells, and vesicles. The AM colonization included infected root rate and AM structures in inoculated treatments given at higher frequencies than in non-inoculated ones (Figs. 3A-E).

A considerable proportion of root length (28.25-61.62%) was arbuscular mycorrhizae in infection rates of Yomogi roots with AM fungi. Colonization by AM fungi was highest in plot 10-6 with inoculated treatment. The level of colonisation in non-inoculated treatments was significantly lower than that of inoculated ones (ANOVA, $p<0.05$). There was a significant increase in typical AM structures in the inoculated treatments (Figs. 3A-E). On other hand, arbuscules, auxiliary cells, and vesicles were absent in some non-inoculated plots or very low in other ones.

The density of AM structures was increasing not only in arbuscules, coil hyphae, and auxiliary cells, but also in vesicles. Meanwhile, a did not form vesicles as part of its life cycle. The inoculum product, Cerakinkong, includes both *Gigaspora margarita* and *Glomus* sp. At the same time, the AM symbiosis of indigenous AM could strongly establish. Those AM strains might affect plant roots together.

Through observation of AM structures under a compound microscope, it was found that density of typical AM structures in inoculated treatments were higher than in non-inoculated ones. Indeed, there were many more arbuscules and auxiliary cells (Figs. 3B, E), which are typical structures of the Gigasporaceae family, in the roots of Yamazakura and Susuki plants in inoculated plots rather than in non-inoculated plots. The frequency of arbuscules and auxiliary cells were very low in inoculated plots. These findings suggest that there have been different kinds of host-AM fungi interaction and that Yamazakura - *G. margarita* containing material could be a better combination for the start of vegetation.

The spores of *Gigaspora* sp. in rhizosphere soil and arbuscules and auxiliary cells in roots formed much more often in inoculated plots than in non-inoculated plots at the Nukui Dam site. This indicates the possibility of survival and propagation of the inoculated AM fungi *G. margarita*. Regarding why AM inoculation enhances AM establishment even after several years, one hypothesis suggests that there is an interaction and competition among host plants. When pairs of plant species growth together with or without the addition of AM inoculum, the outcome of the interaction between them is known to be very different [21].

There was a linear correlation between spore numbers in rhizosphere soil and AM formation for each of the inoculated and non-inoculated plots (Fig. 4).

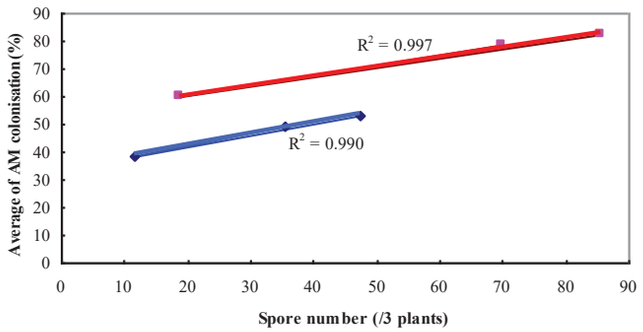

Fig. 4. The correlation between spore number and AM colonisation. Legend: (--■--) Non-inoculated AM; (--▲--) Inoculated AM.

The efficiency of AM fungi propagules to form symbiosis seemed to be higher in inoculated than non-inoculated plots. This, in turn, suggests the vegetation developed in inoculated plots depended on AM more strongly than those in non-inoculated plots.

4. Conclusions

Soil properties in the experiment have improved over time and with vegetation development and a tendency towards nutrient enrichment was slightly promoted in the AM-inoculated plots. Indeed, the coverage of the soil surface was more than 80% and sometimes reached nearly 100% in summer regardless of the soil amendment type.

There was a significant increase in the number of AM spores in inoculated treatments at 5% confidence level (ANOVA, $p<0.05$) in Susuki and Yamazakura. Many more spores of *Gigaspora* sp. occurred in rhizosphere soil of Yamazakura and Susuki plant in inoculated plots than in non-inoculated plots (2.33 and 3.73 times, respectively).

Inoculation of AM fungi promoted the occurrence of spores and colonization to plant roots. The spores of *Gigaspora* sp. in rhizosphere soil as well as arbuscules and auxiliary cells in root formed much more frequently in inoculated plots than in non-inoculated plots at the Nukui Dam site. This indicates the possibility of survival and propagation of inoculated the AM fungi *G. margarita*.

Clearly, AM inoculum improved the symbiosis between AM associations and plant communities and seems to be a key factor for revegetation success.

CRediT author statement

Minh Thi Nguyen: Analysis, Data curation, Writing - Original draft manuscript, Sampling; Kazuhira Yokoyama: Medothology, Software; Takuya Marumoto: Conceptualization, Sampling, Reviewing.

ACKNOWLEDGEMENTS

The authors would like to express their deep gratitude to the Nukui Dam Office supported this work for sampling assistance.

COMPETING INTERESTS

The authors declare that there is no conflict of interest regarding the publication of this article.

REFERENCES

[1] N.C. Johnson, J. Jansa (2017), "Mycorrhizas: At the interface of biological, soil, and earth sciences", *Mycorrhizal Mediation of Soil: Fertility, Structure, and Carbon Storage*, **1**, Elsevier, pp.501-509, DOI: 10.1016/C2015-0-01928-1.

[2] K.M. Rodrigues, B.F. Rodrigues (2014), "Arbuscular mycorrhizal (am) fungi and plant health", *Fungi in Biotechnology*, SIES College, 16pp.

[3] A. Bahadur, Z. Jin, X. Long, et al. (2019), "Arbuscular mycorrhizal fungi alter plant interspecific interaction under nitrogen fertilization", *European Journal of Soil Biology*, **93**, DOI: 10.1016/j.ejsobi.2019.103094.

[4] D.P. Janos (1980), "Mycorrhizae influence tropical succession", *Bio-Tropica*, **12(2)**, pp.56-64, DOI: 10.2307/2388157.

[5] R. Singh, N. Sharma (2019), "Application of arbuscular mycorrhizae in soil management", *Microbial Interventions in Agriculture and Environment*, Springer, DOI: 10.1007/978-981-32-9084-6_4.

[6] D.A. Jasper (1994), "Management of mycorrhizas in revegetation", *Management of Mycorrhizas in Agriculture, Horticulture and Forestry*, Kluwer Academic Publishers, Dordrecht, Netherlands, 9pp.

[7] K. Marumoto, O. Hiroaki, E. Tsugio, et al. (1996), "Application of symbiotic microorganisms to soil conservation and reforestation", *BioJapan '96 Symposium Proceedings*, pp.242-250.

[8] D.D. Douds, W.R. Chaney (1982), "Correlation of fungal morphology and development to host growth in a green ashmycorrhiza", *New Phytol.*, **92(4)**, pp.519-526, DOI: 10.1111/j.1469-8137.1982.tb03410.x.

[9] J.N. Klironomos, P. Moutoglis, B. Kendrick, et al. (1993), "A comparison of spatial heterogeneity of vesicular- arbuscular mycorrhizal fungi in two maple-forest soils", *Can. J. Bot.*, **71**, pp.1472-1480, DOI: 10.1139/b93-178.

[10] J.W. Gerdeman, T.H. Nicolson (1963), "Spores of mycorrhizal Endogone species extracted from soil by wet-sieving and decanting", *Trans. Br. Mycol. Soc.*, **46(2)**, pp.235-244, DOI: 10.1016/S0007-1536(63)80079-0.

[11] P.P. Kormanik, A.C. McGraw (1982), "Quantification of vesicular arbuscular mycorrhizae in plant roots", *Method and Principles of Mycorrhizal Research*, American Phytopathological Society, pp.37-45.

[12] T.P. McGonigle, M.H. Miller, D.G. Evans, et al. (1990), "A new method which gives an objective measure of colonization of roots by vesicular-arbuscular mycorrhizal fungi", *New Phytol.*, **115(3)**, pp.495-501, DOI: 10.1111/j.1469-8137.1990.tb00476.x.

[13] R. Toth, D. Toth (1982), "Quantifying vesicular-arbuscular mycorrhizae using a morphometric technique", *Mycologia*, **74**, pp.182-187, DOI: 10.1080/00275514.1982.12021490.

[14] D.L. Sparks, A.L. Page, P.A. Helmke (1996), "Chemical methods", *Methods of Soil Analysis*, Soil Science Society of America, Inc., USA, 1309pp.

[15] J.H. Zar (1984), *Biostatistical Analysis*, 2nd Edition, Prentice-Hall, Inc., Englewood Cliffs, 718pp.

[16] F.B. Reeves, E.F. Redente (1991), "Importance of mutualism in succession", *Semiarid Lands and Deserts: Soil Resource and Reclamation*, Marcel Dekker, New York, pp.193-217.

[17] A. Varma (1979), "Vesicular-arbuscular mycorrhiza and nodulation in soybean", *Folia Microbiol.*, **24**, pp.501-503, DOI: 10.1007/BF02927183.

[18] K. Singh, A. Varma (1988a), "Mycorrhizal fungi stimulate legume growth and root nodulation in dry arid soils. I. Effect of dual infection of Rhizobium and VAM endomycorrhizal spores on tropical legume Bengal gram (*Cicer arietinum*)", *Proc. Mycorrhizal Worksh.*, Quebec, Canada, pp.356-371.

[19] K. Singh, A. Varma (1988b), "Mycorrhizal fungi stimulate legume growth and root nodulation in dry arid soils. II. Effect of dual infection of Rhizobium and VAM endomycorrhizal spores on soybean (*Glycine Max Merril*)", *Proc. Mycorrhizal Worksh.*, Quebec, Canada, pp.372-392.

[20] M.J. Daft, T.H. Nicolson (1969), "Effect of Endogone mycorrhiza on plant growt. II. Influence of soluble phosphate on endophyte and host in maize", *New Phytol.*, **68(4)**, pp.575-578, DOI: 10.1111/j.1469-8137.1969.tb06494.x.

[21] R. Francis, D.J. Read (1994), "The contributions of mycorrhizal fungi to the determination of plant community structure", *Management of Mycorrhizas in Agriculture, Horticulture, and Forestry*, Kluwer Academic Publishers, Netherlands, 14pp.

DOI: 10.31276/VJSTE.65(1).54-62

Selection index for Duroc pigs based on average daily gain, feed conversion ratio, and intramuscular fat content

Sang Van Le*

University of New England, Armidale, New South Wales, Australia

Received 10 March 2022; revised 9 May 2022; accepted 24 May 2022

Abstract:

This study was conducted to compare the genetic gain per sow per year of Duroc pigs in twelve scenarios. These scenarios were based on the number of traits used such as average daily gain (ADG), feed conversion ratio (FCR), intramuscular fat content (IMF) and were also based on the number of records of phenotype for these traits from the individual animal and its relatives. The values of all relevant genetic and economic parameters were selected from the literature and applied to the multiple trait (MT) index model to calculate the index selection accuracy and response per trait. The results showed that the economic value of FCR was much larger than the economic value of ADG and IMF. The selection response in units of ADG was higher when using phenotypes measured using ADG and FCR only while selection response per unit of IMF was the opposite. The economic weight of the response for IMF using three traits (ADG, FCR, and IMF) information was doubled when using ADG and FCR trait information. The standard deviation (SD) index and genetic gain per year when using information from the three traits were higher than those when using information from ADG and FCR. Within the same number of traits measured, the genetic gain per sow per year was highest at $568.05 when using information of the three traits from the individual animal's phenotype and their progeny. It was the lowest at $473.06 when using ADG and FCR information from only the animal itself.

Keywords: **average daily gain, Duroc pig, feed conversion ratio, intramuscular fat, selection index.**

Classification numbers: **3.1, 3.4**

1. Introduction

The pig industry is one of the main livestock in Vietnam with the world's fifth largest pig inventory and its pork production being the sixth highest on a global scale [1]. According to the General Statistics Office of Vietnam, in January 2021, there were 22,028 million pigs raised in Vietnam that produced 4,036 tons of meat [2]. Pig production accounted for 60% of total livestock output in Vietnam's economy [3]. It is a source of livelihood for approximately three million households of which 77% were smallholders [4]. Also, pork is the most important types of meat produced and consumed in Vietnam, representing 70% of total meat output.

Over the last two decades, Vietnamese pig breeders have focused on efficient lean meat production in pig-intensive systems [5]. As a result, current pig genetic types deposit less fat and are much leaner at market weight than traditional breeds. Because the genetic correlation between IMF and lean content is negative, the selection for increased lean efficiency has led to a decrease in IMF to levels below what is recommended. A.G.D. Vries, et al. (1994) [6] reported that when selection increases by 1% in lean meat, it would lead to a decrease of 0.07% in IMF. A study of L.P. Dai (2017) [7] indicated that IMF of pure breeds, hybrid breeds, local pig breeds, and exotics breeds in Vietnam were low. Pietrain breeds had the lowest IMF with 1.48%, followed by the Mong Cai breed (1.87%), Landrace (2.20%), Yorkshire (2.21%), and Duroc (2.98%). The IMF of commercial pig breeds in Vietnam ranged from 2.04 to 3.05% depending on the parenting breeds and the slaughter weights [7]. Those values of IMF of pig breeds in Vietnam were very low in comparison with other IMFs of other pigs on a global scale. In Europe, breeders select pork with greater than 3% of IMF [8-9] and in the United States, IMF in pork ranges from 3 to 4% [10]. In China, Japan, and South Korea, consumers require the IMF of pork to be greater than 5% [11]. Therefore, this prompted Vietnamese pig breeders to consider IMF as a breeding objective trait in their breeding program. In the pig breeding program, breeders also focus on increasing the lean growth rate,

*Email: lesang86@gmail.com or vle4@myune.edu.au

pork marbling, and reducing the FCR [12]. In other words, breeders try to address the question of how to simultaneously improve lean growth efficiency, IMF, and reduce FCR. To answer this question, the selection index for multiple traits is applied.

The breeding objective traits are ADG, FCR, and IMF. ADG is the average weight a pig gains in a day. ADG is one of the most important traits in production. ADG depends on the feed regimes and increases with an increase in energy intake and metabolizable energy intake. K.G. Santiago, et al. (2021) [13] found a high correlation, 0.8, between feed intake and ADG. FCR is a ratio of the efficiency with which the bodies of animals convert feed into the desired output. IMF is the amount of fat located throughout skeletal muscles. It is a major quality trait of meat affecting sensory attributes such as flavour and texture. IMF is directly related to the juiciness and tenderness of meat [14]. Pork with higher IMF tends to have better flavour, juiciness, and tenderness, resulting in higher overall acceptability [15].

In the early stage of breeding, breeders intentionally selected animals mainly based on the individual animal's phenotype performance to achieve a genetic gain for target traits [16]. After the best linear unbiased prediction was proposed by Henderson [17], breeders also used phenotypic and pedigree information of full/half-siblings, offspring, and relatives to select potential animals [18]. The covariance among full/half-siblings is assumed to be proportional to the pedigree relationship, but the relative may be further correlated because they share a common environment [19]. The information from the offspring was valuable due to it reflecting the true value of breeding value from their parents in a certain environment. However, recording phenotypic data from offspring was time consuming and cost intensive because evaluating offspring phenotypes was often expensive, and phenotyping can be only done when the offspring grow up [16]. Therefore, in the selection index, the breeders could consider different sources of information.

The objective of this study was to evaluate the genetic gain of Duroc pigs in twelve scenarios based on the three traits (ADG, IMF, and FCR) from different sources of information (individual animal's information or including its siblings, relatives, and offspring).

2. Materials and methods

2.1. Economic value

The breeding objective included ADG, FCR, and IMF. The mean and SD of these traits from literature review were summarized in Table 1. These studies were conducted in Duroc breeds. The average of ADG, FCR, and IMF were 919.68 (g/d), 2.69 (kg), and 3.23 (%). The average SDs of these traits were 121.43 (g/d), 0.29 (kg), and 1.45 (%), respectively.

Table 1. The mean and phenotypic SD of the three traits.

Authors	ADG (g/d)		FCR (kg)		IMF (%)	
	Mean	*SD*	*Mean*	*SD*	*Mean*	*SD*
Y. Ramayo-Caldas, et al. (2019) [12]	890	110	3.16	0.31	5.23	2.06
L. Tusell, et al. (2016) [20]	938.5		2.29		1.14	
Y. Miar, et al. (2014) [21]	976.6	145	2.64	0.3	1.26	0.83
K. Suzuki, et al. (2005) [22]	873.6	109.3	2.65	0.27	4.25	1.46
Average	919.68	121.43	2.69	0.29	3.23	1.45

To calculate the economic value for ADG, FCR, and IMF traits, we modelled a production system and also used the parameter values for the production system as summarized in Table 2. D.D. Luc, et al. (2013) [23] reported that the number of Duroc pigs born alive was 9.0 piglet/litter. A recent study on reproductive traits of Duroc pig noted that the number born alive of this breed was 9.39 piglets/litter [24]. These studies on Duroc pigs were conducted in Vietnam. The Duroc pigs were fed with premixed pig food and raised on intensive farms in a closed house with tunnel ventilation. In this case study, we selected a value for the number of Duroc pigs born alive (NBA) to be 9.2 piglets. Days to slaughter (DS) is the age of a pig from birth to slaughter and it was 185 days. The sow index is the number of litters per sow per year. The sow index of the Duroc breed was much lower than Landrace and Yorkshire breeds [13]. In this study, we selected the sow index of the Duroc breed from the T.H. Son, et al. (2019) [24] study, which was 2.1.

Table 2. The constant values and prices for the production model.

Constants	
Number born alive (pig)	9.2
Days to slaughter (day)	185
Average daily feed intake (kg)	1.46
Survival rate from birth to slaughter (%)	85
SD of IMF (%)	1.45
Threshold of price for IMF (%)	3.5
Sow index (litter/sow/year)	2.1
Prices	
Pork price per kg when its IMF <=3.5% ($AUD)	4.38
Pork price per kg when its IMF >3.5% ($AUD)	4.06
Feed cost per kg ($AUD)	1.42
Annual cost per sow ($AUD)	40.00
Proportion below threshold (3.5%)	0.57

The principle of calculation of the profit: income = total profit - total cost. Firstly, we calculated the profit per pork and then calculate the profit/sow/year. The cost and benefit per pig and per sow per year were calculated in Excel version 2019. The income per pig is calculated as:

Income per pig = profit/pork - cost/pork

where profit per pork = body weight (BW) at slaughter x price/kg. The BW was calculated based on the ADG, FCR, DS, and average daily feed intake (ADFI). The price of pork depended on the proportion of IMF in the BW. This proportion could be different based on the actual value of IMF, which can be measured by the population. In this simulation, we used the NORMDIST function in Excel 2016 to calculate the proportion of IMF in a population and this proportion of IMF below the threshold was 0.57. It meant that in this population, 57% of Duroc pigs had an IMF equal to or lower than 3.5% and these pigs would be sold for $4.06 AUD/kg. The rest of the population, 43%, had an IMF greater than 3.5% and were sold at $4.38 AUD/kg.

The following equation:

Cost per pork = DS x ADFI x feed cost per kg

was based on the cost of the feed. Other costs such as housing, electricity, vaccines, and labour would be added to the annual cost per sow per year and in this case, it was assumed to be $40. Therefore, the equation of total income becomes:

Total net income per sow per year = income per pork x NBA x sow index x survival rate from birth to slaughter - annual cost per sow.

The economic values of three traits (ADG, FCR, and IMF) were calculated in the production model in the MTindex program of van der Werf (http://www.personal.une.au/~jvanderw). In the production model, the mean of those traits in Table 1 and constant values and prices in Table 2 were used to calculate the economic value. The economic value for a trait is defined as the change in profit as that trait was an increase of one unit while all other traits were unchanged.

2.2. Heritability

The heritability of ADG, FCR, and IFM traits for Duroc pigs were selected from the literature review and are summarized in Table 3. The heritability for those traits varies from the studies. The average heritability for ADG was 0.33, and it varied from 0.15 to 0.43. The average heritability of FCR and IMF were 0.19 and 0.34, respectively. The heritability for ADG and IMF were moderate while the heritability for FCR was low.

Table 3. Heritability of ADG, FCR, and IFM for Duroc pigs.

Authors	ADG	FCR	IMF
M. Alam, et al. (2021) [25]	0.36		
H.E. Willson, et al. (2020) [26]	0.33		
O.F. Christensen, et al. (2019) [27]	0.15	0.1	
Y. Miar, et al. (2014) [21]	0.3	0.2	0.26
K. Suzuki, et al. (2005) [22]	0.47		0.39
X. Fernandez, et al. (1999) [15]	0.43		0.38
S. Hermesch 1996 [28]	0.27	0.26	
Average	**0.33**	**0.19**	**0.34**

Index calculations were performed using the MTindex program of van der Werf (http://www.personal.une.au/~jvanderw). The component for MTindex was described in Table 4.

Table 4. The parameters needed for MTindex for ADG, FCR, and IMF.

Trait	Name	Units	Phenotypic SD	Heritability	Economic value
1	ADG	g/d	121.43	0.33	7.49
2	FCR	kg	0.29	0.19	-1866.73
3	IMF	%	1.45	0.34	136.74

There are phenotypic and genetic correlations between traits, which can be a positive or negative correlation. Phenotypic correlation is a term that indicates an association between animals with high values of one trait to those that have high or low values for other traits. An association between two traits can be caused by a gene that affects both traits simultaneously and is called a genetic correlation. These correlations are very important to animal breeders. The genetic correlation between traits is presented in Table 5.

Table 5. Phenotypic and genetic correlation between ADG, FCR, and IMF.

	Phenotypic correlation		Genetic correlation	
	FCR	*IMF*	*FCR*	*IMF*
ADG				
Y. Ramayo-Caldas, et al. (2019) [12]	-0.276	0.205	-0.261	0.402
Y. Miar, et al. (2014) [21]	0.31	0.32	-0.19	0.69
M. Bergamaschi, et al. (2020) [29]			-0.21	0.24
K. Suzuki, et al. (2005) [22]		0.06		0.25
X. Fernandez, et al. (1999) [15]				-0.19
S. Hermesch (1996) [28]			-0.2	
Average	**0.017**	**0.195**	**-0.215**	**0.278**
FCR				
Y. Ramayo-Caldas, et al. (2019) [12]		0.138		0.162
M. Bergamaschi, et al. (2020) [29]				-0.14
K. Suzuki, et al. (2005) [22]				0.21
Average		**0.138**		**0.077**

The average phenotypic correlation between ADG with FCR was 0.017. This correlation was negative in the study of Y. Ramayo-Caldas, et al. (2019) [12], but it was strongly positive in the study of Y. Miar, et al. (2014) [21]. The average phenotypic correlation between ADG and IMF was 0.195 and the phenotypic correlation between FCR and IMF was 0.138. The average genetic correlation values were positive between IMF with ADG (0.278) and FCR (0.077). The genetic correlation between ADG and FCR was negative in all studies with an average value of -0.215.

2.3. Selection intensity

It was assumed that the genetic gain was measured for a nucleus farm with 400 Duroc sows. The survival rate and NBA were based on Table 2. The mating ratio was one boar to twenty sows.

The number of piglets per litter for this farm was 400x9.2x0.85=3128 pigs. Assume that the sex ratio was 1:1. Then, the number of weaned males and females was 1564 (pig).

The proportion of males (need 39.1 boars per year, rounding down to 39 boars) was determined as 39/1564x100%=2.49% => i_m=1.96.

The proportion of females (need 50%) was calculated as 170/1564x100%=10.87% => i_f=1.254.

2.4. General interval

Assume that boars are used for the first time at age 13 months, then L_m=13/12=1.083.

The first litter of sows occurred at the age of 18 months, then L_f=18/12=1.5.

2.5. The genetic gain

$$R = \frac{i_m + i_f}{L_m + L_f} \text{ x } {}^{\delta}i = \frac{1.96 + 1.254}{1.083 + 1.5} \text{ x } {}^{\delta}i = 1.244 \text{ x } {}^{\delta}i$$

2.6. The scenarios

Twelve scenarios were based on the number of traits measured and the number of records from different sources. The IMF was a trait that was hard to measure, and it was only measured late in the lifespan (at the slaughter time or on the carcass). Scenarios 1, 3, 5, 7, 9, and 11 were based on two traits measured, which were ADG and FCR. The other scenarios were based on the three traits measured. Scenarios 1 and 2 were based on the individual animal's records. In Scenarios 3 through 12, we used information from the breeders' individual animal records combined with other information resources, which are described in Table 6.

Table 6. Twelve scenarios based on the traits measured and the information sources.

Scenarios	Trait measured	Number of records				
		Indiv.	*Sire*	*Full sibs.*	*Half sibs.*	*Progeny*
1	ADG + FCR	1				
2	ADG + FCR + IMF	1				
3	ADG + FCR	1	1			
4	ADG + FCR + IMF	1	1			
5	ADG + FCR	1		4		
6	ADG + FCR + IMF	1		4		
7	ADG + FCR	1			40	
8	ADG + FCR + IMF	1			40	
9	ADG + FCR	1				4
10	ADG + FCR + IMF	1				4
11	ADG + FCR	1	1	1	1	1
12	ADG + FCR + IMF	1	1	1	1	1

Based on the NBA and the survival rate in Table 2, we assumed that 50% of the animals, which was 4, were tested. Therefore, the number of animals that were used in Scenarios 5, 6, 9, and 10 was 4. In Scenarios 7 and 8, we used 40 half-siblings.

3. Results and discussion

3.1. The economic value

The economic value of this study is presented in Table 7.

Table 7. The economic value achievement per sow per year when increased one unit by selection.

Traits	Units	Economic value ($)
ADG	g/d	7.49
FCR	kg	-1866.73
IMF	%	136.74

There was a difference in economic value for each trait when increasing one unit of the selection. The highest economic value was found in the IMF trait after an increase of 1%, reaching $136.74. The economic value of ADG trait was $7.49. The FCR had the lowest economic value, at minus $1866.73.

The economic values of FCR were dominant in the other traits in this study. An increase of 1 unit of FCR was equal to an increase of 37.2% of the mean FCR. This trait is the average kg of feed per weight. In addition, the cost of the feed made up to 70% of the profit. Therefore, increasing 1 unit of FCR in the selection led to a big weight of economic value for this trait. Meanwhile, increasing 1

unit of ADG accounted for only a 0.1% raise of the mean of this trait. This means that an increase of 1 unit in ADG trait did not significantly change the economic value in comparison with the FCR trait. The IMF trait was only influencing the price of the pork at slaughter.

The three traits ADG, FCR, and IMF have been proposed as a selection index in Thuy Phuong Pig Research and Development Centre (Ha Noi, Vietnam) for the Duroc breed. This breed was mainly used as the terminal sire [22]. The breed had a high growth rate, but the FCR index was high in comparison with the Landrace and Yorkshire breeds. These three traits have a high economic value that is directly related to feed cost and profit. The FCR trait affected the total feed that a pig consumed during its lifespan. The higher the value of FCR, the higher the cost of feed. The IMF was a direct measurement of the lean meat content. Pork with higher IMF tends to have better flavour, juiciness, and tenderness, resulting in higher overall acceptability [27]. Therefore, the most sensible step to start this research was to examine the changes in response if the newly derived economic values were placed in this index. The results demonstrated that the economic value of FCR was dominant in ADG and IFM.

3.2. Response to selection per unit

The selection response per unit of the three traits ADG, FCR, and IMF in different scenarios are described in Table 8.

Table 8. The selection response per unit of ADG, FCR, and IMF in twelve scenarios.

Scenarios	ADG (g/d)	FCR (kg)	IMF (%)
1	39.57	-0.04	0.11
2	39.47	-0.04	0.23
3	41.62	-0.04	0.12
4	41.47	-0.04	0.24
5	44.98	-0.04	0.13
6	44.7	-0.04	0.25
7	44.13	-0.04	0.12
8	43.84	-0.04	0.24
9	46.17	-0.04	0.13
10	45.88	-0.04	0.25
11	69.12	-0.04	0.13
12	45.83	-0.04	0.25

In the twelve scenarios, the selection response per unit was different in ADG and IMF traits while the selection response per unit of FCR was unchanged. The selection response per unit of ADG was the lowest in Scenario 2 where selection response was measured based on information of individual animal's phenotype of ADG, FCR, and IMF. The highest value of selection response per unit of ADG was found in Scenario 11, where the selection response was measured for ADG and FCR based on all sources of information. Meanwhile, the selection response per unit of IMF ranged from 0.11 to 0.25. However, in twelve scenarios, the selection response per unit of FCR was unchanged whereas this selection response was measured based on the phenotype from individual animal's records or from the relative record of two traits (ADG, and FCR) or calculated based on three traits (ADG, FCR, and IMF). The value of selection response per unit of FCR was -0.04. In the breeding program, the target of the producers was increasing ADG and IMF, while decreasing the FCR.

Within the same source of information, the selection response per unit of ADG based on two traits (ADG and FCR) was higher than this index when it was calculated based on information of three traits (ADG, FCR, and IMF). For example, the selection response per unit of ADG using information from two traits in Scenario 5 was 0.28 (g/d) higher than this response in Scenario 6. The difference in selection response per unit of ADG traits based on two traits went from 0.1 to 23.29 g/d, higher than this selection response based on three traits. In contrast, the selection response per unit of IMF trait was higher when the phenotype of IMF recordings was used. On average, the selection response per unit of IMF when using phenotype measured of three traits (ADG, FCR, and IMF) in different information sources was 0.12% higher than those only based on two traits (ADG and FCR). In the same number of records, the selection response per unit of ADG was higher when using phenotypes measured from ADG and FCR while the selection response per unit of IMF was better when IMF was used in the MTindex model.

When using the trait measure ADG and FCR, the selection response per unit of ADG was different depending on the information source. The selection response per unit of ADG was the lowest (39.57 g/d) in Scenario 1 when using only the phenotype of the animal and it was the highest in Scenario 11 (69.12 g/d) when using information from all relatives such as sire, full-sibling, half-sibling, and progeny. Within the same number of records (5 records), the selection response per unit of ADG using just the animal and all relatives (Scenario 11) was higher than this response using the information of itself and from progeny (Scenario 9). The selection response per unit of ADG based on the information about itself and progeny (Scenario 9) was 1.19 g/d higher than this response based on information about itself and full siblings (Scenario 5) even though the

number of records was similar. The selection response per unit of ADG using information from full siblings (Scenario 5) was slightly higher than the response based on ten times the number of records containing half-sibling information (Scenario 7). Therefore, within the same number of traits were measured, the selection response per unit was highest to lowest when using information from all relatives, progeny, full-siblings, half-siblings, sire, and just the single animal's data.

3.3. Response to selection by dollar value

The response for ADG, FCR, and IMF by economic value was different (Table 9). The economic value for ADG ranged from \$295.65 (Scenario 2) to \$345.79 (Scenario 11). The economic value for FCR was the lowest in Scenario 2 with \$65.75 and the highest was found in Scenario 11 with \$81.25. On average, the economic value of ADG was 4.33 times greater than the economic value of FCR and 14.56 times greater than the economic value of IMF. The economic value of FCR was an average of 3.38 times greater than the economic value of IMF. The reason was that the profit achievement was illustrated by the price of pork, which depends on the proportion of IMF in the carcass. Pork with IMF greater than the threshold of 3.5% was sold at 5000 VND (equal to \$0.3125) per kg higher than pork with an IMF lower than the threshold. The response in economic value for ADG was the highest and was the lowest for IMF in all scenarios.

Table 9. The selection response of ADG, FCR, and IMF in twelve scenarios by dollar value.

Scenarios	ADG	FCR	IMF	SD index
1	296.35	68.48	15.44	380.27
2	295.65	65.75	31.10	392.50
3	311.75	72.41	16.22	400.38
4	310.58	69.65	32.20	412.43
5	336.87	79.24	17.45	433.57
6	334.79	76.53	33.67	444.99
7	330.52	78.6	17.07	426.19
8	328.34	76.13	32.66	437.13
9	345.79	81.24	17.92	444.96
10	343.61	78.45	34.57	456.63
11	345.46	81.25	17.90	444.62
12	343.25	78.48	34.47	456.20

The economic value of ADG (Fig. 1) had a similar trend as response per unit of ADG. Within the same number of records and from different sources of information, the economic value of ADG based on two traits (ADG, and FCR) was higher than the economic value of this trait based on information from three traits (ADG, FCR, and IMF). The economic values of ADG in Scenarios 1, 3, 5, 7, 9, and 11 were higher than the economic value of ADG in Scenarios 2, 4, 6, 8, 10, and 12, respectively. The economic value of ADG in Scenario 1, for instance, was \$0.70 higher than in Scenario 2. The difference in economic value of ADG using two traits rose from 0.70 to \$2.21 when the economic value of ADG was calculated using three traits. The economic weight for FCR (Fig. 2) had a similar trend with the economic weight of ADG, and the economic weight of FCR based on three traits measured was lower than the calculation based on two traits. The variation in economic value of the FCR trait in all scenarios was smaller than those of ADG. This difference varied between scenarios for FCR traits, ranging from 2.47 to \$2.79. The economic values of ADG and FCR were higher when using information from measured ADG and FCR.

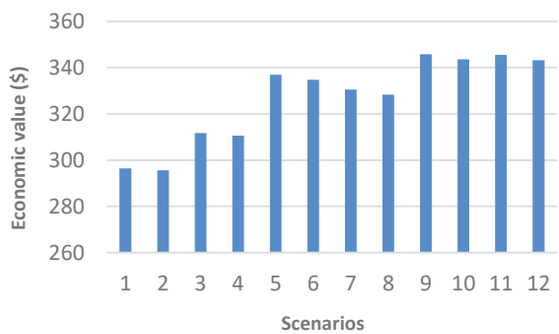

Fig. 1. Economic value (\$) of ADG for Duroc pigs in twelve scenarios.

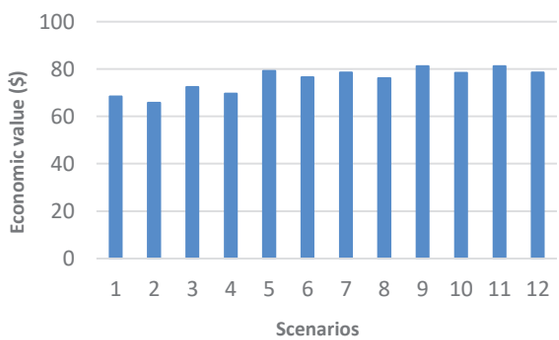

Fig. 2. Economic value (\$) of FCR for Duroc pigs in twelve scenarios.

Using information from two traits, ADG and FCR, the economic value of IMF was lower than its value when including the information from IMF in the model (Fig. 3). The economic value of IMF using the three traits was almost double its value when using information from two traits (ADG, and FCR). For example, using the information of the individual animal's phenotype, the economic value of IMF in Scenario 2 was \$31.10,

which is double the $15.44 in Scenario 1. The economic value of IMF based on three traits measured varied from 31.10 to $34.57, and the economic value of IMF based on two traits measured (ADG, FCR) ranged from 15.44 to $17.92.

The SD index was different among scenarios (Fig. 4). The SD was the total economic value of each trait involved in multiple trait selection. The SD index in this case study varied from 380.27 to $456.63. Scenario 10 had the highest SD index, followed by Scenario 12, and the lowest in Scenario 1.

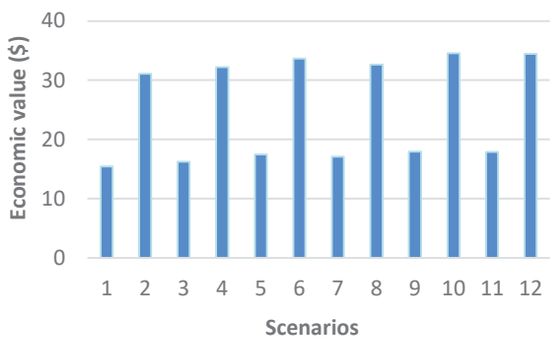

Fig. 3. Economic value ($) of IMF for Duroc pigs in twelve scenarios.

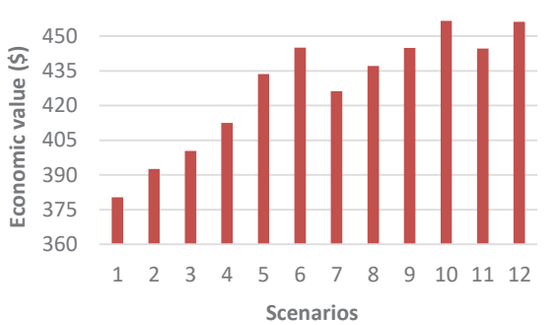

Fig. 4. SD indexes for Duroc pigs based on ADG, FCR, and IMF in twelve scenarios.

Within the same number of records and the same source of information, the SD index calculated based on ADG, FCR, and IMF was higher than the index calculated based on ADG and FCR. Using information from the single animal and all relatives, the SD index based on three traits (Scenario 12) was $11.58 higher than the index based on ADG and FCR (Scenario 11). The SD index based on ADG and FCR was lower (ranged from $10.94 to $12.23) than the index based on three traits. Therefore, the information from three traits gave a higher SD index than only two traits (ADG, FCR).

In the six scenarios (2, 4, 6, 8, 10, and 12) using information from three traits, different sources of information lead to differing SD indexes. Using information from their animal record combined with four records from their progeny (Scenario 10) produced the highest SD index. Using information from all relatives and animal records (Scenario 12), the index was $0.43 lower than that of Scenario 10. However, the SD index in Scenario 12 was $11.21 higher than the index in Scenario 6 using the information from full siblings and the animal itself.

3.4. The genetic gain per sow per year

The accuracy and genetic gain per year of Duroc pigs differed among the scenarios (Table 10). The genetic gain per sow per year of Duroc pigs varied from $473.06 to $568.05. Similar to the SD index, the genetic gain per year of Duroc sows was highest in Scenario 10, followed by Scenario 12, and the lowest occurred in Scenario 1. Scenario 10 had the highest accuracy with a value of 0.7, which was also the case for Scenario 12. Therefore, Scenarios 10 and 12 are the best options for producers and breeders.

Table 10. The accuracy and genetic gain per year of twelve scenarios.

Scenarios	Accuracy	Genetic gain per year ($)
1	0.58	473.06
2	0.60	488.27
3	0.61	498.07
4	0.63	513.07
5	0.67	539.35
6	0.68	553.57
7	0.65	530.18
8	0.67	543.79
9	0.68	553.53
10	0.70	568.05
11	0.68	553.10
12	0.70	567.51

The genetic gain depends on the number of traits involved in the multiple indexes and the correlation between these traits. J. Daigle, et al. (2010) [30] reported the multiple traits used in the Canadian Duroc population were growth rate, FCR, lean depth, loin eye area, and IMF. In this study, the genetic gain of IMF per year for Duroc pigs was 0.27%. C.R. Schwab, et al. (2010) [31] reported that IMF had a strong genetic relationship with BF and the loin eye area. Direct genetic response in the measure of IMF corresponded to a significant decrease in EBV for loin muscle area (with a decrease of 0.9 cm^2 per generation) and an increase of 0.98 mm EBV for backfat thickness in Duroc pigs. In addition, genetic responses in ADG and backfat were favourable. M.

Alam, et al. (2021) [25] reported that, after two decades (from 2000 to 2020), Korean Duroc pigs had significant improvement in both traits (ADG and age at 105 kg body weight) from which the estimated breeding value of ADG increased from -5.23g (2000) to 45.16g (2020) and age at 105 kg body weight decreased to 10.07 days between 2000 and 2020. Improvements of genetics for ADG and BF traits were also reported by J.S. Fix, et al. (2007) [32]. The author reported that ADG improved by 12% (from 0.72 kg/day to 0.81 kg/day) and backfat reduced by approximately 17% (from 2.64 cm to 1.91 cm) from 1980 to 2008. Therefore, we could consider the obtained backfat thickness as a breeding objective trait.

The number of traits and interesting traits in the selection index of the pig industry differs between studies. For example, O.F. Christensen, et al. (2019) [27] reported that different lines in the pig industry have different traits involved in their breeding selection. Some interesting traits for maternal lines included longevity, reproduction traits such as number born alive, number of piglets weaned, and the weaning weight, whereas sire lines were more focused on the growth rate (ADG), feed efficiency (daily feed intake, FCR), and meat content (lean meat percentage, loin eye area). M. Alam, et al. (2021) [25] mentioned that in Korea, they used ADG, age at 105 kg body weight, and BF for Duroc breeds as a sire line whilst using age at first farrowing, total number born, and number born alive for maternal lines such as Landrace and Yorkshire breeds. W.H. Cáceres, et al. (2020) [33] reported using the three traits ADG, backfat thickness, and FCR as objective traits in the selection index for Duroc pigs in Spain. In addition, the Duroc breed had a lower number born alive in comparison with the Landrace and Yorkshire breeds [23]. The number born alive affects the profit of a sow per year. The higher the number born alive, the higher the profit sows made during a year. J.B. Ferraz, et al. (1993) [34] noted that the genetic gain for the number born alive in pigs was 0.012 pigs/year. On the other hand, M.J. Kaplon, et al. (1991) [35] reported that the genetic trend for the number born alive was 0.6 pigs/year.

4. Conclusions

This study investigated the selection index for Duroc pigs based on three traits (ADG, FCR, and IMF) from different sources of information. Among the three traits, the economic value of FCR dominated over the other two traits. The economic weight of IMF based on the information of three traits in the selection index almost doubled its value when only using the information of ADG and FCR. However, when only using the information of ADG and FCR, the economic weight of ADG and FCR was higher than those using information from all three traits.

The yearly genetic gain and the selection response per unit based on ADG, FCR, and IMF for Duroc pigs was the highest in Scenario 10, (where using the record of those traits of the animal itself and its offspring), followed by Scenario 12 (using the information of the animal itself and all relatives). In both scenarios, the accuracies for yearly genetic gain were high at 0.7. Therefore, breeders/producers could choose one of these scenarios for their Duroc breeding program.

COMPETING INTERESTS

The author declares that there is no conflict of interest regarding the publication of this article.

REFERENCES

[1] N.H. Qui, B. Guntoro (2020), "Challenges, opportunities, and prospects of the swine industry in Vietnam", *Proceeding International Conference on Green Agro-Industry*, **4**, pp.189-196.

[2] General Statistics Office (2022), "Data and statistics archive", https://www.gso.gov.vn/en/data-and-statistics/, accessed 5 January 2022.

[3] Ministry of Agriculture and Rural Development (2017), "Current situation of Vietnam pig production", *Presentation at The Workshop Development of Economic Model for Forecasting the Pig Sector Organized by The Institute of Policy and Strategy for Agriculture and Rural Development (IPSARD)*, (in Vietnamese).

[4] Department of Animal Health (2019), "ASF Situation in Vietnam", *Report update by Epidemiology Division* (in Vietnamese).

[5] N.H. Tinh, N.V. Hop, P.N. Trung, et al. (2020), "Production of sire line TS3 selected by EBV and H-FABP, MC4R, and PIT-1 genotypes", *Journal of Vietnamese Animal Science*, **259**, pp.2-7 (in Vietnamese).

[6] A.G.D. Vries, P.G.V.D. Wal, T. Long, et al. (1994), "Genetic parameters of pork quality and production traits in Yorkshire populations", *Livestock Production Science*, **40(3)**, pp.277-289, DOI: 10.1016/0301-6226(94)90095-7.

[7] L.P. Dai (2017), *Research for some Technical Solutions to Increase The IMF in Pigs*, PhD Thesis, Vietnam Academic of Agricultural Sciences, Ho Chi Minh City, Vietnam (in Vietnamese).

[8] T. Daszkiewicz, T. Bak, J. Denaburski (2005), "Quality of pork with different intramuscular (IMF) content", *Polish Journal of Food Nutrition Science*, **55(1)**, pp.31-36.

[9] M. Prevolnik, M.C. Potokar, D. Škorjanc, et al. (2005), "Prediction intramuscular fat content in pork, beef by near infrared spectroscopy", *Journal of Near Infrared Spectroscopy*, **13(2)**, pp.77-85, DOI: 10.1255/jnirs.460.

[10] D.W. Pethick, D.N. D'Souza, F.R. Dunshea, et al. (2005), "Fat metabolism and regional distribution in ruminants and pigs - influences of genetics and nutrition", *RAAN Conference Proceedings*, **15**, pp.39-45.

[11] M. Li, L. Zhu, X. Li, et al. (2008), "Expression profiling analysis for genes related to meat quality and carcass traits during postnatal development of backfat in two pig breeds", *Science in China Series C - Life Sciences*, **51(8)**, pp.718-733, DOI: 10.1007/s11427-008-0090-0.

[12] Y.R. Caldas, E.M. Sánchez, M. Ballester, et al. (2019), "Integrating genome-wide co-association and gene expression to identify putative regulators and predictors of feed efficiency in pigs", *Genetics Selection Evolution*, **51(1)**, pp.1-17, DOI: 10.1186/s12711-019-0490-6.

[13] K.G. Santiago, S.H. Kim, D.H. Lee, et al. (2021), "Estimation of genetic parameters for feeding pattern traits and its relationship to feed efficiency and production traits in Duroc pigs", *Agriculture*, **11(9),** DOI: 10.3390/agriculture11090850.

[14] J.F. Hocquette, F. Gondret, E. Baéza, et al. (2010), "Intramuscular fat content in meat-producing animals: Development, genetic and nutritional control, and identification of putative markers", *Animal*, **4(2)**, pp.303-319, DOI: 10.1017/S1751731109991091.

[15] X. Fernandez, G. Monin, A. Talmant, et al. (1999), "Influence of intramuscular fat content on the quality of pig meat-1. Composition of the lipid fraction and sensory characteristics of m. longissimus lumborum", *Meat Science*, **53(1)**, pp.59-65, DOI: 10.1016/S0309-1740(99)00037-6.

[16] Y. Xu, X. Liu, J. Fu, et al. (2020), "Enhancing genetic gain through genomic selection: From livestock to plants", *Plant Communications*, **1(1)**, DOI: 10.1016/j.xplc.2019.100005.

[17] C.R. Henderson (1985), "Best linear unbiased prediction of nonadditive genetic merits in noninbred populations", *Journal of Animal Science*, **60(1)**, pp.111-117, DOI: 10.2527/jas1985.601111x.

[18] D.S. Falconer, T.F.C. Mackay (1996), *Introduction to Quantitative Genetics*, Benjamin-Cummings Pub. Co., 464pp.

[19] W.G. Hill (2013), "On estimation of genetic variance within families using genome-wide identity-by-descent sharing", *Genetics Selection Evolution*, **45(1)**, DOI: 10.1186/1297-9686-45-32.

[20] L. Tusell, H. Gilbert, J. Riquet, et al. (2016), "Pedigree and genomic evaluation of pigs using a terminal-cross model', *Genetics Selection Evolution*, **48(1),** DOI: 10.1186/s12711-016-0211-3.

[21] Y. Miar, G. Plastow, H. Bruce, et al. (2014), "Genetic and phenotypic correlations between performance traits with meat quality and carcass characteristics in commercial crossbred pigs", *PLOS ONE*, **9(10)**, DOI: 10.1371/journal.pone.0110105.

[22] K. Suzuki, M. Irie, H. Kadowaki, et al. (2005), "Genetic parameter estimates of meat quality traits in Duroc pigs selected for average daily gain, longissimus muscle area, backfat thickness, and intramuscular fat content", *Journal of Animal Science*, **83(9)**, pp.2058-2065, DOI: 10.2527/2005.8392058x.

[23] D.D. Luc, N.X. Trach, N.C. Thanh, et al. (2013), "Reproductive performance of nucleus herd of stress negative Pietrain and Duroc swine raised at the animal farm of Hanoi University of Agriculture", *Journal of Science and Development*, **11(1)**, pp.30-35 (in Vietnamese).

[24] T.H. Son, P.D. Pham, L.Q. Thanh, et al. (2019), "The results of genetic exchange in Landrace, Yorkshire, Duroc and Pietrain breeds in Thuy Phuong pig research and development center", *Journal of Animal Husbandry Association of Vietnam*, **255**, pp.19-25 (in Vietnamese).

[25] M. Alam, H.K. Chang, S.S. Lee, et al. (2021), "Genetic analysis of major production and reproduction traits of korean Duroc, Landrace and Yorkshire pigs", *Animals (Basel)*, **11(5)**, DOI: 10.3390/ani11051321.

[26] H.E. Willson, H.R.D. Oliveira, A.P. Schinckel, et al. (2020), "Estimation of genetic parameters for pork quality, novel carcass, primal-cut, and growth traits in Duroc pigs", *Animals (Basel)*, **10(5)**, DOI: 10.3390/ani10050779.

[27] O.F. Christensen, B. Nielsen, G. Su, et al. (2019), "A bivariate genomic model with additive, dominance and inbreeding depression effects for sire line and three-way crossbred pigs", *Genetics Selection Evolution*, **51(1)**, DOI: 10.1186/s12711-019-0486-2.

[28] S. Hermesch, B. Luxford, H. Graser 1996), "Genetic parameters for lean meat yield, meat quality, reproduction, and feed efficiency traits for Australian pigs", *Livestock Production Science*, **65(3)**, pp.261-270, DOI: 10.1016/S0301-6226(00)00152-4.

[29] M. Bergamaschi, C. Maltecca, J. Fix, et al. (2020), "Genome-wide association study for carcass quality traits and growth in purebred and crossbred pigs", *Journal of Animal Science*, **98(1)**, DOI: 10.1093/jas/skz360.

[30] J. Daigle, C. Gariépy, D. Wilson, et al. (2010), "Prediction of intramuscular fat in live pigs using ultrasound technology and potential use in selection", *Proceedings of 9th World Congress on Genetics Applied to Livestock Production, Leipzig, Germany (No.0668)*.

[31] C.R. Schwab, T.J. Baas, K.J. Stalder (2010), "Results from six generations of selection for the intramuscular fat in Duroc swine using real-time ultrasound. II. Genetic parameters and trends", *Journal of Animal Science*, **88(1)**, pp.69-79, DOI: 10.2527/jas.2008-1336.

[32] J.S. Fix, J.P. Cassady, E.V. Heugten, et al. (2007), "Differences in growth performance, lean growth performance, and leg structure/mobility of commercial pigs representative of 1980 and 2005 genetic types when reared on 1980 and 2005 representative feeding programs", *Livestock Science*, **128(1-3)**, pp.108-114, DOI: 10.1016/j.livsci.2009.11.006.

[34] J.B. Ferraz, R.K. Johnson (1993), "Animal model estimation of genetic parameters and response to selection for litter size and weight, growth, and backfat in closed seedstock populations of large white and Landrace swine", *Journal of Animal Science*, **71(4)**, pp.850-858, DOI: 10.2527/1993.714850x.

[35] M.J. Kaplon, M.F. Rothschild, P.J. Berger, et al. (1991), "Genetic and phenotypic trends in Polish large white nucleus swine herds", *Journal of Animal Science*, **69(2)**, pp.551-558, DOI: 10.2527/1991.692551x.

DOI: 10.31276/VJSTE.65(1).63-69

Skin cancer detection using effective optical parameters and the classification and regression tree algorithm: A novel framework

Thanh Truc Nguyen[1, 2], Duc Minh Nguyen Huu[3], Thanh-Hai Le[4], Quoc-Hung Phan[5], Thi-Thu-Hien Pham[1, 2*]

[1]*School of Biomedical Engineering, International University, Vietnam National University - Ho Chi Minh City, Quarter 6, Linh Trung Ward, Thu Duc City, Ho Chi Minh City, Vietnam*
[2]*Vietnam National University - Ho Chi Minh City, Quarter 6, Linh Trung Ward, Thu Duc City, Ho Chi Minh City, Vietnam*
[3]*Faculty of Traditional Medicine, University of Medicine and Pharmacy at Ho Chi Minh City, 217 Hong Bang, Ward 11, District 5, Ho Chi Minh City, Vietnam*
[4]*Department of Information Technology Specialization, FPT University, Lot E2a-7, Road D1 Hi-Tech Park, Long Thanh My Ward, District 9, Ho Chi Minh City, Vietnam*
[5]*Mechanical Engineering Department, National United University, 2, Lienda, Miaoli, Taiwan*

Received 20 July 2022; revised 23 September 2022; accepted 19 October 2022

Abstract:

Early detection of skin cancer matters because diagnosis, prognosis and treatment plan differ for each skin cancer type at their stages. Medical imaging taking the advantages of the non-invasive and non-ionizing polarized light is emerging as a tool for the development of screening and diagnostic tests. In this work, we proposed a novel framework to classify human melanoma and nonmelanoma skin cancer using the Classification and Regression Tree algorithm (CART). The samples were prepared from twenty-four non-melanoma skin cancer samples (consisting of twelve squamous cell carcinoma and twelve basal cell carcinoma samples); and three melanoma skin cancer samples. We calculated ten optical parameters from anisotropic biological tissues, namely the LB orientation angle (α), the LB phase retardance (β), the CB optical rotation angle (γ), the LD orientation angle (θd), the linear dichroism (D), the circular dichroism (R), the degrees of linear depolarization (e_1 and e_2), the degree of circular depolarization (e_3), and the depolarization index (Δ) using Stokes-Mueller matrix formalism. All effective optical parameters of biological tissue were then input into the CART classifier as predictors. The model yielded an accuracy of 92.6%, which is desirable for any robust and interpretable classification model. The results showed that for biological tissue samples, linear polarization properties dominate over circular ones due to the cellular microstructural composition of tissue, especially under anomalous growth as seen in skin cancer. This novel framework can potentially assist physicians in making timely and well-informed medical decisions.

Keywords: **classification and regression tree algorithm, human skin cancer, Stokes-Mueller matrix formalism.**

Classification numbers: **3.2, 3.6**

1. Introduction

Unfortunately, skin cancer has been rising at alarming rates, fortifying its position as the fifth-most common cancer in 2018 with more than 1.04 million cases of death recorded [1]. Characterized by uncontrolled growth and aggressive spread of skin tissues, skin cancer is categorized into malignant melanoma, squamous cell carcinoma, and basal cell carcinoma, which is listed by increasing frequency of diagnosis and decreasing level of severity. The latter two are collectively called non-melanoma skin cancer (NMSC) for obvious reasons. Both melanoma and NMSC are peculiar: the least common of the three - malignant melanoma - is the most lethal if not quickly diagnosed and treated. Many techniques have been developed for skin cancer detection and diagnosis such as dermatoscopy, reflectance confocal microscopy (RCM), nonlinear optical microscopy, and optical coherence tomography (OCT). Dermatoscopy, also known as epiluminescence microscopy, is a standard physical procedure where the area of the suspected lesion becomes magnified under a bright white light with an occasional application of oil or alcohol to improve the vision field [2]. However, some disadvantages of this imaging technique include a high dependence on the expertise and experience of the examiner as well as a high dependence on the appearance of classic dermoscopic features, which limits early diagnosis or any diagnosis of featureless melanoma [3]. RCM is an optical imaging technique that allows the skin to be analysed with nearly histological resolution at a cellular level [4-5]. Similar to dermoscopy images, real-time images obtained by RCM are horizontally oriented to the skin surface. RCM has been applied in medical settings for the diagnosis of melanoma and non-melanoma lesions and proven to increase diagnostic accuracy when used with dermoscopy [6]. Besides its application in skin oncology, RCM can be useful to delineate indications for inflammatory and infectious skin conditions. The main limitation of RCM is its relatively low skin penetration due to strong light scattering. A penetration depth of ~200 μm can be achieved, which is not sufficient to image in the dermis [6]. Also problematic is the fact that RCM sections are oriented perpendicular to conventional histological sections, making them difficult to interpret. OCT is a non-invasive, cross-sectional, real-time technique that allows conclusions to be drawn with regard to the presence of pathologies. Full-field OCT (FF-OCT) is one particular approach of OCT based on white-light interference microscopy that produces

*Corresponding author: Email: ptthien@hcmiu.edu.vn

en face tomographic images by the arithmetic combination of interferometric images acquired with an area camera and by illuminating the whole field of view with low-coherence light, making it suitable for high spatial resolution (~1.0 μm) imaging in both lateral and axial directions [7]. Line-field OCT (LF-OCT) uses a broadband spatially coherent light source and a line-scan camera in an interference microscope, providing a significant advantage over FF-OCT in terms of imaging penetration depth due to the confocal gate achieved by line illumination and detection [8-9]. S. Batz, et al. (2018) [10] showed that it is possible to distinguish between different nonmelanoma skin cancers by using OCT, but further prospective studies should be conducted to validate the sensitivity and specificity of the criteria. However, melanoma and pigmented elements proved to be a challenge for OCT as confirmed in [11]. Nonlinear optical microscopy is a high-resolution imaging modality based on nonlinear interactions of light with biological tissues [12]. Compared with OCT, nonlinear microscopy offers better spatial resolution, similar to that of RCM. Advances in developing multiphoton excitation microscopes with novel contrast mechanisms, such as second harmonic generation, further allow visualization of skin morphology and function [13]. Key limitations of nonlinear optical microscopy are the orientation of the images (en face sections, like RCM), the small field of view (350 μm × 350 μm with the DermaInspect device, Jenlab), and the relatively weak penetration in skin (~200 μm). Thus, a reliable and simple technique for skin cancer diagnosis applications is still needed.

Classification tree has long been used in biomedical engineering to determine a patient's prognosis after heart attack [14]. H. Henning, et al. (1979) [15] tried to identify patients who are at risk of death within 30 days among those that survived a heart attack for at least 24 hours after hospital admission using the CART classification algorithm. The problem of distinguishing early death from survivors with complete 19-variable from 215 patients produced a simple CART classification tree using only 3 variables. Ten-fold cross validation was employed and the model's performance was evaluated using an adjusted re-substitution of 0.21. L. Goldman, et al. (1982) [16] also used the CART classification algorithm to determine if patients with chest muscle pain would suffer from a heart attack. With an indicative electrocardiogram, characteristic elevation of pain enzyme level, and pain description from 482 patients, CART algorithm produced a much more complicated 13-split classification tree with pruning done based on sensitivity and specificity. The re-substitution overall misclassification cost was 0.07. The CART classification algorithm was also applied to classify immuno-suppression in patients with cancer using 21 continuous variables. The classification tree was pruned to minimize the re-substitution misclassification cost to 0.22 after cross-validation. This study also points out that newer, more expensive tests were not helpful as supplemental information and the variable thought to be a powerful diagnostic tool turned out to be one of the least important variables. These studies mostly deal with a large number of observations, an average number of variables, and only two class labels. The CART classification algorithm has been proven to outperform logistic classification and linear discrimination concerning sensitivity and specificity. CART is also used to detect outliers in a large number of observations and variables. Gait analysis done by D.H. Sutherland, et al. (1980) [17] used data with over 100 variables of 500 children to produce a classification tree with at least 16 terminal nodes. CART detected and helped correct two mistakes. This algorithm determined the relationship of variables to the development of mature gait. Dealing with a large number of variables is not uncommon, and principal component analysis is commonly used during dimensionality reduction before any further analysis. M.Z.F. Nasution, et al. (2018) [18] trained a classification tree using a C4.5 algorithm to detect patients with cervical cancer. The author used principal component analysis to reduce the number of variables from 36 to 12 relevant variables that explained 95% of the variance in the data set. With principal component analysis-based dimensionality reduction, the accuracy was 90.5% compared with an 86.05% rate for a tree without dimensionality reduction. High classification accuracy rates in frameworks with principal component analysis-based dimensionality reduction are reported in [19, 20]. Recently, the present group applied random forest algorithm to classify human skin cancer utilizing 16 Mueller matrix elements. The classifier obtained an average precision of 93% with the lowest score of 81% for basal cell carcinoma and the highest score of 100% for melanoma and squamous cell carcinoma [21]. F.V. Felix, et al. (2020) [22] proposed a machine learning-based method to detect tumours and healthy biological tissues with parameters that were extracted from optical diffuse reflectance spectroscopy. In this work, CART achieved the second highest accuracy of 93% in five applied machine learning models. Besides, M.S. Nogueira, et al. (2021) [23] used the diffuse reflectance spectra technique to extract optical tissue parameters for a training decision tree algorithm to recognize colorectal cancer. The tissue classification model achieved an average accuracy of 87% for both cancer detecting probes.

The present group previously proposed a decoupled analytical technique based on Stokes-Mueller matrix formalism for the successful extraction of all effective properties of turbid media and anisotropic optical samples [24, 25]. The proposed method was applied to extract linear birefringence (LB), linear dichroism (LD), circular birefringence (CB), circular dichroism (CD), linear depolarization (L-Dep), and circular depolarization (C-Dep) properties of various samples including human blood plasma, collagen, and calfskin [26], as well as squamous cell carcinoma and normal tissue in mice [27]. In this study, the classification of human skin cancer was performed using Stokes-Mueller matrix formalism and a CART classification algorithm. The practical feasibility of the proposed technique is examined by characterizing three types of skin cancer samples, namely, squamous cell carcinoma (SCC), basal cell carcinoma (BCC), and melanoma skin cancer (MSC).

2. Stokes-Muller matrix formalism

The decoupled analytical technique of T.T.H. Pham, et al. (2012) [24, 25] has been previously described. This method can

extract ten effective parameters including the LB orientation angle (α), LB phase retardance (β), CB optical rotation angle (γ), LD orientation angle (θ_d), linear dichroism (D), circular dichroism (R), degrees of linear depolarization (e_1 and e_2), degree of circular depolarization (e_3), and depolarization index (Δ).

$$S_c = \begin{bmatrix} s_0 \\ s_1 \\ s_2 \\ s_3 \end{bmatrix} = M_\Delta M_{lb} M_{cb} M_{ld} M_{cd} \hat{S}_c = \begin{pmatrix} m_{11} & m_{12} & m_{13} & m_{14} \\ m_{21} & m_{22} & m_{23} & m_{24} \\ m_{31} & m_{32} & m_{33} & m_{34} \\ m_{41} & m_{42} & m_{43} & m_{44} \end{pmatrix} \begin{pmatrix} \hat{s}_0 \\ \hat{s}_1 \\ \hat{s}_2 \\ \hat{s}_3 \end{pmatrix}_c$$

where M_Δ, M_{lb}, M_{cb}, M_{ld}, and M_{cd} are the Mueller matrices for the depolarization, LB, CB, LD, and CD properties of the sample, respectively, and $\hat{s}_c$ is the input Stokes vector. In the methodology adopted in this study, the sample is radiated by four input linear polarization states, namely, $\hat{s}_{0^\circ} = [1 \;\; 1 \;\; 0 \;\; 0]^T$, $\hat{s}_{45^\circ} = [1 \;\; 0 \;\; 1 \;\; 0]^T$, $\hat{s}_{90^\circ} = [1 \;\; -1 \;\; 0 \;\; 0]^T$, and $\hat{s}_{135^\circ} = [1 \;\; 0 \;\; -1 \;\; 0]^T$) and two input circular polarization states, namely, right-handed $\hat{s}_{R-} = [1 \;\; 0 \;\; 0 \;\; 1]^T$ and left-handed $\hat{s}_{L-} = [1 \;\; 0 \;\; 0 \;\; -1]^T$.

Full details of the experimental procedure used to extract the various parameters are mentioned [24, 25]. This methodology does not require the alignment of the principal birefringence and diattenuation axes. Although only four input polarization states (0°, 45°, 90°, and R-) are sufficient for obtaining all elements of the Mueller matrix, an extra two input polarization states (135° and L-) further improve the experimental results. Moreover, the ability of the analytical model to extract all optical parameters of interest over the measurement range was verified using analytical simulations and error analysis. Thus, the analytical model yielded accurate results even when the output Stokes parameters had errors in the range of ±0.005 or the samples had the minimum measurement of birefringence or dichroism [24, 25].

3. Experimental setup

The polarized light measurement system was set up horizontally to ensure laser source stability and safety during the experiments. This system includes a helium neon laser (wavelength of 632.8 nm, power <5 mW), a quarter-wave plate, polarizers, and a Stokes polarimeter to characterize the linear birefringence, linear dichroism, circular 58 birefringence, circular dichroism, circular depolarization, and circular depolarization properties of a biological anisotropic sample. A frequency-stable He-Ne laser (HNLS008R, Thorlabs Co.) with a central wavelength of 633 nm served as source for input polarized light. A polarizer (GTH5M, Thorlabs Co.) and a quarter-wave plate (QWP0-63304-4-R10, CVI Co.) produced linear polarization light at 0, 45, 90 and 135 degrees; and two circular right-handed and left-handed polarizations. The optics were hooked up to a stage controller connected to a computer to automate the adjustment of polarizer angle. A neutral density filter (NDC-100-2, ONSET Co.) was used to ensure that each of the input polarization lights had the equal intensities. The output Stokes parameters were computed from intensity measurements obtained using a Stokes polarimeter (PAX5710, Thorlabs Co.) at a sampling rate of 33.33 samples per second. A minimum of 1024 data points were obtained for each sample and used to calculate the value of each effective parameter. The system was calibrated against a Poincare sphere after every run by returning the value of the angle to zero before setting the angle to the next value. The arrangement of the measurement system is shown in Fig. 1.

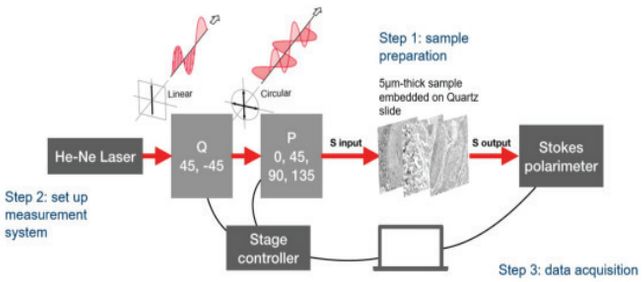

Fig. 1. The illustration of measurement system.

3.1. Sample preparation

Twenty-four non-melanoma skin cancer samples (consisting of twelve SCC and twelve BCC samples) and three MSC samples were acquired from Khanh Hoa General Hospital (Nha Trang city, Vietnam). The sample labels, which were affixed by the hospital, included information on the type of cancer, the stage of the disease, and the date of packaging. All samples were embedded and fixed in formalin and paraffin. The samples were sectioned with a thickness of 5 μm by a microtome and placed on quartz slides. Based on Ref. [28], before cutting samples, the thicknesses of the samples were recorded. After the calibration, the 5-μm thick samples were chosen to ensure both the sensitivity of the received polarized light at the Stokes polarimeter and the ability to characterize the polarization properties of samples. Furthermore, cancerous tissue samples were stained with H&E and observed under an optical microscope (OM) for histopathological analysis.

3.2. Dimension reduction

Principal component analysis reduces data dimensionality by extracting principal components that reflect relevant features in the data [29, 30]. The benefit is that a significant proportion of the variance in the data can be explained by a reduced number of orthogonal components compared to the total number of raw input variables. Principal component analysis was performed by singular value decomposition. The values of the variable were standardized before performing principal component analysis by subtracting the values of each variable by the variable's mean and scaling them with the variable's standard deviation. We included a line in the code to determine if any of the categorical variables were excluded out of the principal component analysis because only numeric variables can be broken down to principal components. The dimensions that explain 95% of the variance

in the data were enough to summarize the maximum amount of information contained in the original set of optical parameters. Sixty-one PCA results were tested for sampling adequacy using a Kaiser-Meyer-Olkin test followed by Bartlett's test of sphericity to test whether the covariance matrix is significantly different from identity [31].

3.3. Training

The predictors used to train the CART classification algorithm are the dimensions selected by principal components analysis. The predictor values are the principal components scores of the dimensions explaining 95% of the variance existing in the data set. The CART algorithm requires the split criterion to be based on the Gini diversity index. Because there is no instance of missing data, surrogate splits were not designated to handle missing data. The prune criterion is led to error. The split predictor was selected to maximize the Gini diversity index over all possible splits of all predictors following the construction of the CART classifier algorithm. The original predictors were passed through a principal component analysis and the new predictor was the principal component scores, hence, they do not reflect the nature of the optical parameter predictors. The maximum number of splits were run from 1 to 10 to produce trees ranging from coarse to fine to see the rate of change in performance as the trees gain more leaves.

3.4. Cross-validation

Ten-fold cross-validations were performed on the classification model and initialized the prediction to the proper size of each fold. The data set was randomly partitioned into 10 folds. To ensure reproducibility, a random number generator was used. For each fold, the process of cross validation mimics the steps described above: predictors and responses of each fold are defined; principal component analysis was conducted on the numeric predictors matrix; the dimensions that cumulatively explain 95% of variance of the data set are kept; a classifier is trained with hyper-parameters described in the training 62 section; and, finally, the prediction is calculated together with the fold score. After going through 10 folds, the correct predictions were identified by comparing fold predictions to the correct responses and validation accuracy was calculated by taking the mean of the correct predictions of all folds. The cross-validation scheme is presented in Fig. 2.

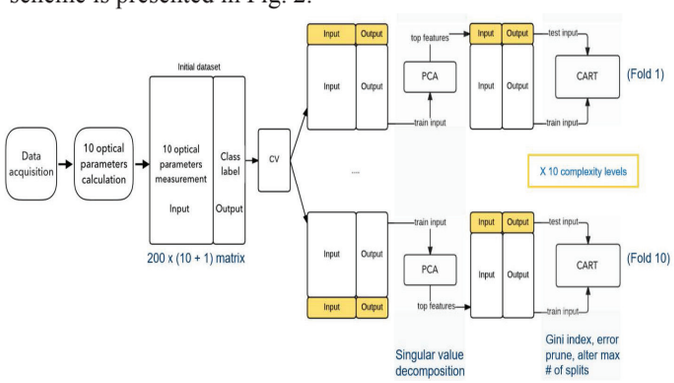

Fig. 2. The cross-validation scheme.

4. Results and discussion

Table 1 shows the values of ten effective optical parameters of normal and cancerous skin samples. The results showed that α presented a degree of differential power across the four sample types with normal skin tissue ranked highest at 15.14 degrees. The same trend was observed for β, γ, and D with normal skin ranking highest at 1.47 degrees, 0.24 degrees, and 0.12, respectively. The opposite trend with normal skin tissue ranked lowest was observed in θ_d of 97.85 degrees. It can be asserted with a high level of confidence that the ten effective optical parameters derived with proposed technique have the ability to differentiate normal human skin tissue from cancerous human skin tissue.

Table 1. Results of ten effective parameters.

		α	β	γ	θ_d	D	R	e_1	e_2	e_3	Δ
Normal skin	Mean	15.14	1.43	0.24	97.85	0.12	-0.04	$3.7x10^{-6}$	$3.9x10^{-6}$	$1.1x10^{-5}$	0.999
	SD*	2.02	0.13	0.03	4.90	0.01	0.008	$2.4x10^{-7}$	$2.3x10^{-6}$	$7.0x10^{-6}$	$4.4x10^{-6}$
Squamous cell carcinoma	Mean	3.05	0.35	0.05	124.49	0.08	-0.022	$9.6x10^{-6}$	$9.5x10^{-6}$	$3.4x10^{-5}$	0.999
	SD*	0.85	0.03	0.007	4.81	0.01	0.002	$2.9x10^{-7}$	$2.6x10^{-7}$	$1.2x10^{-6}$	$7.2x10^{-6}$
Basal cell carcinoma	Mean	7.03	0.55	0.054	125.31	0.05	-0.023	$2.1x10^{-6}$	$3.4x10^{-6}$	$1.6x10^{-5}$	0.999
	SD*	0.94	0.03	0.006	2.58	0.005	0.002	$6.2x10^{-7}$	$8.4x10^{-7}$	$3.2x10^{-6}$	$1.6x10^{-6}$
Melanoma	Mean	5.47	0.44	0.09	126.58	0.07	0.008	$1.7x10^{-6}$	$1.6x10^{-6}$	$1.7x10^{-5}$	0.999
	SD*	0.37	0.02	0.01	3.78	0.01	0.001	$4.6x10^{-7}$	$4.1x10^{-7}$	$3.6x10^{-6}$	$2.1x10^{-6}$

*SD: standard deviation.

4.1. Extracting the principal components

Principal component analysis was used to avoid overfitting by reducing the number of effective optical parameters used as predictors for the CART classification algorithm as illustrated as Fig. 3. As shown, two principal components were yielded from the dataset of 10 different effective optical parameters, which explained 95% of the dataset variance. The first principal component explained the largest proportion, 74.4% of the variance, and was composed of linear optical parameters θ_d and Δ with 76.22 and 27.12%, respectively. The second principal component explained the second largest proportion of 20.6% of the variance and was composed of linear optical parameters with α and β positively contributing 64.23 and 16.67%, respectively.

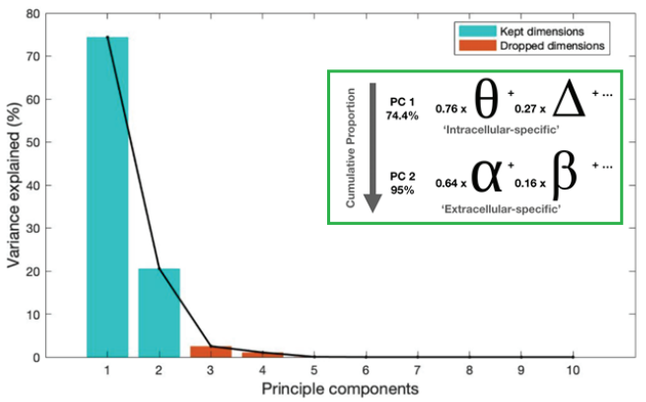

Fig. 3. Breaking down the principal components used as predictors for the CART classifier.

Figure 4 shows the data distributions of the optical parameters α, β, θ_d, and Δ of four skin cancer samples including normal, melanoma, BCC, and SCC.

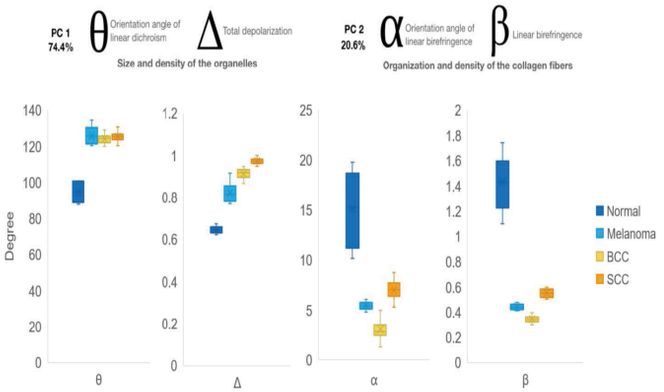

Fig. 4. Breaking down the metrics that matter.

4.2. Evaluation of the CART classification algorithm

The maximum number of splits were run from 1 to 10 to examine the performance of the classification algorithm at increasing levels of complexity, which is determined by the number of nodes and branches. Fig. 5 shows the illustration of the CART classification tree with the maximum number of splits. As shown, the classification ended up with 5 levels of tree complexity at 5 different maximum number of splits, specifically, 1 (Fig. 5A); 2 (Fig. 5B); 3 (Fig. 5C); 4, 5, 6 (Fig. 5D); and 7, 8, 9, 10 (Fig. 5E). The CART classification algorithm returned the same tree, meaning a tree with the same number of splits and nodes, same split predictors, same split points for configurations with a maximum of 4, 5, and 6 splits (Fig. 5C), and applied with configurations with a maximum 7, 8, 9 and 10 splits (Fig. 5D). This is because the Gini index reached a threshold of maximum knowledge gain given the number of splits. The 5 classification trees were evaluated by their training accuracy, testing accuracy, error rate, recall or sensitivity, precision, specificity, and F1 score shown in Table 2. The CART classification tree with a maximum number of splits = 4 performed with the best F1 score of 98.59% describing the overall performance of the models by finding the common ground between recall and precision. F1 is a good indicator when a dataset is unbalanced, such as the dataset with which we were dealing. It is noted that, for the CART classification tree with a maximum number of splits = 1, precision was NaN because the classification tree did not include enough classes to determine precision. Therefore, because F1 reflects precision and recall, it returned as NaN.

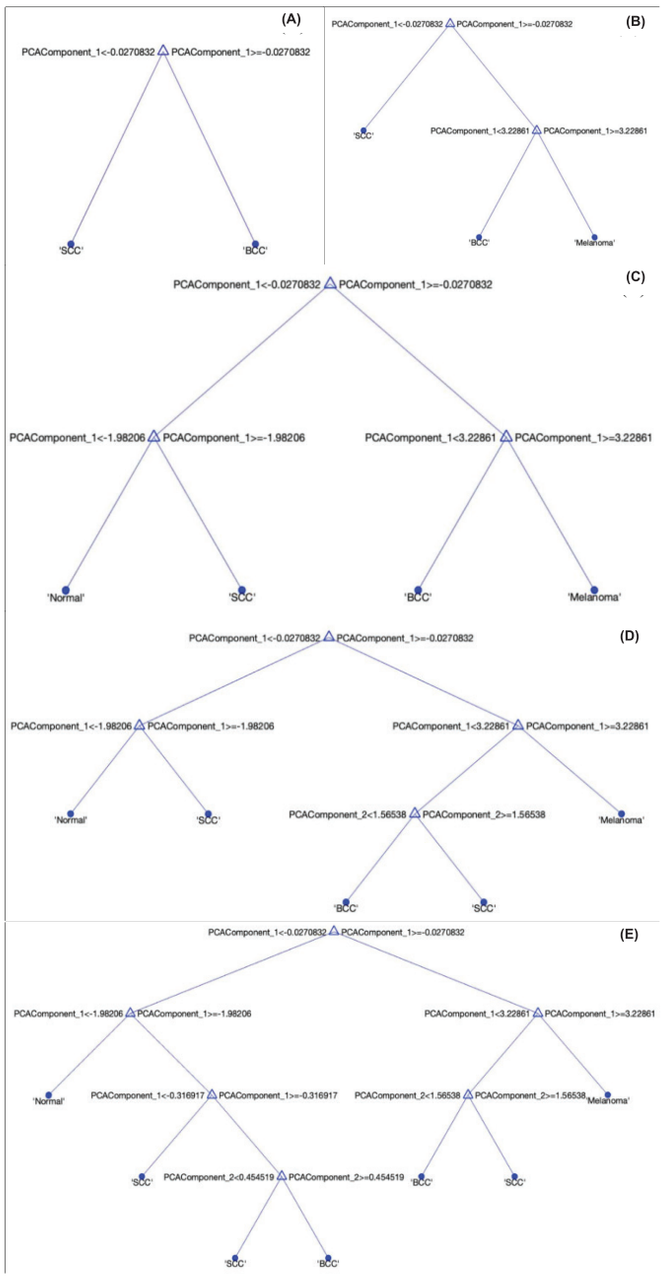

Fig. 5. CART classification tree with maximum number of splits = (A) 1, (B) 2, (C) 3, (D) 4, 5, 6 and (E) 7, 8, 9, 10.

Table 2. Performance evaluation of different CART trees.

Maximum of number of splits	1	2	3	4	7
Training accuracy	81.4%	87.7%	92.9%	93.1%	92.7%
Testing accuracy	78.4%	85.8%	91.3%	92.6%	92.1%
Error rate	20%	16.2%	8.7%	7.8%	8.7%
Recall (Sensitivity)	0%	48.6%	97.1%	100%	97.1%
Precision	NaN	94.4%	97.1%	97.2%	97.1%
Specificity	100%	98.8%	98.8%	99.8%	98.8%
F1	NaN	64.15%	97.1%	98.59%	97.1%

Figure 6 shows the performance evaluation of different CART trees, highlighting the superiority of MaxSplits4 with a maximum number of splits = 4. The capability of this framework as a trustful tool for decision making is shown by a high accuracy of 94% at high speed and low computing cost. With a decision tree-based CART classification algorithm, the visualization of the decision making process regarding which observation belongs to which cancer type is straight forward in logic flow, reflecting the resemblance between the CART classification algorithm and a basic human decision making process. In other words, the decision of which predictor should be used for a split and where to split depends on the extent of the distinguishing impact of the split selection measured by the impurity of the children nodes. Using this decision tree produced by CART, the effective optical parameters that play the most important role in representing the physical properties of the biological anisotropic tissue samples can be determined. It is important to note that with different numbers of features selected as predictors and different configurations specified for CART (most significantly the number of maximum nodes), the most important predictors yielded can vary, which is not necessarily the predictors of the first splits [32].

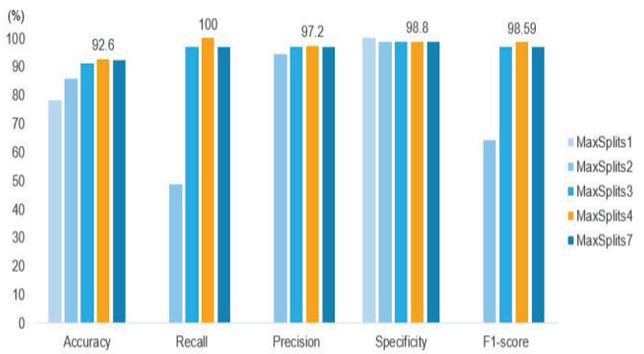

Fig. 6. Performance evaluation of different CART trees, highlighting the superiority of MaxSplits4 (orange) with a maximum number of splits = 4.

When performing the experiments, although the visual image of the Poincare sphere is quite clear, manually adjusting the laser light path to be perpendicular to the optical lens and filter is not guaranteed to be exact. This leads to an average skewness in the ellipticity of 1 to 2 degrees away from the exact 0, 45, 90, and 135-degree targets. Despite each optical parameter being derived from a mathematical formula to obtain an insignificant difference from the accurate target angle of ellipticity and degree of polarization, sequences of distorted results can originate from the system to create an cumulative error when large-scale data is collected. This problem makes it difficult to repeat the experiment for a robust sampling plan. Therefore, constant and accurate calibration and noise factor identification are essential factors to develop a database that delivers proper diagnostics on skin samples in a large-scale clinical investigation in the future. A quick comparison to the ideal state of the linear polarizer will help users reassess the experiment and recalibrate the system. Basically, this study indicates a comprehensive collection of effective parameters of normal skin, which can be used as a reference for further research. The method of using a Muller matrix in the medical/healthcare system is an approach for detecting cancer cells by optical parameters obtained from the measurements of normal and carcinoma human skin tissue. More structural organization and characteristics of human skin tissue can be obtained under the perspective of crude positions of the organelles and the extracellular matrix while reserving the high interpretability of the CART classifier and enhancing its accuracy, which helps differentiate normal, squamous cell carcinoma, basal cell carcinoma, and melanoma.

5. Conclusions

The Stokes-Mueller method allows the extraction of ten structure-dependent effective optical parameters. Using principal component analysis and a highly interpretable CART classification algorithm framework proposed in this work, melanoma, non-melanoma, and healthy skin tissue were able to be classified with an accuracy of 92.6%. The results also showed that linear optical properties dominated the biological anisotropic samples. The investigation into human skin cancer revealed that intracellular-specific properties, driven mainly by linear dichroism, and extracellular specific properties, driven by linear birefringence, are strong indicators of anisotropy and anomalies found in cancer tissues. This framework can potentially assist physicians in making timely and well-informed medical decisions that save lives.

CRediT author statement

Thanh Truc Nguyen: Software, Investigation, Data curation, Writing draft; Duc Minh Nguyen Huu: Visualization, Investigation, Review & Editing; Thanh-Hai Le: Software, Visualization, Investigation, Data curation; Quoc-Hung Phan: Conceptualization, Methodology, Validation; Thi-Thu-Hien Pham: Conceptualization, Methodology, Supervision, Project administration, Funding acquisition, Writing - Review & Editing.

ACKNOWLEDGEMENTS

The authors gratefully acknowledge the financial support provided to this study by the Vietnam National Foundation for Science and Technology Development (NAFOSTED) under grant number 103.03-2019.381.

COMPETING INTERESTS

The authors declare that there is no conflict of interest regarding the publication of this article.

REFERENCES

[1] J.S. Lin, M. Eder, S. Weinmann, et al. (2011), "Behavioral counseling to prevent skin cancer: A systematic review for the U.S. preventive services task force", *Annals of Internal Medicine*, **154(3)**, pp.190-201, DOI: 10.7326/0003-4819-154-3-201102010-00009.

[2] P.A. Ascierto, G. Palmieri, E. Celentano, et al. (2000), "Sensitivity and specificity of epiluminescence microscopy: Evaluation on a sample of 2731 excised cutaneous pigmented lesions", *Br. J. Dermatol.*, **142(5)**, pp.893-898, DOI: 10.1046/j.1365-2133.2000.03468.x.

[3] G. Argenziano, I. Mordente, G. Ferrara, et al. (2008), "Dermoscopic monitoring of melanocytic skin lesions: Clinical outcome and patient compliance vary according to follow-up protocols", *Br. J. Dermatol.*, **159(2)**, pp.331-336, DOI: 10.1111/j.1365-2133.2008.08649.x.

[4] I. Alarcon, C. Carrera, J. Palou, et al. (2014), "Impact of in vivo reflectance confocal microscopy on the number needed to treat melanoma in doubtful lesions", *Br. J. Dermatol.*, **170(4)**, pp.802-808, DOI: 10.1111/bjd.12678.

[5] J. Champin, E. Cinotti, B. Labeille, et al. (2014), "*In vivo* reflectance confocal microscopy to optimize the spaghetti technique for defining surgical margins of lentigo maligna", *Dermatologic Surg.*, **40(3)**, pp.247-256, DOI: 10.1111/dsu.12432.

[6] P. Guitera, G. Pellacani, K.A. Crotty, et al. (2010), "The impact of in vivo reflectance confocal microscopy on the diagnostic accuracy of lentigo maligna and equivocal pigmented and nonpigmented macules of the face", *J. Invest. Dermatol.*, **130(8)**, pp.2080-2091, DOI: 10.1038/jid.2010.84

[7] J. Olsen, J. Holmes, G.B. Jemec (2018), "Advances in optical coherence tomography for dermatology-a review", *J. Biomed. Opt.*, **23(4)**, pp.1-10, DOI: 10.1117/1.JBO.23.4.04090.

[8] S.H. Tsang, T. Sharma (2018), "Optical coherence tomography", *Advances in Experimental Medicine and Biology*, **1085(5035)**, pp.11-13, DOI: 10.1007/978-3-319-95046-4_3.

[9] R.F. Spaide, J.G. Fujimoto, N.K. Waheed, et al. (2018), "Optical coherence tomography angiography", *Prog. Retin. Eye Res.*, **64**, pp.1-55, DOI: 10.1016/j.preteyeres.2017.11.003.

[10] S. Batz, C. Wahrlich, A. Alawi, et al. (2018), "Differentiation of different nonmelanoma skin cancer types using OCT", *Skin Pharmacol. Physiol.*, **31(5)**, pp.238-245, DOI: 10.1159/000489269.

[11] L.F.D. Ruffano, J. Dinnes, J.J. Deeks, et al. (2018), "Optical coherence tomography for diagnosing skin cancer in adults", *Cochrane Database Syst. Rev.*, **12**, DOI: 10.1002/14651858.CD013189.

[12] W.R. Zipfel, R.M. Williams, W.W. Webb, et al. (2003), "Nonlinear magic: Multiphoton microscopy in the biosciences", *Nat. Biotechnol.*, **21(11)**, pp.1369-1377, DOI: 10.1038/nbt899.

[13] K. Koenig, I. Riemann (2003), "High-resolution multiphoton tomography of human skin with subcellular spatial resolution and picosecond time resolution", *J. Biomed. Opt.*, **8(3)**, pp.432-439, DOI: 10.1117/1.1577349.

[14] E.G.R. Olshen, H. Henning, J.R. Jr, et al. (1983), "Risk prediction after myocardial infarction: Comparison of three multivariate methodologies", *Cardiology*, **70(2)**, pp.73-84, DOI: 10.1159/000173573.

[15] H. Henning, E.A. Gilpin, J.W. Covell, et al. (1979), "Prognosis after acute myocardial infarction: A multivariate analysis of mortality and survival", *Circulation*, **59(6)**, pp.1124-1136, DOI: 10.1161/01.CIR.59.6.1124.

[16] L. Goldman, M. Weinberg, R. Olshen, et al. (1982), "A computer-derived protocol to aid in the diagnosis of emergency room patients with acute chest pain", *N. Engl. J. Med.*, **307(10)**, pp.588-596, DOI: 10.1056/NEJM198209023071004.

[17] D.H. Sutherland, R. Olshen, L. Cooper, et al. (1980), "The development of mature gait", *J. Bone Joint Surg. Am.*, **62(3)**, pp.336-353.

[18] M.Z.F. Nasution, O.S. Sitompul, M. Ramli, et al. (2018), "PCA based feature reduction to improve the accuracy of decision tree c4.5 classification", *J. Phys.: Conf. Ser.*, **978**, DOI: 10.1088/1742-6596/978/1/012058.

[19] Y. Zhang, S. Wang, Z. Dong (2014), "Classification of Alzheimer disease based on structural magnetic resonance imaging by kernel support vector machine decision tree", *Prog. Electromagn. Res.*, **144**, pp.171-184, DOI: 10.2528/PIER13121310.

[20] E. Gokgoz, A. Subasi (2015), "Comparison of decision tree algorithms for EMG signal classification using DWT", *Biomed. Signal Process. Control*, **18**, pp.138-144, DOI: 10.1016/j.bspc.2014.12.005.

[21] N.T. Luu, T.H. Le, Q.H. Phan, et al. (2021), "Characterization of Mueller matrix elements for classifying human skin cancer utilizing random forest algorithm", *J. Biomed. Optics*, **26(7)**, DOI: 10.1117/1.JBO.26.7.075001.

[22] F.V. Felix, S.P. Suarez, J.L.A. Diego, et al. (2020), "Application of classification algorithms to diffuse reflectance spectroscopy measurements for ex vivo characterization of biological tissues", *Entropy (Basel)*, **22(7)**, DOI: 10.3390/e22070736.

[23] M.S. Nogueira, M. Raju, J. Gunther, et al. (2021), "Tissue biomolecular and microstructure profiles in optical colorectal cancer delineation", *J. Phys. D: Appl. Phys.*, **54(45)**, DOI: 10.1088/1361-6463/ac1137.

[24] T.T.H. Pham, Y.L. Lo (2012a), "Extraction of effective parameters of turbid media utilizing the Mueller matrix approach: Study of glucose sensing," *J. Biomed. Opt.*, **17(9)**, DOI: 10.1117/1.jbo.17.9.097002.

[25] T.T.H. Pham, Y.L. Lo (2012b), "Extraction of effective parameters of anisotropic optical materials using a decoupled analytical method", *J. Biomed. Opt.*, **17(2)**, DOI: 10.1117/1.JBO.17.2.025006.

[26] H.T.T. Pham, A.L.T. Nguyen, T.V. Vo, et al. (2018), "Optical parameters of human blood plasma, collagen, and calfskin based on the Stokes-Mueller technique", *Applied Optics*, **57(16)**, pp.4353-4359, DOI: 10.1364/AO.57.004353.

[27] D.L. Le, T.N. Huynh, D.T. Nguyen, et al. (2018), "Characterization of healthy and nonmelanoma- induced mouse utilizing the Stokes-Mueller decomposition", *J. Biomed. Opt.*, **23(12)**, pp.1-8, DOI: 10.1117/1.JBO.23.12.125003.

[28] H.R. Lee, P. Li, C. Lotz, et al. (2019), "Digital histology with Mueller microscopy: How to mitigate an impact of tissue cut thickness fluctuations", *J. Biomed. Opt.*, **24(7)**, DOI: 10.1117/1.JBO.24.7.076004.

[29] I.T. Jolliffe (2002), "Graphical representation of data using principal components", *Principal Component Analysis, Springer Series in Statistics*, Springer, pp.78-110, DOI: 10.1007/0-387-22440-8_5.

[30] H. Abdi (2004), "Linear Algebra for neural networks", *International Encyclopedia of the Social & Behavioral Sciences*, pp.1-9, DOI: 10.1016/B0-08-043076-7%2F00609-4.

[31] C.D. Dziuban, E.C. Shirkey, C. Edwin (1974), "When is a correlation matrix appropriate for factor analysis? Some decision rules", *Psychol. Bull.*, **81(6)**, pp.358-361, DOI: 10.1037/h0036316.

[32] L. Breiman, J.H. Friedman, R.A. Olshen, et al. (2017), "Classification and regression trees", *Routledge*, 368pp, DOI: 10.1201/9781315139470.

DOI: 10.31276/VJSTE.65(1).70-75

Correlation of Epstein-Barr virus copy numbers, MICA expression and rs2596542 variant in nasopharyngeal carcinoma tumour

Thanh Dat Ta[1], Khanh Tran Van[1, 2], Thanh Binh Nguyen[3], Manh Thuong Le[4], Long Ha Le Hai[2], Hoang Viet Nguyen[1, 2*]

[1]Center for Gene-Protein Research, Hanoi Medical University, 1 Ton That Tung Street, Trung Tu Ward, Dong Da Dictrict, Hanoi, Vietnam
[2]Faculty of Medical Technology, Hanoi Medical University, 1 Ton That Tung Street, Trung Tu Ward, Dong Da Dictrict, Hanoi, Vietnam
[3]Department of Pathophysiology and Immunology, Hanoi Medical University, 1 Ton That Tung Street, Trung Tu Ward, Dong Da Dictrict, Hanoi, Vietnam
[4]Department of Anatomy, Hanoi Medical University, 1 Ton That Tung Street, Trung Tu Ward, Dong Da Dictrict, Hanoi, Vietnam

Received 4 March 2022; revised 12 April 2022; accepted 25 April 2022

Abstract:

Major histocompatibility complex class I chain-related A (MICA) is a tumour antigen that is greatly expressed on the surfaces of human malignancies and infection cells, which trigger attachment to immune cells. Although many studies have investigated the role of the MICA rs2596542 variant involved in high risk of hepatocellular carcinoma (HCC), the expression regulation of rs2596542 MICA in nasopharyngeal carcinoma (NPC) susceptibility with the Epstein-Barr virus (EBV) is still ambiguous. Therefore, this study was conducted to elucidate the association of rs2596542C/T and EBV load to MICA expression in NPC tissues. A total of 70 tumour tissues from NPC patients were enrolled in the current study. The genetic variant of rs2596542 was identified by Real-time PCR genotyping, and MICA protein expression was quantified by immunohistochemistry staining. A significant difference was observed in the expression of MICA regarding EBV copy numbers ($p<0.01$). High expression of MICA presented a considerably lower EBV status. In addition, higher expression of homologous MICA rs2596542 CC was significantly associated with a lower EBV load ($p<0.001$) thus suggesting a protective role of allele C against the infection of EBV. In summary, rs2596542 MICA plays an important role in the immune response preventing the EBV among NPC patients as well as developing a new predictive biomarker for virus susceptibility to cancers.

Keywords: **Epstein-Barr virus, MICA expression, rs2596542.**

Classification numbers: **3.2, 3.6**

1. Introduction

NPC is a common epithelial cancer that arises from the head and neck area and has a high prevalence in Southeast Asia and Southern China [1]. According to GLOBOCAN 2020, there were 133,354 new cases accounting for 0.69% of all diagnosed cancers, and the mortality rate was approximately 0.8%. Driven from the surface epithelium of the posterior nasopharynx, NPC is classified by World Health Organization (WHO) into three subtypes: squamous cell carcinoma (type I), non-keratinizing carcinoma (type II), and undifferentiated carcinoma (type III) [2]. Various etiological factors of NPC were investigated consisting of genetic susceptibility, environmental, dietary, and EBV infection [3-5]. Of these factors, EBV infection plays a predominant role when mostly associated with NPC type II and III [6]. The presence of EBV is detected in more than 90% of NPC type II, which is the most common type of NPC in the high-risk regions [7]. The relationship between NPC and EBV infection has been evaluated by the existence of EBV-DNA or transcripts determined from tumour cells and precancerous lesions [8]. Also, EBV-DNA load in plasma has been investigated as a potential biomarker of NPC, as it is highly associated with tumour burden and disease stage [9].

EBV, also known as human herpesvirus type 4 (HHV4), was the first human oncogenic virus to be discovered and belongs to the Gamma herpesvirus group. EBV infection affects 90% of people worldwide where primary infection typically occurs in early childhood and

*Corresponding author: Email: hoangviet@hmu.edu.vn

is mostly asymptomatic. However, in progressive cases, EBV can cause infectious mononucleosis (IM), an acute symptomatic, and associated with carcinogenesis as NPC [10]. B lymphocytes are the primary target of EBV infection into epithelial cells through CD21 expression on the cell surface where this virus can establish different latency stages in these lifelong carriers [11]. The EBV latency programs are categorised into four types, arranged from Latency 0 to Latency III, based on the specific genes expressed in normal B cells [12]. During primary infection, both CD8+ T cells and NK cells play a critical role in inhibiting the proliferation of EBV [13, 14]. Immune responses against virus-infected cells occur by downregulation of immunoreceptors including NKG2D (immunoreceptor natural killer group 2 member D) on the surface of effector cells [15]. NKG2D is the key stimulating receptor that remains on CD8+ T cell and NK cell surfaces. The interaction between NKG2D and its ligands and MICA (major histocompatibility complex (MHC) class I-related chain A polypeptides) can mediate signalling pathways to produce cytotoxicity and cytokine to kill EBV-infected cells.

MICA is a gene of MHC class I and is related to human tumorigenesis. It is approximately ~15.5 kb in length and located on the short arm of chromosome 6 (6p21.33). Of all MHC class I genes, MICA is the most polymorphic gene with 108 alleles and 87 identified protein variants [16]. Single nucleotide polymorphism (SNP) rs2596542C/T is located at the MICA promoter region and has been considered a valuable marker to screen HCC. Allele T of rs2596542 could have a higher risk to develop HCC when it can affect the bindings of stress-inducible transcription factors and thus can alter the expression of MICA [17]. Although MICA polymorphisms have been investigated to be highly associated with several types of cancer, only a few studies have been performed in NPC susceptibility EBV [18]. To identify the effect of EBV in tumour cells related to MICA expression and MICA polymorphism, specifically rs2596542, we performed this study to investigate the association between MICA expression and EBV copy numbers in NPC.

2. Materials and methods

2.1. Patients and specimens

This study was accepted by the ethics committee at Hanoi Medical University, Vietnam under number 26/HMUIRB. The case group included 70 patients who were diagnosed with NPC at Hanoi Medical University Hospital from October 2019 to November 2021. Patients who had NPC and did not receive any treatment were confirmed by histology at the Department of Pathology, Hanoi Medical University. All individuals signed an informed consent before the study.

2.2. DNA extraction and SNP genotyping

DNA samples were extracted from formalin-fixed paraffin-embedded (FFPE) tissue sections by QIAamp DNA FFPE Tissue Kit (Qiagen, 56404). The genotypes of the MICA rs2596542C/T polymorphism were determined by Real-time PCR on a Quantstudio3™ Real-Time PCR Systems (Applied Biosystems Inc., Foster City, USA) according to the manufacturer's instructions. In total, the 10-µl volume of the PCR reaction mixes contained 5 µl 2X TaqMan™ Genotyping Master Mix (Applied Biosystems), 0.5 µl 20X Taqman probe (TaqMan®: C___27301153_10, Applied Biosystems), and 4.5 µl of isolated DNA sample. The PCR conditions are as follows: 60ºC for 30 s; denaturation at 95ºC for 10 min; and 40 cycles of (95ºC for 15 s and 60ºC for 1 min) and final step at 60ºC for 30 s.

2.3. EBV copy number measurement

EBV in tumour tissues were detected and measured by Realtime PCR using the GeneProof EBV PCR kit (Cat. No. EBV/ISEX/100, GeneProof) by targeting the EBNA1 gene, according to the manufacturer's protocol. In total 40 µl PCR reactions mix volume contained 30 µl MasterMix and 10 µl DNA isolated sample using the conditions: 37ºC for 2 min, denaturation at 95ºC for 10 min, and 45 cycles of (95ºC for 5 s, 60ºC for 40 s and 72ºC for 20 s). A positive standard curve of EBV copy number was analysed and calculated with a QuantStudio 3 Real-time PCR system (Applied Biosystems, CA, USA). Quantification of EBV in FFPE tumour tissues were calculated as EBV copy numbers per microgram of DNA (copies/µg DNA).

2.4. Immunohistochemical staining (IHC)

The expression of MICA in NPC tissue samples were assessed by IHC examination using an ultraView Universal DAB detection kit (Ventana, USA). Briefly, paraffin-embedded NPC specimens were sliced, deparaffinized in xylene, rehydrated through a graded ethanol series (100-90-80%), and then blocked with endogenous peroxidase. Subsequently, sections were dipped into rabbit anti-human MICA polyclonal antibody (diluted 1:100, Abcam) for 32 min at 37ºC. Positive and negative controls were also stained following the manufacturer's recommendation. After washing by PBS,

sections were incubated with ultraView Universal HRP Multimerto primary detection (Ventana, USA) and then visualized by ultraView Universal hydrogen peroxide (Ventana, USA) and ultraView Universal DAB (Ventana, USA) for 8 min at 37ºC. The DAB was toned by the addition of ultraView Universal Copper (Ventana, USA) for 4 min at 37ºC before specimens were counter-stained with hematoxylin II (Ventana, USA) and then incubated with Bluing Reagent (Ventana, USA) under the same condition. The sections were rinsed by a detergent-water mixture, dehydrated through a graded ethanol series, cleared with xylene, covered by Richard-Allan Scientific Mounting Medium (ThermoFisher Scientific, USA), manually cover-slipped, and finally observed under the microscope.

2.5. Quantitation of MICA protein level on IHC

MICA protein was expressed on the cell membrane of the epithelial cells. Levels of MICA expression were determined by assessing the staining intensity and the percentage of positively stained epithelial cells. The staining intensity and the percentage of positively stained cells were scored following the Allred scoring system, as shown in Table 1. The overall MICA expression score was calculated by adding intensity and percentage score results, which ranged from 0 to 8P. In total, 70 slides were assessed and evaluated by two independent pathologists at Hanoi Medical University after using a blind number code. Conflicting scores were not displayed. Scores of 0 to 5 are considered low expression and scores of 6 to 8 are considered high expression.

Table 1. Allred scoring system.

Positive cells (%)	Proportion score (A)	Intensity	Intensity score (B)
0	0P	None	0P
<1	1P	Weak	1P
1 to 10	2P	Intermediate	2P
11 to 33	3P	Strong	3P
34 to 66	4P	Final score: A+B Range: 0-8P	

2.6. Statistical analysis

Differences in EBV copy numbers based on MICA expression levels associated with the rs2596542 genotype in NPC tissues were calculated using the Student's T-test. In all statistical analyses, $p<0.05$ was considered to indicate a statistically significant difference. All tests were performed with the GraphPad Prism 8 software package (San Diego, USA).

3. Results

3.1. Main characteristics of the study

Among the 70 enrolled patients, 68.57% were male and 31.43% were female. Histopathology of all subjects showed two subtypes of NPC accounting for 82.86% in undifferentiated carcinoma type and 17.14% in squamous cell carcinoma type. Among participants, the average age of participants was 51.73±13.04. All patient characteristics are listed in Table 2.

Table 2. Study population characteristics.

Sex	Proportion/Amount
Male	48 (68.57%)
Female	22 (31.43%)
Histopathological	
Undifferentiated carcinoma	58 (82.86%)
Squamous cell carcinoma	12 (17.14%)
Age (Mean±SD)	51.73±13.04
Total	70

3.2. Frequencies of MICA rs2596542 variant in NPC

The genotype frequencies for the MICA rs2596542 variant in our study were analysed in 70 NPC patients and are described in Table 3. The haplotype frequencies of CC, CT, and TT were 40, 41.43 and 18.57%, respectively. These frequencies were obtained following the Hardy-Weinberg equilibrium (p=0.7).

Table 3. Allele and genotype frequencies of MICA rs2596542 in NPC patients.

Total (n=70)	Genotype			Allele	
	CC	*CT*	*TT*	*C*	*T*
	28 (40%)	29 (41.43%)	13 (18.57%)	85 (60.71%)	55 (39.29%)

3.3. Association between MICA expression and EBV measurements according to rs2596542 genotype

MICA expression in immunohistochemistry was indicated in low and high expression groups by the Allred-scored system. The expression of MICA showed a significant difference with regard to EBV copy numbers ($p<0.01$) (Fig. 1A). High expression of MICA presented a lower significance of EBV status. In addition, in comparison with the different rs2596542 genotypes, patients who carried homozygous CC displayed a high correlation with EBV copy numbers ($p<0.001$) while no significant difference was recorded in the other (Fig. 1B).

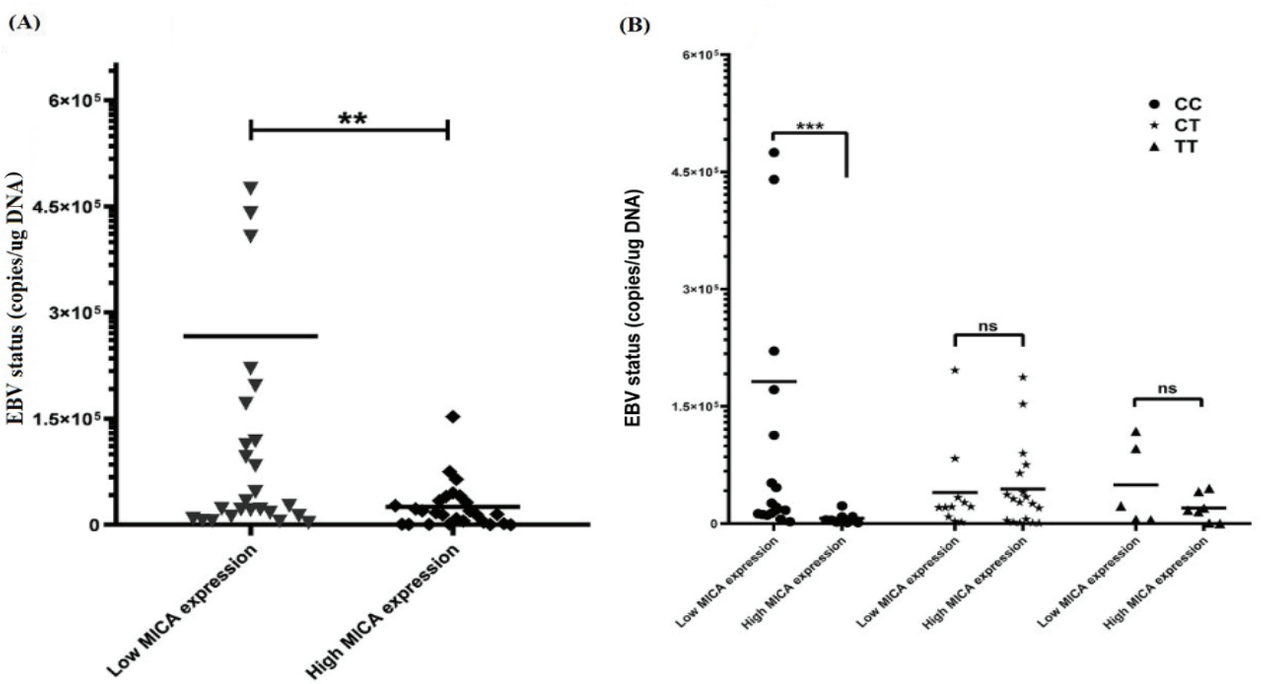

Fig. 1. EBV copy numbers in NPC tissues associated with MICA expression and association with rs2596542 variant. Each dot represents the EBV copy numbers (copies/μg of DNA) of each tumour sample by quantification Realtime-PCR. **(A)** Association between the expression of MICA and EBV copy numbers. **(B)** EBV copy numbers in NPC tissues according to MICA expression related to rs2596542. ns: not significant. **p<0.01 and ***p<0.001.

4. Discussion

Here, we evaluated the correlation between the expression level of MICA and EBV copy numbers in NPC tissue. We found that low MICA expression was associated with higher EBV copies, which suggest that EBV in tumour cells could contribute to regulating MICA expression. MICA is a member of the NKG2D ligand family and expresses broadly in human malignancies and virally-infected tissues. High expression of MICA can increase the cytotoxic activities of effector cells and the subsequent lysis of tumour cells. Numerous regulators have been elucidated to modulate MICA expression including viral infection, oxidative stress, heat sock, and the NF-κB pathway [19-21].

We determined MICA expression was associated with EBV levels among those with CC haplotype but found no significant difference between allele C and T of rs2596542. High expression of rs2596542 CC on the cell surface can inhibit virus infection, which causes the low copy number of EBV in NPC tumours. MICA can be shed on the infected cell surface and thus can lead to downregulating expression and reducing the recognition of NK cells and T-CD8$^+$ cells. H.V. Tong, et al. (2013) [22] postulated the hypothesis that the SNP rs2596542 in the promoter region of MICA has a significant association with MICA expression. Various studies have demonstrated the genetic variant of rs2596542, but their model was mainly focused on patients having HBV or HCV infection and liver cancer. By GWAS analysis, rs2596542 was considered as the molecular marker for HCC. Allele T of rs2596542 showed a higher risk factor than allele C in the occurrence of HCC-induced HCV. A.A. Mohamed, et al. (2017) [23] indicated that patients who carried allele T had a significantly higher risk for HCC (p=0.013, OR=1.93) while allele C was observed to reduce HCC risk. In our data, rs2596542 C (57/70) has a higher frequency among NPC patients suggesting a protective role of allele C against the infection of EBV. These results were in agreement with X.J. Kuang, et al. (2019) [24]. Meta-analysis of the relationship between rs2596542 genotype and the risk of HCC indicated that a higher homozygous rs2596542 CC proportion among healthy controls could indicate a protective effect of the CC genotype in progressive HCC. By contrast, several studies indicated that minor allele T of rs2596542 also presents a protecting effect on the HCC progression in Caucasians [25, 26]. However, we did not observe any significant difference between allele C and T of rs2596542 in our study, which may be related to ethnic characteristics.

Our data suggest that rs2596542 may be a possible genetic target for MICA shedding. Moreover, low expression of rs2596542 CC may be associated with MICA shedding, thus leading to EBV immune evasion by increasing EBV copy number in the tumour cells. To date, the genetic mechanisms for MICA shedding are still ambiguous. MICA shedding contains multiple proteases and has a crucial role in the immunotherapeutic target of cancer. These processes are related to several factors including MICA alpha-3 domain, ERp5 and protease of which the alpha-3 domain is a key proteolytic cleavage initiator. After ERp5 removes a disulfide bond between the amino acid residues 202 and 259, the alpha-3 domain is unfolded and thus exposed to the proteolytic cleave site [27]. Next, under metalloproteases, MICA is cut in somewhere or flank of the stalk in the alpha-3 domain, thus releasing the entire extracellular portion of MICA including the alpha-1 and alpha-2 domains that are the NKG2D binding sites. Using a monoclonal antibody, MICA shedding can be inhibited by blocking the alpha-3 domain that will activate NK cells to secrete IFN-γ and TNF-α thus killing infected cells [28]. Our data suggest that rs2596542 may be a possible genetic target for MICA shedding. Further study should be performed to clarify the contribution of rs2596542 to the shedding of MICA. This application will be a promising strategy for cancer immunotherapy.

On the other hand, MICA expression can be prevented by soluble MICA (sMICA). Overexpression of sMICA in circulation induces a decrease in NKG2DL expression on the cell surface, which results in suppressing NKG2D-mediated anti-tumour immunity [29]. Higher sMICA can have a higher rate of vascular invasion and poorer survival. Additionally, the high TMN (III/IV) stage of HCC patients shows higher levels of sMICA than patients with low TMN stage (I/II) of HCC [30]. Allele rs2596542 T has been demonstrated to be strongly associated with the low-level production of sMICA indicating an important role as a tumour suppressor [17, 31]. P.H.Y. Lo, et al. (2013) [32] explored that the carrying allele T of rs2596542 had a higher significant sMICA level in serum than those of allele C (p=0.00016). V. Kumar, et al. (2012) [31] found a significant level of sMICA in HBV-induced HCC patients. Thus, rs2596542 T was significantly associated with increased sMICA levels (p=0.009). Therefore, the genetic variation of MICA rs2596542 can be applied as a predictive risk biomarker for virus susceptibility to cancers.

5. Conclusions

In this study of 70 patients with EBV-positive NPC, our study indicated that EBV in tumour cells might contribute to regular MICA expression. The patients harbouring the CC genotype of rs2596542 MICA showed a greater immune response against tumours with low EBV concentration than tumours with high EBV concentration. This suggests a protective role of rs2596542C with the infection of EBV among NPC patients. Moreover, SNP rs2596542 may be a possible genetic target for immunotherapy as it is related to the shedding of MICA, which can cause EBV immune evasion. Further studies should be conducted to clarify the affection of rs2596542 to MICA shedding. Our results can be used to investigate the role of rs2596542 as a new predictive biomarker for EBV susceptibility to NPC.

CRediT author statement

Thanh Dat Ta: Data curation, Writing - Original draft preparation; Khanh Tran Van: Visualization, Investigation; Thanh Binh Nguyen: Software, Validation; Manh Thuong Le: Conceptualization, Methodology, Software; Long Ha Le Hai: Writing - Reviewing and Editing; Hoang Viet Nguyen: Supervision.

ACKNOWLEDGEMENTS

This study was supported by the Vietnam National Foundation for Science and Technology Development (NAFOSTED) under grant number 108.02-2018.312.

COMPETING INTERESTS

The authors declare that there is no conflict of interest regarding the publication of this article.

REFERENCES

[1] E.T. Chang, H.O. Adami (2006), "The enigmatic epidemiology of nasopharyngeal carcinoma", *Cancer Epidemiol. Biomarkers Prev.*, **15(10)**, pp.1765-1777, DOI: 10.1158/1055-9965.EPI-06-0353.

[2] E.B. Stelow, B.M. Wenig (2017), "Update from the 4th edition of the World Health Organization classification of head and neck tumours: Nasopharynx", *Head Neck Pathol.*, **11(1)**, pp.16-22, DOI: 10.1007/s12105-017-0787-0.

[3] D. Bakkalci, Y. Jia, J.R. Winter, et al. (2020), "Risk factors for Epstein Barr virus-associated cancers: A systematic review, critical appraisal, and mapping of the epidemiological evidence", *J. Glob. Health*, **10(1)**, DOI: 10.7189/jogh.10.010405.

[4] Y.P. Chen, A.T.C. Chan, Q.T. Le, et al. (2019), "Nasopharyngeal carcinoma", *The Lancet*, **394(10192)**, pp.64-80, DOI: 10.1016/S0140-6736(19)30956-0.

[5] J.X. Bei, X.Y. Zuo, W.S. Liu, et al. (2016), "Genetic susceptibility to the endemic form of NPC", *Chinese Clinical Oncology*, **5(2)**, DOI: 10.21037/cco.2016.03.11.

[6] K. Wei, Y. Xu, J. Liu, et al. (2011), "Histopathological classification of nasopharyngeal carcinoma", *Asian Pac. J. Cancer Prev.*, **12(5)**, pp.1141-1147.

[7] W.I. Wei, J.S. Sham (2005), "Nasopharyngeal carcinoma", *The Lancet*, **365(9476)**, pp.2041-2054, DOI: 10.1016/S0140-6736(05)66698-6.

[8] S.W. Tsao, C.M. Tsang, K.W. Lo (2017), "Epstein-Barr virus infection and nasopharyngeal carcinoma", *Philos. Trans. R. Soc. Lond. B Biol. Sci.*, **372(1732)**, DOI: 10.1098/rstb.2016.0270.

[9] S. Leung, B. Zee, B.B. Ma, et al. (2006), "Plasma Epstein-Barr viral deoxyribonucleic acid quantitation complements tumour-node-metastasis staging prognostication in nasopharyngeal carcinoma", *J. Clin. Oncol.*, **24(34)**, pp.5414-5418, DOI: 10.1200/JCO.2006.07.7982.

[10] R.J. Abbott, A. Pachnio, H.M. Long, et al. (2017), "Asymptomatic primary infection with Epstein-Barr virus: Observations on young adult cases", *J. Virol.*, **91(21)**, DOI: 10.1128/JVI.00382-17.

[11] C.S. Lowe, M. Rowe (2011), "Epstein-Barr virus infection of polarized epithelial cells via the basolateral surface by memory B cell-mediated transfer infection", *PLOS Pathog.*, **7(5)**, DOI: 10.1371/journal.ppat.1001338.

[12] A.M. Price, M.A. Luftig (2015), "To be or not IIb: A multi-step process for Epstein-Barr virus latency establishment and consequences for B cell tumorigenesis", *PLOS Pathog.*, **11(3)**, DOI: 10.1371/journal.ppat.1004656.

[13] D.F. Angelini, B. Serafini, E. Piras, et al. (2013), "Increased CD8+ T cell response to Epstein-Barr virus lytic antigens in the active phase of multiple sclerosis", *PLOS Pathog.*, **9(4)**, DOI: 10.1371/journal.ppat.1003220.

[14] O. Chijioke, A. Muller, R. Feederle, et al. (2013), "Human natural killer cells prevent infectious mononucleosis features by targeting lytic Epstein-Barr virus infection", *Cell Rep.*, **5(6)**, pp.1489-1498, DOI: 10.1016/j.celrep.2013.11.041.

[15] M. Bauer, O. Mandelboim, C. Wickenhauser, et al. (2021), "Epstein-Barr virus-associated malignancies and immune escape: The role of the tumor microenvironment and tumor cell evasion strategies", *Cancers (Basel)*, **13(20)**, DOI: 10.3390/cancers13205189.

[16] X. Yang, S. Kuang, L. Wang, et al. (2018), "MHC class I chain-related A: Polymorphism, regulation and therapeutic value in cancer", *Biomedicine & Pharmacotherapy*, **103**, pp.111-117, DOI: 10.1016/j.biopha.2018.03.177.

[17] V. Kumar, N. Kato, Y. Urabe, et al. (2011), "Genome-wide association study identifies a susceptibility locus for HCV-induced hepatocellular carcinoma", *Nat. Genet.*, **43(5)**, pp.455-458, DOI: 10.1038/ng.809.

[18] D. Chen, U. Gyllensten (2014), "MICA polymorphism: Biology and importance in cancer", *Carcinogenesis*, **35(12)**, pp.2633-2642, DOI: 10.1093/carcin/bgu215.

[19] V. Groh, S. Bahram, S. Bauer, et al. (1996), "Cell stress-regulated human major histocompatibility complex class I gene expressed in gastrointestinal epithelium", *PNAS*, **93(22)**, pp.12445-12450, DOI: 10.1073/pnas.93.22.12445.

[20] K. Yamamoto, Y. Fujiyama, A. Andoh, et al. (2001), "Oxidative stress increases MICA and MICB gene expression in the human colon carcinoma cell line (CaCo-2)", *Biochimica et Biophysica Acta (BBA) - General Subjects*, **1526(1)**, pp.10-12, DOI: 10.1016/S0304-4165(01)00099-X.

[21] D. Lin, H. Lavender, E.J. Soilleux, et al. (2012), "NF-κB regulates MICA gene transcription in endothelial cell through a genetically inhibitable control site", *Journal of Biological Chemistry*, **287(6)**, pp.4299-4310, DOI: 10.1074/jbc.M111.282152.

[22] H.V. Tong, N.L. Toan, L.H. Song, et al. (2013), "Hepatitis B virus-induced hepatocellular carcinoma: Functional roles of MICA variants", *J. Viral Hepat.*, **20(10)**, pp.687-698, DOI: 10.1111/jvh.12089.

[23] A.A. Mohamed, O.M. Elsaid, E.A. Amer, et al. (2017), "Clinical significance of SNP (rs2596542) in histocompatibility complex class I-related gene A promoter region among hepatitis C virus related hepatocellular carcinoma cases", *J. Adv. Res.*, **8(4)**, pp.343-349, DOI: 10.1016/j.jare.2017.03.004.

[24] X.J. Kuang, D.C. Mo, Y. Qin, et al. (2019), "Single nucleotide polymorphism of rs2596542 and the risk of hepatocellular carcinoma development", *Medicine (Baltimore)*, **98(11)**, DOI: 10.1097/MD.0000000000014767.

[25] C.M. Lange, S. Bibert, J.F. Dufour, et al. (2013), "Comparative genetic analyses point to HCP5 as susceptibility locus for HCV-associated hepatocellular carcinoma", *J. Hepatol.*, **59(3)**, pp.504-509, DOI: 10.1016/j.jhep.2013.04.032.

[26] K. Chen, W. Shi, Z. Xin, et al. (2013), "Replication of genome wide association studies on hepatocellular carcinoma susceptibility loci in a Chinese population", *PLOS ONE*, **8(10)**, DOI: 10.1371/journal.pone.0077315.

[27] B.K. Kaiser, D. Yim, I.T. Chow, et al. (2007), "Disulphide-isomerase-enabled shedding of tumour-associated NKG2D ligands", *Nature*, **447(7143)**, pp.482-486, DOI: 10.1038/nature05768.

[28] C. Du, R. Cook, T.N. Lombana, et al. (2019), "MICA immune complex formed with alpha 3 domain-specific antibody activates human NK cells in a Fc- dependent manner", *Journal for Immuno Therapy of Cancer*, **7(1)**, DOI: 10.1186/s40425-019-0687-9.

[29] H.R. Salih, H.G. Rammensee, A. Steinle, et al. (2002), "Cutting edge: Down-regulation of MICA on human tumours by proteolytic shedding", *J. Immunol.*, **169(8)**, pp.4098-4102, DOI: 10.4049/jimmunol.169.8.4098.

[30] K. Kohga, T. Takehara, T. Tatsumi, et al. (2008), "Serum levels of soluble major histocompatibility complex (MHC) class I-related chain A in patients with chronic liver diseases and changes during transcatheter arterial embolization for hepatocellular carcinoma", *Cancer Science*, **99(8)**, pp.1643-1649, DOI: 10.1111/j.1349-7006.2008.00859.x.

[31] V. Kumar, N. Kato, Y. Urabe, et al. (2012), "Soluble MICA and a MICA variation as possible prognostic biomarkers for HBV-induced hepatocellular carcinoma", *PLOS ONE*, **7(9)**, DOI: 10.1371/journal.pone.0044743.

[32] P.H.Y. Lo, Y. Urabe, V. Kumar, et al. (2013), "Identification of a functional variant in the MICA promoter which regulates MICA expression and increases HCV-related hepatocellular carcinoma risk", *PLOS ONE*, **8(4)**, DOI: 10.1371/journal.pone.0061279.

DOI: 10.31276/VJSTE.65(1).76-80

Influence of fetal calf serum on the production of bovine embryos *in vitro*

Khanh Van Nguyen[1], Thi Kim Yen Pham[1], Thi Au Hoang[1], Quang Minh Luu[2], Doan Lan Pham[3*]

[1]Key Laboratory of Animal Cell Biotechnology, National Institute of Animal Science, 9, Tan Phong Street, Thuy Phuong Ward, Bac Tu Liem District, Hanoi, Vietnam
[2]Ministry of Science and Technology, 113 Tran Duy Hung Street, Trung Hoa Ward, Cau Giay District, Hanoi, Vietnam
[3]National Institute of Animal Science, 9, Tan Phong Street, Thuy Phuong Ward, Bac Tu Liem District, Hanoi, Vietnam

Received 21 June 2022; revised 24 August 2022; accepted 13 September 2022

Abstract:

The aim of the present study was to evaluate the effect of foetal calf serum (FCS) on the production of bovine embryo *in vitro*. We conducted two experiments: (1) to evaluate the effect of FCS on the production of bovine embryo *in vitro* and (2) to evaluate the effect of duration of FCS supplementation on the production of bovine embryo *in vitro*. In experiment 1, we divided mature bovine oocytes after *in vitro* fertilization into four embryo culture media: CR1aa, CR1aa+FCS, SOFaa, and SOFaa+FCS. Embryos cultured in CR1aa and SOFaa media supplemented with FCS resulted in a higher cleavage and blastocyst formation rates than when cultured in CR1aa and SOFaa without FCS. Embryos cultured in the medium with FCS had a higher the average number of cells/blastocyst than the medium without FCS. The SOFaa+FCS group had a higher average number of cells/embryos than the other groups (94.32; $p<0.05$). In experiment 2, we added FCS to bovine embryo culture *in vitro* at the following times: 0 h, 48 h, and 120 h after fertilization. The rate of oocyte cleavage, blastocyst formation, and hatching blastocyst rate of the 0-h group were higher than that of 48-h and 120-h groups (82.96 vs 70.5 and 70.24%; 34.51 vs 24.21 and 23.18%; 10.5 vs 6.12 and 4.13%; respectively, $p<0.05$). However, there was no difference in the average number of cells/blastocysts between the groups. In conclusion, the addition of FCS to embryo culture media improved the efficiency of bovine embryo production *in vitro* and *in vitro* bovine embryo quality. The appropriate time to add FCS to bovine embryo culture *in vitro* was 0 h after fertilization.

Keywords: **bovine embryos *in vitro*, embryo development, foetal calf serum.**

Classification numbers: **3.4, 3.5**

1. Introduction

The generation of calves derived from embryos *in vitro*, showing that bovine embryo *in vitro* has a vital role in the cattle industry was first reported in [1]. The success of *in vitro* oocyte maturation techniques, *in vitro* fertilization, and *in vitro* embryo culture have shortened and accelerated the rate of genetic improvement in cattle. The process of *in vitro* embryo culture has fundamental differences compared with *in vivo* embryo culture [2]. *In vitro* embryo culture media play an essential role in developing bovine embryos *in vitro* and have a diverse composition, including simple media defined with salts or complex unspecified media supplemented with serum and unknown components [3]. Factors and protein sources have been used to supplement the embryo culture medium to support embryonic development *in vitro* [4].

Current prevalent *in vitro* bovine embryo culture media are CR1aa or SOF with or without the addition of foetal calf serum (FCS) and amino acids. FCS is often added to the embryo culture medium *in vitro* because it contains nutritional factors and substances beneficial to embryo development such as antioxidants, growth factors, and necessary nutrients required for cell growth and development [5]. Serum affects the division and formation of morula, i.e., follicular bovine oocytes after fertilization. Some studies have shown that the presence of serum in bovine embryo culture media supports blastocyst development and hatching as well as increases the total cell number per blastocyst [6]. However, the presence of FCS in bovine embryo culture *in vitro* increased the lipid content of the embryos, which causes adverse effects on embryo freezing. In addition, bovine serum can carry pathogenic viruses that affect the

*Corresponding author: Email: pdlanvn@yahoo.com

formation and development of the foetus after embryo transfer [7]. Therefore, up to now, there is still much controversy surrounding the use of FCS for *in vitro* bovine embryo culture.

In Vietnam, research on the production of bovine embryos *in vitro* has been carried out since the 1990s and is currently being continued at the Institute of Biotechnology, Vietnam Academy of Sciences; the Key Laboratory of Animal Cell Biotechnology, National Institute of Animal Sciences, and the Vietnam Academy of Agriculture [8]. Researchers are also trying to find ways to improve and enhance the quality of bovine embryos *in vitro* [3]. However, no reports have evaluated the effect of foetal calf serum (FCS) on the production of bovine embryo *in vitro*. This study was conducted to generate quality commercial *in vitro* bovine embryos for cryopreservation or embryo transfer.

2. Materials and methods

2.1. Collection oocytes and in vitro maturation

Ovaries were collected from female beef cattle at slaughterhouses and carried to the laboratory within 2-3 h in Dulbecco's phosphate buffered saline supplemented with antibiotics. Then antral follicles with 3-8-mm diameter were aspirated with 18 G needles attached to a syringe containing oocyte collection medium (TALP-Hepes + calf serum and antibiotics) and the liquid mixture was placed in 15-ml centrifuge tubes for at least 5 min at 37°C. Cumulus oocytes complexes (COCs) were collected under the stereomicroscope after introducing the sediment into an oocyte collection medium. Bovine oocytes after collection were immediately washed three times in the culture medium, then transferred to culture in 4-well plates (Thermo Fisher Scientific, Waltham, MA, USA) containing the culture medium covered by mineral oil (Sigma, USA) and incubated in a humidified atmosphere of 5% CO_2 in air at 38.5°C (50 oocytes/well) for 22-24 h. The maturation culture medium was TCM 199 medium (Invitrogen Co., Carlsbad, CA, USA) supplemented with 1 g/ml cysteamine, 200 µg/ml FSH (follicle-stimulating hormone), 5% foetal bovine serum (Sigma; USA), and antibiotics.

2.2. In vitro fertilization of bovine oocytes

After 22-24 h of maturation, COCs were fertilized with frozen-thawed bull spermatozoa that had been previously tested for IVF as described by N. Saito, et al. (1995) [9]. Frozen-thawed bull spermatozoa were thawed at 37°C and the sperm were washed and pelleted in BO-IVF medium (IVF Bioscience, USA) by centrifuge at 1800 g for 5 min at room temperature and motile sperm were recovered. Then, sperm were diluted in BO-IVF medium (final density of $5x10^6$ sperm/ml). Before fertilization, matured bovine oocytes were kept or partially removed from the surrounding cumulus cell layer and washed in the BO-IVF medium. Thereafter, the diluted sperm and oocytes were transferred to the insemination droplet containing BO-IVF medium and co-culture for 5 h at 38.5°C, 5% CO_2, 5% O_2, and saturated air humidity.

2.3. In vitro bovine embryo culture

After 5 h of co-culture, cumulus cells were removed by repeated pipetting and then matured oocytes with an extruded first polar body (presumed zygotes) were selected with up to 50 presumed zygotes washed and transferred to 4-well dishes containing IVC medium (CR1aa or SOFaa with or without FCS) according to the experimental design below. The dishes were incubated at 38.5°C in a humidified atmosphere of 5% CO_2, 5% O_2 in air. The CR1aa medium contained albumin serum bovine, sodium pyruvate, and glutamic and amino acids. The SOFaa medium contained sodium pyruvate, lactate, amino acid, albumin serum bovine, and myo inositol.

(1) Experiment 1: To evaluate the effect of FCS on the production of bovine embryo *in vitro*, we divided mature bovine oocytes after *in vitro* fertilization into four embryo culture media: CR1aa, CR1aa supplemented with 2.5% FCS (v/v), SOFaa, and SOFaa supplemented with 2.5% FCS (v/v).

(2) Experiment 2: To evaluate the effect of FCS supplementation duration on the production of bovine embryo *in vitro*, we supplemented with 2.5% FCS (v/v) to bovine embryo culture *in vitro* at the following times: Day 0, Day 2, and Day 5 after fertilization.

The cleavage rates were checked on Day 2, the blastocyst rates were checked on Day 7, and the hatching blastocyst rates were checked on Day 8 or Day 9 after *in vitro* fertilization. *In vitro* bovine hatching blastocysts are shown in Fig. 1.

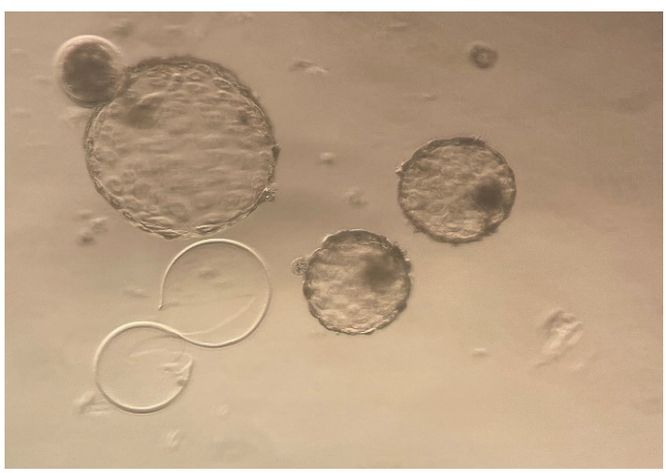

Fig. 1. *In vitro* bovine hatching blastocyst.

2.4. Hoechst 33342 staining method

Oocytes/embryos were washed in PBS solution supplemented with 0.3% PVP. Next, the oocytes/embryos were transferred to the oocytes/embryo staining solution (50 µl Hoechst 33342 stock + 450 µl absolute ethanol) overnight at 4°C (Hoechst 33342 stock: 250 µg Hoechst 33342/ml absolute ethanol). After the oocytes/embryos were stained in staining solution, the oocytes/embryos were transferred to absolute ethanol, and then transferred to a glycerol solution. After being washed in glycerol, the oocytes/embryos were transferred to the slide, one drop per oocyte/embryo, and lined up vertically on the slide. The lamen was placed on the slide and the sample was examined under a fluorescence microscope (Fig. 2).

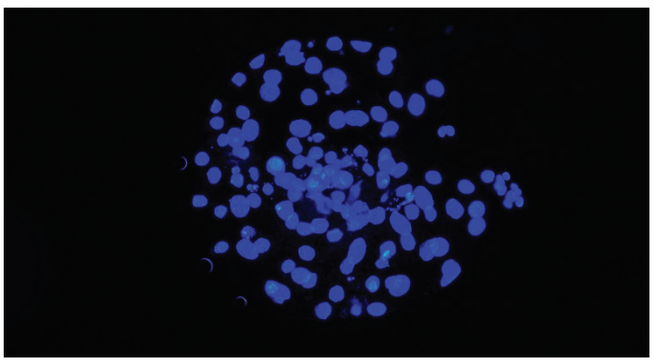

Fig. 2. Bovine blastocysts stained with Hoechst 3332.

2.5. Data analysis

Data were expressed as mean ± SEM values and analysed by t-test with $p<0.05$ defined as the significance level.

3. Results and discussion

3.1. Effect of FCS on the production of bovine embryos in vitro

The success of the production of bovine embryos *in vitro* depends not only on the IVM and IVF media but also on the embryo culture medium. The current basic *in vitro* bovine embryo culture medium is CR1aa or SOFaa with or without serum. To evaluate the effect of FCS on the production of bovine embryos *in vitro*, we divided *in vitro* mature bovine oocytes after *in vitro* fertilization into four different embryo culture media: CR1aa, CR1aa+FCS, SOFaa, and SOFaa+FCS. The effect of FCS on the efficiency of production of bovine embryos *in vitro* was evaluated based on the division rate, blastocyst generation, extruded blastocysts, and the quality of the *in vitro* bovine blastocysts produced (the average number of cells/blastocysts). The results are shown in Table 1.

Table 1. Effect of FCS on *in vitro* bovine embryogenesis.

Medium	Cleaved	Blastocysts	Hatching blastocysts	The average number of cells/blastocysts
CR1aa	71.64^{a}±1.92 (175/245)	4.11^{a}±2.12 (10/245)	0	71.5^{a}±1.98
SOFaa	70.62^{a}±1.76 (184/261)	22.31^{b}±2.09 (58/261)	2.15^{a}±1.98 (5/261)	80.93^{b}±2.31
CR1aa + FCS	74.22^{b}±2.01 (181/244)	16.98^{b}±1.58 (41/244)	4.59^{a}±2.03 (11/244)	81.35^{b}±2.15
SOFaa + FCS	82.96^{c}±1.35 (222/268)	34.51^{c}±1.76 (92/268)	10.54^{b}±1.74 (28/268)	94.32^{c}±2.01

Note: Values in the same column with different letters are significantly different ($p<0.05$).

Table 1 shows that embryo culture in CR1aa and SOFaa medium supplemented with FCS gave higher division and blastocyst formation rates when cultured in CR1aa and SOFaa without serum supplementation (74.22% and SOFaa, respectively, 82.96 vs 71.64 and 70.62%; 4.11 and 22.31% vs 16.98 and 34.51%; $p<0.05$).

To date, there is no consensus among the results of studies on the effects of FCS during *in vitro* bovine embryo culture. Our research results are similar to those of S.B.S. Netto, et al. (2020) [10], still, there were differences from previous studies [7, 11]. According to S.B.S. Netto, et al. (2020) [10], the presence of FCS in the embryo culture medium increased the blastocyst formation rate. According to B.H. Choi, et al. (2019) [7], the division rate when growing bovine embryos *in vitro* in the FCS medium was higher than in the serum-free medium. However, the blastocyst formation rate of the group with FCS was lower than that without FCS. Meanwhile, A.P. Gandhi, et al. (2000) [11] did not find a difference in blastocyst formation rate when growing bovine embryos *in vitro* in media with FCS or without FCS; however, blastocysts derived from SOFaa medium had the highest average number of cells/blastocysts. The difference between experimental results may be due to the origin of bovine oocytes used in the study, experimental conditions, and embryo culture environment.

In vitro embryo culture produces differences from living organisms, especially in ruminants [2]. The *in vitro* embryo culture medium plays an essential role in developing *in vitro* embryos. *In vitro* embryo culture media have a diverse composition, including simple saline solutions or indeterminate complex media supplemented with serum [3]. The presence of FCS in IVC media was proposed because the serum contained components that provide nutrients to the embryo and inactivate toxic agents [7]. According to A.A. Wahab, et al. (2018) [12], the supplementation of FCS into the embryo culture medium is very important, because FCS

contains many hormones, vitamins, transport proteins, and growth factors that optimize oocyte maturation. FCS contains potent antioxidant activities which assist in chelating free radicals and protecting oocytes from oxidative stress conditions. In addition, the presence of FCS in the embryo culture medium reduced hardening of the zona pellucida, thereby improving the efficiency of embryo production and embryo quality *in vitro*.

Blastocyst quality is essential to confirm the pregnancy rate after embryo transfer [13]. The percentage of hatching blastocysts and the average number of cells/blastocysts were considered to some extent as a measure of embryo quality. In this study, the rate of hatching blastocysts was highest when *in vitro* bovine embryos were grown in SOFaa medium supplemented with FCS (10.54%; $p<0.05$). Embryos were produced in medium with FCS had a higher the average number of cells/blastocysts than the medium without FCS. The SOFaa+FCS group had a higher average number of cells/embryos than the others (94 vs 32; $p<0.05$). The percentage of hatching blastocysts and the average number of cells/blastocysts in the SOFaa+FCS group were higher than those reported by A.P. Gandhi, et al. (2000) [11]. According to A.P. Gandhi, et al. (2000) [11], the percentage of hatching blastocysts and the average number of cells/blastocysts of the SOFaa+FCS group reached 9.5% and 92.1%, respectively, meanwhile, according to our research, they reached 10.54% and 94.32%. This difference may be because we used TCM199 medium for maturation, while A.P. Gandhi, et al. (2000) [11] used SOFaa. In addition, the percentage of hatching blastocysts and the average number of cells/blastocysts depend on the quality of oocytes and the quality of sperm used by each laboratory.

Despite the addition of FCS, *in vitro* culture of bovine embryos in SOFaa medium supplemented with serum resulted in a higher rate of blastocyst formation than in CR1aa medium supplemented with FCS (34.51% vs 98%; $p<0.05$). SOFaa is a common medium used for *in vitro* bovine embryo culture. This medium contains the same ingredients as bovine oviduct fluid such as hormones, growth factors, and some amino acids. The presence of these factors in the embryo culture medium increases the ability of embryos to develop before transfer [14].

3.2. Effect of time of bovine serum supplementation on the production bovine embryo in vitro

In this study, to evaluate the effect of FCS supplementation time on *in vitro* bovine embryogenesis efficiency, we added FCS to the embryo culture medium at the following time points: 0 h, 48 h, and 120 h after fertilization. The results are shown in Table 2.

Table 2. Effect of time of FCS supplementation on the production bovine embryo *in vitro*.

FCS supplementation time	Cleaved	Blastocysts	Hatching blastocysts	The average number of cells/ blastocysts
0 h	(222/268) 82.96^{a}±1.35	(92/268) 34.51^{a}±1.76	(28/268) 10.54^{a}±1.74	94.97±1.89
48 h	(194/276) 70.45^{b}±1.68	(66/276) 24.21^{b}±1.42	(16/276) 6.12^{b}±1.33	93.18±1.16
120 h	(183/261) 70.24^{b}±2.01	(60/261) 23.18^{b}±1.89	(10/261) 4.13^{b}±2.69	92.89±1.76

Note: Values in the same column with different letters are significantly different ($p<0.05$).

Table 2 shows that the percentage of oocytes dividing, blastocyst formation rate, and hatching rate of the 0-h group was higher than that of 48-h and 120-h groups (82.96% vs 70.45% and 70.24%; 34.51% vs 24.21% and 23.18%; 10.54% vs 6.12% and 4.13%; $p<0.05$, respectively). However, there was no difference in the average number of cells/blastocysts between the groups (Table 2). Our results differed from those of A.A. Wahab, et al. (2018) [12]. According to A.A. Wahab, et al. (2018) [12], there was no difference in division rate when adding FCS at 20 h or 42 h post-insemination.

This study suggests that the duration of FCS supplementation affected the efficiency of bovine embryo production *in vitro*. The addition of FCS at 0 h after fertilization improved the efficiency of the production of bovine embryo *in vitro*. According to S.B.S. Netto, et al. (2020) [10] and E. Gómez, et al. (2008) [15], the addition of FCS to the embryo culture medium at 0 h after fertilization will accelerate the morula development stage. Although the FCS's role in embryonic development is not entirely understood, it is related to growth factors, amino acids, or FCS's antioxidant capacity in the embryo culture medium. These factors help increase blastocyst generation rate. The quality of embryos generated from culture medium with FCS is better than without FCS [10].

In our study, the addition of FCS at 48 h or 120 h after fertilization reduced blastocyst formation rate. According to S.B.S. Netto, et al. (2020) [10], when cultured in embryo culture with only albumin serum bovine, there might be a lack of factors that stimulate embryo development thereby allowing the post-fertilization oocytes to develop to the blastocyst stage less often. FCS supplementation to embryo culture medium improved cell proliferation and supported dilation [16]. Besides, the presence of FCS in the embryo culture medium reduces cell apoptosis. Apoptosis plays a vital role in embryonic development, acting as a quality control measure by eliminating abnormal, damaged, or dormant cells [10].

Although FCS supports the development of bovine embryos, in this study, we only added FCS to the bovine embryo culture medium *in vitro* at a concentration of 2.5% (v/v). According to M.J. Sudano, et al. (2011) [17], the presence of FCS in embryo culture increased the lipid content of bovine embryos *in vitro*, which was not beneficial for *in vitro* cryopreservation of bovine embryos. Therefore, reducing FCS concentration to 2.5% (v/v) in *in vitro* bovine embryo culture is necessary to maintain quality *in vitro* bovine blastocyst production.

In this study, in order to improve the efficiency of bovine embryo production *in vitro* and *in vitro* bovine embryo quality, bovine embryos were cultured and incubated at 5% CO_2. Regulating the CO_2 level during embryo culture helps maintain the right amount of pH inside the incubator (pH7.2-7.4). It is known that bovine embryos are sensitive to pH as changes in pH can affect cell metabolism and the quality of bovine embryos *in vitro*.

4. Conclusions

The addition of FCS to embryo culture media improved the efficiency of bovine embryo production *in vitro* and *in vitro* bovine embryo quality. The appropriate time to add FCS to bovine embryo culture *in vitro* was 0 h after fertilization.

CRediT author statement

Khanh Van Nguyen: Conceptualization, Methodology, Formal analysis, Writing, Review, Editing; Thi Kim Yen Pham: Data analyst; Thi Au Hoang: Data analyst; Quang Minh Luu: Review, Data analyst; Doan Lan Pham: Conceptualisation, Methodology, Formal analysis, Writing, Review, Editing.

ACKNOWLEDGEMENTS

The projects carried out the study: "Study on the influence of cumulus cells and embryo culture environment on the results of in vitro bovine embryogenesis". The authors sincerely appreciated funding to support regular operations of the Key Laboratory of Animal Cell Biotechnology, National Institute of Animal Science, Hanoi, Vietnam.

COMPETING INTERESTS

The authors declare that there is no conflict of interest regarding the publication of this article.

REFERENCES

[1] B.G. Brackett, D. Bousquet, M.L. Boice, et al. (1982), "Normal development following *in vitro* fertilization in the cow", *Biol. Reprod*, **27**, pp.147-158, DOI: 10.1095/biolreprod27.1.147.

[2] P. Lonergan, D. Rizos, A.G. Adan, et al. (2003), "Temporal divergence in the pattern of messenger RNA expression in bovine embryos cultured from the zygote to blastocyst stage *in vitro* or *in vivo*", *Biol. Reprod.*, **69**, pp.1424-1431, DOI: 10.1095/biolreprod.103.018168.

[3] M. Lane, D.K. Gardner (2007), "Embryo culture medium: Which is the best?", *Best Pract. Res. Clin. Obstet. Gynaecol.*, **21**, pp.83-100, DOI: 10.1016/j.bpobgyn.2006.09.009.

[4] T.C. Sovernigo, P.R. Adona, P.S. Monzani, et al. (2017), "Effects of supplementation of medium with different antioxidants during *in vitro* maturation of bovine oocytes on subsequent embryo production", *Reproduction Domest. Animal*, **52**, pp.561-569, DOI: 10.1111/rda.12946.

[5] M. Murakami, Y.J. Dong, T. Suzuki, et al. (2011), "Development and subsequent cryotolerance of domestic cat embryos cultured in serum-free and serum-containing media", *Cryobiology*, **63**, pp.170-174, DOI: 10.1016/j.cryobiol.2011.06.002.

[6] E. Wydooghe, S. Heras, J. Dewulf, et al. (2014) "Replacing serum in culture medium with albumin and insulin, transferrin and selenium is the key to successful bovine embryo development in individual culture", *Reproduction Fertility and Development*, **26**, pp.717-724, DOI: 10.1071/RD13043.

[7] B.H. Choi, R. Kong, J.J. In, et al. (2019), "Effect of serum and serum free media on the developmental competence of OPU derived bovine IVP embryo", *J. Anim. Reprod. Biotechnol*, **34**, pp.305-310, DOI: 10.12750/JARB.34.4.305.

[8] D.T.K. Lanh, N.T.N. Anh, H.T.K. Chi, et al. (2021), "Improvement of the efficiency of bovine in vitro fertilization embryo production", *Vietnam J, Agri. Sci.*, **19(1)**, pp.25- 32 (in Vietnamese).

[9] N. Saito, D.I. Shimohiara, D.H. Kanagawa (1995), *Manual of Bovine Embryo Transfer*, Japan Livestock Technology Association, pp.332-340.

[10] S.B.S. Netto, J.F.W. Spricigo, L.O. Leme, et al. (2020), "The replacement of foetal bovine serum with bovine serum albumin during oocyte maturation and embryo culture does not improve blastocyst quality after slow freezing cryopreservation", *Biopreserv. Biobank*, **18**, pp.171-179, DOI: 10.1089/bio.2019.0059.

[11] A.P. Gandhi, M. Lane, D.K. Gardner, et al. (2000), "A single medium supports development of bovine embryos throughout maturation, fertilization and culture", *Hum. Reprod.*, **15**, pp.395-401, DOI: 10.1093/humrep/15.2.395.

[12] A.A. Wahab, R.L.A. Aziz, N.A. Helmy, et al. (2018), "The impact of using newborn bovine serum as foetal calf serum substitute in the *in vitro* bovine embryos production system", *Porto Biomed. J.*, **3(2)**, DOI: 10.1016/j.pbj.0000000000000003.

[13] D. Rizos, A.G. Adán, S.P. Garnelo, et al. (2003), "Bovine embryo culture in the presence or absence of serum: Implications for blastocyst development, cryotolerance, and messenger RNA expression", *Biol. Reprod.*, **68**, pp.236-243, DOI: 10.1095/biolreprod.102.007799.

[14] J. Block, P.J. Hansen, B. Loureiro, et al. (2011), "Improving post-transfer survival of bovine embryos produced *in vitro*: Actions of insulin-like growth factor-1, colony stimulating factor-2 and hyaluronan", *Theriogenology*, **76**, pp.1602-1609, DOI: 10.1016/j.theriogenology.2011.07.025.

[15] E. Gomez, A. Rodriguez, M. Munoz, et al. (2008), "Serum free embryo culture medium improves *in vitro* survival of bovine blastocysts to vitrification", *Theriogenology*, **69**, pp.1013-1021, DOI: 10.1016/j.theriogenology.2007.12.015.

[16] J.A. Neira, D. Tainturier, M.A. Pena, et al. (2010), "Effect of the association of IGF-I, IGF-II, bFGF, TGF-β1, GM-CSF, and LIF on the development of bovine embryos produced *in vitro*", *Theriogenology*, **73**, pp.595-604, DOI: 10.1016/j.theriogenology.2009.10.015.

[17] M.J. Sudano, D.M. Paschoal, T.D.S. Rascado, et al. (2011), "Lipid content and apoptosis of *in vitro*-produced bovine embryos as determinants of susceptibility to vitrification", *Theriogenology*, **75**, pp.1211-1220, DOI: 10.1016/j.theriogenology.2010.11.033.

DOI: 10.31276/VJSTE.65(1).81-88

Study on fabrication of ZnO@TiO_2 nanocomposite for perozone degradation of amoxicillin from aqueous solution

Thanh Diem Ngo Thi[1], Xuan Hoan Nguyen[1], Hiep Vu Phung[2], Minh Thanh Le[1], Lan Huong Nguyen[1]*

[1]Ho Chi Minh City University of Food Industry, 140 Le Trong Tan Street, Tay Thanh Ward, Tan Phu District, Ho Chi Minh City, Vietnam
[2]Southern Natural Resources and Environment Company, Ministry of Natural Resources and Environment, 30, 3 Street, Quarter 4, An Khanh Ward, Thu Duc City, Ho Chi Minh City, Vietnam

Received 14 October 2021; revised 18 November 2021; accepted 26 November 2021

Abstract:

In this study, a simple method for fabrication of a ZnO@TiO_2 nanocomposite was developed to degrade amoxicillin (AMX) from aqueous solution by heterogeneous photocatalytic perozone under UV irradiation (O_3/H_2O_2/ZnO@TiO_2/UV). ZnO nanoparticles were formed by the sol-gel method. The ZnO-NPs were then composited with commercial TiO_2 at modification ratios of 0, 10, 20, 30, 40, and 50% of ZnO-NPs to generate ZnO@TiO_2 nanocomposites. The physical-chemical characteristics of ZnO, TiO_2, and ZnO@TiO_2 at the optimal modification ratio were determined using S_{BET}, SEM, EDX, and XRD analysis. The catalytic activity of ZnO@TiO_2 was evaluated by degradation of AMX in an O_3/H_2O_2/ZnO@TiO_2/UV system. The results showed that 10%ZnO@TiO_2 exhibited the highest catalytic activity in degradation (in term of COD removal) of AMX with about 80% for 70 min of reaction time. This efficiency was higher than that of both systems using ZnO or TiO_2 only by double. This primary finding demonstrates the feasibility of 10%ZnO@TiO_2 photocatalysts in perozone systems to degrade persistent organic compounds in practical applications.

Keywords: **amoxicillin, ball milling, perozone, ZnO@TiO_2.**

Classification numbers: **3.4, 3.5**

1. Introduction

Nowadays, water source pollution by antibiotic residuals has become a global environmental problem. Owing to the difficult-to-degrade property of pharmaceutical residues, conventional methods can only partially treat these residues with high cost from industrial effluents [1-3]. As a result, there have been huge amounts of antibiotics discharged into receiving bodies leading to serious effects on human health and ecosystems, even at a low concentration [3, 4]. Among antibiotics, amoxicillin (AMX) is widely used to treat diseases and infections in almost all countries [5]. However, only 10-20% of amoxicillin is ingested by the human body and other organisms [5]. Indeed, AMX has been detected in almost every media such as surface water, domestic and industrial wastewater [6, 7], hospital waste [8], and secondary treated effluent with concentrations ranging from several ng/l to mg/l [9]. Thus, it is necessary to remove AMX residues from these media to conserve water resources for sustainable development.

Advanced oxidation processes (AOPs) are one of the most effective methods for the removal of antibiotic residuals because they possess several advantages such as high oxidation rate, no-secondary pollution, and non-selective oxidation of POPs through the continuous generation of hydroxyl radicals [2, 5, 10-12]. Among AOPs, ozonation- and photocatalysis-based AOPs have been proven effective at the removal of various persistent organic pharmaceutical contaminants [13-18]. However, using ozonation and photocatalysis processes separately meets some drawbacks such as high cost, low stability, low solubility in water, and slow oxidation rates. Thus, in order to overcome these disadvantages, ozonation has recently been combined with various heterogeneous photocatalysis processes to promote overall treatment efficiency [19, 20].

Titanium dioxide (TiO_2) and zinc oxide (ZnO) are photocatalysts that have been applied the most widely to photocatalytic oxidation processes [21, 22]. However, the application of TiO_2 alone in photocatalytic reactions has several limitations. The most conspicuous drawback of TiO_2 is its electron-hole recombination ability after excitation due to a high rate in recombination of photoinduced charge carriers [20-22]. This type of disadvantage leads

*Corresponding author: Email: huongnl@hufi.edu.vn

to difficulties in its practical application to wastewater treatment [13, 19]. Therefore, to overcome the disadvantages of TiO_2, a composite of TiO_2 with other semiconductors has been formed to improve its photolytic activity. In this study, ZnO nanoparticles were chosen to composite with TiO_2 thanks to its similarity in band gap energy (3.34 eV and 3.12 eV, respectively, for ZnO and TiO_2) [23]. Besides, ZnO also has photolytic catalytic activity and a reactive ability that is similar to TiO_2 under irradiation conditions. Especially, there are oxygen vacancies in ZnO NPs when they are fabricated using sol-gel. These oxygen vacancies in ZnO NPs indicate enhanced visible light activity for photocatalytic reactions [23]. The oxygen vacancy defects are also a main defect in TiO_2 materials, which could also play role as the photogenerated electron trapped sites. Thus, ZnO@TiO_2 can also be active under the visible light region [24-26]. For these reasons, ZnO is selected to couple with TiO_2 to form a composite photocatalyst that promotes synergistic effects of heterogeneous photocatalysis perozone to treat AMX in this study.

The aim of this study, therefore, is to develop ZnO@TiO_2 nanocomposites from ZnO nanoparticles and commercial TiO_2 with various modification ratios. Besides, the physical-chemical characteristics of the fabricated materials were described. Initial investigations about photocatalytic ability of obtained catalytic materials in degradation of AMX were also studied.

2. Materials and methods

2.1. Chemicals and materials

All chemicals with analytical grade, including commercial TiO_2, zinc acetate dihydrate ($Zn(CH_3COO)_2.2H_2O$, 99.9%), ethanol (C_2H_5OH, 99.0%), sodium hydroxide (NaOH, 99.9%), sulfuric acid (H_2SO_4, 98.0%), and hydrogen peroxide (H_2O_2, 30%) were purchased from Merck, Germany. Meanwhile, amoxicillin (AMX) was provided by Sigma Aldrich, Germany. Deionized water was used to prepare all chemical solutions.

2.2. Preparation of catalyst materials

In this study, the synthesis procedure of the TiO_2@ZnO composite nanomaterial consists of the following main steps. Firstly, TiO_2 and ZnO nanomaterials were separately synthesized by hydrothermal and sol-gel methods, respectively. For the synthesis of TiO_2 nanoparticles, a micrometre-sized commercial TiO_2 powder was mixed with 10 M NaOH solution and transferred into a sealed Teflon flask. The flask was then placed in an oven set to a constant temperature of 135°C and calcinated for 24 h. Afterward, the Teflon flask was cooled to room temperature (25±2°C), and the mixture in the Teflon flask was filtered and washed several times with hydrochloric acid and distilled water until a constant pH was reached. Finally, the obtained product was dried and calcinated at 300°C for 2 h to form TiO_2 nanoparticles. For the synthesis of ZnO nanoparticles, $Zn(CH_3COO)_2.2H_2O$ 99.9% was firstly mixed with citric acid at a molar ratio of 1:3. The mixture was then continuously magnetically stirred for 1 h at 80°C to achieve the sol-gel state. Next, this sol gel solution was kept at 135°C for 3 h to form xero-gel before calcination at 400°C for 5 h to form ZnO nanoparticles.

From the two synthesized TiO_2 and ZnO nanomaterials, the ZnO@TiO_2 composite nanomaterials were fabricated using ball milling for 2 h with varying ZnO contents of 10, 20, 30, 40 and 50% to form homogenous ZnO@TiO_2 nanocomposite. The synthesis process of ZnO@TiO_2 composite is illustrated in Fig. 1.

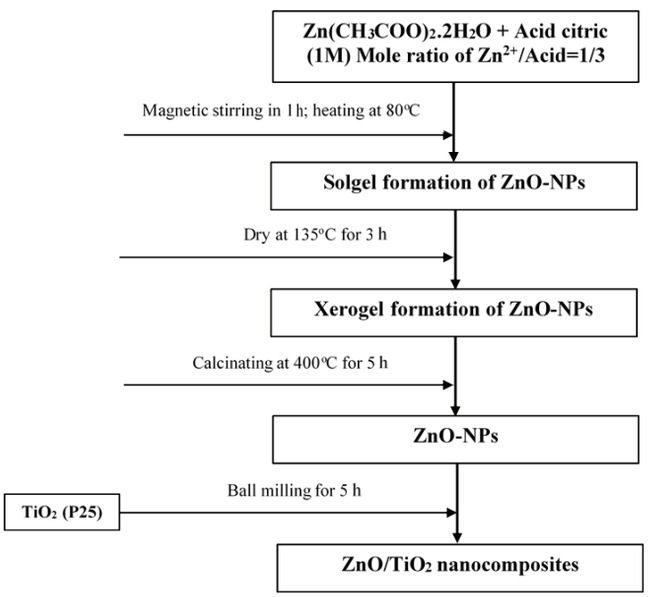

Fig. 1. Schematic description of the synthesis of ZnO@TiO_2 nanocomposites.

2.3. Experiment design

All experiments were performed on simulated wastewater samples with amoxicillin in the laboratory. The experimental set up of perozone degradation of amoxicillin is shown in Fig. 2. The experimental system is designed and installed to conduct research on the treatment of the antibiotic AMX with ozone using ZnO@TiO_2 at different composite ratios as photocatalysts.

AMX degradation was performed in batch experiments. Ozone was generated by an ozone generator (NextOzone 20P, Sinh Phu Joint Stock Company, Vietnam). The maximum capacity and input O_3 capacity at a flow of 15 ml/min were 5.0 g/h and 3.038 g/h, respectively. The oxygen source for the O_3 generator was taken from a pure oxygen tank. O_3 was continuously generated and distributed into a tubular borosilicate glass reactor with a height of 450 mm

and a diameter of 60 mm through a bubble air stone located at the bottom of the tank. The photocatalysts including ZnO, TiO_2 only, 10%ZnO@TiO_2, 20%ZnO@TiO_2, 30%ZnO@TiO_2, 40%ZnO@TiO_2, and 50%ZnO@TiO_2 were separately introduced into the reactors containing 500 ml of 100 mg/l AMX with a catalyst dose of 0.1 g/l at pH of 11 and H_2O_2 of 100 mg/l. Ozone aeration time was 10 min out of the 70 min of each cycle. The residual ozone in the outlet was absorbed by 1500 ml of 2% KI solution contained in a 2000-ml volumetric flask. The perozone reactions for AMX degradation were illuminated by two 35-W UV-Vis lamps at 320 nm. All heterogeneous catalytic perozone reactions were performed in parallel.

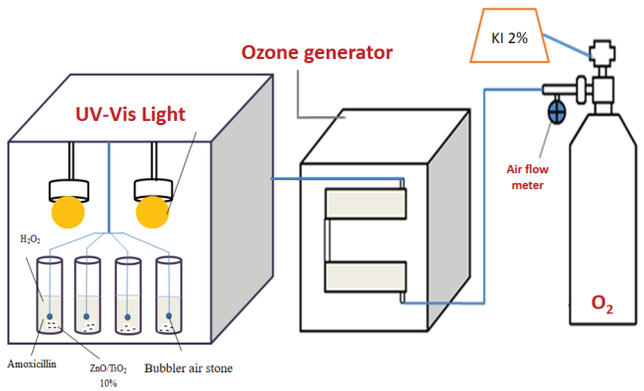

Fig. 2. Scheme of heterogeneous perozone degradation of AMX.

2.4. Analysis method

The N_2 adsorption-desorption isotherms at 77K were applied to analyse the textural properties of the catalysts including BET area, pore size, and pore diameter using Quantachrome Instruments version 11.0-NOVA. The morphology of the photocatalysts was observed by FESEM images using a Hitachi S-4800, Japan. The EDX data and mapping data were obtained by X-ray energy-dispersive spectroscopy analysis using a JSM-IT200 (InTouchScop). The phase composition and crystal structure of the nanomaterials before and after the catalytic process were determined by X-ray diffraction with a scanning speed of 1.25°/min at 2θ values between 20 and 80° using a Bruker D8 with Cu Kα emission (λ=0.1540 nm).

The degree of AMX degradation was assessed through COD measurement according to Standard Method 5220 [27]. pH was measured with a pH meter (Hach).

3. Results and discussion

3.1. Characteristics of catalysts

The effect of composite ratios between ZnO and TiO_2 on the textural properties of ZnO@TiO_2 was evaluated through nitrogen adsorption-desorption isotherms. The resulting data is indicated in Table 1. From this data, it can be seen that compositing ZnO with TiO_2 led to a slight decrease in the surface area and pore volume. Indeed, 10%ZnO@TiO_2 had an S_{BET} of 11.36 m^2/g, which is lower than that of TiO_2 and ZnO. This result was due to an aggregation of ZnO nanoparticles on the surface of TiO_2 [13]. The data in Table 1 also demonstrates that all photocatalysts are classified as a non-porous material because of their poor textural characteristics with low BET specific surface areas of 50.5, 20.6, and 11.36 m^2/g, total pore volume of 0.56, 0.089, and 0.044 cm^3/g and average pore diameters of 2.3, 0.102, and 0.123 nm, respectively, for ZnO, TiO_2, and 10%ZnO@TiO_2. The results suggest that the 10%ZnO@TiO_2 had no well-developed pore size to enhance its surface area. Thus, the contribution to the adsorption mechanism of AMX by 10%ZnO@TiO_2 was negligible in this study (data not shown).

Table 1. Nitrogen adsorption-desorption isotherm data of photocatalytic materials.

	Unit	ZnO	TiO_2	10%ZnO@TiO_2
S_{BET}	m^2/g	50.5	20.6	11.36
V_{pore}	cm^3/g	0.56	0.089	0.044
D_{pore}	nm	2.3	0.102	0.123

The morphological observation of 10%ZnO@TiO_2 through SEM data are presented in Fig. 3, which depicts 10%ZnO@TiO_2 before and after the perozone degradation of AMX. The surface morphology of 10%ZnO@TiO_2 was rough, heterogenous, and non-spherical with ZnO nanoparticles. The particles ranged from 100 to 200 nm in size and their shapes widely varied. Several pores have been narrowed due to surface aggregation of nanoparticles after the catalytic reaction.

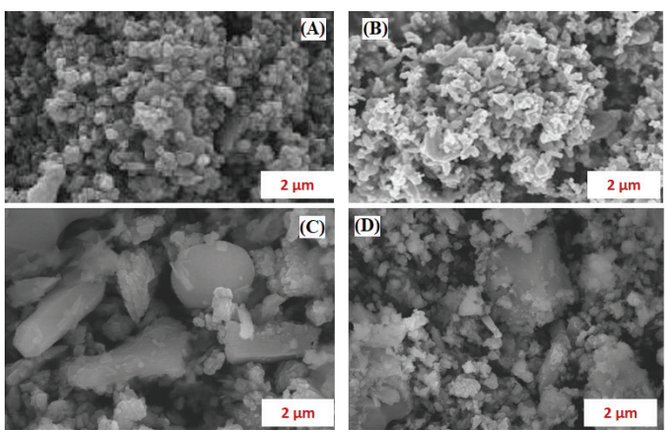

Fig. 3. SEM images of (A) TiO_2, (B) ZnO, and (C, D) 10%ZnO@TiO_2 before and after reaction, respectively.

The EDX spectrum of photocatalysts ZnO, TiO_2, and 10%ZnO@TiO_2 are shown in Fig. 4. The peak position indicates the existence of Zn and O on the EDX of ZnO

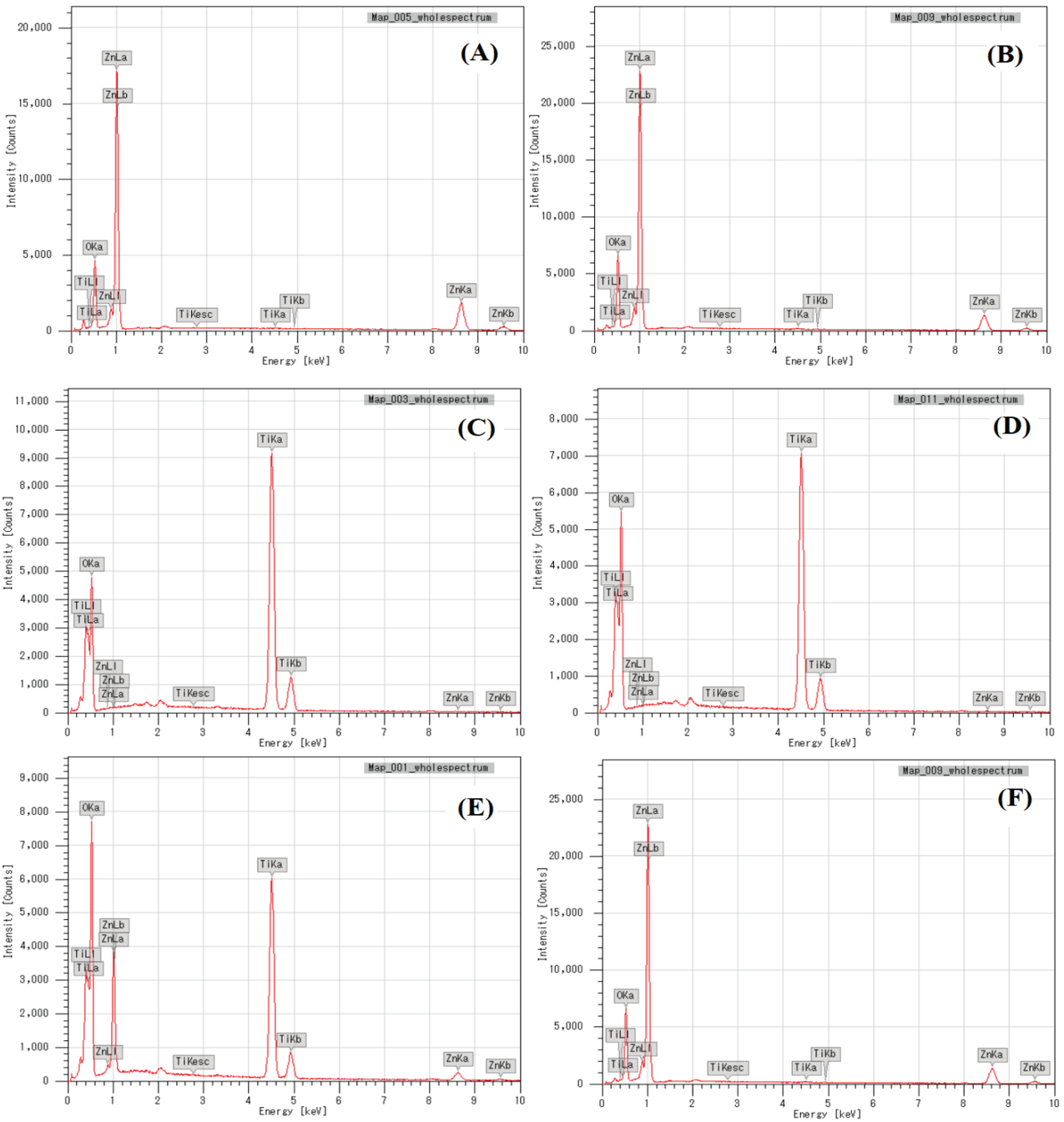

Fig. 4. EDX spectra of photocatalysts before and after reaction: (A, B) ZnO, (C, D) TiO_2, and (E, F) 10%ZnO@TiO_2.

nanoparticles and Ti and O on the EDX of TiO_2. There was an appearance of Zn atoms in the composite constituent of about 10% w.t. in 10%ZnO@TiO_2. The data in Fig. 4E confirmed again the presence of Zn, Ti, and O atoms in the sample. In addition, the EDX spectrum of photocatalysts ZnO, TiO_2, and 10%ZnO@TiO_2 showed that there was a negligible change in the content of Ti compared to Zn after the catalytic reaction (Fig. 4F). Similarly, the amount of Zn and Ti atoms in the ZnO and TiO_2 photocatalysts had an insignificant change, which affirmed the stability of the fabricated photocatalysts.

Figure 5 indicates the crystal structure of ZnO, TiO_2 and the 10%ZnO@TiO_2 composite before and after perozone degradation of AMX. The results are insignificantly changed after the photocatalytic process. As can be seen from the data in Fig. 5, in the XRD pattern of wurtzite ZnO, all the

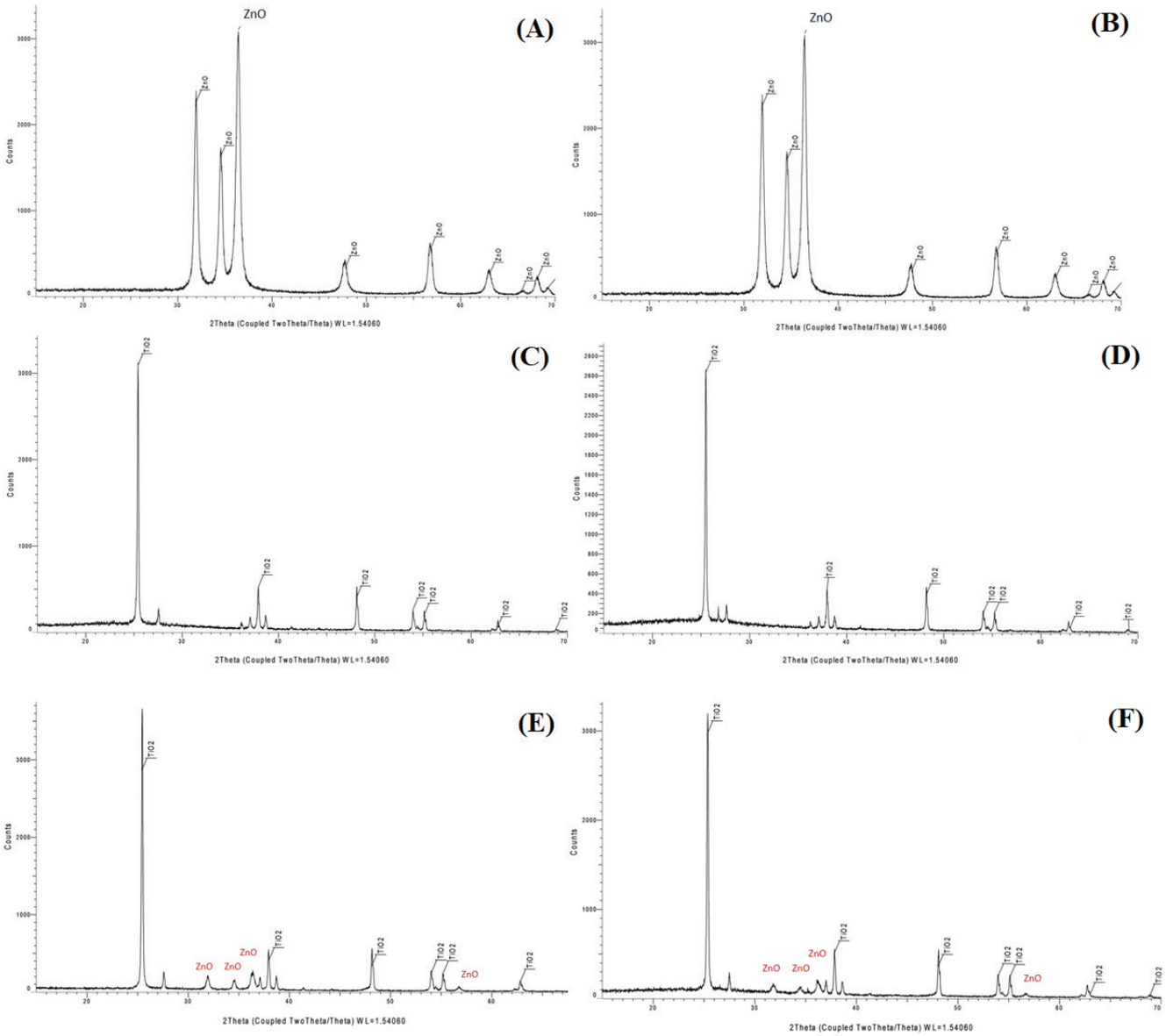

Fig. 5. XRD of the photocatalysts before and after reaction: (A, B) ZnO, (C, D) TiO_2, and (E, F) 10%ZnO@TiO_2.

typical peaks appeared at 2θ=31.94, 34.55, 36.42, 47.71, 56.8, 63.01, and 68.09°, corresponding to the (100), (002), (101), (102), (110), (103), and (112) planes of wurtzite ZnO, respectively (JCPDS card No. 36-1451). Besides, the peaks at 25.45, 37.92, 48.16, 53.97, 55.15, and 62.78° can be respectively ascribed to the (101), (004), (200), (105), (211), and (204) planes of the anatase phase of TiO_2 (JCPDS Card No. 21-1276). Similarly, the other peaks at 2θ = 27.54 and 36.16° correspond to (110) and (101) planes of the rutile phase of TiO_2 (JCPDS Card No. 21-1272) [28]. In the case of 10%ZnO@TiO_2, all typical diffraction peaks of both ZnO and TiO_2 appear in the XRD patterns of ZnO@TiO_2 composite [13]. This result elucidated the co-existence of both ZnO and TiO_2 in the nanocomposite. However, the peak intensity of ZnO is lower than TiO_2, which may explain the smaller content of ZnO compared with TiO_2 in the nanocomposite's composition.

3.2. Degradation of AMX by heterogeneous photocatalytic perozone

Effect of various modification ratios between ZnO-NPs and TiO_2 on AMX removal by heterogeneous photocatalytic perozone (O_3/H_2O_2/catalyst/UV) was carried out in batch reactors. The experiments were conducted at different ratios (w/w) of 10, 20, 30, 40, and 50% of ZnO-NPs with an initial AMX concentration of 100 mg/l, H_2O_2 concentration of 100 mg/l, and catalyst dosage of 0.1 g/l at pH 11 during 70 min of contact time. The obtained results are given in Fig. 6.

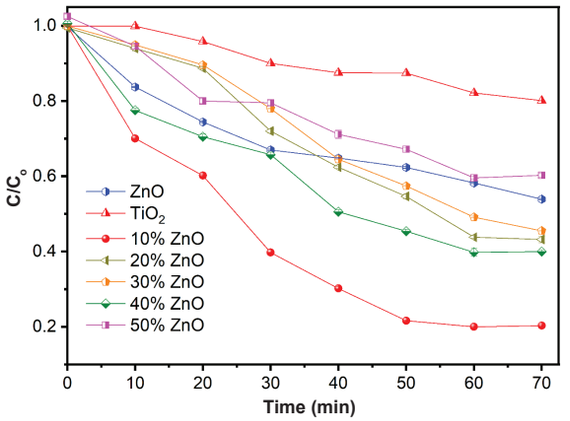

Fig. 6. Time dependence of AMX degradation by O_3/ZnO@TiO_2/H_2O_2/UV at various modification ratios between ZnO and TiO_2.

What stands out from the data in Fig. 6 is that there was a significant difference trend in AMX degradation between perozone systems. Specifically, the AMX perozone degradation by the system using only a TiO_2 catalyst was the lowest with 20.58%. The AMX removal efficiency achieved by O_3/H_2O_2/ZnO/UV was 41.12%, which was higher than that of O_3/H_2O_2/TiO_2/UV by double. However, when ZnO was composited with TiO_2, the AMX removal efficiency of perozone systems improved noticeably. Also, the AMX mineralization strongly depended on the composite ratio between ZnO and TiO_2. Specifically, the AMX removal reached a peak of 81.34% at a modification ratio of 10%, which was higher than that of O_3/H_2O_2/TiO_2/UV by four times and O_3/H_2O_2/ZnO/UV by double. Clearly, the ZnO@TiO_2 nanocomposite expressed excellent photocatalytic activity in comparison with TiO_2 particles and ZnO particles alone. However, when ZnO-NPs/TiO_2 composite ratios were further increased, the catalytic activity of the degradation of AMX by nanocomposite began a downward trend. The degradation of AMX was 62.85%, 59.67%, 60.87%, and 38.91%, respectively, at ZnO-NPs/TiO_2 ratios of 20, 30, 40, and 50% for 70 min of reaction time. An analogous result was reported by T. Yang, et al. (2018) [13] with an optimum modification ratio of 7% between ZnO and TiO_2 for salicylic acid (SA) removal by photocatalytic ozonation due to enriched surface hydroxyl groups of the modified catalyst. The degradation of SA decreased by 10% at a modification ratio of 10%. The degradation rate of ciprofloxacin by photocatalytic ozonation using a TiO_2/carbon dots catalyst dropped with an increase in doping ratio (k=0.320/min for 6 wt% TiO_2/CDs and k=0.247/min for 8 wt% TiO_2/CDs) [4]. In this study, an optimal result was obtained by loading 10% ZnO-NPs on TiO_2. This demonstrated that the combination of ZnO and TiO_2 has significantly enhanced the perozone degradation reaction under UV irradiation of pure TiO_2.

The mineralization kinetics of AMX in aqueous solution were investigated using heterogeneous catalytic perozone processes with photocatalysts at various modification ratios under the most suitable conditions determined by our previous study, which consisted of a pH of 11, catalyst dosage of 0.1 g/l, H_2O_2 concentration of 100 mg/l, and initial AMX of 100 mg/l. The general equation that describes the oxidation reaction of AMX can be written as follows:

$$AMX + {}^{\cdot}OH \rightarrow nCO_2 + mH_2O + \text{intermediates} \quad (1)$$

The reaction rate in Eq. 1 can be described by following kinetic equation:

$$r = k.[C]^a.[OH^*]^b \quad (2)$$

where r is reaction rate (h^{-1}), k is reaction rate constant, and a and b are the reaction orders. However, the advanced oxidation reactions for the degradation of persistent organic compounds is mainly based on the continuous production of hydroxyl radicals with extremely short existence times. Thus, it can assumed that the amount of hydroxyl radicals would reach an equilibrium (i.e., [*OH] = constant). Then, Eq. 2 can be rewritten:

$$r = k'.[C]^a \quad (3)$$

Under the assumption that a perozone reaction follows both pseudo-first-order and pseudo-second-order kinetics, the integral of both sides of Eq. 3 (with a=1 for pseudo-first-order and a=2 for pseudo-second-order kinetics):

$$ln\frac{[C]_o}{[C]_t} = k'.t \quad (4)$$

$$\frac{1}{[C]_t} - \frac{1}{[C]_o} = k''.t \quad (5)$$

From the experimental data, the plot of and versus reaction time was made and the following correlation coefficients (R^2) were obtained: 0.9785 and 0.7678 for pseudo-first-order and pseudo-second-order kinetics, respectively. The obtained results showed that the data was fit to a straight line and the apparent first-order rate constant, k, corresponded to the slope of the straight line. Thus, in this study, the pseudo-first-order kinetic equation was applied to describe the effect of reaction conditions on heterogeneous photocatalytic perozone processes as in:

$$Ln\frac{C}{C_o} = -k_d.t \quad (6)$$

where, C_0 and C are the initial concentration of pollutant at the initial time and after t min of reaction, respectively, k_d is the degradation rate constant, and t is the degradation time.

By plotting ln C/C_o versus reaction time under optimum conditions, the calculated kinetic parameters for the degradation of AMX by heterogeneous photocatalytic perozone systems using the photocatalysts are demonstrated in Fig. 7.

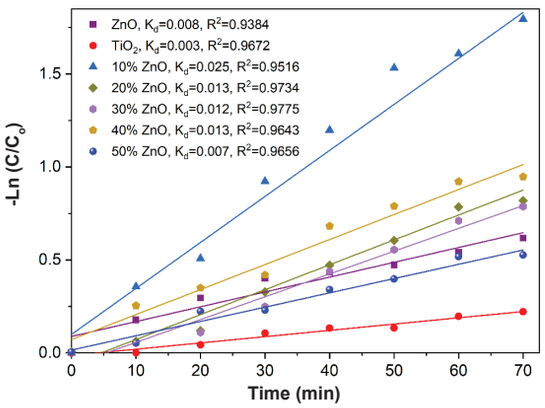

Fig. 7. Degradation kinetics of AMX by O_3/ZnO@TiO_2/H_2O_2/UV.

As expected, all computed k_d values had good agreement with the discussed results of mineralization of AMX at various modification ratios between ZnO and TiO_2. At various modification ratio values, it is clear from Fig. 7 that in all perozone systems for the degradation of AMX, the k_d values followed descending order as follows: O_3/H_2O_2/10%ZnO@TiO_2/UV>O_3/H_2O_2/ZnO/UV>O_3/H_2O_2/TiO_2/UV. The k_d values were the highest at a modification ratio of 10%ZnO@TiO_2/UV with 0.025/min. The results showed that in coupled heterogeneous photocatalytic ozonation process, the synergetic effect of perozone (O_3/H_2O_2) and photocatalysis (10%ZnO@TiO_2/UV) participating in the ozonation reaction proved to enhance the reaction rate, which led to an improvement of the overall treatment efficiency of the contaminants [4, 13, 19, 29]. Also, it is clearly there was a remarkable effect in composite ratio of ZnO-NPs on catalytic activity of materials in perozone degradation of AMX.

3.3. Mechanism of degradation perozone of AMX

In this work, from literature analysis and the discussion of the above results, it is apparent that the maximum AMX mineralization efficiency of 81.0% was obtained by perozone using 10%ZnO@TiO_2 under pH of 11, which proves the main mechanism of AMX degradation by photocatalytic perozone was through *OH radicals. The doping of ZnO-NPs and TiO_2 overcame the drawback of recombination of electron-hole pairs (h^+, e^-). Specifically, XRD data (Fig. 4), SEM, TEM, EDX and mapping data (Fig. 5) indicated the existence of ZnO NPs and TiO_2 mainly in the form of anatase in the nanocomposite catalyst. Furthemore, the S_{BET} of 10%ZnO@TiO_2 was 11.36 m^2/g, which confirms that ZnO@TiO_2 can act as both an adsorbent and catalyst. This nanocomposite catalyst enhanced the adsorbance of AMX on the ZnO@TiO_2's surface, decomposed O_3, and reacted with H_2O_2 in the O_3/H_2O_2/10%ZnO@TiO_2/UV system to increase the production of more *OH radicals. Apparently, composition of TiO_2 with ZnO rose the electron-hole separation thanks to ZnO@TiO_2 acting as electron trap, and modified the surface characteristics of the photocatalyst [13, 28, 30]. The production of more *OH was due to O_3's electrophilic property towards photogenerated electrons generated by photoexcitation of the ZnO@TiO_2 catalyst. In this work, the AMX degradation by O_3 can occur through two major routes, which consist of direct and indirect decomposition of ozone in solution and interfacial interaction reactions between the absorbed AMX on the catalyst's surface and the free radicals formed during photocatalytic perozone. These reactions for perozone degradation of AMX can be described by:

$$ZnO@TiO_2\text{-}e^-_{CB} + O_2 \rightarrow ZnO@TiO_2\text{-}{}^*O_2^- \quad (7)$$

$$2ZnO@TiO_2\text{-}e^-_{CB} + 2O_3 \rightarrow O_2 + 2\ ZnO@TiO_2\text{-}{}^*O_2^- \quad (8)$$

$$2ZnO@TiO_2\text{-}{}^*O_2^- + H_2O \rightarrow H_2O_2 + 2OH^- + O_2 \quad (9)$$

$$ZnO@TiO_2\text{-}\ e^-_{CB} + H_2O_2 \rightarrow {}^*OH + OH^- \quad (10)$$

$$ZnO@TiO_2\text{-AMX} + h^+_{VB}\ ({}^*OH \text{ or } {}^*O_2^-) \rightarrow CO_2 + H_2O + \text{intermediates} \quad (11)$$

In conclusion, the joint application of photocatalysis and perozone could give a much higher ·OH radical yield than the photocatalysis alone, which explains the synergistic effect between ozone and the role of the photocatalyst in inhibiting recombination of the photogenerated electrons and holes. Based on above results and discussion, it is clear that the composite of ZnO nanoparticles considerably enhanced the mineralization efficiency of AMX thanks to its multiple roles when modified with TiO_2. The functions of ZnO doped with TiO_2 include increasing electron transfer, electron storage, and enriching –OH groups on the photocatalyst's surface.

4. Conclusions

In this study, ZnO-NPs with various contents were composited with commercial TiO_2 to fabricate ZnO@TiO_2 composites that exhibited a high photocatalytic activity of heterogeneous perozone degradation of AMX. Data about the characteristics of synthesized composite materials showed benefits for catalytic reactions due to inhibiting the recombination of photogenerated electrons and holes, which led to the enhancement of *OH content in order to mineralize AMX. The degradation efficiency of AMX was shown to depend strongly on the modification ratio of ZnO. A modification ratio of 10%ZnO produced the highest removal efficiency of AMX with 81%. Also, data about the properties of the photocatalyst indicated a high stability after reaction suggesting its feasibility in practical application to remove persistent organic compounds from wastewater.

CRediT author statement

Thanh Diem Ngo Thi and Lan Huong Nguyen: Conceptualization, Methodology, Software; Lan Huong Nguyen, Hiep Vu Phung: Data curation, Writing- Original draft; Xuan Hoan Nguyen and Lan Huong Nguyen: Visualization, Investigation, Supervision; Hiep Vu Phung, Minh Thanh Le: Conducted experiments, Software, Validation; Lan Huong Nguyen: Writing- Reviewing and

Editing. All authors provided critical feedback and helped shape the research, analysis and manuscript.

ACKNOWLEDGEMENTS

The study was supported by The Youth Incubator for Science and Technology Program, managed by Youth Development Science and Technology Centre - Ho Chi Minh Communist Youth Union and Department of Science and Technology of Ho Chi Minh City, Vietnam under the contract number 23/2020/HD-KHCNT-VU.

COMPETING INTERESTS

The authors declare that there is no conflict of interest regarding the publication of this article.

REFERENCES

[1] E.M. Rodriguez, G. Marquez, E.A. Leon, et al. (2013), "Mechanism considerations for photocatalytic oxidation, ozonation and photocatalytic ozonation of some pharmaceutical compounds in water", *J. Environ. Manage.*, **127**, pp.114-124, DOI: 10.1016/j.jenvman.2013.04.024.

[2] N.F.F. Moreira, C.A. Orge, A.R. Ribeiro, et al. (2015), "Fast mineralization and detoxification of amoxicillin and diclofenac by photocatalytic ozonation and application to an urban wastewater", *Water Res.*, **87**, pp.87-96, DOI: 10.1016/j.jenvman.2013.04.024.

[3] S. Rodriguez-Mozaz, S. Chamorro, E. Marti, et al. (2015), "Occurrence of antibiotics and antibiotic resistance genes in hospital and urban wastewaters and their impact on the receiving river", *Water Res.*, **69**, pp.234-242, DOI: 10.1016/j.watres.2014.11.021.

[4] Y. Zeng, D. Chen, T. Chen, et al. (2019), "Study on heterogeneous photocatalytic ozonation degradation of ciprofloxacin by TiO_2/carbon dots: Kinetic, mechanism and pathway investigation", *Chemosphere*, **227**, pp.198-206, DOI: 10.1016/j.chemosphere.2019.04.039.

[5] F.S. Souza, A. Arenzon, C.K. Rosin, et al. (2018), "Comparison of different advanced oxidation processes for the removal of amoxicillin in aqueous solution", *Environ. Technol. (United Kingdom)*, **39(5)**, pp.549-557, DOI: 10.1080/09593330.2017.1306116.

[6] E. Zuccato, S. Castiglioni, R. Bagnati, et al. (2010), "Source, occurrence and fate of antibiotics in the Italian aquatic environment", *J. Hazard. Mater.*, **179(1-3)**, pp.1042-1048, DOI: 10.1016/j.jhazmat.2010.03.110.

[7] E.S. Elmolla, M. Chaudhuri (2010), "Degradation of amoxicillin, ampicillin and cloxacillin antibiotics in aqueous solution by the UV/ZnO photocatalytic process", *J. Hazard. Mater.*, **173(1-3)**, pp.445-449, DOI: 10.1016/j.jhazmat.2009.08.104.

[8] E.A.S. Galvis, F. Ferraro, J.S. Agredo, et al. (2017), "Degradation of highly consumed fluoroquinolones, penicillins and cephalosporins in distilled water and simulated hospital wastewater by UV_{254} and UV_{254}/persulfate processes", *Water Res.*, **122**, pp.128-138, DOI: 10.1016/j.watres.2017.05.065.

[9] S.A. Maadheed, I. Goktepe, B. Shomar, et al. (2019), "Antibiotics in hospital effluent and domestic wastewater treatment plants in Doha, Qatar", *J. Water Process Eng.*, **28**, pp.60-68, DOI: 10.1016/j.jwpe.2019.01.005.

[10] N. Nasseh, F.S. Arghavan, S.R. Couto, et al. (2020), "Preparation of activated carbon@ZnO composite and its application as a novel catalyst in catalytic ozonation process for metronidazole degradation", *Adv. Powder Technol.*, **31(2)**, pp.875-885, DOI: 10.1016/j.apt.2019.12.006.

[11] J. Jeong, W. Song, W.J. Cooper, et al. (2009), "Degradation of tetracycline antibiotics: Mechanisms and kinetic studies for advanced oxidation/reduction processes", *Chemosphere*, **78(5)**, pp.533-540, DOI: 10.1016/j.chemosphere.2009.11.024.

[12] L.M.P. Martinez, J.L. Faria, J.M.D. Rodriguez, et al. (2012), "Degradation of diphenhydramine pharmaceutical in aqueous solutions by using two highly active TiO_2 photocatalysts: Operating parameters and photocatalytic mechanism", *Appl. Catal. B Environ.*, **113-114**, pp.221-227, DOI: 10.1016/j.apcatb.2011.11.041.

[13] T. Yang, J. Peng, Y. Zheng, et al. (2018), "Enhanced photocatalytic ozonation degradation of organic pollutants by ZnO modified TiO_2 nanocomposites", *Appl. Catal. B Environ.*, **221**, pp.223-234, DOI: 10.1016/j.apcatb.2017.09.025.

[14] R. Saravanan, S. Karthikeyan, V.K. Gupta, et al. (2013), "Enhanced photocatalytic activity of ZnO/CuO nanocomposite for the degradation of textile dye on visible light illumination", *Mater. Sci. Eng. C.*, **33(1)**, pp.91-98, DOI: 10.1016/j.msec.2012.08.011.

[15] D. Dimitrakopoulou, I. Rethemiotaki, Z. Frontistis, et al. (2012), "Degradation, mineralization and antibiotic inactivation of amoxicillin by UV-A/TiO_2 photocatalysis", *J. Environ. Manage.*, **98**, pp.168-174, DOI: 10.1016/j.jenvman.2012.01.010.

[16] F. Biancullo, N.F.F. Moreira, A.R. Ribeiro, et al. (2019), "Heterogeneous photocatalysis using UVA- LEDs for the removal of antibiotics and antibiotic resistant bacteria from urban wastewater treatment plant effluents", *Chem. Eng. J.*, **367**, pp.304-313, DOI: 10.1016/j.cej.2019.02.012.

[17] W. Yao, S.W.U. Rehman, H. Wang, et al. (2018), "Pilot-scale evaluation of micropollutant abatements by conventional ozonation, UV/O_3, and an electro-peroxone process", *Water Res.*, **138**, pp.106-117, DOI: 10.1016/j.watres.2018.03.044.

[18] E. Illes, E. Szabo, E. Takacs, et al. (2014), "Ketoprofen removal by O_3 and O_3/UV processes: Kinetics, transformation products and ecotoxicity", *Sci. Total Environ.*, **472**, pp.178-184, DOI: 10.1016/j.scitotenv.2013.10.119.

[19] A.C. Mecha, M.N. Chollom (2020), "Photocatalytic ozonation of wastewater: A review", *Environ. Chem. Lett.*, **18**, pp.1491-1507, DOI: 10.1007/s10311-020-01020-x.

[20] M. Mehrjouei, S. Muller, D. Moller (2015), "A review on photocatalytic ozonation used for the treatment of water and wastewater", *Chem. Eng. J.*, **263**, pp.209-219, DOI: 10.1016/j.cej.2014.10.112.

[21] W.S. Koe, J.W. Lee, W.C. Chong, et al. (2020), "An overview of photocatalytic degradation: Photocatalysts, mechanisms, and development of photocatalytic membrane", *Environ. Sci. Pollut. Res.*, **27**, pp.2522-2565, DOI: 10.1007/s11356-019-07193-5.

[22] M.R.D. Khaki, M.S. Shafeeyan, A.A.A. Raman, et al. (2017), "Application of doped photocatalysts for organic pollutant degradation - A review", *J. Environ. Manage.*, **198**, pp.78-94, DOI: 10.1016/j.jenvman.2017.04.099.

[23] P.V. Viet, T.H.T. Vinh, N.T.N. Dung, et al. (2021), Facile ball-milling synthesis of TiO_2 modified ZnO for efficient photocatalytic removal of atmospheric nitric oxide gas under solar light irradiation", *Chem. Phys. Lett.*, **775**, DOI: 10.1016/j.cplett.2021.138642.

[24] S.N. Nguyen, T.K. Truong, V.V. Pham, et al. (2019), "Investigation on photocatalytic removal of NO under visible light over Cr-Doped ZnO nanoparticles", *ACS Omega.*, **4**, pp.12853-12859, DOI: 10.1021/acsomega.9b01628.

[25] T.K. Truong, T.V. Doan, H.H. Tran, et al. (2019), "Effect of Cr doping on visible-light-driven photocatalytic activity of ZnO nanoparticles", *J. Electron. Mater.*, **48**, pp.7378-7388, DOI: 10.1007/s11664-019-07566-z.

[26] L.P.P. Ha, N.T. Thuy, C.M. Tri, et al. (2021), "Visible-light-driven photocatalysis of anisotropic silver nanoparticles decorated on ZnO nanorods: Synthesis and characterizations", *J. Environ. Chem. Eng.*, **9**, DOI: 10.1016/j.jece.2021.105103.

[27] American Public Health Association (2012), *Standard Methods for The Examination of Water and Wastewater*, 541pp.

[28] R. Zha, R. Nadimicherla, X. Guo (2015), "Ultraviolet photocatalytic degradation of methyl orange by nanostructured TiO_2/ZnO heterojunctions", *J. Mater. Chem. A.*, **3**, pp.6565-6574, DOI: 10.1039/C5TA00764J.

[29] C.V. Rekhate, J.K. Srivastava (2020), "Recent advances in ozone-based advanced oxidation processes for treatment of wastewater - A review", *Chem. Eng. J. Adv.*, **3**, DOI: 10.1016/j.ceja.2020.100031.

[30] F.A. Akgul (2016), "Influence of Ti doping on ZnO nanocomposites: Synthesis and structural characterization", *Compos. Part B Eng.*, **91**, pp.589-594, DOI: 10.1016/j.compositesb.2016.02.015.

Phytoplankton and relationship between phytoplankton community and environmental parameters of some water bodies in Soc Trang province

Thi Trang Le*, Doan Dang Phan, Van Tien Tran, Van Tu Nguyen

Institute of Tropical Biology, Vietnam Academy of Science and Technology,
9/621 Hanoi Highway, Linh Trung Ward, Thu Duc District, Ho Chi Minh City, Vietnam

Received 6 January 2022; revised accepted 4 April 2022

Abstract:

This study was carried out to evaluate the seasonal variation of phytoplankton and its relationship with environmental parameters of some inland water bodies in Soc Trang province. A total of 171 phytoplankton taxa belonging to Cyanophyta (24 species), Chrysophyta (2 species), Bacillariophyta (65 species), Chlorophyta (43 species), Euglenophyta (34 species), and Dinophyta (3 species) were studied. The phytoplankton species composition during the rainy season was higher than in the dry season, in which Bacillariophyta dominated in both seasons. Surface water quality was classified into class A2 for pH, phosphate, and nitrate whereas class B2 for dissolved oxygen (DO), total suspended solids (TSS), ammonium, chemical oxygen demand (COD), and biochemical oxygen demand (BOD) (according to QCVN 08:2015/BTNMT). Canonical correspondence analysis (CCA) results revealed that environmental factors influenced the phytoplankton community. Of which the factors of pH, electric conductivity (EC), salinity, turbidity, TSS, and phosphate affected the phytoplankton assemblage in both seasons. The results confirm the potential of using phytoplankton as a bioindicator for surface water quality assessment.

Keywords: **correlation, phytoplankton, Soc Trang province, water quality.**

Classification numbers: **5.1, 5.3**

1. Introduction

Phytoplankton, also known as microalgae, are small-sized organisms that live floating in the water. Various species live solitary like *Closterium*, *Navicula*, *Phacus*; colonies like *Volvox*, *Microcystis*, *Merismopedia;* filament like *Oscillatoria*, *Arthrospira, Lyngbya*, and chain like *Melosira, Anabaena, Skeletonema.* They are present in all kinds of water bodies. Phytoplankton play a significant role in aquatic ecosystems because they are the base of several aquatic food webs [1, 2]. Phytoplankton are extremely sensitive to environmental changes, so they are usefully applied to evaluate water quality status [3]. Community structure and abundance of phytoplankton are mainly controlled by nutrient availability and other factors e.g., temperature, light availability, mixing, and current circulation [4]. Analysing basic information from phytoplankton to improve water quality and prevent the occurrence of water blooms has been necessary [5]. Some species of phytoplankton can be considered as an indicator organism of environmental pollution and eutrophication [6].

In Vietnam, phytoplankton have been studied for some time such as several works [7-11]. However, studies on the relationship between the phytoplankton community and environmental parameters are still minimal. T.T. Duong, et al. (2014) [12] reported that suspended solid factors affected the distribution of phytoplankton structure in the Red river. In another study, T.S. Dao (2016) [13] announced the phytoplankton distribution had closely relation to the factors of pH, turbidity, EC, COD, iron, and aluminium in Lak lake, whereas the transparency indicated the most evident correlation with phytoplankton distribution in Bien Ho. T.S. Dao, et al. (2016) [14] studied the correlation of species number and biodiversity with environmental parameters in the Vam Co river. T.L. Pham (2017b) [15] described that nutrient concentration and turbidity related to the distribution of phytoplankton structure in the Dong Nai river. Phytoplankton assemblage was affected by nitrate, phosphate, and salinity in the Can Gio mangrove [2].

Soc Trang is one of the provinces in the Mekong delta of southern Vietnam and has relatively high biodiversity.

*Corresponding author: Email: letrangenvi@gmail.com

The aquatic flora, especially the phytoplankton of Soc Trang province, have not yet been fully explored. The previous investigations reported 82 species of phytoplankton in the Cu Lao Dung mangrove ecosystem in Soc Trang province [16]. However, the overall investigation of phytoplankton and their interaction with environmental parameters have not yet been carried out here. Thus, this study aims to determine the composition, abundance, distribution of phytoplankton, and the relation between phytoplankton and environmental factors in water bodies of the Soc Trang province.

2. Materials and methods

2.1. Study area

Soc Trang is a province in the Mekong delta system, Vietnam. It is surrounded by Tra Vinh, Vinh Long, Bac Lieu, and Hau Giang provinces, and the East Sea. There are 72 km seaside, three main river mouths, and 30,000 ha alluvium ground.

The study was implemented in April (dry season) and October (rainy season) 2020. The samples were collected at eighteen sites in some inland water bodies of Soc Trang province (Table 1, Fig. 1).

Table 1. Coordinates and locations of the sampling sites.

Sampling sites	Local names	Longitude	Latitude
M1	Kenh Xang bridge - Soc Trang city	105°57'51.67	9°36'51.29
M2	30/4 bridge - Soc Trang city	105°58'36.63	9°36'21.90
M3	Maspero bridge - Soc Trang city	105°59'37.78	9°36'31.05
M4	Rach Mop bridge -Nhon My commune, Ke Sach district	106°02'20.91	9°46'43.87
M5	Thanh Loi bridge - My Xuyen district	105°59'57.78	9°33'20.29
M6	Co Co market - My Xuyen district	105°56'25.15	9°25'37.56
M7	Vinh Chau bridge -Vinh Chau town	105°58'49.05	9°19'35.11
M8	Saintard bridge - Soc Trang city	106°02'13.52	9°37'25.72
M9	Ke Sach market, Ke Sach district	105°59'10.60	9°46'08.93
M10	Nhu Gia bridge - Thanh Phu commune, My Xuyen district	105°51'10.52	9°30'09.25
M11	Phu Loc market - Thanh Tri district	105°44'44.56	9°25'43.60
M12	Nga 5 market, Nga Nam town	105°35'53.05	9°33'54.19
M13	Cai Con bridge - An Lan Thon commune, Ke Sach district	105°53'27.75	9°55'48.00
M14	Huynh Huu Nghia bridge - My Tu district	105°48'39.19	9°38'10.13
M15	Lich Hoi Thuong bridge - Tran De district	106°08'48.47	9°28'38.64
M16	Thuan Hoa bridge -Chau Thanh town	105°37'21.35	9°37'59.23
M17	Khoan Tan bridge -Long Phu town	106°07'12.04	9°37'16.26
M18	Dinh river station - Soc Trang city	106°01'21.47	9°36'13.28

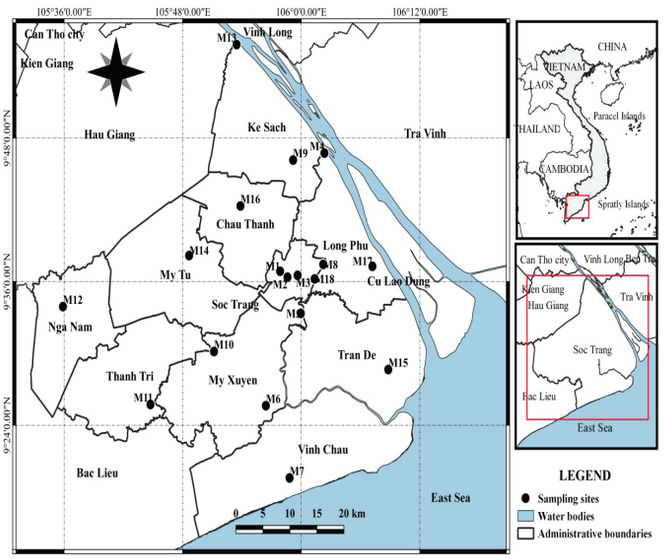

Fig. 1. Map of sampling sites of some water bodies in Soc Trang province.

2.2. Sample collection

Water samples such as temperature, pH, EC, salinity, turbidity, and DO were measured *in situ* using a multi-parameter (AAQ Rinko). Besides, surface water samples for other chemical parameter analyses were also taken, kept in ice, and carried to the laboratory. The process of taking samples and preserving samples was ensured by QCVN 08:2015/BTNMT [17].

The qualitative samples of phytoplankton were collected by a towing phytoplankton net (mesh size of 25 µm). Quantitative phytoplankton samples were done by filtering water samples as large as 60 l through the net. Then, the samples were preserved in the bottle with a volume of 250 ml and fixed with 5% formalin. The sampling method was performed by APHA (2012) [18].

2.3. Sample analysis

The water quality parameters such as COD, BOD_5, TSS, ammonium (NH_4^+), nitrate (NO_3^-), phosphate (PO_4^{3-}), and total P were analysed according to the standard method [18].

Phytoplankton were observed under Olympus BX41 optical microscope with magnification from 100 to 400 times and morphologically identified according to classification books [7-11, 19]. A Sedgewick Rafter counting chamber was used to determine phytoplankton cell density and the counting way was according to G.B. Edward, et al. (2015) [20]. The phytoplankton taxon was arranged according to AlgaeBase's taxonomy system [21].

2.4. Data analysis

Using Excel 2010 software to analyse statistical data. CCA was used to determine the main environmental factors affecting the phytoplankton community by PAST software. Only species that have an abundance higher than 5% in each sample were used in this analysis to minimise the effect of rare species.

3. Results

3.1. Environment parameters

The results of the characteristics of the physical and chemical parameters from 18 collected samples for each factor in Soc Trang are presented in Table 2. The temperature of surface water ranged from 28.3°C to 31.1°C, relatively stable among the sampling sites. The pH and turbidity were between 6.58-7.53 and 19-265 Nephelometric turbidity unit (NTU), respectively. Both pH and turbidity in the dry season were lower than those in the rain season. The EC of the water was from 29.5-1428 mS/m in the dry season and from 14.5-329.7 mS/m in the rainy season. Salinity of water varied from 0.33-6.99‰ (mean 0.99‰) in the dry season and from 0.00-1.51‰ (mean 0.16‰) in the rainy season. During both the dry and rainy seasons, the DO concentration ranged from 2.05-6.12 mg/l. The TSS fluctuated from 16.0-290.7 mg/l in the dry season and 20.3-245.3 mg/l in the rainy season.

The COD and BOD_5 concentrations in dry season ranged from 9.7-44.9 mg/l and 3.1-11.8 mg/l, respectively. Those concentrations in the rainy season were 11.0-36.9 mg/l and 2.6-10.8 mg/l, respectively. The ammonium concentration in the dry season (0.00-1.31 mg/l) was higher than those in the rainy season (0.03-0.79 mg/l). The nitrate and phosphate concentrations in the dry season were from 0.04-0.71 mg/l and 0.00-0.17 mg/l, respectively. Those concentrations in the rainy season fluctuated 0.10-0.64 mg/l and 0.01-0.59 mg/l, respectively. The total phosphorus concentration was from 0.17-0.83 mg/l in the dry season, and 0.21-0.99 mg/l in the rainy season (Table 2).

Table 2. The water quality parameters of 18 sites in Soc Trang during the 2020 dry and rainy seasons.

Parameters	Dry season			Rainy season		
	Min	*Max*	*Mean±SE*	*Min*	*Max*	*Mean±SE*
Temperature (°C)	28.3	31.1	29.7±0.2	29.3	30.9	30.0±0.1
pH	6.72	7.28	7.06±0.03	6.58	7.53	6.93±0.05
EC (mS/m)	29.5	1428.0	233.7±100.2	14.5	329.7	53.5±16.7
Salinity (‰)	0.03	6.99	0.99±0.49	0.00	1.51	0.16±0.08
Turbidity (NTU)	19.0	186.8	84.6±11.2	30.2	265.0	110.4±16.6
DO (mg/l)	2.05	6.09	3.17±0.25	2,14	6.12	3.28±0.26
TSS (mg/l)	16.0	290.7	92.9±16.1	20.3	245.3	98.7±16.5
COD (mg/l)	9.7	44.9	29.7±2.6	11.0	36.9	23.3±1.8
BOD_5 (mg/l)	3.1	11.8	5.7±0.7	2.6	10.8	5.2±0.5
NH_4^+ (mg/l)	0.00	1.31	0.66±0.11	0.03	0.79	0.42±0.07
NO_3^-(mg/l)	0.04	0.71	0.30±0.04	0.10	0.64	0.32±0.05
PO_4^{3-} (mg/l)	0.00	0.17	0.06±0.01	0.01	0.59	0.17±0.04
Total P (mg/l)	0.17	0.83	0.34±0.04	0.21	0.99	0.60±0.07

3.2. Phytoplankton

A total of 171 algal species were recorded, and species belonging to 6 divisions, namely, Cyanobacteria, Chrysophyta, Bacillariophyta, Chlorophyta, Euglenophyta, and Dinophyta. Of these, Bacillariophyta was the most diverse group with 65 species occupying 38.0% of the total species, followed by Chlorophyta with 43 species occupying 25.1%. Euglenophyta and Cyanobacteria had 34 and 24 species, respectively. Finally, Chrysophyta and Dinophyta had the lowest species group with 2 and 3 species, respectively. The number of phytoplankton species in the rainy season was higher than that in the dry season (Table 3). Representatives of phytoplankton genera in the study area were *Anabaena, Microcystis, Oscillatoria, Navicula, Nitzschia, Cyclotella, Melosira, Synedra, Closterium, Cosmarium, Dictyosphaerium, Pandorina, Pediastrum, Scenedesmus, Euglena, Lepocinclis,* and *Phacus*. These genera are typically for freshwater. Besides, a few of them originated from the estuary or coastal region like *Coscinodiscus, Gyrosigma,* and *Thalassionema*.

The cell number of phytoplankton ranged from 5050-212983 cells/l in the dry season and from 1596-448243 cell/l in the rainy season (Fig. 2). These results showed that phytoplankton abundance in the rainy season decreased for eleven of eighteen sampling sites compared with the dry season. In both seasons, the dominant species were mainly species belonging to the cyanobacteria group such as *Oscillatoria perornata*, *O. acuta*, *O.* sp., and *Jaaginema* sp. These species had dominant rates ranging from 26.8 to 78.8% of the total densities in the dry season, and from 16.3 to 73.9% in the rainy season, respectively. Besides, diatoms species (*Coscinodiscus subtilis*, *Aulacoseira granulata*) and green algae species (*Pandorina morum*) were also dominant at several sites, which occupied from 22.5-81.6% in the dry seasons and from 31.9-43.7% in the rainy season.

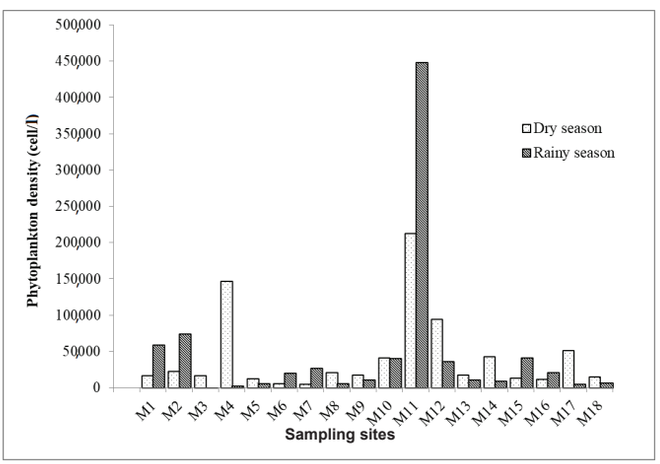

Fig. 2. The temporal and seasonal distributions of phytoplankton density in Soc Trang.

Table 3. List of phytoplankton taxa of water bodies in Soc Trang province (K = dry season, M = rainy season).

No	Taxa
Phylum Cyanobacteria	
1	*Anabaenopsis circularis* (G.S.West) Woloszynska & V.V. Miller, 1923[K M]
2	*Aphanocapsa delicatissima* West & G.S.West, 1912[M]
3	*Arthrospira platensis* Gomont, 1892[K M]
4	*Dolichospermum circinale* (Rabenhorst ex Bornet & Flahault) P.Wacklin, L.Hoffmann & J.Komárek, 2009[M]
5	*Dolichospermum affine* (Lemmermann) Wacklin, L.Hoffmann & Komárek, 2009[M]
6	*Dolichospermum spiroides* (Klebhan) Wacklin, L.Hoffmann & Komárek, 2009[M]
7	*Geitlerinema splendidum* (Greville ex Gomont) Anagnostidis, 1989[K M]
8	*Jaaginema* sp.[K M]
9	*Komvophoron schmidlei* (Jaag) Anagnostidis & Komárek, 1988[K M]
10	*Lyngbya martensiana* Menegh. ex Gomont, 1892[K M]
11	*Merismopedia tranquilla* (Ehrenberg) Trevisan, 1845[K M]
12	*Microcystis aeruginosa* Kützing, 1846[K M]
13	*Microcystis panniformis* Komárek, 2002[K M]
14	*Microcystis protocystis* Crow, 1923[K]
15	*Microcystis wesenbergii* Komárek, 2006[M]
16	*Oscillatoria acuta* Bruhl et Biswas, 1932[K M]
17	*Oscillatoria perornata* Skuja, 1949[K M]
18	*Oscillatoria princeps* Vaucher ex Gamont, 1892[K M]
19	*Oscillatoria tenuis* Agardh, 1813[K M]
20	*Oscillatoria* sp.[K M]
21	*Phormidium chalybeum* (Mertens ex Gomont) Anagnostidis & Komárek, 1988[M]
22	*Planktothrix agardhii* (Gomont) Anagnostidis & Komárek, 1988[K M]
23	*Raphidiopsis mediterranea* Skuja, 1937[M]
24	*Sphaerospermopsis aphanizomenoides* (Forti) Zapomelová, Jezberová, Hrouzek, Hisem, Reháková & Komárková, 2010[K M]
Phylum Chrysophyta	
25	*Dinobryon sertularia* Ehrenberg, 1834[M]
26	*Mallomonas caudata* Iwanoff [Ivanov], 1899[M]
Phylum Bacillariophyta	
27	*Actinoptychus annulatus* (Wallich) Grunow, 1883[K M]
28	*Amphiprora alata* (Ehrenberg) Kützing, 1844[K]
29	*Biddulphia mobiliensis* (Bailey) Grunow, 1882[K]
30	*Campylodiscus daemelianus* Grunow, 1874[K]
31	*Campylodiscus undulatus* Greville, 1863[K]
32	*Climacosphenia moniligera* Ehrenberg, 1843[K M]
33	*Coscinodiscus asteromphalus* Ehrenberg, 1844[K M]
34	*Coscinodiscus jonesianus* (Greville) Ostenfeld, 1915[K]
35	*Coscinodiscus excentricus* Ehrenberg, 1839[K M]
36	*Coscinodiscus gigas* Ehrenberg, 1841[K M]
37	*Coscinodiscus lineatus* Ehrenberg, 1841[K M]
38	*Coscinodiscus marginatus* Ehrenberg, 1843[K M]
39	*Coscinodiscus radiatus* Ehrenberg, 1841[K M]
40	*Coscinodiscus rothii* (Ehrenberg) Grunow, 1878[K M]
41	*Coscinodiscus subtilis* Ehrenberg, 1841[K M]
42	*Coscinodiscus* sp.[K M]
43	*Cocconeis* sp.[K M]
44	*Cyclotella comta* (Ehrenberg) Kützing, 1849[K M]
45	*Cyclotella meneghiniana* Kützing, 1844[K M]
46	*Cymbella lanceolata* (C.Agardh) Kirchner 1878[K M]
47	*Cymbella cistula* (Ehrenberg) Kirchner, 1878[K M]
48	*Diploneis crabro* (Ehrenberg) Ehrenberg,1854[M]
49	*Eunotia rabenhorstiana* (Grunow) Hustedt, 1949[K M]
50	*Eunotia pectinalis* (Kützing) Rabenhorst, 1864[K M]
51	*Fragliria* sp.[K M]
52	*Gomphonema angustatum* (Kützing) Rabenhorst, 1864[M]
53	*Gyrosigma acuminatum* (Kützing) Rabenhorst, 1853[K M]
54	*Gyrosigma attenuatum* (Kützing) Rabenhorst, 1853[K]
55	*Gyrosigma balticum* (Ehrenberg) Rabenhorst, 1853[K M]
56	*Gyrosigma sinensis* (Ehrenberg) Desikachary, 1988 [K M]
57	*Gyrosigma fasciola* (Ehrenberg) J.W.Griffith & Henfrey, 1856[K M]
58	*Hydrosera triquetra* G.C.Wallich, 1858[K M]
59	*Licmophora flabellata* (Greville) C.Agardh 1831[M]
60	*Aulacoseira granulata* (Ehrenberg) Simonsen 1979[K M]
61	*Melosira varians* C. Agardh, 1827[K M]
62	*Navicula cryptocephala* Kützing, 1844[K M]
63	*Navicula marina* Ralfs, 1861[K M]
64	*Navicula radiosa* Kützing, 1844[K M]
65	*Navicula placentula* (Ehrenberg) Kützing 1844[K]
66	*Navicula* sp.[K M]
67	*Nitzschia closterium* (Ehrenberg) W.Smith, 1853[K M]
68	*Nitzschia lorenziana* Grunow, 1880[K M]
69	*Nitzschia paradoxa* (J.F.Gmelin) Grunow, 1880[K M]
70	*Nitzschia plana* W.Smith, 1853[K M]
71	*Nitzschia sigma* (Kützing) W. Smith, 1853 [K M]
72	*Nitzschia sigmoidea* (Nitzsch) W.Smith, 1853[M]
73	*Paralia sulcata* (Ehrenberg) Cleve, 1873[K M]
74	*Pinnularia braunii* (Grunow) Cleve, 1895[K M]
75	*Pinnularia major* (Kützing) Rabenhorst, 1853[K M]
76	*Pleurosigma angulatum* (Queckett) W.Smith, 1853[K M]
77	*Pleurosigma elongatum* W.Smith, 1852[K]
78	*Skeletonema costatum* (Greville) Cleve, 1873[K]
79	*Synedra ulna* (Nitzsch) Ehrenberg, 1832[K M]
80	*Synedra* sp.[M]
81	*Surirella biseriata* Brébisson, 1835[K M]
82	*Surirella gemma* Ehrenberg, 1839[K]
83	*Surirella robusta* Ehrenberg, 1840[K M]
84	*Surirella ovata* Kützing 1844[K M]
85	*Surirella tenera* W.Gregory, 1856[K]
86	*Thalassionema nitzschioides* (Grunow) Mereschkowsky, 1902[K M]
87	*Trachyneis aspera* (Ehrenberg) Cleve, 1894[K]
88	*Trachyneis debyi* (Leuduger-Fortmorel) Cleve,1894[K]
89	*Triceratium alternans* J.W.Bailey, 1851[K M]
90	*Triceratium favus* Ehrenberg, 1839[K M]
91	*Vanheurckia lewisiana* (Greville) Brébisson, 1869[K M]

No.	Taxa
Phylum Chlorophyta	
92	*Actinastrum hantzschii* Lagerheim, 1882[K M]
93	*Ankistrodesmus falcatus* (Corda) Ralfs 1848[M]
94	*Ankistrodesmus gracilis* (Reinsch) Korshikov, 1953[M]
95	*Chlamydomonas* sp.[M]
96	*Chodatella subsalsa* Lemmermann, 1898[M]
97	*Coelastrum microporum* Nägeli, 1855[M]
98	*Cosmarium obtusatum* (Schmidle) Schmidle, 1898[M]
99	*Cosmarium quadrum* P.Lundell, 1871[M]
100	*Closterium gracile* Brébisson ex Ralfs, 1848[K M]
101	*Closterium intermedium* Ralfs, 1848[K M]
102	*Closterium kuetzingii* Brébisson, 1856[M]
103	*Closterium macilentum* Brébisson, 1856[M]
104	*Closterium moniliferum* Ehrenberg ex Ralfs, 1848[K M]
105	*Closterium* sp.[K M]
106	*Crucigenia quadrata* Morren, 1830[K M]
107	*Crucigenia lauterbornii* Schmidle, 1900[M]
108	*Desmidium baileyi* (Ralfs) Nordstedt, 1880[M]
109	*Dictyosphaerium pulchellum* H.C.Wood, 1873[K M]
110	*Dimorphococcus lunatus* A.Braun, 1855[M]
111	*Eudorina elegans* Ehrenberg, 1832[M]
112	*Hyalotheca dissiliens* Brébisson ex Ralfs, 1848[M]
113	*Micractinium pusillum* Fresenius, 1858[K M]
114	*Mougeotia* sp.[M]
115	*Gonium pectorale* O.F.Müller, 1773[M]
116	*Oedogonium vulgare* (Wittrock ex Hirn) Tiffany,1934[K M]
117	*Pandorina morum* (Müller) Bory de Saint-Vincent, 1824[K M]
118	*Pediastrum biradiatum* Meyen 1829[M]
119	*Pediastrum duplex* Meyen, 1829[K M]
120	*Pediastrum simplex* Meyen, 1829[K M]
121	*Pediastrum tetras* (Ehrenberg) Ralfs, 1845[K M]
122	*Scenedesmus acuminatus* (Lagerheim) Chodat, 1902[K M]
123	*Scenedesmus arcuatus* Lemmermann, 1899[M]
124	*Scenedesmus denticulatus* Lagerheim, 1882[K]
125	*Scenedesmus quadricauda* (Turpin) Brébisson, 1835[K M]
126	*Sphaerocystis schroeteri* Chodat, 1897[M]
127	*Sphaerocystis polycocca* Korshikov, 1953[M]
128	*Spirogyra ionia* Wade, 1949[K M]
129	*Staurastrum arctiscon* (Ehrenberg ex Ralfs) P.Lundell, 1871[M]
130	*Staurastrum gracile* Ralfs ex Ralfs, 1848[M]
131	*Staurastrum dickiei* Ralfs, 1848[K M]
132	*Staurastrum leptocladum* Nordstedt, 1870[M]
133	*Tetraëdron gracile* (Reinsch) Hansgirg, 1889[K M]
134	*Volvox aureus* Ehrenberg, 1832[M]
Phylum Euglenophyta	
135	*Euglena acus* Ehrenberg, 1830[K M]
136	*Euglena deses* Ehrenberg 1834 [K M]
137	*Euglena gracilis* Klebs, 1883[K M]
138	*Euglena oxyuris* Schmarda, 1846 [K M]
139	*Euglena oblonga* F.Schmitz, 1884[M]
140	*Euglena polymorpha* P.A.Dangeard, 1902[K M]
141	*Euglena rostrifera* L.P.Johnson, 1944[K M]
142	*Euglena spirogyra* Ehrenberg, 1832[K M]
143	*Euglena viridis* Ehrenberg, 1830[K M]
144	*Euglena* sp.[K M]
145	*Lepocinclis fusiformis* (H.J. Carter) Lemmermann, 1901[K M]
146	*Lepocinclis ovum* (Ehrenberg) Lemmermann, 1901[K M]
147	*Lepocinclis reeuwykiana* W.Conrad, 1934[K M]
148	*Lepocinclis salina* F.E.Fritsch, 1914[K M]
149	*Phacus contortus* Bourrelly, 1952[K M]
150	*Phacus hamatus* Pochmann, 1942[K M]
151	*Phacus helikoides* Pochmann, 1942[K M]
152	*Phacus lefevrei* Bourrelly, 1952[K M]
153	*Phacus longicauda* (Ehrenberg) Dujardin 1841[K M]
154	*Phacus ovalis* (Woronichin) Popowa 1955[K M]
155	*Phacus pleuronectes* (O.F. Müller) Dujardin, 1841[K M]
156	*Phacus trapezoides* Stawinski, 1969[K M]
157	*Phacus tortus* (Lemmermann) Skvortzov, 1928[K M]
158	*Phacus suecicus* Lemmermann, 1910[M]
159	*Strombomonas australica* (Playfair) Deflandre, 1930[K M]
160	*Strombomonas fluviatilis* (Lemmermann) Deflandre,1930[K M]
161	*Strombomonas limonensis* Yacubson[K M]
162	*Strombomonas longicauda* (Swirenko) Deflandre,1930[K M]
163	*Strombomonas napiformis* (Playfair) Deflandre, 1930[K M]
164	*Trachelomonas armata* (Ehrenberg) F.Stein, 1878[K M]
165	*Trachelomonas acanthostoma* A.C.Stokes,1887[K]
166	*Trachelomonas hispida* (Perty) F.Stein, 1878[K M]
167	*Trachelomonas volvocina* (Ehrenberg) Ehrenberg, 1834[K M]
168	*Trachelomonas volzii* Lemmermann, 1906[K M]
Phylum Dinophyta	
169	*Ceratium hirundinella* (O.F.Müller) Dujardin, 1841[K M]
170	*Protoperidinium pentagonum* (Gran) Balech, 1974[K M]
171	*Peridinium* sp.[K M]

3.3. Relationship between phytoplankton community and environmental parameters

The study used CCA for analysis of the relationship between phytoplankton and environmental factors. In the dry season, thirteen taxa were chosen with a relative abundance ≥5% and were included in data analysis using CCA (Table 4). The first two axes explain 76.9% of the total variance with 52.1% for axis 1 and 24.8% for axis 2 (Fig. 3A). The first axis was positively correlated with nitrate and DO, but negatively related to EC and COD. The second axis was positively correlated with PO_4^{3-}, turbidity, total P, TSS, pH, NH_4^+, and BOD_5, but negatively correlated with temperature. Besides, Fig. 3A showed that the abundance of *Geitlerinema splendidum*, *Oscillatoria acuta,* and *O. tenuis* were positively related to turbidity (r=0.54-0.64; p=0.01-0.02) and TSS (r=0.72-0.74; p<0.01). Meanwhile, the abundance of *Coscinodiscus subtilis* was positively correlated with DO (r=0.58; p=0.01) and NO_3^- (r=0.50; p=0.04). The abundance of *Microcystis aeruginosa* was positively related to pH (r=0.55; p=0.02), EC (r=0.82; p<0.01), and salinity (r=0.80; p<0.01). The abundance of *Microcystis panniformis*

was positively related to EC (r=0.61; p<0.01) and salinity (r=0.58; p=0.01). Some factors of COD, BOD_5, NH_4^+, and PO_4^{3-} were positively correlated with the abundance of *Arthrospira platensis* (r=0.55-0.65; p=0.01-0.02).

Table 4. Codes of key species were collected in dry and rainy in Soc Trang for the canonical correspondence analysis.

Species	Code	Dry	Rainy	Dry abundance (mean ± SE) cell/litre	Rainy abundance (mean ± SE) cell/litre
Sphaerospermopsis aphanizomenoides	Saph		+	-	150±123
Arthrospira platensis	Apla	+	+	238±67	1158±619
Geitlerinema splendidum	Gspl	+		379±337	-
Jaaginema sp.	Jaag	+	+	7318±3400	15920±15117
Microcystis aeruginosa	Maer	+	+	42±27	249±89
Microcystis panniformis	Mpan	+	+	35±25	37±15
Oscillatoria acuta	Oacu	+	+	1475±815	224±47
Oscillatoria perornata	Oper	+	+	14517±6820	16067±6652
Oscillatoria princeps	Opri		+	-	168±42
Oscillatoria tenuis	Oten	+	+	277±143	230±42
Oscillatoria sp.	Osci	+	+	1902±703	1022±409
Phormidium chalybeum	Pcha		+	-	59±36
Planktothrix sp.	Plan	+	+	2098±1105	1760±614
Coscinodiscus subtilis	Csub	+	+	12740±7809	139±40
Aulacoseira granulata	Agra		+	-	741±391
Eudorina elegans	Eele		+	-	151±63
Pandorina morum	Pmor		+	-	1873±1014
Lepocinclis salina	Lsal	+	+	203±111	1744±756
Phacus longicauda	Plon		+	-	187±50
Strombomonas longicauda	Slon	+		55±36	-
Protoperidinium pentagonum	Ppen		+	-	390±187
Total species		**13**	**19**		

(- : not available).

In the rainy season, nineteen taxa were collected with relation abundance ≥5% and were included in data analysis using CCA (Table 4). A total of 63.4% of the relationship between selected species and environmental variables were elucidated by the first two axes of CCA with 39.5% for axis 1 and 23.9% for axis 2 (Fig. 3B). The first axis was negatively related to NO_3^-, PO_4^{3-}, pH, and BOD_5. The second axis was positively correlated with temperature and ammonium and negatively related to DO, TSS, turbidity, and total P. Fig. 3B showed that the abundance of *Coscinodiscus subtilis* was positively correlated with the turbidity (r=0.69; p<0.01) and TSS (r=0.69-0.64; p<0.01). Meanwhile, the abundance *Phacus longicauda* was negatively related to the turbidity (r=-0.55; p=0.01) and TSS (r=-0.54; p=0.01). Some factors of pH, EC, and salinity were positively correlated with the abundance of *Oscillatoria acuta* (r=0.50-0.63; p=0.01-0.04). The abundance of *Arthrospira platensis* and *Oscillatoria* sp. were positively related to PO_4^{3-} (r=0.81; p<0.01 and r=0.55; p=0.01, respectively). The abundance of *Phormidium chalybeum* was positively correlated with turbidity (r=0.49; p=0.03) and negatively related to the temperature (r=-0.64; p<0.01).

4. Discussion

The water temperature at the water bodies of Soc Trang was within the range of 28-31°C, which was similar to the water temperature of some other water bodies in Southern Vietnam [14, 15]. However, this temperature was higher than those in the Red river from Northern Vietnam (around 24°C) [12]. The water quality of Soc Trang has a water pH of slightly neutral, which was higher compared to the pH in the Vam Co river (pH=3.9-7.0) [14] but lower than in the Red river (pH=7.5-7.7) [12], Dong Nai river (pH=6.2-8.9) [15], and Ba Lai river (pH=7.2-8.5) [22]. The current study, the mean salinity of water in the rainy season (0.16±0.08‰) was lower than in the dry season (0.99±0.49‰). In the dry season, except at the Vinh Chau site with the highest salinity of 6% near the coastal area of Soc Trang, the remaining sites had salinity less than 0.5‰. Whereas, in the rainy season,

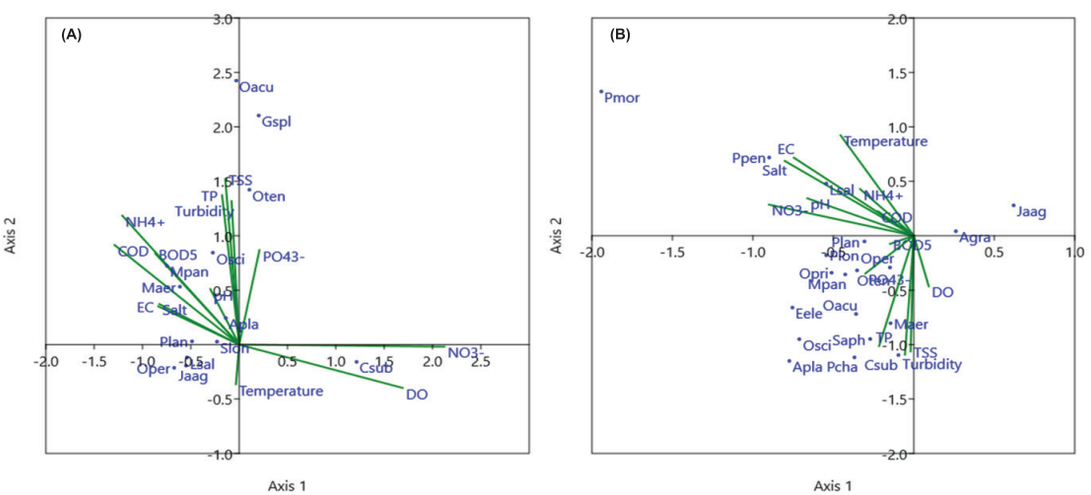

Fig. 3. CCA based on environment parameters and relative abundance of phytoplankton for sampling sites in Soc Trang province in (A) dry season and (B) rainy season.

the salinity in Vinh Chau cut down to 1.51‰ and the other sampling sites had salinities less than 0.2‰. Soc Trang is one of the provinces in the Mekong delta affected by salinization. However, at the time of the study, the inland water bodies of Soc Trang were not saline. The salinity of water in Soc Trang was lower than Ba Lai river (Ben Tre province, 4.8±3.2‰) [22]. The turbidity of the water in this study area was quite high thus it should strongly contribute to the TSS (16-290.7 mg/l in the case of water bodies of Soc Trang), which was clearly shown by in situ measurement. The value of DO in Soc Trang was lower than that in the Red river [12], Dong Nai river [15], and Ba Lai river [22]. In addition, the COD and BOD_5 values recorded were higher than in Bien Ho and Lak lake [13]. The nitrate and ammonium concentrations in this study were within the range of inorganic nitrogen concentration from Vam Co river at 0.28-0.43 mg/l [14] and not as high as that in the Red river, which ranged from 0.23-0.86 mg/l [12]. The phosphate concentration in Soc Trang ranged from 0.00-0.59 mg/l (Table 1) and the total phosphorus concentration should be higher than the phosphate concentration. According to C.F. Reynolds (2006) [23], the water bodies within Soc Trang are characterised by mesotrophic and eutrophic conditions, therefore, they are favourable for the development of phytoplankton. Generally, according to QCVN 08:2015/BTNMT [17], the value of pH and nutrients (nitrate, phosphate) were classified into class A2, which is only acceptable for domestic purposes, whereas the concentration of COD, BOD_5, DO, TSS, and ammonium matched into class B2, which is only acceptable for irrigation and transportation.

Regarding phytoplankton, many studies have been conducted and published. T.S. Dao, et al. (2016) [14] found 290 algal species belonging to 7 groups in the Vam Co river, and green algae were the dominant species in number. T.L. Pham (2017b) [15] recorded 139 species of phytoplankton in the Dong Nai river, and diatom was the most abundant in the phytoplankton composition structure. In another study, H.T.T. Hoang, et al. (2018) [24] identified 87 taxa belonging to 7 groups in the Day river, and green algae had the highest number of species of them. In the current study, 172 species of phytoplankton were recorded and the phytoplankton in Soc Trang were higher than in the Day and Dong Nai rivers, but lower than that of the Vam Co river. Besides, the salinity recorded in the study area was at a low level, which is suitable for freshwater species to grow. Phytoplankton densities during the monitoring period were relatively high with a mean value of 40,370 cells/l in the dry season and 56,243 cells/l in the rainy season. This high density will be an abundant food source for aquatic species, especially in aquaculture. On the other hand, N.G. Jafari, et al. (2006) [25] found some genera such as *Oscilatoria*, *Microcystis*, *Euglena*, and *Phacus,* which indicate organically-polluted water. Similar genera were also recorded in the present investigation.

The life and growth of phytoplankton depends on their environmental conditions. Therefore, the seasonal variations of environmental factors would lead to the change of phytoplankton. The CCA analysis was carried out to reflect the correlation between phytoplankton communities and environmental factors. Z. Ke, et al. (2012) [4] reported that silicate, nitrate, and temperature were the most relevant environmental factors to regulate the horizontal pattern of early-summer phytoplankton. Some other studies conduct CCA analysis like that of H.J. Zhao, et al. (2015) [26] showed that total nitrogen, salinity, and COD influenced the growth of *Pseudanabeana limnetica*, temperature and COD affected the growth of *Raphidiopsis curvata*, and temperature, phosphate, ammoniacal nitrogen, and pH impacted the growth of *Chlorella vulgari* and *Cosmarium* sp. Then, Z. Xu, et al. (2016) [27] presented that the abundance of *Dinophysis fortii* was negatively correlated with seawater temperature suggesting that harmful algal blooms caused by this species may primarily occur in spring. W. Zhenjiang, et al. (2017) [6] recorded the distribution of phytoplankton was affected by iron ion, transparency, pH, water depth, and temperature. Another study by N. Wang, et al. (2018) [28] using redundancy analysis revealed that the most significant environmental factors influencing the phytoplankton community were water temperature, dissolved total phosphorus, salinity, and total nitrogen. In Vietnam, there are published studies involving the relationship between phytoplankton and environmental parameters in Refs. [2, 5, 12-15, 22, 29]. Those studies present phytoplankton assemblages that are correlated with environmental factors. However, depending on the water quality characteristics in each area, certain parameters were the key factors affecting the phytoplankton assemblage there. In the present study, during the dry season, the abundance of *Coscinodiscus subtilis* was affected by DO and NO_3^- while the abundance of *Geitlerinema splendidum*, *Oscillatoria acuta,* and *O. tenuis* were influenced by turbidity and TSS. Besides, the pH, EC, and salinity impacted the abundance of *Microcystis aeruginosa* and *M. panniformis* and the abundance of *Arthrospira platensis* was affected by COD, BOD_5, NH_4^+, and PO_4^{3-}. Whereas during the rainy season, the phytoplankton-environment relationship changed such as the turbidity and TSS impacting the abundance of *C. subtilis* and *Phacus longicauda*; the abundance of *Phormidium chalybeum* was influenced by turbidity; the PO_4^{3-} affected the abundance of *A. platensis* and *Oscillatoria* sp., and the pH, EC, and salinity influenced the abundance of *O. acuta*. Most of the phytoplankton species that had relationships with environmental factors were freshwater species. In general, the phytoplankton assemblage was influenced by pH, EC, salinity, turbidity, TSS, and PO_4^{3-} during both seasons.

5. Conclusions

In the current study, the environmental parameters and phytoplankton community were seasonally investigated of some water bodies in Soc Trang province. Results showed that water quality was placed into class B2, except for pH, nitrate, and phosphate, which were placed into class A2. The nutrient concentration (nitrate, phosphate) in Soc Trang are appropriate

for the growth of phytoplankton. There are 171 phytoplankton taxa belonging to the six divisions Cyanophyta, Chrysophyta, Bacillariophyta, Chlorophyta, Euglenophyta, and Dinophyta of which Bacillariophyta had the highest contribution in species number. The phytoplankton community is related to environmental factors during both dry and rainy seasons. The phytoplankton assemblage was influenced by environmental factors. The results of this study contributed not only essential information on phytoplankton composition and abundance, but possibly also using algae as an indicator for surface water quality assessment in Soc Trang province.

CRediT author statement

Thi Trang Le: Sample analysis, Taxonomic identification, Data processing, Writing the manuscript; Doan Dang Phan: Samples collection, Supporting data analysis; Van Tien Tran: Samples collection, Map drawing; Van Tu Nguyen: Supervise and comment on editing the manuscript for completeness.

COMPETING INTERESTS

The authors declare that there is no conflict of interest regarding the publication of this article.

REFERENCES

[1] S.X. Long, C. Chen, Z.W. Liu, et al. (2013), "Relationship between phytoplankton and environment factors in Lake Hongfeng", *Journal of Environmental Biology*, **34(2)**, pp.445-449.

[2] T.L. Pham (2017a), "Environmental gradients regulate the spatio-temporal variability of phytoplankton assemblages in the Can Gio mangrove biosphere reserve, Vietnam", *Ocean Science Journal*, **52(4)**, pp.537-547, DOI: 10.1007/s12601-017-0045-0.

[3] Y. Ye, Y. Luo, Y. Wang, et al. (2017), "Relation between diversity of phytoplankton and environmental factors in waters around Nanri island", *Applied Ecology and Environmental Research*, **5(3)**, pp.241-252, DOI: 10.15666/aeer/1503_241252.

[4] Z. Ke, Y. Tan, L. Huang, et al. (2012), "Relationship between phytoplankton composition and environmental factors in the surface waters of southern South China sea in early summer of 2009", *Acta Oceanologica Sinica*, **31(3)**, pp.109-119, DOI: 10.1007/s13131-012-0211-2.

[5] T.H. Le, T.L. Nguyen, T.H. Bui (2016), "The relationships between environmental factors and phytoplankton diversity indices in some estuarine ecosystems of Vietnam", *Natural Sciences and Technology*, **32(1S)**, pp.33-38.

[6] W. Zhenjiang, Y. Hongxian (2017), "Canonical correspondence analysis of phytoplankton community and environmental factors in Genhe river", *Asian Agricultural Research*, **9(9)**, pp.24-27, DOI: 10.22004/ag.econ.267658.

[7] A. Shirota (1966), *The Plankton of South Vietnam: Fresh Water and Marine Plankton*, Overseas Technical Cooperation Agency, 462pp.

[8] N.A. Truong (1993), *Taxonomy of Bacillariophyta Plankton in Marine Water of Vietnam*, Science and Technics Publishing House, 314pp (in Vietnamese).

[9] D.T. Duong (1996), *Cyanobacteria Taxonomy in Vietnam*, Agriculture Publishing House, 219pp (in Vietnamese).

[10] D.T. Duong, H. Vo (1997), *Vietnam Fresh Algae Taxonomy of Order, Chlorococcale*, Agriculture Publishing House, 503pp (in Vietnamese).

[11] V.T. Nguyen (2003), *Algal Biodiversity in Vietnam inland Waterbody*, Agriculture Publishing House, 485pp (in Vietnamese).

[12] T.T. Duong, T.P.Q. Le, T.C. Ho, et al. (2014), "Phytoplankton community structure and water quality of Red river, Vietnam", *Journal of Vietnamese Environment*, **6(1)**, pp.27-33, DOI: 10.13141/jve.vol6.no1.pp27-33.

[13] T.S. Dao (2016), "Relationship between phytoplankton and environmental variables from Bien Ho and Lak lakes in Central Highland of Vietnam", *Journal of Environment and Ecology*, **7(2)**, pp.1-20, DOI: 10.5296/jee.v7i2.9704.

[14] T.S. Dao, T. Bui (2016), "Phytoplankton from Vam Co river in Southern Vietnam", *Environmental Management and Sustainable Development*, **5(1)**, pp.113-125, DOI: 10.5296/emsd.v5i1.8775.

[15] T.L. Pham (2017b), "The seasonal and spatial variations of phytoplankton community in corrections with environment factors in the Dong Nai river, Vietnam", *Journal of Science, Ho Chi Minh City University of Education*, **14(3)**, pp.149-161.

[16] T.H.O. Duong, T.G. Huynh, V.U. Nguyen (2014), "Phytoplankton communities biodiversity in the Cu Lao Dung mangrove, Soc Trang province", *International Conference Proceeding: Aquaculture and Environment: A Focus in The Mekong delta, Vietnam*, Can Tho University, 20pp.

[17] Vietnam Ministry of Natural Resources and Environment (2015), *QCVN 08:2015/BTNMT, National Technical Regulation on Surface Water Quality*, 13pp (in Vietnamese).

[18] American Public Health Association (2012), *Standard Methods for The Examination of Water and Wastewater*, 541pp.

[19] T.V. Desikachary (1959), *Cyanophyta*, University of Madras, Indian Council of Agricultural Research, 686pp.

[20] G.B. Edward, D.C. Sigee (2015), *Freshwater Algae: Identification and Use as Bioindicators*, 2nd Edition, Wiley-Blackwell, 296pp, DOI: 10.1002/9781118917152.

[21] Algae Base (2021), "Listing the world's Algae", http://www.algaebase.org, accessed 10 October 2021.

[22] T.L. Pham, T.N.D. Tran, T.T. Trse, et al. (2017), "Seasonal variations of phytoplankton community structure in relation to physico-chemical factors in Ba Lai river, Ben Tre province", *Vietnam J. Agri. Sci.*, **15(5)**, pp.631-641 (in Vietnamese).

[23] C.S. Reynolds (2006), *Ecology of Phytoplankton*, Cambridge University Press, 535pp, DOI: 10.1017/CBO9780511542145.

[24] H.T.T. Hoang, T.T. Duong, K.T. Nguyen, et al. (2018), "Impact of anthropogenic activities on water quality and plankton communities in the Day river (Red river delta, Vietnam)", *Environmental Monitoring and Assessment*, **190(2)**, pp.1-18, DOI: 10.1007/s10661-017-6435-z.

[25] N.G. Jafari, V.R. Gunale (2006), "Hydrobiological study of algae of an urban freshwater river", *Journal of Applied Sciences and Environmental Management*, **10(2)**, pp.153-158, DOI:10.4314/jasem.v10i2.43697.

[26] H.J. Zhao, Y. Wang, L.L. Yang, et al. (2015), "Relationship between phytoplankton and environmental factors in landscape water supplemented with reclaimed water", *Ecological Indicators*, **58**, pp.113-121, DOI: 10.1016/j.ecolind.2015.03.033.

[27] Z. Xu, Y. Chen, X. Meng, et al. (2016), "Phytoplankton community diversity is influenced by environmental factors in the coastal East China sea", *European Journal of Phycology*, **51(1)**, pp.107-118, DOI: 10.1080/09670262.2015.1107138.

[28] N. Wang, J. Xiong, X.C. Wang, et al. (2018), "Relationship between phytoplankton community and environmental factors in landscape water with high salinity in a coastal city of China", *Environmental Science and Pollution Research*, **25(28)**, pp.28460-28470, DOI: 10.1007/s11356-018-2886-1.

[29] T.T. Tran, N.H. Doan, B.D. Le (2015), "Seasonal variation of phytoplankton in Tuyen Lam reservoir in Da Lat, Vietnam", *Journal of Biology*, **37(3)**, pp.300-311, DOI: 10.15625/0866-7160/v37n4.6650.

General Instructions on using this template and submitting a manuscript to VJSTE: Thank you for preparing a manuscript for submission to VJSTE. Using this template, or following the guidelines below, will help us in processing your article.

The structure of different types of articles may vary according to the type of study, and the content of the article.

The following are the detailed main components of the original research and review articles submitted to the journal.

From 2023 onwards, you can submit your article at: https://mc04.manuscriptcentral.com/mostvjste

Original research

The original research should have three following parts:

Preliminary section: It includes title, list of all contributing authors with their institutional affiliation, and abstract (160-250 words) with at least 3 keywords.

Title: How to format a science article (replace with your real title)

Author(s): List the author name(s) separated by commas. Use superscript numbers to link affiliations, and symbols *†‡ for author notes. For example, Y. Obsie[1*], S.A. Adem[1, 2]

**Corresponding author(s):* Include the email addresses or telephone numbers of the corresponding author(s). Please use the asterisk (*) symbol for the corresponding author information. This information is at the bottom of the manuscript's first page.

Author's affiliation addresses:

[1]Affiliations should be preceded by superscript numbers corresponding to the author list

[2]For any institutions, please provide the institution name, street, district, city, country

Received ; revised ; accepted

Abstract:
Start your abstract here…
Keywords: **keyword 1, keyword 2, keyword 3…**
Classification number(s): **1.1, 3.4, 5.3, etc.**

Abstract: The abstract should range between 160 and 250 words and be structured in a single paragraph following keywords in a separate line. The abstract should represent the main part of the research manuscript. It should reflect a brief and comprehensive background following the aim of the study (main questions to be addressed), methods used for investigating the problem, a summary of significant findings, main conclusions, and implications of the results.

Keywords: They should come immediately after the abstract and contain 3-7 specific and relevant keywords. They should reflect the research study and the relevant field of research.

Classification numbers: Depend on the Journal's Classification Scheme.

Author(s) are encouraged to write a "Highlights" that summarises the most exciting, interesting points from your manuscript.

Manuscript section: It is the main body of the scientific manuscript including: 1) Introduction; 2) Material(s) and method(s); 3) Results and discussion (separation of these two sections is acceptable); 4) Conclusions; 5) Recommendations/Suggestions/Implications/Study limitations...(if any). These sections may slightly vary depending on the type of research approach and design used in the research. Each section should be numbered.

All of the Figures, Tables, and Equations should be cited in numerical order.

Figures

Fig. #: (Begin each figure caption with a label, "**Fig. 1.**" for example, as a new paragraph).

Fig. 1. The figure caption should begin with an overall descriptive statement of the figure followed by additional text. They should be immediately after each figure. Figure parts are indicated with capital letters **(A)**. If you prefer, you can place both the actual figures and captions logically through the text near where they are cited rather than at the end of the file (but not both). If a paragraph in the main text begins with the name of a figure, write out "Figure" in full (e.g., <para> "Figure 1 shows...").

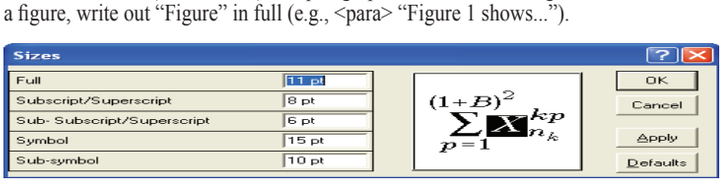

Fig. 1. The figure caption.

Tables

Table #: (Begin each table caption with a label "**Table 1.**", etc. as a new paragraph).

Table 1. Start this caption with a short description of your table. Format tables using the Word Table commands and structures. Do not create tables using spaces or tabs characters.

Table 1. Caption.

a	b	c	d	e
f				
g				
h				

Equations

$$\int_a^b xdx \tag{1}$$

Equations can be included. We do not recommend using the native Word 2007, 2008, 2010 or 2011 equation editor. This can in some cases produce less reliable MathML, the online markup language we use, which may result in display errors. Instead, use the legacy equation editor in Word (Insert menu; select insert object; select word equation) or use MathType (recommended). If you enter equations in simple LaTeX, check that they will convert accurately (Word 2007 and higher can convert simple LaTeX equations).

Closing section: It includes appendices/supplementary materials/data availability statement (if applicable), CRediT author statement (for multiple authors), acknowledgements (if applicable), competing interests, ethics (if any) and a complete list of references corresponding to all the citations given in the text of the manuscript. The appendices/supplementary materials may include data files and other material relevant to the research that should be submitted in separate files if required.

APPENDICES (if any)

The appendices should ideally be under 1000 words (approximately 2 A4 pages) for printing version. With longer appendices, they are only accepted for online publication.

CRediT author statement (for multiple authors)

CRediT offers authors the opportunity to share an accurate and detailed description of their diverse contributions to the published work.

ACKNOWLEDGEMENTS (if applicable)

This section is for the researchers who were funded for the research projects, and it should enclose all sources of financial support.

COMPETING INTERESTS

The author(s) declare(s) that there is no conflict of interest regarding the publication of this article.

REFERENCES

For in-text citation: References should be cited in the bracket with a number [1]. Multiple reference citations are separated by commas [2, 3] or if a series, dashes [4-6]. When citing sources with the author(s) and the year, they should be shortened to the first author's name, followed by et al. (with more than one author) and the year.

For reference list: With less than or equal to three authors, list all the author(s). With more than three authors, the first three should be listed and followed by et al.

References are listed in numerical order, and in the same order in which they are cited in text. The reference list should include all and only those references you have cited in the text. The reference list appears at the end of the article.

The reference consists of: Initial(s) and first/last name of the author(s), author' names separated by commas (Year of publication), "Titles of journal articles or chapter of book", *Title of Journal, Book or Other Publication*, **Volume(Number)** (if any), page numbers (if any), DOI (if any), URL and accessed date (if any) (in its original language if not English).

To cite a website and online/electronic resources, please include the accessed date (day month year).

Example of a reference list:

[1] T. Binzoni, T.S. Leung, D. Boggett, et al. (2003), "Non-invasive laser Doppler perfusion measurements of large tissue volumes and human skeletal muscle blood RMS velocity", *Phys. Med. Biol.*, **48(1)**, pp.2527-2549, DOI: 10.1088/0031-9155-48-15-318.

[2] H.W. Bischoff, H.C. Bold (1963), *Some Soil Algae from Enchanted Rock and Related Algal Species*, University of Texas Publications, 95pp.

[3] R. Busi (2016), "Weedy rice in the Philippines and Vietnam", https://www.aciar.gov.au/publication/technical-publications/weedy-rice-philippines-and-vietnam-final-report, accessed 15 July 2018.

Review articles

They should be different from the original research as they would contain different sections on the literature review. Authors may structure this part as per nature, background, and available literature on the issue argued in the manuscript.

For more detailed instructions, please visit our website: vietnamscience.vn or vietnamscience.vjst.vn

This manuscript template has been used from 2021 onwards.

P-ISSN 2525-2461 • E-ISSN 2615-9937

Vietnam Journal of Science, Technology and Engineering

MARCH 2023 • VOLUME 65 NUMBER 1

EDITORIAL BOARD

EDITORIAL OFFICE

113 Tran Duy Hung Str., Cau Giay Dist., Hanoi, Vietnam

Tel: (84.24) 39436793; Fax: (84.24) 39436794

Email: vjste@most.gov.vn

Website: vietnamscience.vn or vietnamscience.vjst.vn

PUBLICATION LICENCE

No. 459/GP-BTTTT 20th July 2021

No. 50/GP-BTTTT 1st February 2023